DOKUZ EYLÜL UNIVERSITY

GRADUATE SCHOOL OF NATURAL AND APPLIED SCIENCES

OPTIMIZATION OF SUPERCONDUCTING AND MECHANICAL PROPERTIES OF COATED SUPERCONDUCTOR FILMS

by

Osman ÇULHA

April, 2011

İZMİR

OPTIMIZATION OF SUPERCONDUCTING AND MECHANICAL PROPERTIES OF COATED SUPERCONDUCTOR FILMS

A Thesis Submitted to the
Graduate School of Natural and Applied Sciences of Dokuz Eylül University
In Partial Fulfillment of the Requirements for the Degree of Doctor of
Philosophy in Metallurgical and Materials Engineering,
Metallurgical and Materials Engineering Program

by
Osman ÇULHA

April, 2011
İZMİR

Ph.D. THESIS EXAMINATION RESULT FORM

We have read the entitled "**OPTIMIZATION OF SUPERCONDUCTING AND MECHANICAL PROPERTIES OF COATED SUPERCONDUCTOR FILMS**" completed by **OSMAN ÇULHA** under supervision of **DOÇ. DR. MUSTAFA TOPARLI** and we certify that in our opinion it is fully adequate, in scope and in quality, as a thesis for the degree of Doctor of Philosophy.
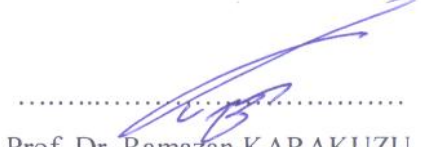
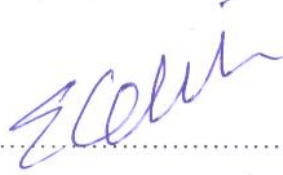Doç. Dr. Mustafa TOPARLI

Supervisor
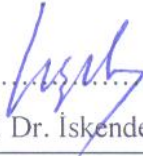
Prof.Dr. Tevfik AKSOY

Jury Member

Prof. Dr. Ramazan KARAKUZU

Jury Member

Prof. Dr. Erdal ÇELİK

Examining Committee Member

Prof. Dr. İskender IŞIK

Examining Committee Member

Prof. Dr. Mustafa SABUNCU

Director

Graduate School of Natural and Applied Science

ACKNOWLEDGEMENTS

OPTIMIZATION OF SUPERCONDUCTING AND MECHANICAL PROPERTIES OF COATED SUPERCONDUCTOR FILMS

ABSTRACT

The aim of this study is to determine microstructure, superconducting and mechanical properties of Yttrium (1) Barium (2) Copper (3) Oxygen (6.56) (YBCO) and YBCO thin films with Manganese (Mn) addition and Barium Manganese oxide formation as a flux pinning center. With this regard, YBCO superconducting films with/without Mn were coated onto (100) Strontium Titanate (STO) single-crystal substrates by metalorganic deposition using trifluoroacetate (TFA-MOD) technique. In order to determine solution characteristics which influence thin film structure; turbidity, pH values and rheological properties of the prepared solutions were measured by turbidimeter, pH meter and rheometer machines before drying and heating processes. In order to use suitable process regime, to define chemical structure and reaction type of intermediate temperature products, Differential Thermal Analysis-Thermograviometric (DTA-TG) and Fourier Transform Infrared (FT-IR) analysis were performed in the powder production using xerogels. Structural analysis of the produce films was performed through multipurpose X-ray Diffractometer (XRD). Surface morphologies of the films were investigated with help of Scanning Electron Microscope (SEM) and Atomic Force Microscope (AFM). Mechanical properties of the thin films were determined as a function of Mn addition by CSM instruments nanoindentation tester by calculating Young's modulus and hardness due to load–unload sensing analysis. Elastic properties and limit (E and yield stress) of the film and substrate materials were designated by using finite element method (FEM) and nanohardness experiments. Failure stress, contact-deformation characteristics of films depend on amount of formed Barium Manganese Oxide particles were obtained using algorithm with FEM and comparison of experimental and simulation results of indentation.

Keywords: YBCO based thin films, superconducting properties, nanoindentation and finite element modeling.

KAPLANMIŞ SÜPERİLETKEN FİLMLERİN SÜPERİLETKENLİK VE MEKANİK ÖZELLİKLERİNİN OPTİMİZASYONU

ÖZ

Bu çalışmanın amacı, sol-jel kaplama tekniğiyle üretilen Yitriyum (1) Baryum (2) Bakır (3) Oksijen (6.56) (YBCO) esaslı süperiletken ince filmlere Mn ilave edilmesiyle oluşan Baryum Manganoksit akı iğnelemsi merkezinin, filmin mikroyapısında, süperilektenlik özelliklerinde ve mekanik davranışında meydana gelen değişimlerinin belirlenmesidir. Bu kapsamda, farklı Mn içerikli filmler (001) Stronsiyum Titanat (STO) tek kristal altlıklar üzerine metalorganik depozitleme işlemi ile trifluoroacetate (TFA-MOD) yöntemi kullanılarak üretilmiştir. Film yapısına etki eden solüsyon karakteristiklerini belirlemek için bulanıklılık, ph ve reolojik özelliklerin belirlenmesi amacıyla Türbidimetre, pH metre ve Reometre cihazları kullanılmıştır. Başlangıç sıcaklarda oluşan ürünlerin reaksiyon tiplerini, kimyasal yapısını ve uygun ısıl işlem rejiminin belirlenmesi için Diferansiyel Termal Analysis-Termogravimetrik analiz (DTA-TG) ve Fourier Geçiş kızılötesi spektrometresi (FTIR) kullanılmıştır. Üretilen filmlerin faz analizleri X-ışını difraktometresi (XRD) kullanılarak, yüzey morfolojisi incelemeleri ise Enerji Saçılım Spektroskopu ilaveli Taramalı Elektron Mikroskobu (SEM/EDS) cihazı ve atomik kuvvet mikroskobu (AFM) kullanılarak yapılmıştır. YBCO esaslı ince filmlerin Mn ilavesine bağlı olarak değişen mekanik özellikleri, CSM nanosertlik ölçüm cihazından elde edilen yükleme-yük boşaltma eğrilerinden faydalanılarak belirlenmiştir. Filmlerin tek kristal altlığa olan yapışma mukavemeti ise Shimadzu Scratch tester cihazı kullanılarak elde edilen kritik kuvvetlerden hesaplanmıştır. YBCO esaslı filmlere ait Mn ilave ile değişen elastisite modülü ve sertliğin yanı sıra akma mukavemeti veya hasar mukavemeti, temas-deformasyon karakteristikleri deneysel olarak elde edilen yükleme-yük boşaltma eğrilerinin karşılaştırılmasının sonlu elemanlar modelleme programı ile yapılmasıyla belirlenmiştir.

Anahtar Kelimeler: YBCO esaslı ince film, süperilektenlik, nanosertlik ve sonlu elemanlar modelleme.

CHAPTER ONE

INTRODUCTION

After the discovery of High-T_c Superconductor (HTS), various applications of superconductor are attempted in various technological areas. Especially, these materials lead to an increase in performance of machines such as intensively using magnetic resonance imaging (MRI) in medicine, energy storage systems in transformer, magnetic separators, levitation, nuclear magnetic resonance (NMR), generators, engines, cables, superconducting wires and tapes, accelerators, electromagnets, electronic transistors and bolometers (Babu, Lida & Cardwell, 2006; Yoshida et al., 2006).

High-T_c thin films with a sharp resistive transition, high critical current density J_c and low flux noise which also show chemical integrity offer the potential for such applications (Lakew, Brasunas, Aslam and Pugel, 2004). Extensive studies are currently being carried out through worldwide on $YBa_2Cu_3O_{6.56}$ (YBCO) films grown on different single crystal and metal based substrates (Dwir et al, 1989). Many YBCO thin films have been developed using different deposition processes. Most of them use high vacuum techniques such as pulse laser deposition (PLD) and magnetron sputtering which can obtain high critical current densities on YBCO thin films. Nevertheless, they require significant start-up costs for long length coated conductor production (Jee et al., 2001). On the other hand, thin films prepared by non-vacuum techniques like metal organic decomposition using triflouro acetic acid (TFA-MOD) which is a sol–gel related method, exhebits similar superconducting properties and are relatively simple and inexpensive (Yamada et al., 2001). High quality YBCO films with high J_c can be fabricated by TFA-MOD process (Cui et al, 2005). Finding optimum process parameters for coating solution can be challenging but once the coating solution is found, it is very easy to obtain high J_c YBCO superconductors with supreme reproducibility. In spite of the fact that the TFA-MOD process using metal acetates as starting materials is more cost effective than vacuum

processes, highly purified metal acetates are expensive and thus it is desirable to find a more economic route. Recently, several attempts to use oxide powders such as commercially available YBCO powder as starting materials are reported and they showed comparable J_c for the YBCO films (Lee et al., 2006).

In this research, we presented a new approach by combining superior properties of solvent, especially 2, 4-pentanedionate, and commercially available YBCO powder with TFA, acetone and propionic acid as a preliminary study. Therefore, YBCO superconducting films were produced with $BaMnO_3$ from solutions prepared by using cheap and commercially available YBCO powders and Mn 2, 4-pentanedionate, TFA propionic acid, acetone and 2, 4-pentanedione without further purification or modification.

In practical applications, importance of mechanical properties of YBCO based films cannot be ignored. Superconducting films with poor mechanical properties are useless, even if they possess a good transport and flux pinning properties. Since additive particles as a pinning center are important changes in microstructure, their effect on micromechanical properties such as Young's modulus, hardness and adhesion strength have to be investigated depending on additional particles type and quantity. As the main aim of this study was to determine the additional particle effects on mechanical (hardness and Young's modulus) and superconducting properties (T_c) of YBCO, finite element modeling of pure YBCO and YBCO with Mn addition ones were investigated for determining elastic limit of films. In addition, mechanical property variations of pure YBCO and YBCO thin films with Mn (react as $BaMnO_3$) were obtained by indentation and scratch techniques. Thus, $BaMnO_3$ nanoparticle effects on superconducting, structural and mechanical properties of films were studied.

CHAPTER TWO

THEORETICAL BACKROUND

2.1 Superconductor and Superconductivity

Superconductivity is defined and the basic phenomena as well as theories are described. Crystal structures and physical properties of high temperature superconducting (HTSC) materials are then examined in some detail. Key factors of HTSC such as grain boundaries and defects are discussed with a particular emphasis on the effect of weak links, and pinning centers on electromagnetic properties. Some applications of HTSC in power industry and electronics are summarized finally (Xu, 2003).

2.1.1 Definition of Superconductivity and Basic Phenomenon

As most high-purity metals are cooled down to temperatures nearly 0 K, the electrical resistivity decreases gradually, approaching some small yet finite value that is characteristic of the particular metal. There are a few materials, however, for which the resistivity, at a very low temperature, abruptly plunges from a finite value to one that is virtually zero and remains there upon further cooling. Materials that display this latter behavior are called *superconductors,* and the temperature at which they attain **superconductivity** is called the critical temperature T_c. The resistivity–temperature behaviors for superconductive and non-superconductive materials are contrasted in Figure 2.1. The critical temperature varies from superconductor to superconductor but lies between less than 1 K and approximately 20 K for metals and metal alloys. Recently, it has been demonstrated that some complex oxide ceramics have critical temperatures in excess of 100 K (Callister, 2000, p.790).
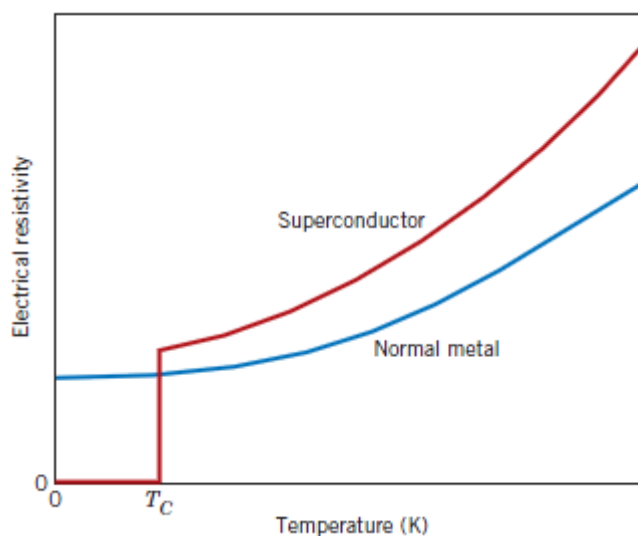
Figure 2.1 Temperature dependence of the electrical resistivity for normally conducting and superconducting materials in the vicinity of 0 K (Callister, 2000, p.793).

At temperatures below the superconducting state will cease upon application of a sufficiently large magnetic field, termed the critical field which depends on temperature and decreases with increasing temperature. The same may be said for current density; that is, a critical applied current density J_c exists below which a material is superconductive. Figure 2.2 shows schematically the boundary in temperature-magnetic field-current density space separating normal and superconducting states. The position of this boundary will, of course, depend on the material. For temperature, magnetic field, and current density values lying between the origin and this boundary, the material will be superconductive; outside the boundary, conduction is normal. The superconductivity phenomenon has been satisfactorily explained by means of a rather involved theory. In essence, the superconductive state results from attractive interactions between pairs of conducting electrons; the motions of these paired electrons become coordinated such that scattering by thermal vibrations and impurity atoms is highly inefficient. Thus, the resistivity, being proportional to the incidence of electron scattering, is zero. On the basis of magnetic response, superconducting materials may be divided into two classifications designated as type I and type II (Callister 2000, p. 793).
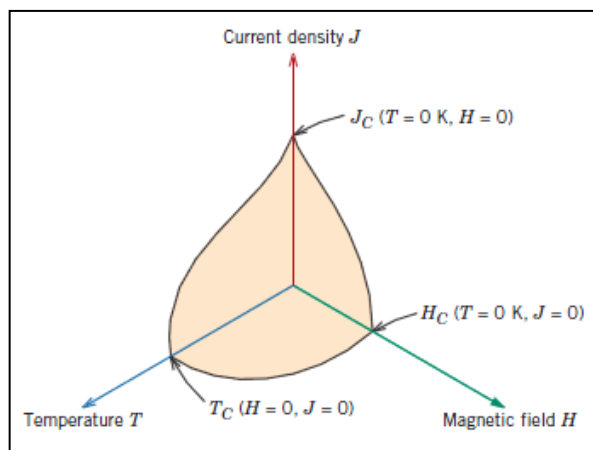
Figure 2.2 Critical temperature, current density, and magnetic field boundary separating superconducting and normal conducting states (schematic) (Callister 2000, p.793).

Type I materials, while in the superconducting state, are completely diamagnetic; that is, all of an applied magnetic field will be excluded from the body of material, a phenomenon known as the *Meissner effect,* which is illustrated in Figure 2.3. As H is increased, the material remains diamagnetic until the critical magnetic field is reached. At this point, conduction becomes normal, and complete magnetic flux penetration takes place (Callister 2000, p. 794).

Several metallic elements including aluminum, lead, tin, and mercury belong to the type I group. Type II superconductors are completely diamagnetic at low applied fields, and field exclusion is total. However, the transition from the superconducting state to the normal state is gradual and occurs between lower critical and upper critical fields, designated and respectively. The magnetic flux lines begin to penetrate into the body of material at and with increasing applied magnetic field, this penetration continues; at field penetration is complete. For between fields and the material exists in what is termed a mixed state—both normal and superconducting regions are present. Type II superconductors are preferred over type I for most practical applications by virtue of their higher critical temperatures and critical magnetic fields (Callister 2000, p. 794).
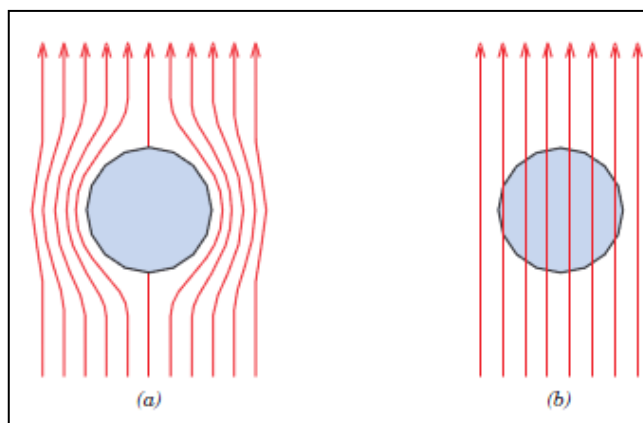
Figure 2 3 Representation of the Meissner effect. (*a*) While in the superconducting state, a body of material (circle) excludes a magnetic field (arrows) from its interior. (*b*) The magnetic field penetrates the same body of material once it becomes normally conductive (Callister, 2000; Warnes, 2003).

Diamagnetism is a very weak form of magnetism that is nonpermanent and persists only while an external field is being applied. It is induced by a change in the orbital motion of electrons due to an applied magnetic field. The magnitude of the induced magnetic moment is extremely small, and in a direction opposite to that of the applied field. Thus, the relative permeability, μ_r, is less than unity (however, only very slightly), and the magnetic susceptibility is negative; that is, the magnitude of the *B* field within a diamagnetic solid is less than that in a vacuum. The volume susceptibility, χ_m, for diamagnetic solid materials is on the order of -10^{-5}. When placed between the poles of a strong electromagnet, diamagnetic materials are attracted toward regions where the field is weak (Callister, 2000; Warnes, 2003.) Figure 2.4 illustrates schematically the atomic magnetic dipole configurations for a diamagnetic material with and without an external field; here, the arrows represent atomic dipole moments, whereas for the preceding discussion, arrows denoted only electron moments. The dependence of *B* on the external field *H* for a material that exhibits diamagnetic behavior is presented in Figure 2.5. Diamagnetism is found in all materials; but because it is so weak, it can be observed only when other types of magnetism are totally absent. This form of magnetism is of no practical importance (Warners, 2003, p.1032).
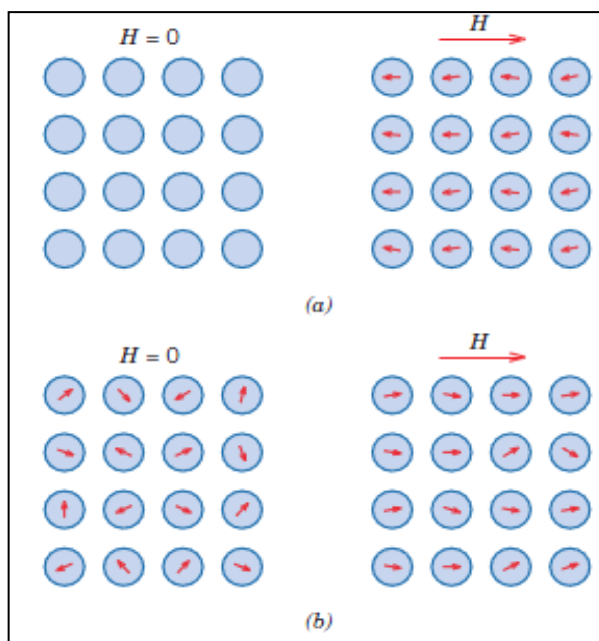
Figure 2.4 (*a*) The atomic dipole configuration for a diamagnetic material with and without a magnetic field. In the absence of an external field, no dipoles exist; in the presence of a field, dipoles are induced that are aligned opposite to the field direction. (*b*) Atomic dipole configuration with and without an external magnetic field for a paramagnetic material (Callister 2000, p. 770).

For some solid materials, each atom possesses a permanent dipole moment by virtue of incomplete cancellation of electron spin and/or orbital magnetic moments. In the absence of an external magnetic field, the orientations of these atomic magnetic moments are random, such that a piece of material possesses no net macroscopic magnetization. These atomic dipoles are free to rotate, and **paramagnetism** results when they preferentially align, by rotation, with an external field as shown in Figure 2.4.

These magnetic dipoles are acted on individually with no mutual interaction between adjacent dipoles. Inasmuch as the dipoles align with the external field, they enhance it, giving rise to a relative permeability that is greater than unity, and to a relatively small but positive magnetic susceptibility.
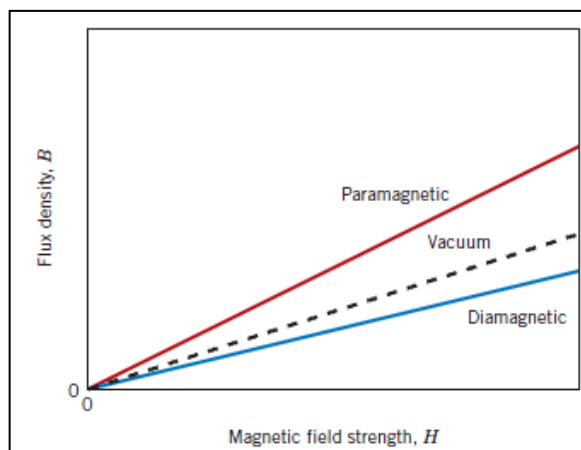
Figure 2.5 Schematic representation of the flux density
B versus the magnetic field strength *H* for diamagnetic
and paramagnetic materials.

A schematic *B*-versus-*H* curve for a paramagnetic material is also shown in Figure 2.5. Both diamagnetic and paramagnetic materials are considered to be nonmagnetic because they exhibit magnetization only when in the presence of an external field. Also, for both, the flux density *B* within them is almost the same as it would be in a vacuum (Callister 2000, p. 770).

Certain metallic materials possess a permanent magnetic moment in the absence of an external field, and manifest very large and permanent magnetizations. These are the characteristics of **ferromagnetism,** and they are displayed by the transition metals iron (as BCC ferrite), cobalt, nickel, and some of the rare earth metals such as gadolinium (Gd) (Callister 2000, p. 771).

Superconductivity is a state of matter that is characterized by two distinct effects: zero resistance and diamagnetism, which means the expulsion of magnetic fields. With the successfully liquefied helium, a serial of experiments such as resistivity measurements can be performed at very low temperatures. Superconductivity was first observed in 1911 by the Dutch physics Professor H.K. Onnes at the University of Leiden. In one of his low temperature experiments, Onnes found the resistance of mercury did not fall continuously as expected, but instead dropped suddenly to zero at around 4.2 K over a range of a few hundredths of a degree. This phenomenon, a

real disappearance of the resistivity rather than just a decrease below measure value of the voltmeter, was defined as superconductivity. In the following decades, many other superconductors, including lead at 7.2 K, niobium at 8 K, and niobium nitrides at 15 K, and niobium germanium at 23 K, were discovered. In 1933, 25 years were to pass before Meissner and Ochsenfeld found that superconductors also exclude magnetic flux. This was another very important discovery in the property of superconductivity. One would expect, due to the perfect conductivity, that the excluding from entering a superconductor of magnetic flux should be related to the order of the applying magnetic field and the cooling through the transition temperature. However, in their experiment of applying magnetic field to Pb and Sn at low temperature, Meissner and Ochsenfeld found surprisingly that the magnetic field was always zero inside superconductor and nothing to do with the sequence of applying magnetic field. This phenomenon is termed the "Meissner Effect". The existence of the Meissner Effect requires a flow of circulating screen current and a real zero resistance in the superconducting state (Callister, 2000; Warnes, 2003).

2.1.2 General History of Superconductivity

The history of superconductivity can be divided into two stages: low temperature superconductor (LTSC) and high temperature superconductor. The chronological discovery of superconducting materials is shown in Figure. 2.6. From 1930 to 1980, the discovery of superconducting (SC) materials continued at moderate rate and it is called LTSC time. By 1933, Walter Meissner and R. Ochsenfeld discovered that superconductors are more than a perfect conductor of electricity and they also have an interesting magnetic property of excluding a magnetic field. A superconductor will not allow a magnetic field to penetrate its interior. It causes currents to flow that generate a magnetic field inside the superconductor that just balances the field that would have otherwise penetrated the material. This effect called the Meissner Effect (Sheahen, 2002). Later, the first widely-accepted theoretical understanding of superconductivity was outlined in 1957 by American physicists John Bardeen, Lean Cooper and John Schrieffer. Their theory of superconductivity known as the BCS Theory won them a Nobel Prize in 1972. It describes how and why the electrons in

the conductor may form an ordered superconducting state, and may predictions about many properties of superconductors which are in good agreement with experimental information (Whelan, 2003).

In 1962, Brian D. Josephson predicted that electrical current would flow between two superconducting materials even when they are separated by a non-superconductor or insulator. This tunneling behavior is known as the "Josephson Effect" and has been successfully applied to electronic devices.

Superconductivity progress was extremely slow up to 1986. Initial materials identified to be superconductive were elemental metals like Hg, Pb, Nb, followed by solid solutions like NbTi and intermetallics Nb_3Sn, V_3Si and Nb_3Ge. New breakthroughs in SC materials and higher critical or transition temperature were observed since 1986, especially between 1988 and 1990. The record of the transition temperature 23 K (Gavaler, 1973) was broken through by Bednorz and Muller (1986) with a successfully synthesized compound La_2CuO_4, which remains superconducting up to 30 K. Soon after in 1987, Pual Chu at University of Houston (Wu et al., 1987) announced the discovery of the yttrium barium copper oxide (YBCO) compound with a critical temperature of 90 K followed by the publishing of the composition of YBCO.

Until 1986, the highest critical transition temperature (T_c) achieved was 23 K. Liquid helium was still required for cooling. Then in 1986, a truly breakthrough discovery was made. Alex Muller and Georg Bednorz created a brittle ceramic compound that has a T_c of 30 K, (12 degrees above the old record for a superconductor). This discovery was so remarkable because ceramics normally do not conduct electricity well at all so, researchers had not considered them as possible superconductor candidates. The discovered ceramic compound was lanthanum, barium, copper and oxygen compound. This discovery won the two men a Nobel Prize the following year. It was later found that tiny amounts of this material were actually superconducting at 58 K, due to small amount of lead having been added as a calibration standard (Owens & Poole, 1996, p.3).

In February of 1987, a perovskite ceramic material, YBCO, was found to superconduct at 90 K. That was a significant discovery because it became possible to use liquid nitrogen as a coolant which is a commonly available one inasmuch as these materials superconduct at significantly higher temperatures; they are referred as High Temperature Superconductors (HTS). The world record T_c is 138 K which is held by thallium doped mercuric-cuprate comprised of the elements mercury, thallium, barium, calcium, copper and oxygen, under extreme pressure, its T_c can be coaxed up even higher approximately 25-30 degrees more at 300,000 atmospheres (Escudero, n.d.). Also in 2001, MgB_2 was discovered as a new material which does not contain any copper oxide and it was the first all-metal perovskite superconductor. Even though it has a T_c of only 39 K, it is cheap, easy to fabricate and much easier to work into wires than other HTS materials.
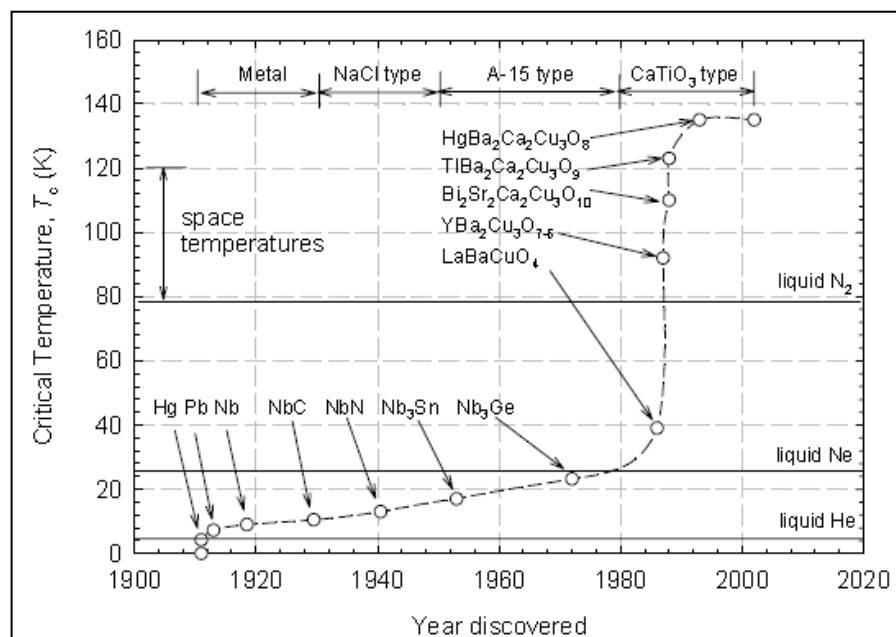
Figure 2.6 Chronological discoveries of superconducting materials (Xu, 2003).

2.1.3 Type I and Type II Superconductor

Based on the solution of the Ginzburg-Landau equations (Ginzburg, 1950.) by Abrikosov (Abrikosov, 1957) in 1957, superconductors fall in to two distinct categories: type I and type II superconductors. A type I superconductor ($\kappa < 1/\sqrt{2}$)

exhibits two characteristic properties, namely zero dc electrical resistance and perfect diamagnetism, when it is cooled below its critical temperature T_c. The second property of perfect diamagnetism, also called the Meissner effect, means that the magnetic susceptibility has the value $\chi = -1$, so a magnetic field cannot exist inside the material. There is a critical magnetic field Bc with the property that at the 0 K, applied fields $B_{app} \geq B_c$ drive the material normal. The temperature dependence of the critical field $B_c(T)$ can often be approximated by the equation (2.1):

$$Bc(T) = B_c[1 - (T/Tc)^2] \tag{2.1}$$

where $B_c(0) = B_c$
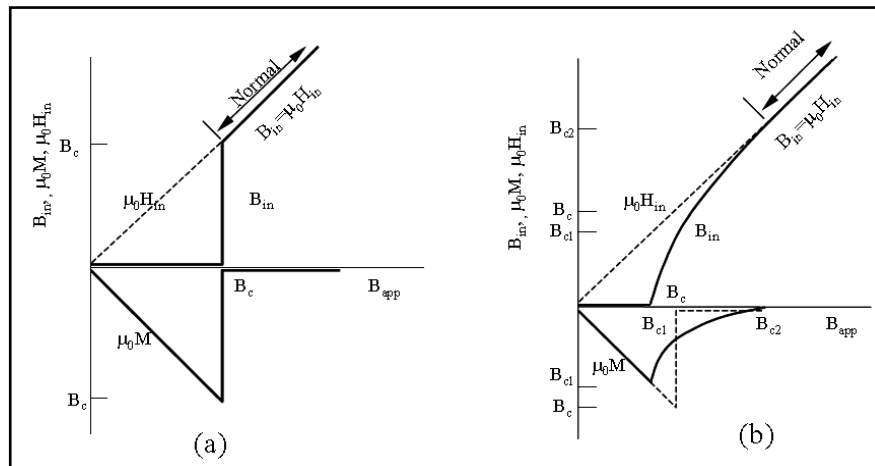
Figure 2.7 Type I and II superconductor, (a) Internal fields B_{in}, H_{in} and Magnetization M for an ideal Type I superconductor; (b) Internal fields B_{in}, H_{in} and Magnetization M for an ideal Type II superconductor. Flux is only partially excluded when the applied field is in the range from B_{c1} to B_{c2}. The type I superconductors are elements, whereas alloys and compounds are type II (Xu, 2003).

A type II superconductor ($\kappa > 1/\sqrt{2}$) is also a perfect conductor of electricity, with zero dc resistance, but its magnetic properties are more complex. It totally excludes magnetic flux in the Meissner state when the applied magnetic field is below the lower critical field B_{c1}, as indicated in Figure 2.7.

Very pure samples of lead, mercury and tin are examples of type I superconductors. High temperature ceramic superconductors such as YBCO, BiCaSrCuO are examples of type II. Figure 2.8 (a) is a graph of induced magnetic field versus applied magnetic field. When an external magnetic field is applied to a type I superconductor, the induced magnetic field cancels that applied field until there is an abrupt change from superconducting state to the normal state. Type I superconductors are very pure metals that typically have critical fields too low for use in superconducting magnets.

Figure 2.8 (b) is a graph of induced magnetic field of a type II superconductor versus applied field. Below H_c, the superconductor excludes all magnetic field lines. At field strengths between H_{c1} and H_{c2}, the field begins to intrude into the material. When this occurs the material is said to be in the mixed state, with some of the material in the normal state and some part still superconducting. Type I superconductors have H_c too low to be useful. However, type II superconductors have much larger H_{c2} values. YBCO superconductors have upper critical field values as high as 100 Tesla (T) (Xu, 2003).

Higher H_c and J_c values depend upon two important parameters which influence energy minimization; penetration depth and coherence length. Penetration depth is the characteristic length of the fall of a magnetic field due to surface currents. Coherence length is a measure of the shortest distance over which superconductivity may be established. The ratio of penetration depth to coherence length is known as the Ginzburg-Landau parameter. If this value is greater than 0.7, complete flux exclusion is no longer favorable and flux is allowed to penetrate the superconductor through cores known as vortices. Currents swirling around the normal cores generate magnetic fields parallel to the applied field. These tiny magnetic moments repel each other and move to arrange themselves in an orderly array known as fluxon lattice. This mixed phase helps to preserve superconductivity between H_{c1} to H_{c2}. It is very important that these vortices do not move in response to magnetic fields if superconductors are to carry large currents. Vortex movement results in resistivity. Vortex movement can be effectively pinned at sites of atomic defects, such as

inclusions, impurities and grain boundaries. Pinning sites can be intentionally introduced into superconducting material by the addition of impurities or through radiation damage (Xu, 2003).
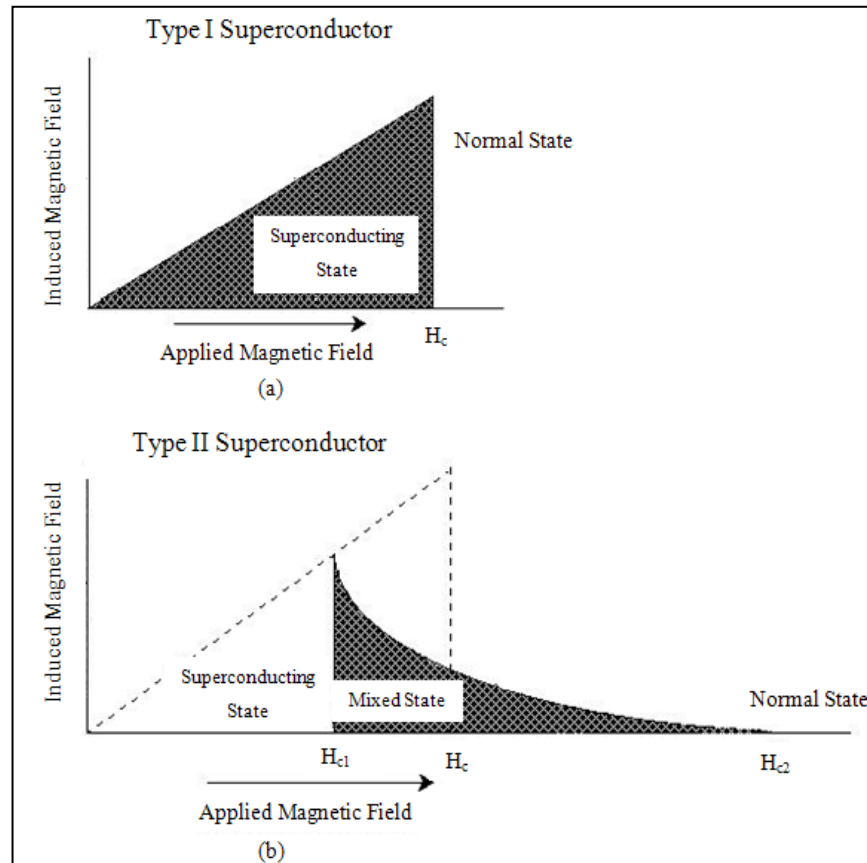
Figure 2.8 Induced magnetic field versus applied magnetic field for (a) type I superconductors and   (b) type II superconductors (Birlik, 2006).

Properties referred as Meissner Effect, zero resistance, etc. are macroscopic properties of superconductivity. We will now focus on microscopic properties like electron tunneling. It is a process arising from the wave nature of the electron. It occurs owing to the transport of the electrons through spaces that are forbidden by classical physic rules because of a potential barrier. The tunneling of a pair of electrons between superconductors separated by an insulating barrier was first discovered by Brian Josephson in 1962. Josephson discovered that if two superconducting metals were separated by a thin insulating barrier such as an oxide layer 10 to 20 Å thick, it is possible for electron pairs to pass through the barrier

without resistance. This is known as the dc Josephson Effect and is contrary to what happens in ordinary materials, where a potential difference must exist for a current to flow. The current that flows in through a dc Josephson junction has a critical current density which is characteristic of junction material ad geometry. Pairs of superconducting electrons will tunnel through the barrier. As long as the current is below the critical current for the junction, there will be zero resistance and no voltage drop across the junction. If it is placed next to a wire with a current running through it, the magnetic field generated by the wire lowers the critical current of the junction. The actual current passing through the junction does not change, but has become greater than the critical current which was lowered. The junction than develops some resistance which causes the current to branch off. Figure 2.9 (a) illustrates the Josephson Effect and Figure 2.9 (b) is a graph of the current-voltage relation for a josephson junction. Josephson junctions can perform switching functions such as switching voltages approximately ten times faster than ordinary semiconducting circuits. This is a distinct advantage in a computer, which depends on short on-off electrical pulses. Since computer speed is dependent on the time required to transmit signal pulses the junction devices exceptional switching speed make them ideal for use in super fast and much smaller computers (Xu & Shi, 2003).
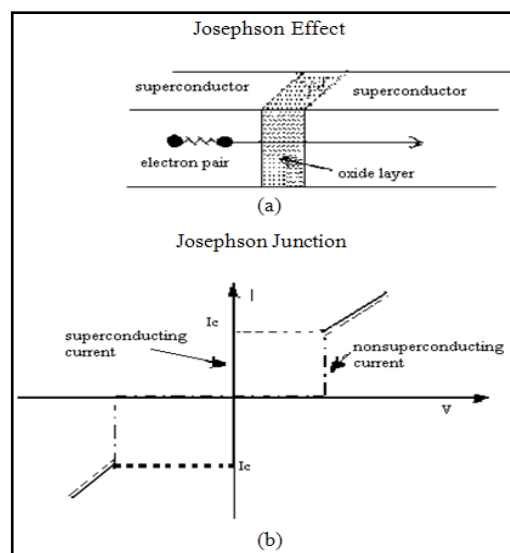
Figure 2.9 Illustration of the Josephson Effect,
(b) graph of the current-voltage relation for a
Josephson junction (Xu, 2003).

2.1.4 Model and Theories

In 1935, two years after the discovery of the Meissner effect (1933), the London brothers (1935) proposed a simple theory to explain the Meissner effect. Ginzburg and Landau (1950) advanced a macroscopic theory that described superconductivity in terms of an 2nd order phase transformation, and they provided a derivation of the London equations in 1950. The universally accepted theory of superconductivity is the BCS theory, formulated by Bardeen, Cooper, and Schrieffer (1957), which provides our present theoretical understanding of the nature of superconductivity. They showed that bound electron pairs called cooper pairs carry the supercurrent, and that there is an energy gap between the normal and superconducting states.

2.1.4.1 Meissner Effect

Because the zero-resistance feature of superconductors was discovered first, it is widely believed that this is the most fundamental property of superconductors. Actually, the Meissner effect is of equal or greater significance, and plays a central role in the magnetic phenomena associated with superconductivity.

As stated above, the Meissner effect is the expulsion of a magnetic field from within a superconductor. It is important to be precise here. This expulsion is different from merely not letting in an external field; any metal with infinite conductivity would do the latter. If a magnetic field is already present, and a substance is cooled through to T_c become a superconductor, the magnetic field is expelled. The significance of the difference is that the Meissner effect cannot be explained merely by infinite conductivity. Rather, it is necessary to develop a totally different picture of what is going on inside the superconductor.

No superconductor can keep out very strong magnetic fields. In fact, at any temperature (below the transition temperature T_c of course), there is some magnetic field of sufficient strength such that the Meissner effect can be overcome and superconductivity vanishes. This is known as the critical magnetic field, and is

denoted by $H_c(T)$. At zero temperature, the upper limit of critical magnetic field is $H_c(0)=H(0)\Delta T_c$ the critical magnetic field goes to zero: $H_c(T_c)=0$. It is desirable to find superconductors with high critical field values, and these are generally associated with materials having a high T_c value (Xu, 2003).

A typical type I superconductor excludes all magnetic fields below H_c and admits magnetic fields without hindrance when H exceeds H_c. This behavior is termed perfect diamagnetism. In any material, the applied magnetic field H is related to the magnetization M and the magnetic induction B by the simple Relation 2.2:

$$B=\mu_o(H+M) \tag{2.2}$$

2.1.4.2 The London Theory

In 1935, the London brothers F. London and H. London (1935) provide the following equations which relate the electric and magnetic fields E and B, respectively, inside a superconductor to the current density J:

$$E = \mu_o \lambda_L^2 \frac{d}{dt}J \tag{2.3}$$

$$B = -\mu_o \lambda_L^2 \nabla x J \tag{2.4}$$

The constant of proportionality in these expressions is the London penetration depth λ_L:

$$\lambda_L = \left(\frac{m}{\mu_o n_s e^2}\right)^{1/2} \tag{2.5}$$

where n_s is the density of superconducting electrons. Equation (2.4) can be combined with the Maxwell equations $\nabla x B = \mu_o J$ to give:

$$\nabla^2 B = {B}/{\lambda_L^2} \tag{2.6}$$

$$\nabla^2 J = J \Big/ \lambda_L^2 \tag{2.7}$$

The solution of London equation is the exponentially decaying:

$$B_{(x)} = B_a . exp\left(-x \Big/ \lambda_L\right) \tag{2.8}$$

which is shown in Figure 2.10.
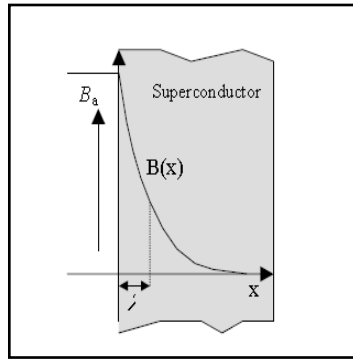
Figure 2.10 The decaying of magnetic field with penetrating depth in superconductor (Xu, 2003).

2.1.4.3 The Ginzburg-Landau Theory

The Ginzburg-Landau (1950) proposed their theory, which provides a good description of many of the properties of both classical and high-temperature superconductors. Based on Landau's general theory of 2nd order phase transitions, this theory assumes that in the superconducting state the current is carried by super electrons that were described by a superconducting electronic wave function, ψ, which is zero at phase transformation and $|\psi|^2 = ns$. By expanding the free energy expression, a differential equation may be derived for ψ:

$$\frac{1}{2m}(-i\hbar\nabla - eA)^2\Psi + \alpha\Psi + \beta(\Psi^2)\Psi = 0 \tag{2.9}$$

with the boundary condition:

$$n(-i\hbar\nabla\Psi - eA)\Psi = 0 \tag{2.10}$$

and:

$$\frac{1}{\mu_o}\nabla x B = -\frac{\hbar e}{2im}(\Psi^*\nabla\Psi + \Psi\nabla\Psi^*) - \frac{e^2}{m}\Psi^2 A = J_s \tag{2.11}$$

and:

$$nx\left(\frac{B}{\mu_o} - H_a\right) = 0 \tag{2.12}$$

where, A is the magnetic vector potential such that $B = \nabla \times A$.

The Ginzburg-Landau equations lead to two characteristic lengths, the G-L penetration depth, λ, and coherence length, ξ, respectively. Assuming $H_a \approx 0$, the values of λ and ξ are:

$$\lambda_{GL}^2 = \frac{m}{\mu_o e^2 \Psi_0^2} \tag{2.13}$$

$$\xi(T)^2 = \frac{\hbar^2}{2m\alpha} \tag{2.14}$$

The ratio $\kappa = \lambda/\xi = 1/\sqrt{2}$ divides superconductors into the two types: $\kappa \leq 1/\sqrt{2}$ Type I and $\kappa \geq 1/\sqrt{2}$ Type II. Type II superconductors have lower, thermodynamic, and upper critical fields given by:

$$B_{c1} = \frac{\Phi_o ln\kappa}{4\pi\lambda^2}, \ B_c = \frac{\Phi_o}{2\sqrt{2}\pi\lambda\xi}, \ B_{c2} = \frac{\Phi_o}{2\pi\xi^2} \tag{2.15}$$

where, Φ is the flux quantum with value $\Phi = h/2e = 2.0678 \times 10^{-15}$ Tm^2.

2.1.4.4 Bardeen-Cooper-Schrieffer Theory (BCS)

The understanding of superconductivity was advanced in 1957 by John Bardeen, Leon Cooper and John Schrieffer. They proposed a theory that explained the microscopic origins of superconductivity and could quantitatively predict the properties of superconductors. Their theory is known as BCS theory. Prior to this, there was Ginzburg-Landau theory, which was a macroscopic one. The BCS theory explains superconductivity at temperatures close to absolute zero. Electrons are forced to pair up into teams that could pass all of the obstacles which caused resistance in the conductor. These groups of electrons are known as Cooper Pairs.

According to BCS theory, as one negatively charged electron passes by positively charged ions in the conductor lattice, the lattice distorts. This in turn causes phonons to be emitted which form a trough of positive charges around the electron. Figure 2.11 illustrates a wave of lattice distortion due to attraction to a moving electron. Before the electron passes by and the lattice springs back to its normal position, a second electron is drawn in to the trough. Then the two electrons which should repel one another, link up. The forces exerted by the phonons overcome the electrons natural repulsion. The electron pairs are coherent with one another as they pass through the conductor in unison. The electrons are screened by the phonons and are separated by some distance. When one of the electrons that make up a cooper pair and passes close to an ion in the crystal lattice, the attraction between the negative electron and the positive ion cause a vibration to pass from ion to ion until the other electron of the pair absorbs the vibration. The net effect is that the electron has emitted a phonon and the other electron has absorbed the phonon. It is this exchange that keeps the Cooper pairs together. It is important to understand that the pairs are constantly breaking and reforming. Since the electrons are indistinguishable particles, it is easier to think of them as permanently paired (Whelan, 2003).

The Cooper pairs within the superconductor are supercurrent carriers and they experience perfect conductivity. From a mathematical aspect, cooper pair is more stable than a single electron within the lattice, it experiences less resistance. Also

physically the cooper pair is more resistant to vibrations within the lattice therefore pairs move through the lattice relatively unaffected by thermal vibrations below the critical temperature (Shekhter et al., 2003). Electrical resistance is caused by the scattering of electrons due to defects, impurities and thermal vibrations in the crystal lattice of a conductor. However the binding of electrons in the cooper pairs eliminates scattering and thus electrical resistance disappears. Above a specific critical temperature (T_c), thermal vibrations disrupt the Cooper pairs and the material becomes resistive again. Intense magnetic fields and high currents can also disrupt the pairs and destroy superconductivity. The phonon-linkage mechanism associated with cooper pairs in low-temperature superconductor cannot work at high temperatures, since thermal vibrations would quickly break the phonon linkages. The most popular theory is that the pair coupling occurs due to subtle magnetic effects created by the HTS lattice, but there is not a clear explanation how it happens (Birlik, 2006).
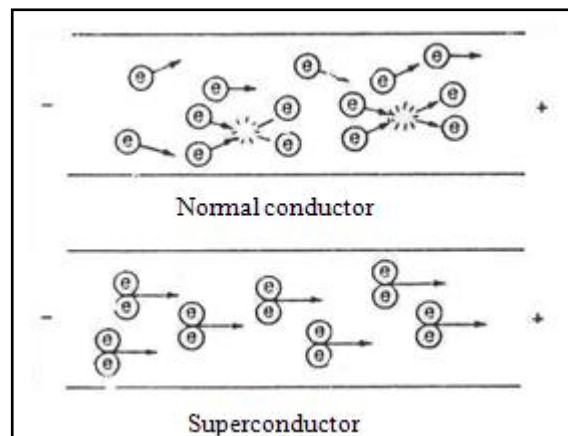
Figure 2.11 Schematic illustrating the difference, according to the BCS theory, between normal conduction and zero-resistance super conduction (Birlik, 2006).

The BCS theory successfully shows that electrons can be attracted to one another through interactions with the crystalline lattice. This occurs despite the fact that electrons have some charge when the atoms of the lattice oscillate as positive and negative regions; the electron pair is alternatively pulled together and pushed apart

without a collision. The electron pairing is favorable because it has the effect of putting the material into a lower energy state. When electrons are linked together in pairs, they move through the superconductor in an orderly fashion (Goebel, n.d.).

Bardeen, Cooper, and Schrieffer (1965) proposed the general microscopic theory of superconductivity that quantitatively predicts many properties of superconductors and is now widely accepted as providing a satisfactory explanation of many phenomena. The BCS theory can be summarized as:

1. An attractive interaction between electrons can lead to a ground state separated from excited state by an energy gap E_g at low temperature.
2. Electrons interact with lattice electrons which cause electrons to form pairs at low temperature, line up, and staying in the continuously moving in low energy state with no resistance.
3. With the assumption that at temperature $T=T_c$, the excited electrons occupied the possible state for cooper pairs' electrons, the temperature that the cooper pairs cannot be formed is the critical transition temperature T_c:

$$T_c = 1.14. \ominus . exp\left[\frac{-1}{U.D(E_f)}\right] \qquad (2.16)$$

4. The boundary between a normal and superconducting state region cannot be sharp. The density of superconducting electrons can rise from zero in the normal region gradually over a distance equal to about the coherence length ξ as discussed above.
5. Magnetic flux through a superconducting ring is quantized and effective charge is $2e$ rather than e.

BCS theory predicts several parameters such as isotope effect (Equation 2.17), T_c expression (Eq. 2.16), the jump of electronic specific heat at T_c from normal state value $C_e=\gamma T$ to its superconducting state value C_s, (Equation 2.18), and the specific heat $C_s(T)$ depends exponentially on the inverse temperature below T_c, (Equation 2.19).

$$M^{\alpha} T_c = const. \tag{2.17}$$

$$\frac{C_s - \gamma.T_c}{\gamma.T_c} = 1.43 \tag{2.18}$$

$$C_s(T) = \alpha.\exp\left(-\Delta/k_B T\right) \tag{2.19}$$

However, BCS theory is only applied to conventional low temperature superconductors (LTS) and has difficulties in explaining the phenomena of high temperature superconductor.

2.2 Low Temperature Superconductors

Elements in a particular column of periodic table have the same number of valance electrons (N_e). The alkali elements of lithium (Li), sodium (Na), potassium (K), and cesium (Cs) are all metals that conduct electricity well and are all in the first column, $N_e = 1$. Some elements in the periodic table as Li, Ba, Cr, Pd, Se, Sb, Te, Bi, Ce and Eu cannot be made superconductive by simple cooling them. They become superconductor only when irradiated, subjected to high pressure or made into thin films. The great majority of the superconducting elements are Type I. These elements are not suitable for applications because of their low transition temperatures and low critical fields. Generally, the transition temperature T_c of some elements is raised dramatically by preparing them in thin films for example; the T_c of tungsten (W) was increased from its bulk value of 0.015 K to 5.5 K in a film.

Among the elements niobium not only has the highest T_c, but it is also a constituent of many higher T_c compounds, like Nb_3Ge. The transition temperature of binary alloys can be higher than that of both elements, between the two values or lower than either one alone (Owens & Poole, 1996, p.74-80).

The highest transition temperatures of the older superconductors were obtained with the A-15 compounds A_3B. A notation is used for elements and B for AB

compounds. Typical A-15 compounds A_3B only form for the 3:1 ratio of A atoms to B atoms. This ratio is important to produce higher transition temperatures. Even though A-15 compounds exhibit the highest transition temperatures of the classic superconductors, they are not widely used in applications because they are too brittle and not flexible enough to be drawn into wires. There are a number of superconducting binary compounds AB in which A is a metallic element and B is a nonmetallic element. Examples are NbN (T_c= 17 K) and MoC (T_c= 14.3 K). In addition to these, there are several dozen metallic AB_2 compounds called Laves phases that are superconducting. Some of them have critical temperatures above 10 K and high critical fields. These materials also have the advantage of not being so hard and brittle as some other compounds and alloys with comparable transition temperatures (Owens & Poole, 1996, p.77).

The Chevrel-phase compounds $A_xMo_6X_8$ are mostly ternary transition metal compounds, where A can be almost any element and the element X is one of the S, Se or Te. These compounds have relatively high transition temperatures and critical magnetic fields B_{c2} of several Tesla, but their critical currents are rather low (Owens & Poole, 1996, p.82).

2.3 High Temperature Superconductor

In 1986, the discovery of the high temperature superconductors (HTSC) by Bednorz and Muller marked the beginning of a new era, not only in the field of superconductivity but for solid state physics in general. The compound La_2CuO_4 synthesized by Bednorz and Muller remains superconducting up to 30 K. Soon after that, Professor Paul Chu in University of Huston reported a T_c of 92 K in the YBCO system (Wu, 1987). This is significant because it is greater than the boiling point of liquid nitrogen at ambient pressure. The prospect of new applications and the initially fast climbing record critical temperature (T_c) attracted a large number of scientists who published a vast amount of work. The following years, a serial of cuprates were reported with even higher T_c as shown in Figure 2.6. All these HTSCs are highly anisotropic, containing perovskite structure, and with layered CuO_2 planes in which

the superconducting charge carriers are thought to be localized. However, although the knowledge of the new materials has increased remarkably over the last years, no complete theoretical picture has yet emerged, particularly because the binding mechanism of electron pairs is still unknown. Considerable progress towards application of the HTSC in practical devices has been achieved, but so far only a small number of niche products are on the market.

The following years, a serial of cuprate were reported with even higher T_c. These superconductors are often called as cuprate because they contain copper atoms bonded to oxygen, constitute different classes of compounds than the old ones, raising the possibility of an entirely new mechanism of superconductivity (Owens & Poole, 1996, p.97). Some common characteristics of the high temperature superconductors are that they are ceramic, "flaky" oxides, which are poor metals at room temperature, are difficult materials with which to work, contain few charge carriers compared to normal metals, and display highly anisotropic electrical and magnetic properties which are remarkably sensitive to oxygen content, contain perovskite structure, and with layered CuO_2 planes in which the superconducting charge carriers are thought to be localized (Balian, Flocard & Veneroni, 1999).

The most commonly examined HTS materials with superconducting transition temperatures T_c above the temperature of liquid nitrogen are $ReBa_2Cu_3O_{7-x}$ ('123', Re=Y or rare earth element, typical transition temperature T_c=90–95 K, $Bi_2Sr_2CaCu_2O_8$ (Bi-2212) (T_c=90 K), $Bi_2Sr_2Ca_2Cu_3O_{10}$ (Bi-2223) (T_c=120 K), $Tl_2Ba_2CaCu_2O_8$ (T_c=110 K), $Tl_2Ba_2Ca_2Cu_3O_{10}$ (T_c=127 K), and $HgBa_2CaCu_2O_8$ (T_c=134 K). For HTS cryoelectronic devices, thin films are mainly grown from '123' material. The reasons are among others the poisonous components Tl or Hg necessary in other compounds, the phase stability, high crystalline quality, high flux pinning level, low surface resistance and the possibility of using a single deposition step with in situ oxygenization. The main problem of this candidate is the reversible oxygen content which can vary between 0<x<1 connected with the transition between the nonsuperconducting tetragonal phase and the superconducting orthorhombic phase (Xu & Shi, 2003).

However, although the knowledge of the new materials has increased remarkably over the last years, no complete theoretical picture has yet emerged, particularly because the binding mechanism of electron pairs is still unknown. Considerable progress towards application of the HTS in practical devices has been achieved, but so far only a small number of products are on the market.

The deposition of high-quality thin HTS films is strongly hampered by a number of properties of the material. First, the quasi two-dimensional (2D) nature of the oxide superconductors related to their layered structure leads to a large anisotropy in nearly all parameters. Anisotropy factors of $\Gamma = (\xi_{ab}/\xi_c)^2 = (\lambda_c/\lambda_{ab})^2 \approx 25$–29 in YBCO, $\Gamma \approx 3000$–15 000 in Bi compounds and $\Gamma \geq 10^5$ in Tl compounds are reported for the anisotropy between the crystallographic c and a–b directions. Furthermore, extremely small coherence lengths are determined for the HTSs. For Bi-2212 values of $\xi_c = 0.02$–0.04 nm and $\xi_{ab} = 2$–2.5 nm, for YBCO $\xi_c = 0.3$–0.5 nm and $\xi_{ab} = 2$–3 nm are measured, which, however, strongly depend on sample quality and oxygen content. Therefore, local variations in the sample properties on the scale of ξ will automatically result in a spatial variation of the superconducting properties. Because of the extremely small coherence length along the crystallographic c-axis, the current directions along the a–b direction (along the CuO planes) are utilized for most applications. This implies an epitaxial c-axis orientation of the film. Second, the superconducting properties strongly depend on variations in stoichiometry, especially in the oxygen concentration. Because of the complex crystallographic structure and the small coherence length, extreme requirements are imposed on the uniformity and stability of the deposition process (Birlik, 2006).

Finally, the HTS material usually grows with a granular morphology. In the case of polycrystalline or textured HTS material, the intergranular properties clearly dominate superconducting properties such as the current density J_c or microwave surface resistance R_s. Nevertheless, even for epitaxial films small-angle grain boundaries cannot be avoided. The effect the grain boundaries have on J_c can be summarized as with increasing misorientation angle J_c decreases. At large angles the grain boundary imposes a Josephson-type behavior, which can be utilized for

fabrication of Josephson contacts, e.g. by deposition of HTS thin films on bicrystalline substrates. However, large-angle grain boundaries also lead to unwanted effects such as enhanced voltage noise due to vortex motion within the grain boundary. Due to these extraordinary properties, special precautions have to be taken while depositing HTS material. These precautions certainly depend on the application for which the film will be used. For most applications epitaxial films are needed without large-angle grain boundary, secondary phases and outgrowths, high critical current density J_c or low microwave surface resistance R_s. In a number of cases, smooth surfaces are needed (e.g. for submicrometer patterning and multilayers) or defects have to be implemented in order to provide pinning centers or to release internal stress in the sample, which might lead to microcracks if a critical thickness is exceeded (Wördenweber, 1999).

It was shown by several authors that single phase compounds can be form by substitution of Y by the rare-earths. The rare-earth cuprates $LnBa_2Cu_3O_7$ (Ln=lanthanides) are isostructural compounds and their superconducting critical temperature is above 90 K except in the case of $PrBa_2Cu_3O_7$ which does not exhibit superconductivity (Suryanarayanan et al., 2001).

The oxides $La_{2-x}Ba_xCuO_4$ are superconductors with T_c ranging from 20 to 38 K. They can be described as an intergrowth of single perovskite layers with single rock-salt-type layers. In other words this structure can also be described as a stacking of $[CuO_2]_\infty$ and $[La_{1-x}Ba_xO]_\infty$ planes alternating according to the sequence "Cu-La-La-Cu".

In January 1988, a Japanese scientist, H. Maeda (1988), reported the discovery of a new family of high temperature superconductors consisting of bismuth-strontium-calcium-copper oxide having a T_c around 110 K. After that, Alan M. Hermann and Z. Z. Sheng of the University of Arkansas reported an even higher transition temperature of 125 K in a similar series of materials namely thallium-barium-calcium-copper oxide. In this family there are many compositional variations that give superconductivity and some of them involve the addition of lead. The bismuth

compound shows similar processing problems as the YBCO, but in contrast to YBCO, are more difficult to synthesize as a single phase. A high T_c phase (110 K) is found at the composition Bi-2223 with a lower transition 85 K phase forming at Bi-2212. The major advantage of this compound over the YBCO is its relative insensitivity to oxygen loss during processing, and it does not require special low temperature oxygenation to achieve optimum superconducting properties (Birlik, 2006). Recently there has been considerable interest in the growth of $NdBa_2Cu_3O_7$ (NBCO) thin films as an alternative high temperature superconducting (HTS) material to YBCO for electronic applications. There are reports that it can be grown with better crystallinity and a smoother, more stable surface than YBCO. In addition, bulk NBCO has the highest measured T_c=98.7 K of the ReBaCuO (Re = Rare Earth) family. In 1994, a new superconductor $HgBa_2Ca_2Cu_3O_{8+x}$ was synthesized that had zero resistance at 133 K, some samples had an onset of superconductivity as high as 140 K. There is much interest in this superconductor for two reasons. Measurements of the effect of pressure on the material indicate that the onset transition temperature increases to 147 K when pressure is raised to 140.000 times atmospheric pressure. The result excited many researchers because pressure on a material can be created chemically by replacing some fraction of ions by a similar ion of smaller radius.

The obvious choice in this case was to replace the larger barium with smaller strontium. The other reason for interest in this material seems much more important. Resistance measurements in DC magnetic fields show that fields up to 10 T do not increase the resistance at 77 K. This means that flux is more strongly pinned in this superconductor than in other cuprates at 77 K. Therefore if the mercury material can be fabricated into wires, it may be possible to have a high temperature superconducting magnet that operates with liquid nitrogen as the coolant (Owens & Poole, 1996, p.80).

2.3.1 Crystal Structure

Normally, HTSC materials have layered, oxygen-deficient perovskite structure (Figure 2.12) in which fourfold planar-coordinated copper oxide (CuO) layers

effectively form the conducting sheets. There are about one-third of oxygen positions vacant. The unit cell of $YBa_2Cu_3O_{7-\delta}$ compound is built up by having triple perovskite structure stacked along the c-axis to result in a tetragonal or orthorhombic structure.
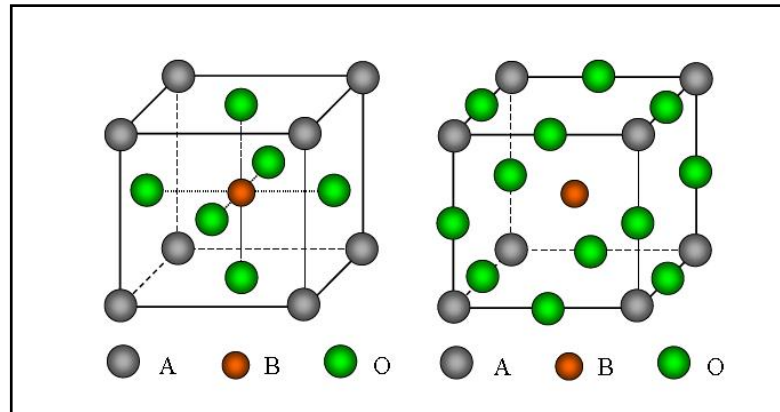
Figure 2.12 Two views of the unit cell of compound with the perovskite structure (ABO_3).

There are two Cu-O sheets in each unit cell, one on either side of the Y layer (yttrium layer). Conduction perpendicular to these planes is very small because the oxygen linking the adjacent copper layers in that direction is almost absent, i.e., in the Y layer. This material can be treated as a two-dimensional superconductor. The conductivity in these materials is very anisotropic and may even exhibit semiconducting-like characteristic along the c-axis.

The large anisotropy of the crystal structure has consequences for the physical properties as the effective mass of the electrons moving in the a-b plane, m_{ab}, is different from that in the c direction, m_c. This difference is characterized by an anisotropy parameter, γ, such that $\gamma^2 = m_c/m_{ab}$. The anisotropy parameter is a measure of the ratio of the coherence length and the penetration depth in the a-b plane and c-direction. For YBCO, γ is approximately 5-7 as demonstrated by the values shown in Table 2.1.
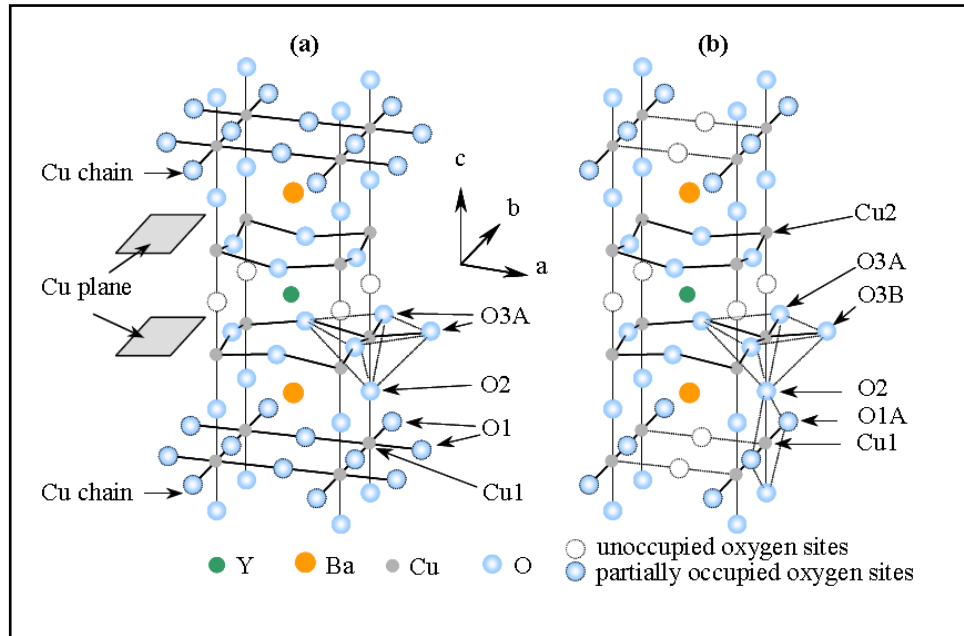
Figure 2.13 The crystal structure of YBa$_2$Cu$_3$O$_{7-\delta}$ is tetragonal for $\delta \geq 0.5$ (a) and orthorhombic for $\delta \leq 0.5$ (b). Copper chains and copper planes are shown in (a), also positions of oxygen atoms are labeled in (b) (Xu, 2003).

For the YBCO material there is a layer of copper-oxide chains along the b axis, in addition to the Cu-O sheets shown in Figure 2.13. Parallel layers of CuO$_2$ planes are a common structural feature of all high temperature superconductors with $T_c > 40$ K. The oxygen content (δ) of YBa$_2$Cu$_3$O$_{7-\delta}$ can be changed from 0 to 1 simply by pumping oxygen in and out of the parallel chains of CuO. The variation of oxygen content of YBa$_2$Cu$_3$O$_{7-\delta}$ can happen during the oxygen annealing process, which results in the phase transformation of YBa$_2$Cu$_3$O$_{7-\delta}$ from tetragonal phase ($\delta<0.5$, non-superconducting) to the orthorhombic phase ($\delta>0.5$, superconducting) (Xu, 2003). Upon the phase transformation, dimension of the cell along *a* axis is shorter and one along *b* axis is longer. The YBCO unit cell consists of an YCuO$_3$ cube with adjacent BaCuO$_3$ cubes above and below, but with some oxygen sites not occupied. The oxygen sites on the same horizontal plane as the yttrium atom are never occupied; allowing the O$_3$ atoms to slightly move towards the Y.

The oxygen sites on the basal plane can have average occupancies between 0 (δ = 1) and 0.5 (δ = 0). Oxygen is comparatively mobile in this plane and nearly full oxygen (δ = 0.03) is crucial to obtain samples with high transition temperature.

Table 2.1 Anisotropy of ξ and λ in some HTSC (T=0 K).

Materials	Coherence Length, ξ (nm)	Penetration Depth, λ (nm)
YBCO a-b	2.00	140
YBCO c-	0.30	900
BSCCO-2212 a-b	3.00	300
BSCCO-2212 c	0.40	500
BSCCO-2223 a-b	2.00	-
BSCCO-2223	0.04	-

The dependence of T_c on δ is shown in Figure 2.14. The dimensions of the unit cell in the tetragonal case ($\delta \approx 0.5$) $a=b=0.387$ nm, $b=0.388$ nm and $c=1.172$ nm, in the orthorhombic case ($\delta = 0.1$) $a=0.382$ nm, $b= 0.388$ nm and $c=1.168$ nm. Orthorhombic YBCO is formed when the tetragonal phase is slowly cooled in a sufficiently concentrated oxygen environment at roughly 680°C. The change of lattice constant with δ in $YBa_2Cu_3O_{7-\delta}$ is shown in Figure 2.15.
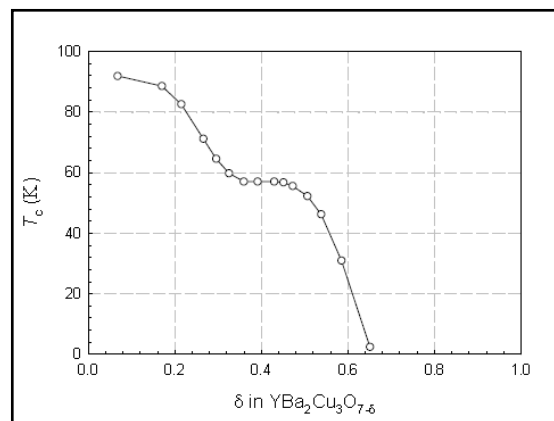
Figure 2.14 The δ dependence of T_c in $YBa_2Cu_3O_{7-\delta}$ materials (Xu, 2003).
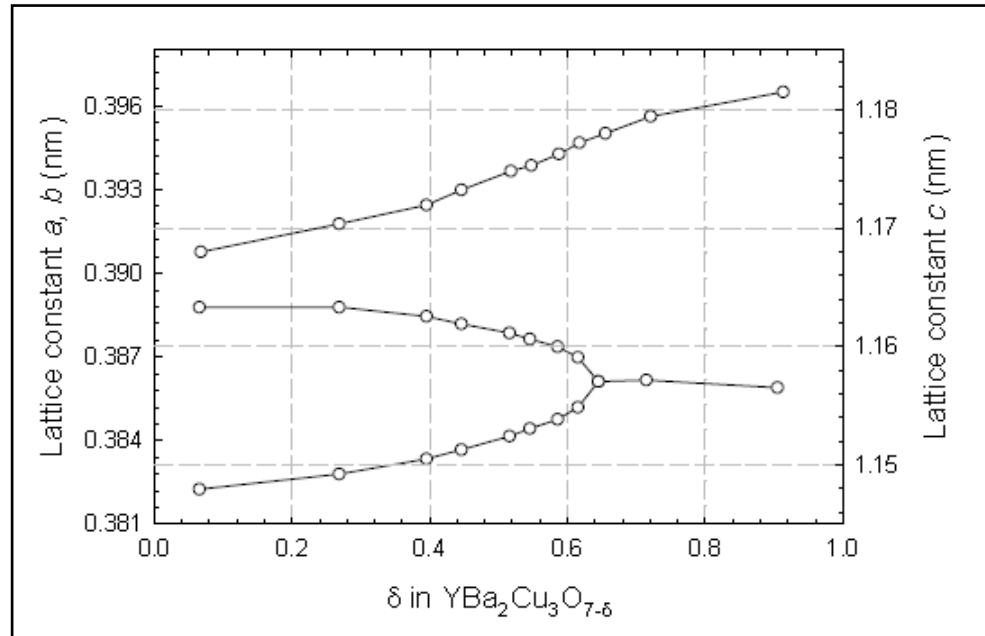
Figure 2.15 The lattice constant of $YBa_2Cu_3O_{7-\delta}$ as a function of the oxygen content (Xu, 2003).

2.3.2 Flux Pinning Properties

HTS technology is close to the levels for commercialization and many applications will involve higher magnetic fields. In YBCO thin films at 77 K high values of J_c are required under high magnetic fields. However, the ability for HTS bolometers to carry currents is significantly reduced with increasing temperature in magnetic fields (Johansen, 2000). The main reasons of the J_c depression are recognised to be the intrinsic crystalline anisotropy of HTS and the thermal fluctuations. Nevertheless, the lack of effective pinning centers should be noted as one of the main reasons. In order to counteract this effect, various methods to increase the HTS current-carrying abilities in magnetic fields by flux pinning have been developed through the pinning of the quantized flux lines by nanoscale crystalline defects and impurities. Depending on these reasons, a novel technology has been developed by means of a nanostructure engineering to create artificial pinning centres in HTS materials (Mele et al., 2005). This requirement has stimulated extensive exploration of various means of introducing effective pinning centers into YBCO. Therefore, improving flux pinning within YBCO films is one of the chief

concerns for the development of HTS bolometer technology. Generally, the value of J_c depends on lattice disorders. The sources of enhanced pinning in YBCO films are the natural point, line and volume imperfections, probably the most significant of these being the dislocations perpendicular to the substrate plane of film. Dislocations are nearly ideal for pinning magnetic flux lines. Nevertheless, the density of dislocations is dominated by growth island size and their spacing is estimated to be rather large. To increase dislocation density, an obvious way would be to decrease the island size which the dislocations bound, by reducing growth temperature but this is non-trivial because the crystalline quality of the film would be compromised (Barnes et al., 2005). The flux pinning forces from naturally introduced pinning centers during the fabrication process, e.g. oxygen vacancies, dislocations and twin boundaries are not enough to achieve high J_c at 77 K. In order to enhance J_c, strong pinning centers must be introduced into superconductors (Haruto et al., 2006). Many kinds of crystalline defects such as fine precipitates of non-superconducting phases, dislocations, vacancies, grain boundaries and so on are considered to act as pinning centers. One of the biggest challenges for introducing HTS into power applications is the grain boundary problem. Due to the extremely short coherence length (ξ) of these materials, comparable with their lattice spacing, dislocations in small-angle grain boundaries, or a complete interface in the case of large-angle grain boundaries, reduce the critical current density nearly exponentially with misorientation angle. Therefore, much effort was put into solving this problem during the last years in, for example, avoiding large angle grain boundaries or enhancing J_c of grain boundaries by doping. In grain boundary networks, the manifold of different grain boundaries leads to a percolative nature of the current flow. That's why J_c depends not only on the materials properties but also on conductor length and width. It was shown recently that the J_c limitation due to grain boundaries is found only in fields lower than a certain cross-over field, H_{co}, at which the pinning properties of the adjacent grains become dominant for the J_c limitation (Cui et al., 2006).

Flux pinning in YBCO thin films can be engineered by materials processing for bolometer developments. Columnar defects and antiphase boundaries provide extended linear defects as strong pinning centers. Currently, a few other methods to

increase flux pinning have been realized for YBCO films. These are; including multilayering of YBCO with second-phase materials, mixed rare-earth doping, target compositional modifications either by second phase $BaMeO_3$ (Me: Zr, Hf, Mn, Mo, Nb, Ir, Os, Re, In, Sb, Sn and so on) inclusions or create defects comprised of self-aligned $BaMeO_3$ nanodots and nanorods, process induced modifications with excess yttrium and decoration of substrate surfaces by nanoscaled particles. The main reasons for the choice of $BaMeO_3$ are; (a) while it can grow heteroepitaxially with YBCO, it has a large lattice mismatch (~ 9%) so strain between the phase could introduce defects for enhanced pinning, (b) it is a high melting temperature phase and so growth kinetics should be slow, leading to small particles, and (c) Me does not substitute in the YBCO structure (Yamada et al., 2005). It is important to control the doped defect density. A defect density which is too high will inevitably degrade superconductivity, and a balance between the increased pinning strength and loss of superconductivity must be found by optimizing the dopant concentration. The pinning centers, in order to be effective, need to be nanoparticles, less than 10 vol. % of the superconductor, and be randomly distributed to provide isotropic 3-dimensional pinning. A defect density which is too high will invitably degrade superconductivity, and a balance between the increasing pinning strength and loss of superconductivity must be found by optimizing the dopant concentration (Varanasi et al., 2006).

2.4 Applications and Frustrations

The recent achievement of critical currents exceeding 1,000,000 A/cm^2 at 77 K in YBCO deposited on suitable textured substrate has stimulated interest in the potential application of coated conductors in high temperatures and high magnetic fields (Goyal, 1996). Superconducting films have opened up new possibilities for passive and active microwave and optical components, namely, filters, delay lines, micro strip patch antennas, power combining circuits, solid-state devices, kinetic induction phase shifters, MRI sensors, SQUID devices, A/D converters, optical detectors, generators, motors, and especially in wire industry. However, the technical difficulties originated from the grain boundaries and commercialization

consideration of the scale-up and high fabrication cost have been challenging the research and development of HTSCs (Xu, 2003).

2.4.1 Applications

Most electrical applications using HTSs are based on their high J_c values that are not obtainable using conventional materials. HTS materials have several advantages over low T_c superconductors as they have higher B_{irr} and potential savings in cryogen consumption costs and reducing the design complexity of cryogenic system. The highlighted applications in power industry now include: Electrical transmission and distribution, power generator and electric motor and energy storage. As the demand for electrical power is increasing, one of the challenges for the utility industry is to find new ways to transport large amount of power from the generation plant to consumers. The market in electrical transmission and distribution is large especially in urban areas where the demand of electricity is increasing while there is limited clearance for overhead cables. Thus, using underground HTS cables capable of carrying three to five times more power than copper cables of the same size, and thus using existing rights of way is an attractive solution (Dawley, 2001). Furthermore, significant portions of the existing cables are aging and need replacement in the near future. Not only that HTS cables can transmit electricity with minimal resistive losses, in addition, the liquid nitrogen used to cool underground HTS cables is less expensive and presents less environmental risk than the dielectric oil used in copper cables. HTS transformers offer many benefits over conventional power transformers for utility applications. The major practical advantage is the reduction in weight and size, as the losses in the windings are significantly reduced allowing smaller number of ampere-turns used. This, in turn, reduces the iron-core losses due to the smaller amount of generated magnetic flux. HTS transformers are expected to be half the weight and size of conventional ones, which would, among others, reduce the area required for a power substation, ease the transportation, and replace the dielectric oil with environmental friendly and non-flammable liquid nitrogen. HTS generators and motors have the advantages of higher power density, higher efficiency, smaller size and weight, due to the capability of producing high magnetic fields from the lossless

superconducting winding and hence smaller rotor coils. Electric motors consume large amount of electricity, thus there are a lot of interests in utilizing superconductors to improve their efficiency. However, electric motors are generally rather efficient (Shedan, 1994), therefore HTS motors have to be even more efficient to offset the cost of their cryogenic system.

There are two types of energy storage systems that could potentially benefit from using superconductors: superconducting magnetic energy storage (SMES) and superconducting flywheels. Such applications in energy storage would be useful for meeting peak-hour electricity demand and as an emergency power source. In SMES, energy is stored in the magnetic field produced by superconducting coils that carry a large DC current with zero resistive losses; the current will persist for as long as the coil is kept below its T_c. On the other hand, a superconducting flywheel is based on the principle of the Meissner effect that produces an extremely low-friction bearing. Electrical energy is used to spin the flywheel and cut off when it reaches its top speed such that the energy is stored in rotational kinetic form by the spinning flywheel with very low frictional or air-drag losses (when housed in a vacuum) (Xu, 2003).

Another application of superconductors in electrical transmission is the fault current limiter (FCL) that uses the superconducting-normal (SN) transition of a superconductor to reduce the fault current in an electric circuit. In the event of a fault current, the J_c of the superconductor is exceeded whereby the material turns into its normal state that limits the large fault current. The FCL is capable of reducing a fault current nearly instantaneously and is highly sought since the increasing power consumption and demand make it useable where the short-circuit capacity of power system would exceed the capacity of a conventional circuit breaker. HTS materials connected in series are very effective in controlling rising fault currents within milliseconds since the SN transition can occur in less than 1 ms. A newly designed RF element shown in Figure 2.16 is an electronic application of HTS film. Low surface resistance, R_s, is a key property of conductors used in RF device applications. For a normal conductor such as copper, the surface resistance is on the order of 0.01

Ω at the frequency of 2 GHz (Paul, 1988; Shi, 1995). The surface resistance is many orders of magnitude below this at the same frequency range in a well-textured YBCO, making this HTSC material an attractive candidate for RF components.
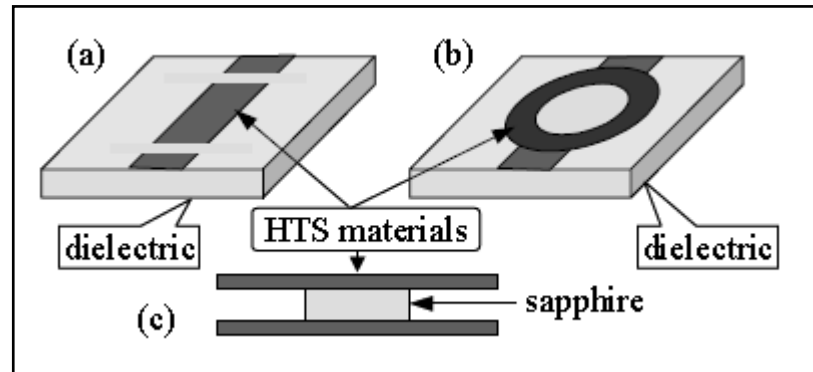
Figure 2.16 HTSC resonator structure layout, (a) Micro strip, (b) Ring resonator and (c) Parallel plate shunted by a dielectric resonator (Xu, 2003).

2.4.2 Frustrations

High critical current densities were demonstrated in YBCO thin films, but the critical current density goes down quickly with the increase of film thickness. Though there are occasionally reports that high current density was achieved on thick films, the poor reproducibility tells the difficulty in fabrication of thick films. Several factors like texture, stoichiometry, and grain boundary aggregation may be responsible for the low J_c of thick films, but the real reason is still unknown now. Many technical difficulties are facing researchers when transfer HTS fabrication techniques to industry, because the fabrication of the long length flexible metallic substrates is not coming easy and the performances of these substrate are much inferior compared with single crystal or short substrates.

Another frustration comes from the cost consideration, if the ratio of performance over cost is not a big jump or even comparable with traditional conductors like copper, industry would not be interest in this technique. For electronic industry, low surface resistance is necessary for active microwave and optical components. The

current approaches in processing HTS are thin film technologies, which can produce epitaxial films with low surface resistance. Typically, HTS thin film components such as resonator shown in Figure 2.16 have a dielectric substrate, which is a source of surface resistance. Single domain YBCO is a hopeful substitutional material. The surface resistance of the single-domain YBCO measured at 77 K and 0.8 GHz has reached 0.05 mΩ, that is about three magnitudes lower than copper, but at high frequency, surface resistance goes up quickly and frustrates many possible applications. YBCO single domain is actually a two phases system. Normally there are 15~30% of YBCO 211 phase in the YBCO 123 substrate. 211 YBCO is a no superconducting phase and it is a source of surface resistance. One approach is making YBCO single crystal with 100% 123 phases, but at present there are technical difficulties in crystal growth. An effective approach may be to cover the YBCO substrate with YBCO film (Xu, 2001). In this approach grow YBCO 123 epilayer with in plane and out-of-plane textures are the key factor.

2.5 A Review of Coated Conductor Development

In this part, the development of coated conductor technology has been reviewed. It is shown that the critical current density of high-T_c wires can be greatly enhanced by using three-fold approaches: grain alignment, grain boundary doping, and optimization of the grain architecture. Major advances have been made in the last 16 years mainly in the three aspects: substrates, buffer layers and the YBCO layer. Cost is still the main concern for scale up, especially for the approach through vapor depositions, such as the PLD method. TFA-MOD or other CSD methods may be the trend to overcome cost and speed consideration during the scale-up. However, high reliability and reproducibility will be the new focus for these techniques. Ni-alloy tapes seem to have advantages over pure Ni in terms of mechanical strength and oxidation resistance. Depositing a pure Ni layer on top of Ni-based alloys (such as Ni-Cr and Ni-W alloys) solves the problem of low strength of Ni and poor texture of Ni alloys.

The rolling assisted biaxially textured substrate (RABiTs) and ion beam assisted deposition (IBAD) are the two robust approaches for the texture generation. But the buffer materials and architectures being investigated remain unclear, though $CeO_2/YSZ/CeO_2$ and MgO are commonly used buffer layers for RABiTS and IBAD respectively. For the case where a buffer layer is unavoidable, a non-vacuum processes would be suitable for low cost and scale up. However there is none of the buffer layer fabrication processes through CSD has been demonstrated results good enough for long length coated conductor applications. While, a high J_c superconducting layer can be produced by TFA-MOD, which brings a bright future for coated conductors. Clearly, there are still a lot of scientific and technological barriers to be overcome before any long length of high J_c coated conductor be produced commercially. But theoretical analyses and technological progress show the potential for the practical application of coated conductor wires in the near future (Xu, 2003).

2.5.1 Historical Perspective

The discovery of the cuprates high temperature superconductor of $YBa_2Cu_3O_{7-\delta}$ (YBCO) at 90 K in 1986 marked the beginning of a new era not only in the theoretical value in solid state physics in general, but also in the aspect of potential applications in industry. Soon after the discovery, the quest for the practical applications let to the investigation on the current carrying capacity of this new material at the boiling point of liquid nitrogen of 77 K. The first experiment on the sintered polycrystalline bulk YBCO samples, known as the first generation HTS, was rather disappointing, because the large angle grain boundaries severely limited supercurrent flow especially in a magnetic field. With the knowledge that textured cuprates films can carry high current density, the "second generation" HTS materials become promising in practical applications.

The quick success on small single crystal substrates introduced the idea of depositing HTS film on a flexible inexpensive metal tape substrate with a proper texture in long length. The cost consideration highlights the use of a metal tape

together with a cheap film making method, which can be scale up for commercial applications. The traditional ultra-high vacuum (UHV) thin film vapor deposition techniques are not ideal compared with chemical solution deposition (CSD), because in a practical application the engineering critical current density of a final tape is a crucial factor. Compare with other cuprates (especially BSCCO), YBCO seems to be the most promising material because of the current carrying ability in a magnet field and high current density in self-field. The use of the RABiTS and IBAD makes textured coated conductor applicable.

Nowadays, long length YBCO coated conductor is on the way and people can expect their applications before long. Two major problems limiting the applications of coated conductors are weak intergrain pinning and weak intergrain coupling. As the origin of a weak intergrain pinning is from the structural in nature, it is important to choose a material that has strong intrinsic flux pinning capability at a high temperature and in a magnetic field. Despite the relative ease of fabrication, Bi-containing compounds have limited applications in a high magnetic field at 77 K due to their intrinsically low irreversibility fields ($B_{irr.}$) as shown in Figure 2.17 (Larbalestier et al., 2001; Mannhart, 2001; Hilgenkamp, 2002).

The superconductor of MgB_2 is getting hot in the past ten years; however its current carrying ability has not been comparable with YBCO coated conductor, so the theoretical importance of MgB_2 is more than the possible applications. Other HTS materials, for example Tl- and Hg-containing materials, though have a relatively high T_c and higher Birr. than Bi compounds, low J_c values still remain due to the existent of weak-link dominated intergrain coupling problems (Mannhart, 2001; Hilgenkamp, 2002). In addition, both Tl and Hg are toxic and their productions usually involve a second step for the incorporation of Tl or Hg into the crystal structure. Thus, ReBCO type compounds remain the choice for coated conductor applications because of their high J_c at 77 K in the presence of high magnetic fields usually required for power applications, as well as their relative ease of fabrication among superconductors with higher B_{irr}.
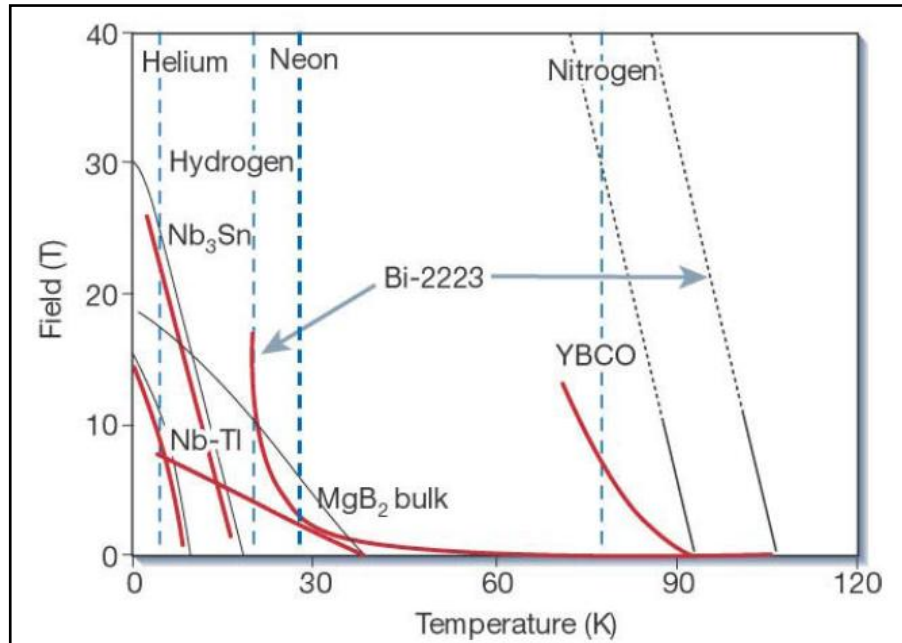
Figure 2.17 Magnetic field-temperature diagram for some superconductors (Larbalestier et al., 2001), black line: upper critical field H_{c2} and red line: irreversibility field B_{irr}.

The driving force for the development of coated conductor is originated from the possible engineering application in magnetic field and theoretical values as well. A high quality and low cost (less than \$50/KA-m) will lead to an industrial-scale commercialization. Factors that must take into account in developing high quality low cost coated conductors are shown in Figure 2.18 It is critical that a superconducting layer is deposited on a substrate with both in-plane and out-of-plane texture. Biaxial alignment of the grains is necessary because high angle grain boundaries create weak links that limit current flow as shown in Figure 2.19.

Indeed, most of the key techniques in developing ReBCO superconductors are focus on the three critical parts: substrate (as a carrier), buffer layers (as a texture base), and superconductor layer (current carrier). Many traditional techniques such as liquid phase epitaxial growth (LPE), vapor deposition (VD), and liquid deposition (LD) were introduced both in buffer layer development and YBCO fabrications. Two well established texture generation methods known as the RABiTS and IBAD were

developed to generating in plane and out-of plane textures on metallic tape and on the buffer layer itself respectively.
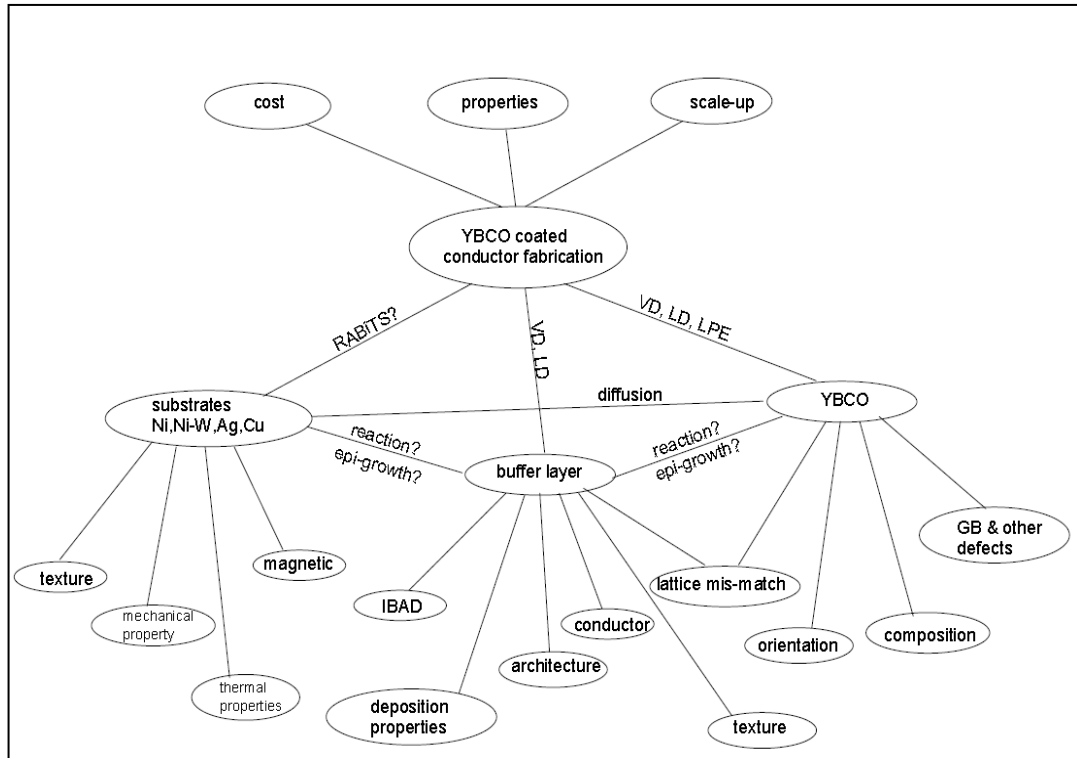
Figure 2.18 Factors to be considered in developing coated conductor with high quality and low cost (Xu, 2003).

The idea in making RABiTS is to form biaxial texture on a metallic tape with cool roll and recrystallization, a thermo-mechanical process. This approach was pioneered by Hitachi on textured Ag tape (Doi, 1994) and by Oak Ridge National Laboratory (ORNL) on textured Ni and Ni-alloy tapes (Goyal, 1996; Norton, 1996). RABiTS are known as a bulk method in as much as the textured metallic tape can be generated in a fast way and subsequent deposition of textured buffers layer is a simple process of extension of substrate texture to a buffer layer.

The architectures of buffer layers have been developed from YSZ single layer to CeO_2-YSZ-CeO_2 multilayers and so on. But in the IBAD approach, an untextured tape requires a thicker buffer layer around 1 μm deposited by a VD method at

temperature less than 100°C. Consequently, compared with the RABiTS process, this is a slow process in biaxial texture generating.
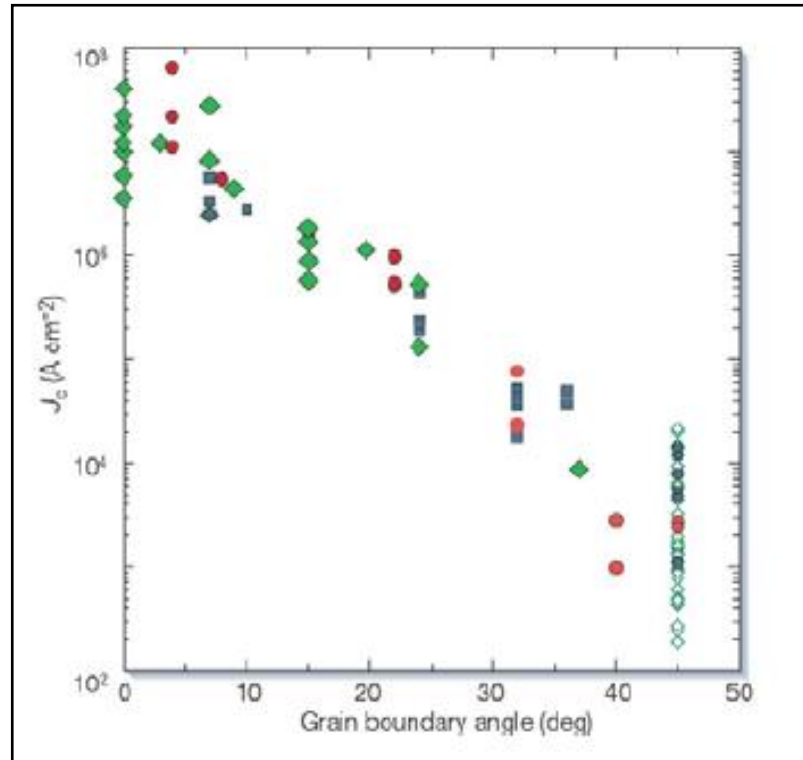
Figure 2.19 Transport critical current density measured at 4.2 K or converted from 77 K by multiply a factor (Xu, 2003).

However, MgO was applied and viewed as a quick way compared with traditional YSZ buffer layers in the IBAD approach (Wang, 1997; Groves, 1999). As the RABiTS approach could generate a biaxially textured metallic substrate, a more straightforward method known as *self-oxidation epitaxy* (SOE) was developed by Matsumoto et al. (1998). SOD may have the advantage of easy to generate an oxide layer (buffer layer) with the same texture as the substrate through a controlled oxidation. Reproducible high quality YBCO film with a current density over 1 MA/cm^2 can be made routinely through PLD method (an in-situ approach), and through e-beam deposition of Y, BaF$_2$ and Cu followed by high temperature anneal (an ex-situ method). But one of the non-vacuum MOD approach known as the TFA (trifluoroacetate) method attracts most of the attention recently. The TFA is a CSD approach pioneered by Gupta (1988) and optimized by McIntyre and Cima (1990).

Recently American Superconductor Corp. (AmSC) announced their newly achievement of over 100 Amps per centimeter of width over 10 meters wires by TFA. This is an astonishing news because the wire was made by using a high volume, low-cost manufacturing method and reproducible. This means the TFA method can be expected to scale up for making long length second generation coated conductor wires with excellent electrical performance with a price-performance ratio below that of copper. Another MOD approach, a fluorine-free TMAP (Xu, 2001; Shi, 2002) method, is being developed and shows promising results on single crystal substrates and on the RABiTS substrates (Xu, 2003). Other focus in developing ReBCO coated conductors lie in: thick film development, substrate select, processing monitor, current flow modeling, termination study, buffer layer architecture, buffer layer developing through CSD, grain boundary doping, and other new techniques such as PED *etc.*

2.5.2 Substrates for Coated Conductors

Substrate including buffer layers is the carrier of any form of coated conductors. Lattice match and suitable orientation are prerequisites for the epitaxial growth of a HTS film. Other fundamental factors that affect the choice of a substrate include thermal expansion coefficients with buffer layer as well as with the superconductor layer (Utke et al, 1997), chemical compatibility and high-temperature stability, dielectric and magnetic properties, suitable mechanical properties (e.g., ductility and strength), size availability (length, width, and thickness) as well as cost effectiveness for a large-scale production. Substrates of chemistry inert to the HTS layer are required during the fabrication through a high temperature process. According to the application, substrates can be classified into two categories: dielectric and metallic substrates. Dissipation factor and dielectric constant as a function of temperature and frequency are of the most critical substrate parameters when coated conductor is applied for the electronic devices in an alternative field. Various dielectric substrate materials are used in microwave, optical and micro-electronic components and circuits.

Table 2.2 Room temperature properties of the commonly used materials for substrates and buffer layers.

Materials	Crystal Structure	Lattice Constant (nm)	Plane Space, d (nm)	Misfit to YBCO (%)	Dielectric Constant (ε)	α ($10^{-6}/$ °C)	Melting Point (°C)
$YBa_2Cu_3O_{6.88}$	Orthorhombic	a= 0.3817 b=0.3883 c=1.1683	(a+b/2)= 0.385	0		7.9 (11)	1150
$Zr_{0.8}Y_{0.2}O_{1.9}$	Cubic	0.5147	0.3640	-5.45	27	10.3	2680
$Zr_{0.85}Y_{0.15}O_{1.93}$	Cubic	0.5139	0.3636	-5.56			2730
CeO_2	Cubic	0.5411	0.3826	-0.62	15	9.9-13.2	2600
$SrTO_3$	c.p.	0.3905	0.3905	+1.43	300	10.4	2080
$LaAlO_3$	r.p.	0.3792	0.3792	-1.51	25.4	9.2	2100
LSAT	c.p.	0.3868	0.3868	+0.47	22	10	1840
$LaMnO_3$	c.p.	0.3880	0.3880	+0.78			
$La_2Zr_2O_7$	c.p.	1.0786	0.3813	-0.96			
$BaZrO_3$	c.p.	0.4193	0.4193	+8.91			
$BaCeO_3$	c.p.	0.4377	0.4377	+1.37			
Y_2O_3	Cubic (Mn_2O_3)	1.055	0.3723	-3.30	13	8.5	2410
MgO	Cubic (Al_2MgO_4)	0.4216	0.4226	+9.35	9.8	8.0-12.8	2852
$NdGaO_3$	o.p.	a= 0.543 b=0.550 c=0.770	0.384 0.389	-0.26 +1.04	25	7.8	1600
NiO	cF8 (NaCl)	0.4177	0.4177	+8.49	10		1990
Si	CF8 (C)	0.543	0.384	+0.27	11-12	3.12	1410
SiO_2 (Quartz)		a= 0.515 c=1.386			3.8	0.59	1720
Al_2O_3 (Sapphire)	Hexagonal	a= 0.4758 c=1.299			9.4-11.5	8.31-9.03	2040

α= coefficient of thermal expansion
o.p.=Orthorhombic perovskite;
c.p.= Cubic perovskite
r.p.=Rhombohedral perovskite

Dielectric substrates can be classified as soft and hard. The lowest values of both the dielectric constant and the dissipation factor are necessary to achieve minimum

dielectric losses at microwave and MM-wave frequencies. Sapphire, alumina ceramic, fused silica or quartz, strontium titanate ($SrTiO_3$), magnesium oxide (MgO), yttrium stabilized zirconate (YSZ), and lanthanum aluminate ($LaAlO_3$) belongs to the hard substrate category. These materials have been widely used in the development of superconducting passive and active microwave components and circuits. Also, single crystals like YSZ, $SrTiO_3$ (STO), $LaAlO_3$ (LAO), and MgO are used as substrates to demonstrate the properties for various methods. Most of the commonly used substrates are listed in Table 2.2 and 2.3. The magnetic properties of substrates could be important especially in cases where AC losses are of major concern. Metallic substrates with non-magnetic or minimum magnetic hysteresis loss are preferred for the application of superconductor wire in alternative magnetic field. Several factors, notably flexibility and availability in long length, prohibit the use of ceramic substrates for large-scale applications.

Table 2.3 Properties of some of the commonly used metallic substrates

Materials	Crystal Structure	Lattice Constant (nm)	Plane Space, d (nm)	Misfit to YBCO (%)	Curie T. (K)	α ($10^{-6}/$ ^{o}C)	σ_y (MPa)	Melting Point (^{o}C)
$YBa_2Cu_3O_{6.88}$	Orthorhombic	a= 0.3817 b=0.3883 c=1.1683	(a+b/2)= 0.385	0		7.9 (11)		1150
Ag	cF4	0.4086	0.4086	+6.13	0	16 (33)		961
Cu	cF4	0.3615	0.3615	-6.10	0	18.9-25.17	75	1083
Ni	cF4	0.3524	0.3524	-8.57	627	13-17.4	59	1455
Ni-7 at. % Cr	cF4				250		64	1430
Ni-9 at. % Cr	cF4				124		87	1430
Ni-11 at. % Cr	cF4				20		102	1430
Ni-13 at. % Cr	cF4				0		157	1430
Ni-V	cF4	0.3520	0.3520	-8.57		11		1425
Ni-Fe	cF4	0.3590	0.3590	-6.75		12		1450
Ni-5% W	cF4				334	12.9	254	
Ni-2%Fe-3%W	cF4						183	
Inconel 601	cF4						337	1384
Haselloy							360	1370

Metallic substrates have obvious advantages in making long and flexible tapes. Silver (Ag) is an attractive candidate, because textured Ag tape usually does not

require a buffer layer for coated conductors. Ag also has non-magnetic and inert and nonpoisonous to ReBCO compounds. Nonetheless, Ag has its major drawbacks such as its low melting point (~961°C) and extreme softness after annealing. With alloying, higher intensities can be expected, but the trade off is an even lower eutectic temperature. The difficulty to get high quality biaxial textures is another drawback for a silver substrate. Iron and its alloys usually are not considered as the candidate substrates for the coated conductor because most of them belong to a magnetic material and cannot resist oxidation at high temperature during the ReBCO formation as well. Among the metallic materials considered, Ni and Ni-based alloys have very good stability and oxidation resistance at an elevated temperature. High quality biaxial textures have been demonstrated on these materials through the RABiTS technique with cubic percentage even higher than 99%. Different categories of Ni base alloys, such as Ni-Cr and Ni-W, have been developed in the consideration of mechanical and magnetic properties. For example, Ni- 5% W alloy though has a curie temperature of 334 K (>77 K), the magnetic losses are 0.086W/KA-m at 60Hz, a factor of 5 lower than that of the Ni substrate (Rubich, 2002). For the Ni-Cr alloys, the Curie temperature drops below the boiling point of liquid nitrogen (77K) when the content of Cr is higher than 10 %. Another potential substrate is copper. Textured copper with FWHMs of 9° and 8° for the rocking curve and phi-scan respectively has been prepared through the RABiTS approach by Jin *et al.* (2000).

The mechanical properties of substrates are important especially in cases where the engineering critical current density J_e, which is defined as current per total cross sectional area of superconductor and sheath, is of a major concern. It is preferable to use a thin (but strong) substrate in order to provide good mechanical support for handling of the conductor in various processing steps during and after the deposition. Typically, 50 μm thick substrates are commonly used nowadays (Goyal, 2001). But if chose a high strength material, 10-30 μm or even thinner substrates are more preferable. Reasonable high yield strength is necessary because a un-recoverable deformation (ductile deformation) usually damages the buffer and the ReBCO layer and makes the handing more difficult. It is important to match (<10%, (Utke, 1997))

the thermal expansion coefficients of the substrate with the buffer layer and the superconducting film.
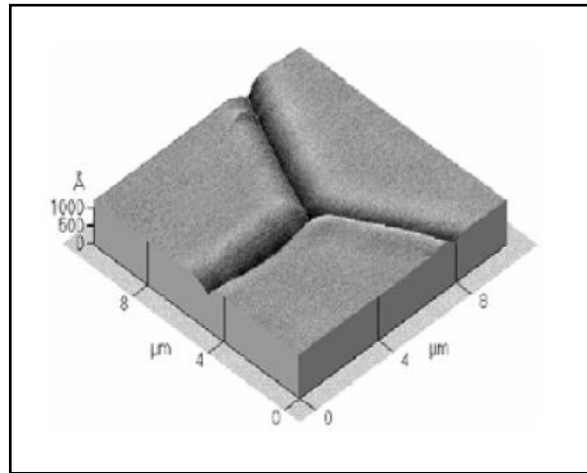
Figure 2.20 AFM image showing the a thermal grooving in Ni grain boundary annealed at 800 °C (Goyal, 2001).

Based on the present setup, usually the thickness of substrate is in the range of 50-100 μm, much thicker than the YBCO film or even the total (< 3 μm) of the YBCO and the buffer layer, as no big difference of the Young's modules between the substrate and the film, thus, the substrate thermal expansion properties will determine that of the overall wire. From the mechanical point of view, cracking possibility will reduce if a lightly compress stress generated in the YBCO film as well as in a buffer layer upon cooling from a growth temperature. That means an ideal substrate should have a thermal expansion coefficient that matches or is slightly larger than those of films. If keeping alloy content (especially W) in a low level, the thermal expansion coefficient of the currently used substrate is just in a good range as described above. Surface quality of substrates such as roughness, cleanliness, and grain boundary grooving play a significant role for the buffer and the YBCO growth. As a Ni-based RABiTS substrate was formed through cool deformation and high temperature anneal (>800°C), high grain boundary energy usually will generate thermal grooving at grain boundaries (GB) as shown in Figure 2.20. Preliminary experimental data have not shown adversely affect of a GB grooving on J_c (Goyal, 2001).

2.6 Production of Superconducting Films

A textured substrate obtained from either the RABiTS process or the IBAD process provides a starting material over which the epitaxial layer of YBCO (HTS) can be applied using various candidate options. Among these options, PLD, RF-sputter, PED, e-beam based deposition and electrophoresis are physical deposition processes, and Metal-Organic Chemical Vapour Deposition (MOCVD), sol-gel, Chemical Vapour Deposition (CVD), aerosol/spray pyrolysis and MOD are chemical deposition methods. In addition, pulse laser deposition (PLD), sputter and e-beam based deposition are the processes that can result in a thin/thick film of YBCO on the substrate and require no additional post thermal treatment, called in-situ methods; and the other processes such as e-beam Y-BaF$_2$-Cu, MOCVD, sol-gel, CVD, aerosol/spray pyrolysis, MOD, electrode-position and electro-phoresis all require post thermal treatment to complete the crystallization and oxidation of the deposited films to the desired YBCO phase, called exsitu methods. Of these methods, PLD, e-beam Y-BaF$_2$-Cu, and MOD/sol-gel are most prominent and popular for the ReBCO coated conductor development.

2.6.1 In-situ Methods

Most of the in-situ methods are originally from thin film depositions usually utilize physical vapor deposition (PVD) techniques where the film grows at an atomic-scale increment. Examples of these processes include pulsed laser ablation, sputter, and e-beam evaporation *etc*. The early work was well established on the optimizing of the deposition conditions such as the deposition temperature, oxygen partial pressure, as well as the setting up of the YBCO phase diagram (Feenstra, 1991). High quality YBCO films can now be produced. Based on thin film technologies (PVD), very high critical current densities over 1,000,000 A/cm^2 (77K self-field) of YBCO coated conductors have been achieved routinely in many groups in the world. However, several problems frustrate these in-situ techniques to be used for the coated conductor applications. First, there is a widespread concern that such vapor phase techniques may not be financially viable for many applications mainly

due to its high capital cost of high vacuum system used in these processes; second, in-situ routes are of slow processing rates due to the atomic-scale increment in thickness. The deposition is confined to very limited area because of the chamber size and local conditions (T and PO_2) *etc*., this may cause difficulties in scaling-up for a production. Another problem is that there exists an upper limit to the film thickness over which the desired *c*-axis oriented epitaxial growth cannot be properly maintained (Macmanus, 1998; Scheeel, 1991), though there are occasionally report on thick film with current density over 10^6 A/cm^2. Other concerns like only a small fraction of target materials be used for the film deposition because of the uniform evaporation in the chamber may result in an over consumption of target materials, consequently, the change of target may introduce extra problems for a long length tape as well. Though with the difficulties, big progress have been made recently, Peterson (2002) from Los Alamos National Laboratory reported a 600 A/cm for shorted sample and an over 200 A/cm for 1 meter long tape by PLD YBCO on IBAD MgO substrates. Freyhardt (2002) from University of Goettingen (Germany) got a critical current of 223 A/cm over a 10-meter length with a current density exceed 2×10^6/cm^2 by the PLD YBCO on the IBAD-YSZ tape.

2.6.2 Ex-situ Methods

Ex-situ methods attract a lot of attentions recently. Compared with in-situ approaches, ex-situ methods have only been developed in recent years, it was originally developed in the consideration of simple operation, low cost and easy to scale up. Most of the ex-situ approaches are viewed as thick film processes and are not very well established. However, there are breakthroughs on ex-situ BaF$_2$ process, MOD-TFA and MOCVD method, other routes are booming for example, ultrasonic spray pyrolysis and non-fluorine sol-gel approaches (Xu, 2003). The LPE had been viewed as one of the most promising routes for high-rate growth of ReBCO, as it is a one-step process capable of growing films at high growth rates. Whilst the relatively low current density and high processing temperatures, which may result in over oxidation, interface reaction and ruin the buffer layer, make this method step out in the competition. Usually ex-situ routes involve two processing steps whereby a

precursor layer is first deposited either by ultrasonic spray, spin or dip coating, or the *ex-situ* BaF$_2$ process *etc*. The precursor layer is subsequently heat treated to convert to a crystallized ReBCO layer in order to obtain the desired biaxial texture. In the *ex-situ* BaF$_2$ process, the precursor film is co-evaporated by e-beam from Y, Cu, and BaF$_2$ sources, followed by an *ex-situ* heat treatment under a controlled humidified atmosphere. The exact mechanism of the heat treatment process is still under investigation; however, Solovyov (2000) proposed that the metal-oxifluoride precursor decomposes as the temperature increase in the presence of H$_2$O vapor while releasing HF, and the decomposed precursor product is converted into a Y123 phase. Hence, it is important for the conversion process to go to a completion, which is generally a straightforward process for short samples. However, problems arise for longer samples where non-uniform YBCO conversion is reported (Lee, 2002); this is thought to be due to the built-up of HF to a saturation level, leaving part of the precursor film un-reacted. Recently, Lee (2002) from ORNL reported 90 A/cm, one meter long with 0.82 μm YBCO film on RABiTS and Feenstra (2002) reported 270 A/cm-w for 3-meter long and 3 μm YBCO film on RABiTS.

Actually, ex-situ CSD approaches were developed soon after the discovery of YBCO HTSC in 1986. In the early time, there were three commonly used solutions applied for the ReBCO deposition (Lange, 1996; Paranthaman, 2002; Schwartz, 1997):

1. Sol-gel processes that used 2-methoxyethanol as a reactant and solvent,
2. Hybrid processes that use chelating agents such as acetylacetonates or diethanolamine to reduce alkoxide reactivity,
3. Metal organic decomposition (MOD) techniques that use high-molecular-weight precursors and water insensitive carboxylates, 2-ethyl-hexanoates, etc.

These CSD routes have been used to grow both oxide buffer layers and superconductor films. The early research failed in developing high current density films and people believe that the carbon-contained precursors might result in the formation of stable BaCO$_3$ at the grain boundaries (Parmigiani, 1987). Gupta (1988) firstly reported a method by using metal trifluoroacetate precursors, called TFA

method, to generate textured YBCO films on crystal substrates, McIntyre and Cima (1990) further developed this method and high current density was achieved in thin YBCO films.

The use of TFA salts appears to avoid the formation of the $BaCO_3$ because the stability of barium fluoride is believed greater than that of barium carbonate and fluorine can be removed during the high temperature anneal (>650°C) in a humid, low oxygen partial pressure environment (McIntyre, 1992). Now metalorganic deposition using trifluoroacetate salt (TFA-MOD) is a better known and well established sol-gel route attempted by several groups towards coated conductor fabrication (Smith, 1999; McIntyre, 1995; Araki, 2001, Gupta, 1998). Spin or dip coating is usually used to deposit the precursors that are then calcined under various O_2 partial pressures. High J_c values ranging from 6.7 MA/cm^2 to 7.5 MA/cm^2 on single crystalline $LaAlO_3$ substrates and 1.7-2.5 MA/cm^2 on the IBAD-YSZ and Hastelloy substrates have been reported. Nonetheless, all these high J_c films were very thin, ranging from 85 nm to 180 nm, resulting in a low J_e Even with a recent result on a 3-cm long Hastelloy tape with J_c of 2.5 MA/cm^2, where the YBCO film was only 230 nm thick. A real breakthrough attributed to the researchers in American Superconductor Corporation (AmSC), Malozemoff et al. (2002) reported one meter long YBCO film with thickness over 1 μm and a current density over 1 MA/cm^2.

More recently AmSC announced more than 10 meters long reproducible YBCO coated conductor wire with over 100 A/cm^2 of width with 1 μm thick YBCO film. These results are comparable with some vapor deposition approaches on metallic substrates. MOCVD is another promising ex-situ approach; it offers several advantages for the large-volume production of coated conductors. Precursors are maintained outside the vacuum chamber and therefore refill is simple during a long deposition cycle. The deposition zone can be unlimited size since it can be configured to be as long and as wide as the showerhead, which is extremely beneficial for a high output.

Recently Lee et al. (2002) reported a meter long YBCO coated conductor wire by MOCVD with over 90 Amps per centimeter of width and a current density over 1.2 MA/cm^2 on a IBAD substrate. Recently Xu et al. (2001) and Shi et al. (2002) restarted the non-fluorine MOD research for the YBCO coated conductor development, preliminary results show that in a humid low oxygen atmosphere, carbon contain precursor can be converted to high quality YBCO film with ideal textures and good electrical properties (T_c=90 K, J_c=1.6 MA/cm^2) on single crystal substrates. The results show importance both in theoretical and in practical applications, because a re-assess of the function of carbon in precursor and/or in a YBCO film bring out the topic: how much is the carbon contaminate in a YBCO film, the compare of the function of C with F during the conversion of precursor films; and also a most important being that the removal of fluorine in the form of HF at high temperatures in TFA approach is a non-trivial process. There appear to be many issues related to fluid-flow and complicated reactor designs may be required for the scale-up.

2.7 Chemical Solution Deposition (CSD) Method

Chemical solution deposition (CSD) methods have been widely used for thin film growth especially thin films for electronic applications such as conducting, dielectric, pieozoelectric, pyroelectric, electrooptic and magnetic films. These methods were effectively used in not only electronic films but also electrochemistry, nanotechnology, protective, decorative and photocatalytic applications. These methods are discovered soon after the discovery of YBCO.

The main advantages of the CSD method over other methods are:

1. It is easy to control the composition of such compounds by changing the stoichiometric ratio of the starting material to ensure high homogeneity,
2. It has a relatively low processing temperature and it does not take longer time to prepare as compared to solid state reactions,

3. It is cost effective and a large number of film compositions can be quickly tested in a cost effective manner by quick prototyping.

A common feature of CSD processes is that the as deposited film is transported into the desired crystalline state through an amorphous intermediate. It has been reported by many researchers that microstructural variations may be induced through changes in chemical precursor, processing route or heat treatment profile (Birlik, 2006). A range of requirements must be fulfilled by the solution chemistry, substrates and processing conditions for successful implementation of the CSD method. These are:

1. Sufficient solubility of precursors in the solvent to form a stable coating solution,
2. Synthesis of precursors that decompose or may be pyrolysed without undesirable residues during thermal processing, all of the elements except the cations and oxygen ions must be released into the gas phase during the heat treatment,
3. No macroscopic phase separations of precursor components during drying or pyrolysis, crystallization of the individual components upon solvent evaporation should be avoided and homogeneity at an atomic level should be retained,
4. Acceptable wetting of the substrate,
5. Solution rheology adjusted to the deposition approach and the deposition parameters employed to avoid thickness variations (striations),
6. No crack formation or compositional non-uniformities during pyrolysis or crystallization,
7. Minimal interdiffusion of film and substrate constituents,
8. Minimal degradation of substrate properties during film processing,
9. Sufficient long-term stability of the solution to avoid non-reproducible film properties that is dependent on solution ageing.

If all of these requirements are fulfilled and the processing conditions are optimized, the CSD technique represents a rapid and cost-effective method for synthesizing high quality electronic oxide thin films (Bhuiyan, Paranthaman & Salama, 2006).

The general principle involved in the solution deposition is to prepare a homogeneous solution of the necessary cations species. Fabrication of thin films by CSD method involves four basic steps:

1. Synthesis of the precursor solution,
2. Deposition by spin coating, dip coating or spraying,
3. Low temperature heat treatment for drying, pyrolysis of organic species (generally at 300-400°C), and formation of an amorphous film,
4. Higher temperature heat treatment at 600-1100°C for densification and crystallization of the coating into the desired oxide phase (Pierre, 1996).

For most solution deposition techniques, the final three steps are similar despite differences in the characteristics of the precursor solution. Depending upon the solution route employed, different deposition and thermal processing conditions may be employed to control film densification and crystallization for the preparation of materials with optimized properties. The selection of the starting reagants is dictated by solubility and reactivity considerations and the type of solution precursor species desired. In addition to precursor characteristics, film processing characteristics like substrate wetting can also play a role in determining the solution chemistry that must be developed. Film properties that can necessitate changes in solution chemistry include poor thickness uniformity (striations), crack formation, crystallization behavior and lack of phase purity and compositional non-uniformities.

The chemical solution for deposition is generally prepared by dissolving and reacting the individual precursors or precursor solutions. The interactions that occur between the starting reagents during solution synthesis depend on the chemical reactivity of the compounds and the solution preparation conditions. Depending on the procedure utilized during coating, solution preparation, gelation behavior of the deposited film and reactions that take place during thermal annealing, the various chemical routes utilized in CSD film fabrication can be grouped into several groups. First one is the hybrid processes using chelating agents such as acetylacetones or diethanolamine to reduce alkoxide reactivity. Second one is the sol-gel process that

used 2-methoxyethanol as a reactant and solvent and the last one is the metal organic deposition (MOD) techniques that use high molecular weight precursors of water-insensitive carboxylates, 2-ethylhexanoates. In addition, other processes that have been less extensively used are; diol and suspension process, nitrate method, citrate method and Pechini process (Bhuiyan et al., 2006).
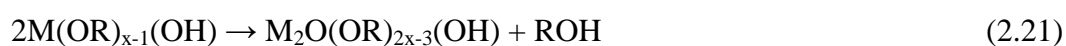
2.7.1 Sol-Gel Method

During solution synthesis, the chemical interactions that take place between the starting reagents will depend on both the reactivity of the compound and the solution preparation conditions, such as reflux temperature. In true sol-gel processing routes, the reactivity of the reagents is high, and if alcohol exchange occurs or if modifying ligands are used, the structure of the species in solution can bear little resemblance to the starting compounds. In this case, the species that are generated are frequently oligomeric in nature and can contain more than one type of cation (Chae, 1994; Ma and Payne, 1994; Kessler, 1994). Although other alcohols have also been utilized, the solvent, 2-methoxyethanol ($CH_3OCH_2CH_2OH$), is most extensively used in the chemical synthesis of perovskite materials. Processes based on 2-methoxyethanol (Dey, Budd and Payne, 1988) are most appropriately considered sol-gel processes and the key reactions leading to the formation of the precursor species are hydrolysis and condensation of the alkoxide reagents, in which metal-oxygen-metal (M-O-M) bonds are formed.

Hydrolysis:

$$M(OR)_x + H_2O \rightarrow M(OR)_{x-1}(OH) + ROH \qquad (2.20)$$

Condensation (alcohol elimination):

$$2M(OR)_{x-1}(OH) \rightarrow M_2O(OR)_{2x-3}(OH) + ROH \qquad (2.21)$$

Condensation (water elimination):

$$2M(OR)_{x-1}(OH) \rightarrow M_2O(OR)_{2x-2} + H_2O \qquad (2.22)$$

Prehydrolysis of less reactive alkoxides may also be used to improve solution compositional uniformity. Another key reaction in the use of this solvent is the alcohol-exchange reaction that results in a decrease in the hydrolysis sensitivity of starting reagents such as zirconium *n*-propoxide and titanium isopropoxide used in the production of films:

Alcohol exchange:

$$M(OR)x + xR'OH \rightarrow M(OR')x + ROH \tag{2.23}$$

where OR is a reactive alkoxy group and OR' is the less reactive methoxyethoxy group.

It has also been demonstrated that through manipulation of the above reactions, i.e., by controlling the reflux, catalysis, and hydrolysis conditions, the nature of the resulting solution precursors and gels may be controlled, allowing for control of material properties. Solution processes based on the use of methoxyethanol are perhaps the most widely used of any of the CSD routes, primarily due to the ability of this solvent to solubilize a variety of starting reagents.

When properly carried out, sol-gel processes offer excellent control and reproducibility of process chemistry, and nonhydrolyzed solutions exhibit minimal aging effects. Thin films with excellent properties have been prepared by sol-gel for a number of materials including PZT (high dielectric constant and ferroelectric hysteresis) (Dey, Budd and Payne, 1988), $LiNbO_3$ (electrooptic coefficient) (Hirano and Kato, 1987), $BaTiO_3$ (high dielectric constant), and YBCO (high critical current capabilities) (Kakihana, 1996).

However, for the non-chemist, the procedures involved in solution synthesis can be rather complex. Thus while the control over precursor characteristics is good, process simplicity is low. In addition, 2-methoxyethanol is a known teratogen, which presents a significant safety concern and inhibits its use in most manufacturing facilities. Recently, the replacement of methoxyethanol by 1,3-propanediol in this

process has been reported (Kakihana, 1996). As with the original process, the key reaction that defines the nature of the precursor species is alcohol exchange between propanediol and the original alkoxy groups.

2.7.2 Metallorganic Organic Decomposition (MOD) Solution Synthesis

The solution synthesis approach employed for perovskite film formation, metalloorganic decomposition (MOD), has historically used large carboxylate compounds (West and Xu, 1988). The basic approach consists of simply dissolving the metalloorganic compounds in a common solvent, usually xylene, and combining the solutions to yield the desired stoichiometry. For solution preparation, investigators have used both commercially available precursors and have synthesized starting reagents in-house (West and Xu, 1988). Since the starting compounds are water-insensitive, they do not display the oligomerization behavior discussed above, and the precursor species that exist in solution retain a strong resemblance to the starting molecules. This aspect of the process, together with the use of no interacting solvents, allow us to characterize the solution as a simple mixture of the starting compounds. Solution synthesis is straightforward, and the approach allows for rapid compositional mapping of material systems. It has been used for a number of ferroelectric materials (Klee, 1992), for the preparation of perovskite films suitable for magneto resistive applications (Manabe, 1997), and for high-temperature superconductors (Gross, 1988). While the process is straightforward, it does possess a number of limitations. First, the large organic ligands of the most commonly used starting reagents may cause cracking during thin-film processing due to the large weight loss and shrinkage that can occur. To circumvent this difficulty, proper control of solution concentration and thermal processing is required. Second, while some researchers might justifiably deem this an advantage, most process engineers would consider the minimal reactivity of the starting reagents to be a further limitation. Because the characteristics of the precursor species can exhibit dramatic effects on thin-film properties, the inability to "tailor" the properties of the low-reactivity starting compounds through reactions such as chelation and hydrolysis and condensation restricts process flexibility. Hence, control of structural evolution and

thin-film microstructure becomes limited to variations in solvent and solution concentration, and film deposition and heat treatment conditions (Xu, 2003).

The standard MOD process using large carboxylate compounds is still widely employed, but Haertling (1995) has developed an elegant, alternative MOD strategy that minimizes the first problem discussed above. This route is seeing more widespread use in the fabrication of PZT films, and the concepts involved in its development merit further consideration. In his process, low reactivity starting reagents are again employed, but in this case, short-chain carboxylate (e.g., acetate) and β-diketonate (e.g., acac) compounds are used. The compounds used are both water-insensitive and commercially available, and solution synthesis is straightforward for the nonchemist. The lower organic content of the precursors reduces film shrinkage after deposition, decreasing problems with film cracking. Films with properties comparable to those prepared by sol-gel and chelate processes are obtained. The precursor solutions therefore exhibit aging (and a change in film properties); however, the aging rates are apparently slower than those for chelate processes (Xu, 2003).

2.7.5 Trifluoroacetate (TFA) Method

In conventional MOD, a gel film is deposited onto a substrate using a coating solution and dried. Then the gel film is calcined and fired to become a superconducting film at ambient pressure. This MOD greatly reduces the production cost but does not have excellent reproducibility in forming high J_c (over 1 MAcm^{-2} (77 K, 0 T)) superconductors. Such low reproducibility is considered to result from non-equilibrium chemical reactions based on the decomposition of chemicals. Stable $BaCO_3$ distributes as a carboxylic group and degrades J_c of the YBCO films (Araki et al., 2003). Furthermore, nucleation of nanocrystallites in the precursor films causes YBCO grains to take on a random orientation during the firing process. Obtaining large area uniform high-J_c YBCO films with this process is difficult because the temperature and partial oxygen pressure must be simultaneously controlled precisely in order to decompose $BaCO_3$ entirely. The rapid heating and cooling processes are

also disadvantages for fabricating large-area uniform superconductors. The metal organic deposition using trifluoroacetates (TFA-MOD) belongs to a category of the chemical solution deposition methods, which have various advantages like precise controllability of metal contents, wide flexibility for coating object and low-cost, non-vacuum approach to YBCO superconductors (Araki et al., 2002). The TFA-MOD method has a prominent feature as it is considered to have equilibrium chemical reactions in forming YBCO superconductors. Such a prominent feature leads to high reproducibility in fabricating high J_c superconductors. It is firstly introduced by Gupta in 1988 after many trails in YBCO film fabrications. First, he started with the nitrate precursors on heated substrates by spray deposition. Two things that bother this research are high annealing temperature and polycrystalline features which degraded severely the current carrying ability and broaden the T_c transition. In effort to get rid of these, Gupta changed his research to metal trifluoroacetate precursors (Xu, 2005). After that, McIntyre improved the solution making procedure by directly dissolving the acetates of barium, yttrium and copper in deionized water and reacted with a stoichiometric quantity of trifluoroacetic acid at room temperature. This process made the process simplier and easier to control, which makes the TFA method a standard procedure; though some minor revisions have been made such as the introduction of a purifying step reported by Araki (2001) and co-workers. In TFA-MOD, TFA (trifluoroacetic acid) produces a fluorinated precursor film and the fluorides cause very different chemical reactions at each stage of the process compared with those of conventional MOD. TFA has similar structure with acetic acid but its chemical nature is very different. Each atom has electron negativity which indicates how strong the atom withdraws/loses an electron from/to another atom. Fluorine has the highest electron negativity of all the elements. From the periodic table, elements in the upper right have stronger electron negativity and those in the lower left have weaker electron negativity.

As a summary, TFA-MOD process has several advantages according to MOD. Nanocrystallites of the precursor film never influence the structure of the resulting YBCO film, the total firing time is simply proportional to the film thickness and the

harmful carbon content is entirely eliminated during the calcining process (Birlik, 2006).

2.8 Indentation Technique

Indentation tests, in many cases referred to as hardness tests, have for a long time been a standard method for material characterization. The hardness test consists of loading an indenter made of diamond or any other hard material (e.g., Tungsten Carbide) and pressing it into the surface of a softer material to be examined. The further into the material the indenter sinks (for a given load), the softer the material is and the lower its yield strength. Hardness is not an intrinsic material property dictated by precise definitions in terms of fundamental units of mass, length and time. A hardness property value is the result of a defined measurement procedure. Hardness tests are the most commonly used non-destructive testing procedures in the metal industry and in research because they provide an easy, inexpensive and reliable method of evaluating basic properties of developed or new materials. The hardness test indenter is so small that it scarcely damages the bulk material; therefore, it can be used for routine batch tests on small samples of materials to ascertain that they are up to specifications on yield without damaging them. The usual method to achieve a hardness value is to measure the depth or area of an indentation left by an indenter of a specific shape, with a specific force applied for a specific time. There are three principal standard test methods for expressing the relationship between hardness and the size of the impression, these being Vickers, Rockwell and Brinell. The Vickers indenter is a square based pyramid with an angle of 136 degrees between the faces and a ratio of diagonals of 1:1 (as shown in Figure 2.21). The Vickers hardness number is one of the most widely used measures of hardness in engineering and science. The Vickers diamond hardness, HV, is calculated using the indenter load and the actual surface area of the impression. The resulting quantity is usually expressed in kgf/mm^2 (Yao, 2005).

F= Load in kgf

d = Arithmetic mean of the two diagonals, d_1 and d_2 in mm (Figure 2.21)
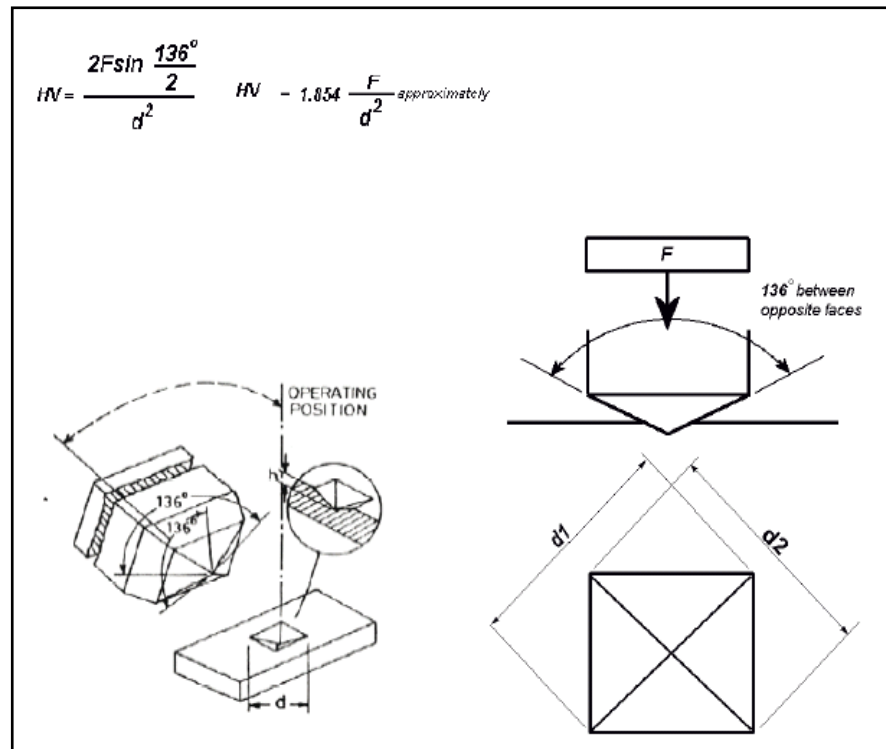
HV = Vickers hardness

Figure 2.21 Scheme of Vickers hardness test and Vickers impression (Yao, 2005).

The Rockwell hardness test method consists of indenting the test material with a diamond cone or hardened steel ball indenter. The indenter is forced into the test material under a preliminary minor load F_0 usually 10 kgf. Once equilibrium has been reached, an indicating device, which follows the movements of the indenter and so responds to changes in depth of penetration of the indenter, is set to a datum position. Whilst the preliminary minor load is still applied an additional major load is applied with resulting increase in penetration.

When equilibrium has again been reach, the additional major load is removed but the preliminary minor load is still maintained. Removal of the additional major load allows a partial recovery, so reducing the depth of penetration. The permanent increase in depth of penetration, resulting from the application and removal of the additional major load is used to calculate the Rockwell hardness number as shown in Figure 2.22 (Yao, 2005).
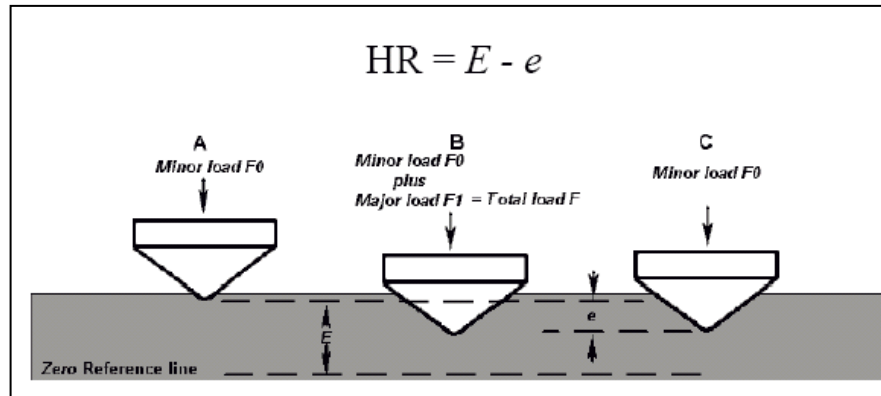
$$HR = E - e$$

Figure 2.22 Schematic diagram of Rockwell hardness test (Yao, 2005).

The Brinell hardness test method consists of indenting the test material with a 10 mm diameter hardened steel or carbide ball subjected to a load of 3000 kg. For softer materials the load can be reduced to 1500 kg or 500 kg to avoid excessive indentation. The full load is normally applied for 10 to 15 seconds in the case of iron and steel and for at least 30 seconds in the case of other metals. The diameter of the indentation left in the test material is measured with a low powered microscope. The Brinell harness number is calculated by dividing the load applied by the surface area of the indentation as seen in Figure 2.23.

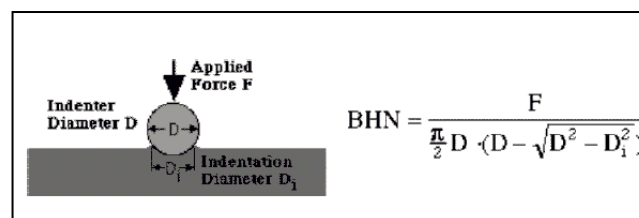$$BHN = \frac{F}{\frac{\pi}{2}D \cdot (D - \sqrt{D^2 - D_1^2})}$$

Figure 2.23 Schematic diagrams Brinell hardness test

The Meyer hardness is similar to the Brinell hardness except that the projected area of contact rather than the actual curved surface area is used to determine the hardness. In this case, the hardness number is equivalent to the mean contact pressure between the indenter and the surface of the specimen. The mean contact pressure is a quantity of considerable physical significance. The Meyer hardness is given by:

$$H = Pm = \frac{P}{A} = \frac{P}{\Pi a^2}$$ (2.24

in which, A is the projected contact area and a is the real contact radius during indentation.

The development of indentation methodologies for the micro mechanical characterization of materials requires a precise understanding of the correlation between uniaxial mechanical properties and hardness. One of such fundamental correlations was found by Tabor (1951) for pyramidal (Vickers) indenters. Considering indentation experiments conducted in specimens of pure copper and mild steel which were previously subjected to different amounts of strain hardening, Tabor proposed that hardness is, to a great extent, proportional to the uniaxial stress at a plastic strain of 0.08. Namely,

$$H = C\sigma_r$$ (2.25)

where H= hardness, C=constant and σ_r= Yield stress.

Most of investigations about deformation mechanisms come from studies on bulk materials characterized under a relatively simple state of stress such as uniaxial tension or compression. Indentation tests are perhaps the most commonly applied means of testing the mechanical properties of materials. Nevertheless, small specimens are difficult to work with conventional experiments used to investigate bulk materials whereas the growing interest in observations of the mechanical properties in microscopic specimens such as thin films and nano-wires. Nanoindentation testing offers the possibility to measure the mechanical properties on a very small scale. Therefore, nanoindentation technique has been increasingly relied to describe the mechanical properties of small specimens and the technique might be a useful as a screening technique for characterizing many samples. Instrumented indentation or generally referred to as nanoindentation, when conducted on a submicron regime, primarily consists of a controlled load (P) applied through a diamond tip that is in contact with a specimen. The penetration depth (h) of

the tip into the material is recorded as a function of the applied load. A typical nanoindenter can record depths to sub-nanometer and loads to sub-mN resolution, respectively. From the recorded load (P)-depth (h) response, various characteristic mechanical properties such as Young's modulus, strain-hardening exponent, fracture toughness, etc., can be estimated. A hard indenter, usually a diamond, transfers the load on to the material and makes an impression. The analysis of the depth of the impression in conjunction with the loading characteristics is used to determine the mechanical properties. Indenters may be sharp (e.g., Berkovich, Vickers, cube corner, etc.), spherical or even flat-ended cylindrical punches. It is a convenient tool for mechanical characterization related to the performance and reliability of small-volume structures (e.g., thin films for microelectronic/optoelectronic devices, surface coatings for optical, magnetic, thermal, environmental and tribological performances). Conventional testing methods such as tensile testing cannot be easily used to obtain mechanical properties at these size scales. Often times this need for small scale mechanical characterization is not merely limited to cases involving mechanical functionality, but extends to applications where functionality is coupled with mechanical behavior (e.g., assessing the thermo-mechanical reliability of patterned Cu or Al interconnect lines in microprocessors). It requires small sampling volumes and consequently can be used to test materials not immediately available in bulk volumes. Examples include amorphous metals or metallic glasses that are not amenable to fabrication in large quantities due to the difficulties associated with suppressing crystallization, or shape-memory alloys with controlled transformation temperatures that are typically fabricated as prototype button-melts to save costs prior to large-scale production. It is a technique that can be used over multiple length scales, i.e., nano-, micro- and macroscales, by simply varying the geometry and penetration depth of the indenter. It probes the multiaxial deformation characteristics of a material, given that the stress state under an indenter is inherently multiaxial.

A hard indenter, usually a diamond, transfers the load on to the material and makes an impression. The analysis of the depth of the impression, in conjunction with the loading characteristics, is used to determine the mechanical properties. Indenters may be sharp (e.g., Berkovich, Vickers, cube corner, etc.), spherical or

even flat-ended cylindrical punches. Spherical indenters may be preferred over sharp indenters owing to the non singular nature of the stress fields below the indenter and additionally, due to the concomitant restraint they impose on damage and plasticity. This means that the onset of plasticity upon indentation is delayed when a spherical indenter is employed. However, this becomes a hindrance to the application of nanoindentation in assessing the properties of thin films or small volumes of material, where the large indent size cannot be physically accommodated due to geometrical constraints. By contrast, sharp indenters induce plastic deformation at an earlier stage during loading and hence are more amenable to nano- and microscale measurements (Rajagopalan e al., 2005).

2.9 Instrumented Indentation Procedure of Materials

The indentation technique has been developed in the last two decades from a simple method (Oliver and Pharr, 1992) to the one with high-resolution testing equipment to observe the materials parameters, such as hardness, yield strength, strain hardening exponent and Young's modulus at the micrometer and nanometer scale. The main objective of indentation tests is to extract these mechanical properties of the specimen from load displacement measurement. Indentation technique leads to the size of the residual impression of only a few microns and it makes difficulties to measure the indentation size using optical techniques. Therefore, the depth of penetration beneath of the indenter is measured as the load is applied to the indenter so that it allows the size of the area of contact to be determined. Indentation hardness testing is generally conducted using either spherical or pyramidal indenters. Most common indenter tip, Berkovich indenter, was also used in the present study and an image of Berkovich indenter tip and schematic parameters of the indenter are shown in Figure 2.24 (a) and (b), where A is the projected area of contact, h_p is depth of penetration measured from the edge of the area of contact, and θ is a semi-angle at the faces (Ficher-Cripps, 2002), respectively. The Berkovich indenter shown in Figure 2.24 (a) is generally used in small scale indentation studies and has the advantage of easy construction of the pyramidal edges to meet at a single point.
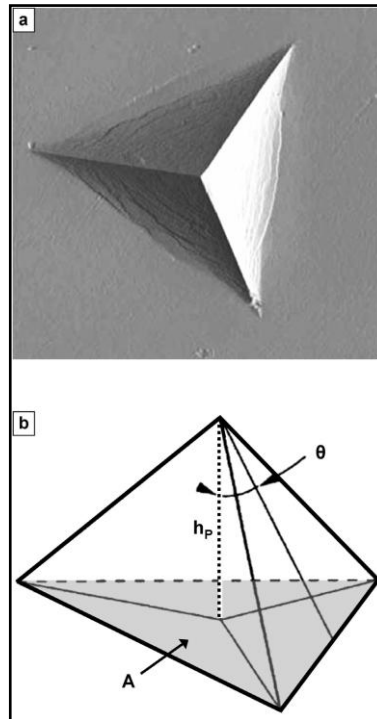
Figure 2.24 (a) SEM image of an indentation made by Berkovich indenter tip and (b) indentation parameters of the Berkovich tip (Ahn, 2008).

The method was developed to measure the mechanical parameters of hardness and elastic modulus from indentation load-displacement data obtained during one cycle of loading and unloading. A schematic plot of a typical load-displacement data set obtained with Berkovich indentation is displayed in Figure 2.24, where P designates the load and h is the displacement relative to the initial undeformed surface (Oliver and Pharr, 2004). From the load displacement data, there are three important quantities must be measured: the maximum load, P_{max}, the maximum displacement, h_{max}, and the elastic unloading stiffness, $S = dP/dh$, defined as the slope of the upper portion of the unload curve during the initial stages of unloading (the constant stiffness) and total, elastic-plastic work values of materials. Additional important parameter is the final depth, h_f, which is the permanent depth of penetration after the indenter is fully unloaded (Ahn, 2008).
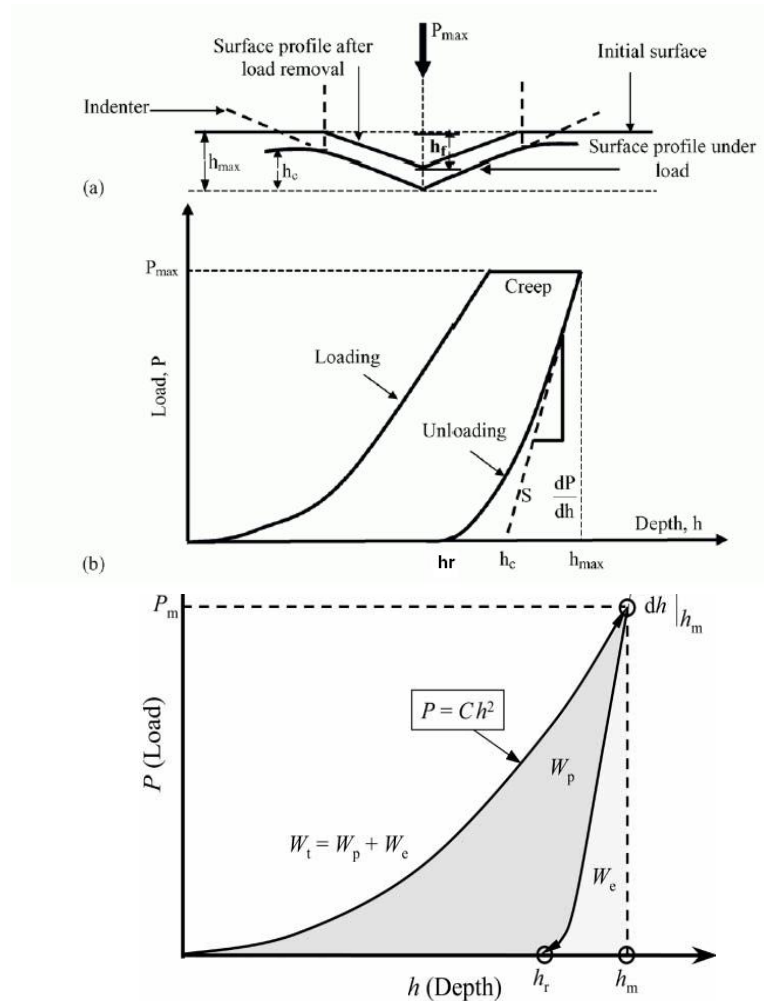
Figure 2.25 Schematic plot of an indentation load-displacement curve showing important parameters (Ahn, 2008).

During loading, the response generally follows the relation described by Kick's Law: $P=Ch^2$, where C is the loading curvature. The average contact pressure, $p_{ave}=P_{max}/A_{max}$ can be identified with the hardness of the indented material. The W_t term is the total work done by load P during loading, W_e is the released (elastic) work during unloading, and the stored (plastic) work $W_p = W_t-W_e$. The residual indentation depth after complete unloading is h_r.

The exact processes to measure the hardness, H, and elastic modulus, E, are based on the unloading procedures shown schematically in Figure 2.25, where h_c is the

vertical distance along which contact is made (the contact depth) and h_s is the displacement of the surface at the perimeter of the contact (Oliver and Pharr, 1992). The basic assumption is that the periphery of the indenter sinks in a manner that is described by models for indentation of a flat elastic half-space by rigid punches of simple geometry. Then, supposing pile-up of material at the contact periphery is negligible, the elastic models show that the amount of sink-in, h_s, is given as follows:

$$h_s = \varepsilon \frac{P_{max}}{S} \tag{2.26}$$

where ε is a constant that depends on the geometry of the indenter. Using Equation 2.26 and following the geometry of Figure 2.25, the vertical displacement of the contact periphery, h_c, is given by:

$$h_c = h_{max} - \varepsilon \frac{P_{max}}{S} \tag{2.27}$$

When the contacting area, A, is described as a function of h_f, the hardness of specimen is estimated by:

$$H = \frac{P_{max}}{A} \tag{2.28}$$

It should be noted that the estimated hardness value may deviate from the traditional hardness value if there is significant elastic recovery during unloading whereas it is important to consider only when the material has a very small value of *E/H*. The measured unloading stiffness is then estimated by:

$$S = \frac{dP}{dh} = \beta \frac{2}{\sqrt{\pi}} E_{eff} \sqrt{A} \tag{2.29}$$

where β is dimensionless parameter, and E_{eff} is the effective elastic modulus defined by :

$$\frac{1}{E_{eff}} = \frac{1-v^2}{E} - \frac{1-v_i^2}{E_i} \qquad\qquad (2.30)$$

in which E and v are Young's modulus and Poisson's ratio, respectively, for the specimen and E_i and v_i are the same parameter for the indenter. There are possible variations on the basic load-unload cycle including partial unloading during each loading increment, superimposing an oscillatory motion on the loading, and holding the load steady at a maximum load and recording changes in depth. These different types of testing give opportunities to measure the viscoelastic properties of the material. Practically, nanoindentation testing is performed using a variety of substances from soft polymers to diamond-like carbon thin films. Therefore, the shape of the load displacement curve is displayed to be a rich source of information, not only for measuring the mechanical parameters of the material, but also for the indentation of nonlinear events such as phase transformations, cracking and delamination of films. Schematic example of commonly observed load-displacement curves for different materials are depicted in Figure 2.26 (Ficher-Cripps, 2002). It should be noted that in many cases the permanent deformation or residual impression is not the result of plastic flow but may involve nonlinear event of cracking or phase changes within the specimen. Along with the miniaturization of materials, and with the development of advanced materials, the mechanical properties of materials are measured by nanoindentation techniques. But hardness measurements based on the conventional method presented by Oliver and Pharr (2002) showed various errors at measuring the small indentation depth and some relate them to indentation size effects. There have been several reports recording some of the factors causing errors in indentation test data including adhesion due to the presence of adsorbed liquid on the surface of the specimen, creep of the material being tested, surface roughness, tip radius of the indenter and the methodology itself of the nanoindentation experiments (Ficher-Cripps, 2002). Moreover, errors in testing data are associated with the pile-up or sink-in of the material on the edges of the indent during the indentation process. When nanoindentation testing is employed, care must be exercised at small indentation depth. As the indentation depth approaches zero, the method may yield erroneous hardness and Young's modulus mainly because the contact area approaches zero and the testing may not provide accurate values for the contact depth

or area. This error may become a contributing factor to indentation size effect in nanometer scales.
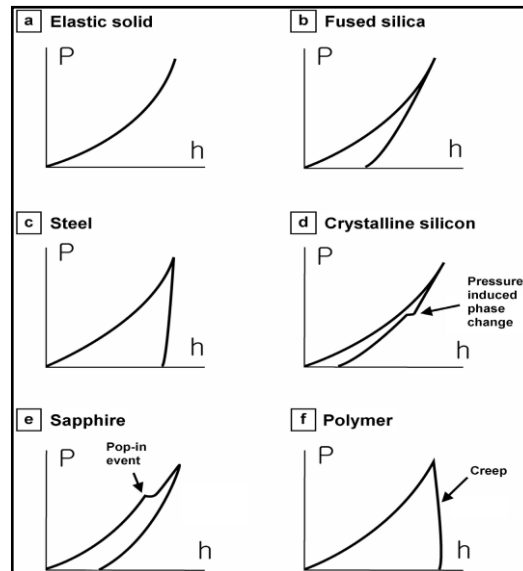

Figure 2.26 Schematic examples of load-displacement curves for different material responses and properties: (a) elastic solid, (b) brittle solid, (c) ductile solid, (d) crystalline solid, (e) brittle solid with cracking during loading, and (f) polymer exhibiting creep (Ficher-Cripps, 2002)

For the past two decades, the advent of nano- and micro- scale science, engineering and technology coupled with substantial progress in instrumentation has resulted in 'instrumented' indentation or 'load-depth sensing' indentation. Figure 3.5 denotes that typical load-depth sensing indentation test graph. It primarily consists of a controlled load (P) applied through a diamond tip that is in contact with a specimen. The penetration depth (h_s) of the tip into the material is recorded as a function of the applied load. There is no question that the loading part is elastic-plastic response. The unloading part is usually considered pure elastic rebound of the material. It is only related to the elastic property of the material. If the area in contact is assumed to remain constant during initial unloading, the elastic behavior may be

modeled as that of a blunt punch indenting an elastic solid. Loubet et al. (1984), Doerner and Nix (1986) adopted the solution of Sneddon (1965) and equated the projected area of contact with the indenter to the area of the flat-ended punch.

Fischer-Cripps (2001) showed that the substitution of reduced modulus in Equation 3.7 for indentation test data is valid. Owing to the utilization of the slope or unloading stiffness, it makes no difference whether or not the deflection of the indenter is accommodated explicitly or transferred to that occurring within the specimen by artificially reducing the specimen modulus from its true value to lower value, the reduced modulus. Usually the indenter is assumed to be perfectly rigid.

Pharr, Oliver and Brotzen (1992) have shown that $E = \dfrac{1-\nu^2}{2}\sqrt{\dfrac{\pi}{A}}\dfrac{dP}{dh_s}$ is applicable to any indenter that can be described as a body of revolution of a smooth function. To evaluate independently the projected contact area A, Bhattacharya and Nix (1988) proposed a simple empirical method based on extrapolating the initial linear portion of the unloading curve to zero load and using the extrapolated depth with the indenter shape function to determine the contact area. One of the more commonly used methods to get contact area by analyzing micro indentation load-displacement data is that of Oliver and Pharr (1992), which expands on ideas developed by Loubet et al. (1984) and Bhattacharya and Nix (1988). They found the load-displacement curves during unloading are not linear for most materials, even in the initial stages. The analysis begins by fitting the unloading curve to the power-law relation:

$$P = B(h_s - h_f)^m \tag{2.31}$$

where P is the indentation load, h_s is the displacement, B and m are empirically determined fitting parameters, and h_f is the final displacement after complete unloading. By differentiating above equation at the maximum depth of penetration, $h_s = h_m$, giving stiffness S:

$$S = \frac{dp}{dh_s}(h_s = h_m) = mB(h_m - h_f)^{m-1} \qquad (2.32)$$

The depth along which contact is made between the indenter and the specimen, h_c, can also be estimated from the load-displacement data using:

$$h_c = h_m - \varepsilon \frac{P_m}{S} \qquad (2.33)$$

where P_m is the peak indentation load and ε is a constant which depends on the geometry of the indenter. With these basic measurements, the projected contact area, A, is derived by evaluating an indenter shape function at the contact depth, h_c, that is $A=f(h_c)$. Finally, substitute S in Equation 2.32. It is important to note these equations were derived from pure elastic contact solution derived by Sneddon (1965), and how well they work for elastic/plastic indentation is not entirely clear. One important way in which the elastic solution fails to properly describe elastic/plastic behavior concerns pileup and sink-in of material around the indenter. In the pure elastic contact solution, material always sinks in, while for elastic/plastic contact, material may either sink in or pile up. Since this has important effects on the indentation contact data, it is not surprising that the Oliver-Pharr method has been found to work well for hard ceramics, in which sink-in predominates, but significant errors can be encountered when the method is applied to soft metals that exhibit extensive pileup.

Bolshakov and Pharr (1998) discussed the influences of pileup on the measurement of Young's modulus and pointed out that when pileup is large, the areas deduced from analysis of the load displacement curves underestimates the true contact areas by as much as 60 %. This, in turn, leads to overestimate the hardness and elastic modulus. The parameter, $\dfrac{h_f}{h_{max}}$ which can be measured experimentally and correlated with the material parameters E, v, σ_y and n ($\dfrac{d\sigma}{d\varepsilon}$) which control indentation deformation, can be used as an indication of whether or not pileup is an important

factor. Pileup is significant only when $\dfrac{h_f}{h_{max}} > 0.7$ and the material does not appreciably work harden. When, $\dfrac{h_f}{h_{max}} < 0.7$ or in all materials that moderately work harden, pileup is not a significant factor and the Oliver-Pharr data analysis procedure can be expected to give reasonable results. They used Finite Element Method (FEM) to complete their analysis and the real contact area is available by examining of the contact profiles in the finite element mesh.

2.9.1 Indentation Analysis of Bulk Materials

Instrumented indentation methods, which provide a continuous record of the variation of indentation load, *P*, as a function of the depth of penetration, *h*, into the indented specimen, have been the topics of considerable attention in recent years. Such interest can be attributed to the following possible applications of the methods:

1. Properties such as Young's modulus, yield strength, and strain hardening exponent (Suresh, Alcala & Giannakopoulos, 1996), as well as fracture toughness (e.g. (Lawn, 1993)) of materials can be estimated by recourse to continuous indentation.

2. The magnitude and sign of any preexisting residual stresses can be assessed, in some cases, from indentation of surfaces (Suresh & Giannakopoulos, 1998).

3. To the extent that continuum analyses adequately characterize indentation, the mechanical properties and residual stresses can be probed at different size scales by the appropriate choice of commercially available instrumentation, as well as indenter load, size and shape.

4. In materials with spatially varying composition, microstructure or dislocation density, the "inverse problem" of the determination of gradients in Young's modulus and yield strength can be accomplished, in some cases, by means of instrumented indentation (e.g. Suresh, Alcala & Giannakopoulos, 1997; Suresh & Giannakopoulos, 1998).

Most of these applications of instrumented indentation are limited, however, by complications in clearly interpreting the indentation results. Such a complication arises from the "pile-up" or "sink-in" of the material around the indenter, which is primarily affected by the plastic properties of the material (Giannakopoulos, Larson & Vestergaard, 1994). In a low-strain-hardening alloy, plastically displaced material tends to flow up to (and pile-up against) the faces of the indenter due to the incompressibility of plastic deformation. The result is a "barrel-shaped" impression due to pile-up around the sharp polygonal indenter, as shown in Figure 2.27 (a). On the other hand, for high-strain-hardening materials, the plastically deformed region is pushed out from the indenter with the imprint sinking below the initial surface level. The result is a "pin-cushion like" impression around the sharp indenter, as shown in Figure 2.27 (b). Methods which properly account for pile-up or sink-in around the indenter are essential for the interpretation of the plastic properties of materials by recourse to instrumented indentation. As a consequence of pile-up or sink-in, large differences may arise between the true contact area (which is influenced by the pile-up and sink-in of the materials and which is often difficult to assess *in-situ* during indentation) and the apparent contact area which is usually observed after indentation. A knowledge of the relationship between the indentation load and the true (projected) contact area, however, is essential to extract the mechanical properties from instrumented indentation. This difficulty can be overcome if explicit expressions, relating the true contact area A and the depth of penetration of the indenter h into the material being tested, are known *a priori* for different indenter geometries (Suresh & Giannakopoulos, 1999).

Suresh and Giannakopoulos (1999) identified a general theoretical framework for instrumented sharp indentation and outline a methodology which enables the determination of elastic and plastic properties of materials by employing instrumented sharp (i.e. Vickers, Berkovich or conical) indentation. A key feature of the method outlined here is that it provides unique correlations between penetration depth h and true contact area A for commercially available sharp indenters; the method also circumvents the need for contact area measurement through visual observations while, at the same time, taking into account pile-up and sink-in. This

paper also presents some new results on the equivalence between an energy approach and the displacement approach to indentation.
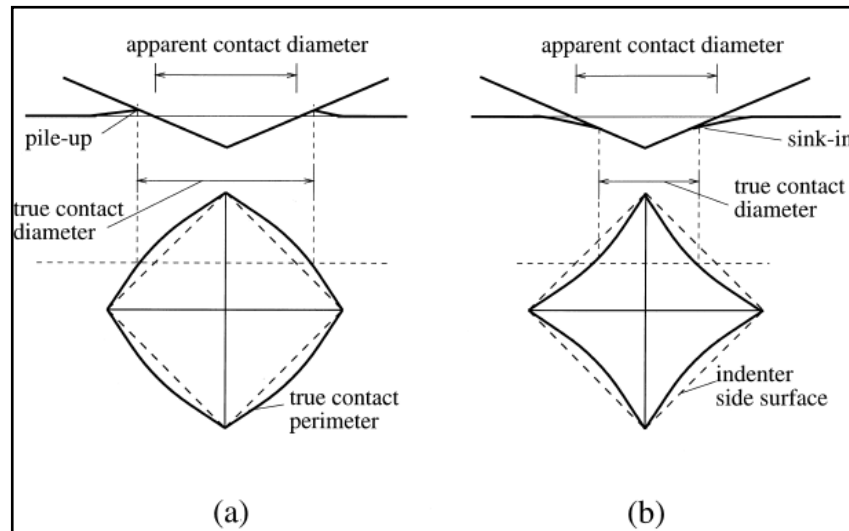

Figure 2.27 Schematic illustrations of (a) pile-up and (b) sink-in around a sharp indenter (Suresh & Giannakopoulos, 1999)

When used in conjunction with the results reported (Suresh & Giannakopoulos, 1998), the method outlined here also facilitates the isolation of the effects of pre-existing residual stresses on sharp indentation response. Whereas attention is confined to sharp indentation in this paper, similar discussions for spherical indentation can be found elsewhere (Alcala, 1998). Details of the numerical simulations from which the present results are extracted are not reported here because of space restrictions; they can be found (Giannakopoulos, Larson & Vestergaard, 1994; Giannakopoulos & Larson, 1997; Larson, 1996). Within the context of continuum analyses, sharp pyramidal or conical indenters lead to geometrically similar indentation states. That is, for a given indenter shape or included tip angle, the average contact pressure, $p_{av}=P/A$, is independent of the indentation load P or the true contact area A. It depends only on the included angle at the tip of the indenter (e.g. Suresh & Giannakopoulos, 1998). This average contact pressure is identified with the hardness H. Detailed three-dimensional, large-strain, plasticity simulations (Giannakopoulos, Larson & Vestergaard, 1994; Giannakopoulos & Larson, 1997; Larson, 1996) reveal that the tip radius of the

sharp indenter, *R*, has a negligible effect on indentation and the *P-h* curve provided that the depth of penetration of the indenter into the material, $h > R/40$. In addition, adhesion and friction between the indenter and the substrate were found to have only a small effect on the hardness and the *P-h* curve.
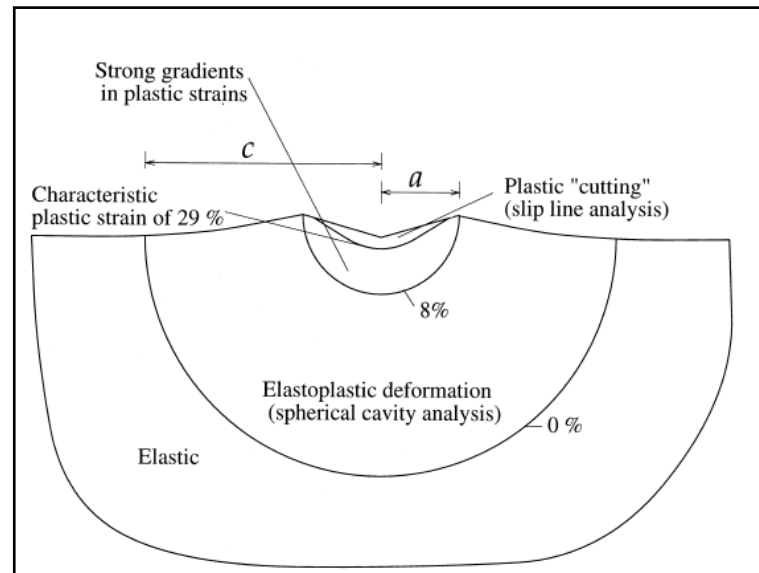
Figure 2.28 Different regimes of plastic flow at the tip of a sharp indenter (Suresh & Giannakopoulos, 1999)

Experiments (Chaudhri, 1998) and computations (Giannakopoulos, Larson & Vestergaard, 1994) also show that there exists a unique characteristic equivalent plastic strain, which separates different modes of plastic deformation directly beneath the sharp indenter. This is schematically represneted in Figure 2.28. The innermost region comprises a zone where the material is "cut" by the sharp indenter; this cutting mode is amenable to analysis by means of the classical slip-line theories of rigid-perfect plasticity (Lockett, 1963). Surrounding this region is a zone of strong gradients in plastic strains which is engulfed by an elastoplastic regime where the so-called "cavity" model of Johnson (1970) can be applied to extract the hemi-spherically shaped elastoplastic boundary. A unique characteristic strain separates the innermost "cutting" region from its surroundings. Although Tabor (1951) proposed a value of 0.08 for this characteristic plastic strain, more elaborate studies (Giannakopoulos, Larson & Vestergaard, 1994; Giannakopoulos & Larson, 1997;

Larson, 1996; Chaudhri, 1998) suggest a value in the range 0.25– 0.36. The characteristic strain is independent of the indenter size or indentation load (provided that $h>R/40$), but is weakly influenced by the tip angle of the sharp indenter. Spherical or other blunt indenters do not lead to such a characteristic strain. Invoking the existence of this characteristic strain is a key step in the determination of mechanical properties and residual stresses by sharp indentation (Suresh & Giannakopoulos, 1997).
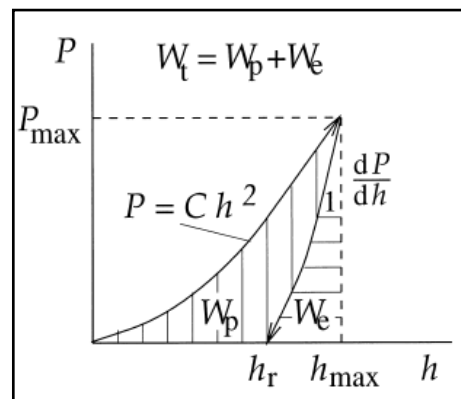

Figure 2.29 *P -h* curves for loading and unloading (Suresh & Giannakopoulos, 1999).

Figure 2.29 is a schematic of the load-penetration depth (*P-h*) curve for a sharp indenter. During loading, the curve generally follows the relation, $P=Ch^2$, where *C* is the indentation curvature which is a measure of the "resistance" of the material to indentation. The contact pressure, $p_{av}= P_{max}/A_{max}$, can be identified with the hardness of the indented material; P_{max} is the maximum indentation load which makes the indenter penetrate the material by a depth h_{max}, thereby creating a true (projected) contact area A_{max} on the indented surface. Three-dimensional finite-element simulations of elastoplastic indentation along with experiments (Suresh, Alcala & Giannakopoulos, 1996; Suresh & Giannakopoulos, 1998) provide the following result:

$$C = \frac{P}{h^2} = M_1\sigma_{0.29}\left\{1 + \frac{\sigma_y}{\sigma_{0.29}}\right\}\left\{M_2 + ln\left(\frac{E^*}{\sigma_y}\right)\right\} \ for \ 0.5 \leq \frac{p_{av}}{\sigma_y} \leq 3.0 \qquad (2.34)$$

In Equation 2.34, σ_y is the yield strength and $\sigma_{0.29}$ is the stress corresponding to the characteristic plastic strain of 0.29 for the indented material in uniaxial compression, as shown schematically in Figure 2.30. The constants in this equation are *M=7.143* and *M=-1* for the Vickers pyramid indenter with an included tip angle of 136°. The corresponding values for the Berkovich indenter are *M=6.618* and *M=-0.875* with an included tip angle of 130.6°. Circular conical indenters also follow the same results as the Vickers or Berkovich depending on the apex angle of the cone. If p_{av}/σ_y falls outside the bounds given in Equation 2.34, the indentation response is either elastic (for $p_{av}/\sigma_y = 0.5$) or elastic-perfectly plastic (for $p_{av}/\sigma_y = 3$). By accounting for the effects of strain hardening on pile-up and sink-in, and on the true contact area through three-dimensional simulations, the following relationship between A_{max} and h_{max} has been derived for elastoplastic materials:

$$\frac{A_{max}}{h_{max}^2} = 9.96 - 12.64\,(1-S) + 105.421(1-S)^2 - 229.57(1-S)^3 +$$

$$157.67(1-S)^4, with\ S = \frac{p_{av}}{E^*} \tag{2.35}$$
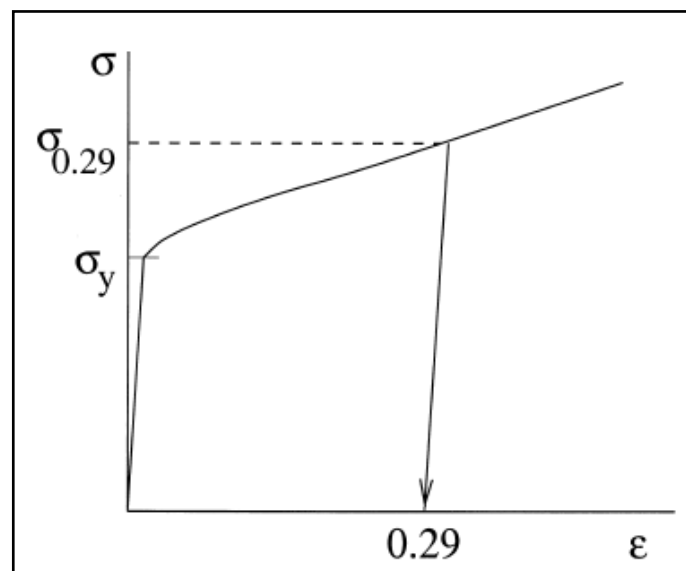
Figure 2.30 Uniaxial compression stress-strain curve and the characteristic strain (Suresh & Giannakopoulos, 1999).

Table 2.4 Numerically Determined Correlations Between Material Strain Hardening, Residual Impression Depth, and Maximum Contact Area (Suresh & Giannakopoulos, 1999).

$\dfrac{\{\sigma_{0.29} - \sigma_y\}}{0.29E^*} + 11\dfrac{\sigma_y}{E^*}$	$\left(\dfrac{h_r}{h_{max}}\right) = \left(\dfrac{W_p}{W_t}\right)$	$\dfrac{A_{max}}{h_{max}^2}$
1	0.0	9.82
0.33	0.76	16.00
0.27	0.85	24.50
0.05	0.91	25.50
0.025	0.94	28.99
0.0	1.00	41.65

Note: (a) Pile-up occurs when $0.875 < (h_r/h_{max}) \leq 1$.

(b) Sink-in occurs when $0 \leq (h_r/h_{max}) < 0.875$.

(c) No pile-up or sink-in when $(h_r/h_{max}) = 0.875$, where the true contact area A and the apparent contact A_{app} are equal, i.e. $A = A_{app} = 24.5h^2$.

This equation is a polynomial fit to the computationally determined values of A_{max}/h^2_{max}, which are listed in Table. More accurate analytical fits to the results can be obtained from the results of Table 2.6 using higher order polynomials or other functional approximations. In Equation 2.35, the effective elastic modulus of the indenter-specimen system, E^*, is defined as:

$$E^* = \left[\frac{1-\nu^2}{E} - \frac{1-\nu_{in}^2}{E_{in}}\right]^{-1} = \frac{1}{c^*\sqrt{A_{max}}}\left(\frac{dP}{dh}\right) \tag{2.36}$$

where ν is Poisson's ratio, E is Young's modulus, the subscript 'in' denotes properties of the indenter, and dP/dh is the slope of the *P-h* curve of the initial stages of unloading from P_{max} (see Figure 2.29). The constant $c^* = 1.142$ for the Vickers pyramid indenter, 1.167 for the Berkovich indenter, and 1.128 for the circular conical indenter of any included apex angle. The ratio of the residual depth of penetration, h_r upon complete unloading (see Figure 2.32) to the maximum penetration depth, h_{max}, prior to unloading, is indicative of the extent of plastic deformation and strain hardening, such that:

$$\frac{\sigma_{0.29} - \sigma_y}{0.29E^*} = 1 - 0.142\frac{h_r}{h_{max}} - 0.957\left(\frac{h_r}{h_{max}}\right)^2 \tag{2.37}$$

This result holds for Vickers, Berkovich as well as circular conical indenters. This equation, which is a polynomial fit to the computational results of Table 2.6, converges to the correct trends in the following two limiting cases. (1) For elastic indentation where $h_r=0$, the right hand side of Equation 2.37 obviously reduces to 1 indicating that $(\sigma_{0.29}-\sigma_y)/0.29=E^*$ for linear elastic response. (2) For the case of a rigid-perfectly plastic material where h_r/h_{max}, the right hand side of Equation 2.37 reduces to zero indicating no strain hardening. Different intermediate hardening responses during sharp indentation can be quantified with greater precision using the results shown in Table 2.6, and accounting for the influence of the initial yield strain, σ_y/E^*. Elastoplastic finite element analyses of the sharp indenter, performed in the present study using numerical simulations similar to those reported (Giannakopoulos, Larson & Vestergaard, 1994), also reveal that:

$$\frac{h_r}{h_{max}} = 1 - d^* \frac{p_{av}}{E^*} = 1 - d^* S \qquad (2.38)$$

where $d^*=5$ for the Vickers pyramid indenter and $d^*=4.678$ for the Berkovich indenter; the conical indenter has results similar to Vickers or Berkovich depending on the included apex angle. Equation 2.38 is in reasonable accord with the empirical result of Breval and MacMillan (1985) who employed Vickers indentation for a variety of materials. As shown in Table 3.1, $h_r/h_{max}=0.875$ gives the critical strain hardening for which there is neither a pile-up nor a sink-in of the material around the indenter. Combining Eqs. (2.35) and (2.37) readily provides a unique relationship between A_{max} and h_{max}, i.e., the true contact area which takes into account pile-up and sink-in can be extracted directly from the P-h curve without the need for any visual observations.

Numerical simulations also reveal that the elastoplastic boundary underneath the sharp indenter in Figure 2.28 has a hemi-spherical shape with radius, $c = \sqrt{(0.3P_{max}/\sigma_y)}$. This result matches the experimentally based estimates of Zielinski et al. (1993) who found that $c = \sqrt{(3P_{max}/2\pi\sigma_y)}$ Johnson's cavity model can sometimes significantly overestimate c.

With the above theoretical framework, a step-by-step method for the estimation of local and bulk mechanical properties was obtained. The proposed method involves the following steps:

1. Experimentally determine the P-h curve, during complete loading and unloading, for the material whose properties are to be determined. Use a Vickers, Berkovich or conical indenter (whose apex angle is the same as that of Vickers or Berkovich).

2. From the P-h curve, identify h_r and h_{max} and calculate h_r/h_{max}.

3. Using this value of h_r/h_{max}, find $S=p_{av}/E^*$ from Equation 2.38.

4. With S so determined, and h_{max} directly observed from the P-h curve, and obtain the true contact area at maximum load, A_{max}, from Equation 2.35 or Table 2.6.

5. Obtain E_{in} and υ_{in} for the indenter material directly from the manufacturer or from standard data tables available from the literature. If Young's modulus, E, and Poisson's ratio, υ, of the indented material are known, compute E^* from Equation 2.36. Use the value of p_{av}/E^* found in Step 3 and calculate p_{av}. If the elastic properties of the indenter and the indented material are not known *a priori*, determine the initial unloading slope dP/dh, use A_{max} from Step 4, and calculate E^* using the second part of Equation 2.36.

6. Using the value of h_r/h_{max} found in Step 2, and E^* from Step 5, use Equation 2.37 or Table 1 and find the quantity ($\sigma_{0.29}$-σ_y).

7. With P_{max} and h_{max} identified from the P-h curve, use the relation $P_{max}=Ch^2_{max}$ and estimate C using least-square fit. With this value of C and ($\sigma_{0.29}$-σ_y) from Step 6, iterate Equation 2.34 and estimate σ_y and $\sigma_{0.29}$.

8. Calculate the strain hardening exponent n=ln{$\sigma_{0.29}$-ln (σ_y)}/5.

The question remains whether these parameters are sufficient to uniquely determine the indented material's elasto-plastic properties. Plastic behavior of many pure and alloyed engineering metals can be closely approximated by a power law description, as shown schematically in Figure 2.31. A simple elasto-plastic, true stress–true strain behavior is assumed to be:

$$\sigma = \begin{cases} E\varepsilon, \ for \ \sigma \le \sigma_y \\ R\varepsilon^n, \ for \ \sigma \ge \sigma_y \end{cases} \tag{2.39}$$

where E is the Young's modulus, R a strength coefficient, n the strain hardening exponent, σ_y the initial yield stress and ε_y the corresponding yield strain, such that

$$\sigma_y = E\varepsilon_y = R\varepsilon_y^n \tag{2.40}$$

here the yield stress σ_y is defined at zero offset strain. The total effective strain, ε, consists of two parts, ε_y and ε_y:

$$\varepsilon = \varepsilon_y + \varepsilon_p \tag{2.41}$$

where ε_p is the nonlinear part of the total effective strain accumulated beyond ε_y. With Equations 2.40 and 2.41, when $\sigma > \sigma_y$, Equation 2.39 becomes:

$$\sigma = \sigma_y \left(1 + \frac{E}{\sigma_y} \varepsilon_p \right)^n \tag{2.42}$$
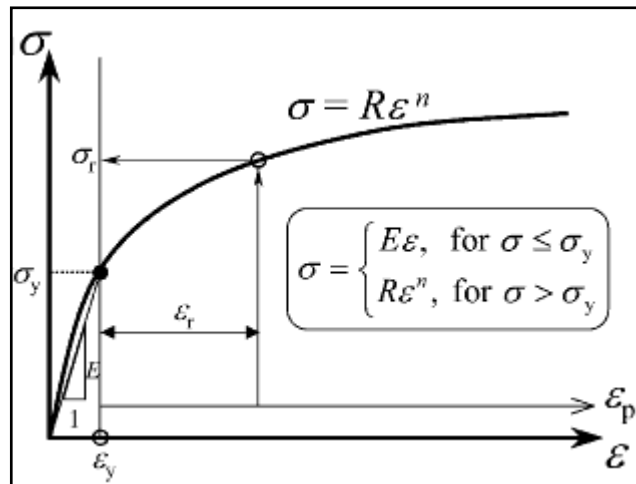
Figure 2.31 The power law elasto-plastic stress–strain behavior used in the current study (Dao et al., 2001).

To complete the material constitutive description, Poisson's ratio is designated as n, and the incremental theory of plasticity with Von Misses effective stress is assumed. With the above assumptions and definitions, a material's elasto-plastic behavior is fully determined by the parameters E, n, σ_y and n. Alternatively, with the constitutive law defined in Equation 2.39, the power law strain hardening assumption reduces the mathematical description of plastic properties to two independent parameters. This pair could be described as a representative stress σ_r (defined at $\varepsilon_p = \varepsilon_r$, where er is a representative strain) and the strain-hardening exponent n, or as σ_y and σ_r.

As discussed, one can use a material parameter set (E, n, σ_y and n), (E, n, σ_r and n) or (E, n, σ_y and σ_r) to describe the constitutive behavior. Therefore, the specific functional forms of the universal dimensionless functions are not unique (but different definitions are interdependent if power law strain hardening is assumed). For instrumented sharp indentation, a particular material constitutive description (e.g., power-law strain hardening) yields its own distinct set of dimensionless functions.

One may choose to use any plastic strain to be the representative strain ε_r, where the corresponding σ_r is used to describe the dimensionless functions. However, the representative strain which best normalizes a particular dimensionless function with respect to strain hardening will be a distinct value.

Here, Dao et al. presents a set of universal dimensionless functions and their closed-form relationship between indentation data and elasto-plastic properties (within the context of the present computational results). This set of functions leads to new algorithms for accurately predicting the *P-h* response from known elasto-plastic properties (forward algorithms) and new algorithms for systematically extracting the indented material's elasto-plastic properties from a single set of *P-h* data (reverse algorithms).

For a sharp indenter (conical, Berkovich or Vickers, with fixed indenter shape and tip angle) indenting normally into a power law elasto-plastic solid, the load P can be written as, $P = P(h, E, v, E_i, v_i, \sigma_y, n)$, where E_i is Young's modulus of the indenter, and v_i is its Poisson's ratio. Using dimensional analysis, a new set of dimensionless functions was constructed to characterize instrumented sharp indentation. From these functions and elasto-plastic finite element computations, analytical expressions were derived to relate indentation data to elasto-plastic properties. Forward and reverse analysis algorithms were thus established; the forward algorithms allow for the calculation of a unique indentation response for a given set of elasto-plastic properties, whereas the reverse algorithms enable the extraction of elasto-plastic properties from a given set of indentation data. A representative plastic strain ε_r was identified as a strain level which allows for the construction of a dimensionless description of indentation loading response, independent of strain hardening exponent n. The proposed reverse analysis provides a unique solution of the reduced Young's modulus E^*, a representative stress σ_r, and the hardness p_{ave}. These values are somewhat sensitive to the experimental scatter and/or error commonly seen in instrumented indentation.

With this information, values of σ_y and n can be determined for the majority of cases considered here, provided that the assumption of power law hardening adequately represents the full uniaxial stress–strain response. These plastic properties, however, are very strongly influenced by even small variations in the parameters extracted from instrumented indentation experiments. Comprehensive sensitivity analyses were carried out for both forward and reverse algorithms, and the computational results were compared with experimental data for two materials. The forward analysis leads to prediction of the *P-h* response from known elasto-plastic properties. With the available dimensionless functions, the forward analysis algorithm is readily constructed. One such set of algorithms is shown in Figure 2.32. The reverse analysis implies estimation of the elasto- plastic properties from one complete (i.e., loading and full unloading) *P-h* curve. In a similar manner, the dimensionless functions allow us to construct the reverse algorithms. A set of the reverse analysis algorithms is shown in Figure 2.33 (Dao, 2001).
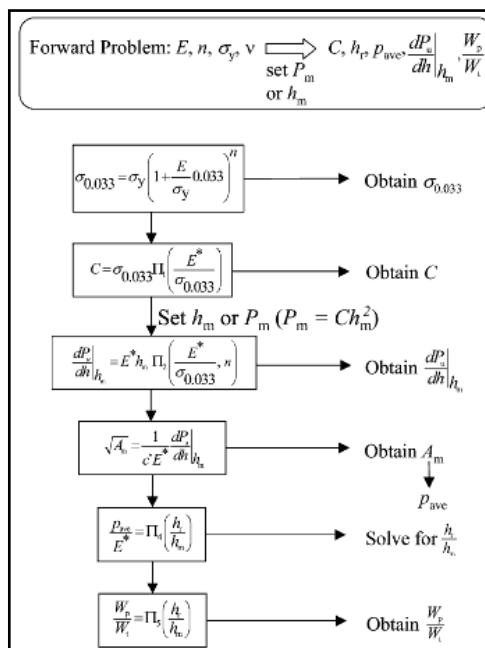
Figure 2.32 Forward Analysis Algorithms
(Dao et al., 2001).
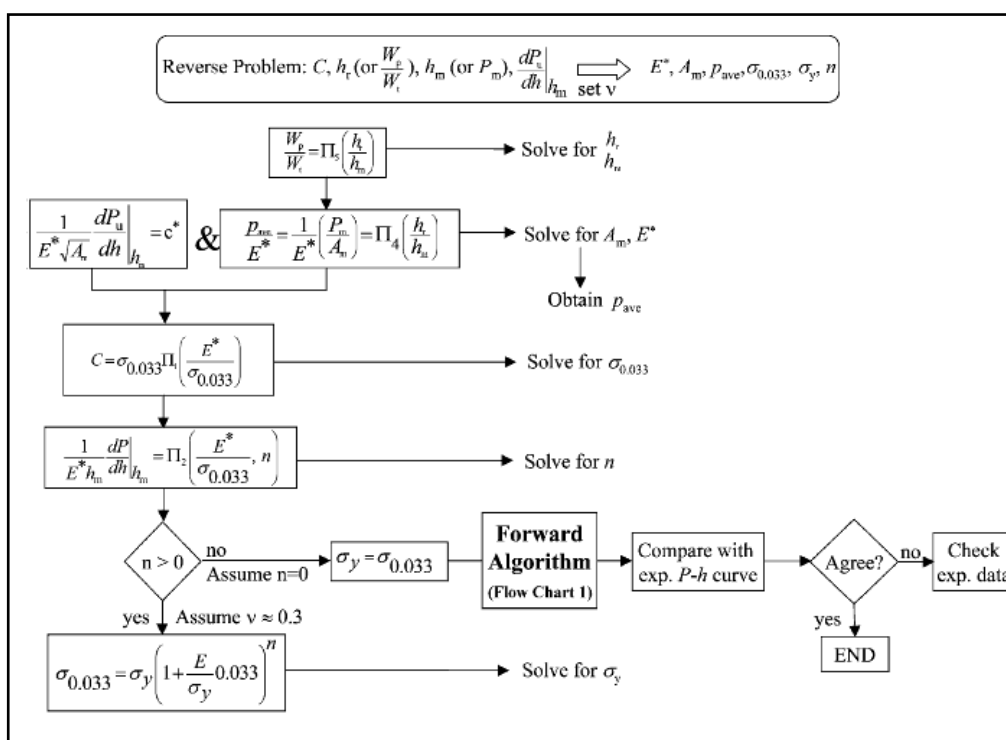
Figure 2.33 Reverse Analysis Algorithms (Dao et al., 2001).

2.9.2 Indentation Analysis of Thin Films

Nanoindentation has been used routinely in the mechanical characterization of thin- films and thin-surface layers in recent years (Bull, 2005). The technique applies a programmed function of increasing and decreasing load to the surface of interest with an indenter of well-defined shape and continuously measures the indenter displacement. The advantage of this method is that mechanical information, such as elastic modulus, can be obtained through the analysis of the load–displacement behavior alone with a coating of the material to be tested on a substrate made from different material. This makes it an ideal tool. The technique has been used to assess the elastic and plastic properties of coatings on a range of substrates but there are limitations in measuring the properties of much thinner coatings, particularly when elastic properties are required (Korsunsky, 1998; Chen & Bull, 2006). For coatings of a few hundred nano-meters thickness, it has been suggested that extrapolating the properties determined at a range of peak loads or indenter displacements to zero load/depth can be used to determine the coating only properties. With high quality, sharp indenters it is possible to assess coatings down to 100 nm thick by this method (Chen & Bull, 2009).

The indentation systems frame stiffness and the diamond tip shape was carefully calibrated with a fused silica test sample, using the standard Oliver and Pharr method (1992), before and after measurements with no change in either recorded. Nano-indentation load (P) vs. displacement (h) curves were then recorded for each indent and only those where evidence of plastic deformation was observed (i.e. the loading and unloading curves are different) were used in the analysis of Young's modulus by the Oliver and Pharr method (1992). The indenter displacement is in fact made up of two components: the plastic depth of the indent, or contact depth, and the elastic deflection of the surface at the edge of the contact. The relationship between the contact depth (h_c) and the maximum displacement (h_{max}) can be determined from:

$$h_c = h_{max} - \varepsilon \frac{P_{max}}{S} \tag{2.43}$$

where P_{max} is the maximum loading and ε is a constant that depends on the shape of the indenter (Pharr, 1998). Empirical studies have shown that for a Berkovich indenter, the typical value of e is about 0.75. S is the unloading stiffness, which comes from:

$$S = \frac{dP}{dh}|_{h-h_{max}} = mB(h_{max} - h_f)^{m-1}$$

(2.44)

where, m and B are fitting parameters, and h_f is the final displacement after completely unloading. In this approach, S, the initial slope of the unloading curve, can finally be used to determine the reduced elastic modulus of the sample (effectively from the recovery of the elastic deflection of the surface) based upon the Sneddon flat punch solution (Sneddon, 1965) and the following Equation:

$$E_r = \frac{1}{\beta} \frac{\sqrt{\pi}}{2} \frac{S}{\sqrt{A}}$$

(2.45)

where, A is the contact area which can be deduced from h_c based upon an accurate knowledge of the tip end shape, and β is a constant also depends on the geometry of the indenter ($\beta = 1.034$ for the Berkovich indenter).

The relation $h_c=f(h)$ between contact depth (h_c) and the measured instant maximum depth (h) can be calibrated before the experiments through Eq. (2.43). Knowing $h_c=f(h)$ and the area function of the nanoindenter tip. $A=F(h_c)$, it is possible to evaluate also the instant hardness H in a creep process following $H=P/A$. Note that H also signifies the mean pressure, or the average stress $\bar{\sigma}$ that can be sustained under the indentation load (Freund & Suresh, 2004), i.e.:

$$\bar{\sigma} = \frac{P}{A}$$

(2.46)

The determination of an equivalent indentation strain is more complicated. A schematic of a nanoindentation test with a spherical shaped tip and a sharp trigonal

pyramid tip is illustrated in Figure 2.34 (a) and (b). In Figure 2.34 (a), a represents the contact radius, defined by:

$$a = \sqrt{\frac{A}{\pi}} \approx 0.5642\sqrt{A} \qquad (2.47)$$

where A is the tip area function defined previously. In Figure 2.34 (b), a is the contact semi-width. Given that the projected area is an equilateral triangle, we can easily derive:

$$a = 2\sqrt{\frac{A}{3\sqrt{3}}} \approx 0.8774\sqrt{A} \qquad (2.48)$$
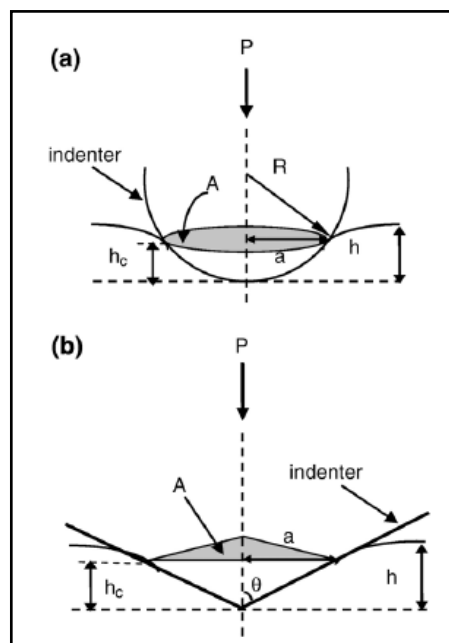
Figure 2.34 Schematic of the indentation process with (a) a spherical shaped tip, and (b) a sharp pyramidal tip (Cao, 2008).

At very small depth, even the shapes of the conical and pyramidal tips (collectively called geometrically self-similar tips) are rounded, thus only Equation 2.47 applies. If we assume that the blunt tip profile is approximately circular with

radius R, the maximum contact depth, δ_o, below which the indent shape is spherical can be estimated.

$$\delta_o = R(1 - sin\theta) \tag{2.49}$$

where θ is the semi-angle of the indenter tip. Johnson's (1950) contact mechanics analysis of the indentation process shows that for geometrically self-similar tips, the equivalent indentation strains at shallow depth can be estimated by:

$$\varepsilon_I = K\frac{h_c}{a} \tag{2.50}$$

where K is a constant, and can be determined by indenting a standard sample material with known Young's modulus. The indentation strain ε_I is adopted as Equation 2.50 only when a/R is small. This is because in the case of sharp self-similar indentation of the pyramidal Berkovich and Cube Corner tips, where a/R is typically much higher, Equation 2.50 may no longer be applicable. Instead, when $h_c > \delta_o$ we turn to the expressions of indentation strain rate ε_I for sharp self-similar indentation, which has been validated by a number of researchers (Poisl, 1995; Hill, 1992; Storåkers & Larsson, 1994) through both rigorous theoretical modeling and experiments:

$$\varepsilon_I = \frac{1}{h}\frac{dh}{dt} \tag{2.51}$$

In our experiments, we find that the relation $h_c=f(h)$ is approximately linear for sharp indenters such as the Berkovich and Cube Corner tips. Thus Equation 2.51 is rewritten as:

$$\varepsilon_I = \frac{1}{h_c}\frac{dh_c}{dt} \tag{2.52}$$

Integration of Equation 2.52 yields:

$$\varepsilon_I = log\left(\frac{h_c}{\delta_o}\right) + K\frac{\delta_o}{\sqrt{\frac{A(\delta_o)}{\pi}}} \quad (h_c \geq \delta_o) \tag{2.53}$$

A full nanoindentation stress–strain curves can now be obtained by combining Equations 2.51, 2.52 and 2.53.

During the forward analysis, the parameters characterizing the shape of the P–δ curves are correlated with known material elastoplastic properties; perhaps more importantly, by solving the functions established in the forward analysis, the material properties of interest may be obtained through a reverse analysis based on the measured P–δ data (Cheng, 2004). The micro or nanoindentation experiments can be performed quickly and do not require removal of the film from its substrate, and it has been proven particularly useful in measuring the hardness and stiffness of thin films (Chen & Vlassak, 2004).

In general, nanoindentation experiments with contact depths of less than 10–20% of the film thickness (h) are needed in order to obtain the intrinsic film properties and to avoid the so-called substrate effect. For very compliant substrates, this requirement is not sufficient and nanoindentation measurements are still affected by the substrate properties. On the other hand, even if very shallow indentation depths as small as several nanometers can be made by a high-end commercial nanoindenter, there are still many experimental issues interfering with measurements at this extremely small length scale.

First, when the contact depth is of the same order as the surface roughness, it is very difficult to determine the contact area/depth accurately. Second, adhesion between the indenter tip and specimen may play an important role and hence the nanoindentation force may not be measured properly. Third, even a brand new indenter tip is blunt at the nanoscale, with a radius of curvature typically tens of nanometers; thus, the conventional sharp indentation analysis cannot be applied directly to the blunt tip at a small-scale. Fourth, when δ is well below 1 μm, size-dependent indentation effects have been measured that are related to size-dependent

plasticity and the effects of strain gradients on strength (Figure 2.35). In addition, nanoindentation results may vary depending on whether the experiment is performed within a grain or at a grain boundary. These effects complicate the measurement significantly and make it more difficult to extract intrinsic film properties, such as the elastic modulus, yield strength and work hardening exponent.
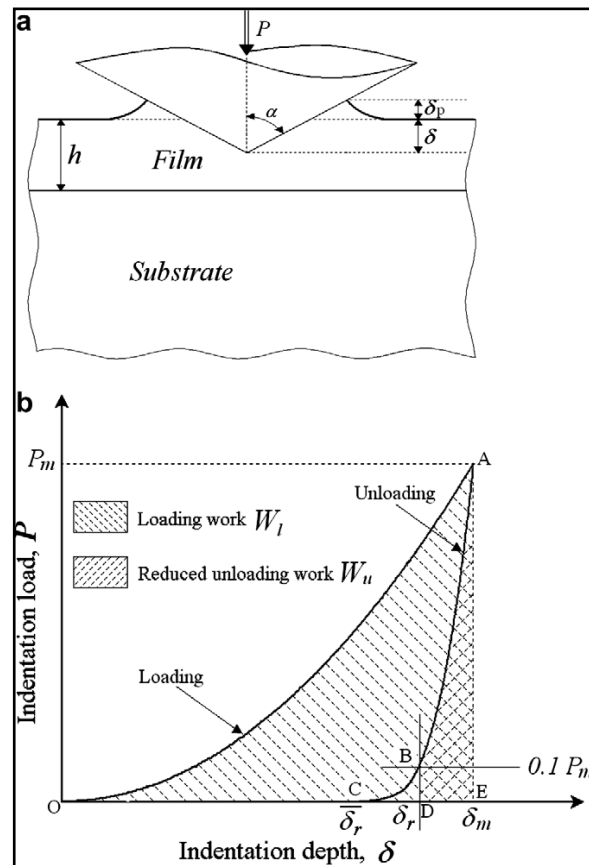
Figure 2.35(a) Schematic of the conical indentation on a film/substrate system. The half apex angle of the indenter is a, the indentation load is P and the indentation depth is d. (b) Typical indentation load–depth (P–δ) curve obtained from a conical indentation test. The shadowed areas under loading curve OA and partial unloading curve AB represent the loading work and the reduced unloading work, respectively. In this paper, the reduced residual penetration dr is defined as the unloading depth when P is reduced to 10% of the maximum load (point D) (Zhao, 2007).

In order to circumvent these issues encountered at extremely small length scales, it is desirable to perform microindentation experiments at moderate indentation depths, e.g. depths on the order of a fraction of a micron. Thus, depending on film thickness, it may be inevitable that the substrate should affect the indentation measurement. Indeed, as the indenter approaches the interface between film and substrate, the measured hardness and stiffness are in fact combinations of film and substrate properties. The key issue is to understand the substrate effect and then subtract it from the microindentation measurement, so as to obtain the intrinsic film properties. Although the analysis becomes somewhat complicated, the approach is straightforward and can be based on well-established continuum mechanics, without the uncertainties at the nanoscale (Nix, 1989; Nix & Gao, 1988). Huber (2002) have deduced film and substrate hardness and stiffness using a neural network approach, in which they utilized indentation data recorded at multiple depths. We note that, in their work, the indentation depth is up to twice the film thickness; since the indenter tip penetrates into the substrate and in order to avoid cracking, this method cannot be applied to cases with brittle substrate (e.g. Si) that are widely used in microelectronics. In an elastoplastic film/elastic substrate system, four material parameters (E_f, σ_f, n_f, E_s) need to be identified in the reverse analysis. If one could first flip over the film/substrate system and carry out an indentation test on the substrate, then the elastic modulus of substrate, E_s, can be measured in a straightforward manner. During the reverse analysis, the postulated film properties are varied over a large range, and the combination of (E_f, σ_f, n_f) that minimizes the total error represents the elastoplastic properties of the film. The flow chart of the reverse analysis is given in Figure 2.36.

For instance, thin films often experience very high stresses during service which can lead to (1) distortion of the device, (2) deformation, fracture or decohesion of the film and (3) degradation of the film due to enhanced diffusion or corrosion; and all these could eventually affect the functionality of the thin film/substrate layered system. Furthermore, the micro structural aspects of materials in the form of thin films can be quite different from those of the same materials in bulk form which can lead to unexpected mechanical behavior (Dao, 2001; Chollacoop, 2003). Therefore,

in order to understand, predict and improve the reliability of devices containing thin films, it is necessary to characterize the mechanical properties of thin films.
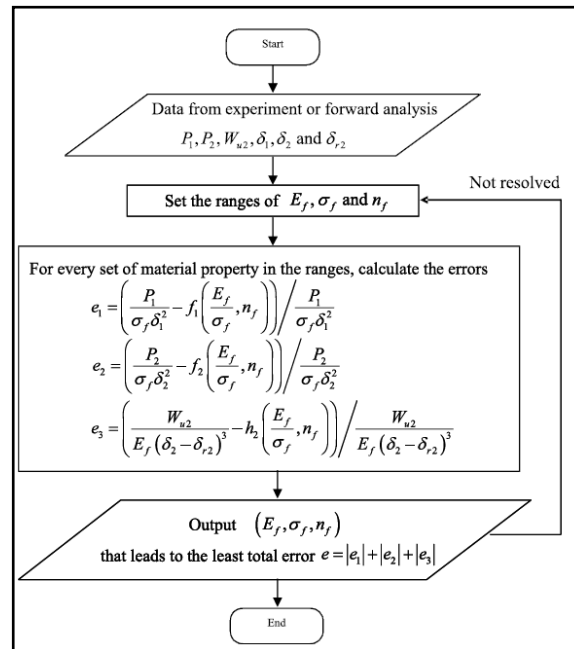
Figure 2.36 The flow chart of the reverse analysis

One of the challenges in studying mechanical properties of thin films is that the traditional methods used to evaluate mechanical properties of bulk materials are not applicable for thin films and so far there is no standard test method for the evaluation of mechanical properties of thin films. New methods, such as depth-sensing nanoindentation, microbridge test, uniaxial tensile test and ultrasonic method are being developed (Oliver & Pharr, 1992; Casals & Alcala, 2005; Zhao, 2006) for the measurement of mechanical properties of thin films. Among these methods, depth-sensing nanoindentation technique has been an area of considerable attention in recent years due to its high resolution at low load scale and continuous record of variation of indentation load with penetration depth into the specimen.

However, most previous studies about depth-sensing nanoindentation technique demonstrate that: to extract the mechanical properties of the coatings or films from the indentation test, we should limit the indentation depth less than 10–20% of the film thickness (Gamonpilas & Busso, 2004; Panich & Sun, 2004). As we know,

during nanoindentation experiments, especially when the indentation depth is about 100–1000 nm, size-scale-dependent indentation effects come to play (e.g., Gerberich et al., 1996; Fleck & Hutchinson, 1993; Gao et al., 1999; Ma et al., 2008). These possible size-scale-dependent effects on hardness have been modeled using higher order theories (e.g., Fleck and Hutchinson, 1993; Gao et al., 1999) and these effects can be also related to bluntness of the nominally sharp indenters (e.g., Borodich et al., 2003; Kindrachuk et al., 2006). When the tip bluntness is on the same order as the indentation depth, Borodich and Keer's (2003) have proposed the fundamental relations for depth of indentation, size of the contact region, load, hardness, and contact area for various boundary conditions. If the indentation is sufficiently deep (typically deeper than 1 μm), then the scale dependent effects become small and negligible. Therefore, the limitation of the indentation depth less than 10–20% of the film thickness for the films with the thickness of micrometer is a not good rule. However, when the indentation depth is deeper than 1 μm the deformation of the substrate would have the effect on the extracting the mechanical properties of the film from the indentation test for very thin films. Saha and Nix (2002) examined the effects of the substrate on the determination of hardness and elastic modulus of thin films by nanoindentation. They found that the effect of substrate hardness on the film hardness was negligible in the case of soft films on hardness and the substrate hardness affected the measured film hardness for the case of a hard film on a soft substrate. Compared to hardness, the nanoindentation measurement of the elastic modulus of thin films was more strongly affected by the substrate.

Recently, as for an elastic–plastic film coated on an elastic substrate system, Ma et al. (1999) and Zhao et al. (2007) have proposed the techniques which can extract the film elastic–plastic properties considering the influence of the elastic substrate from one conical indentation test using the FEM. But it becomes extremely difficult to obtain the elastic–plastic properties of the film coated on an elastic–plastic substrate from the indentation test because not only the effect of elastic deformation but also the plastic deformation of the elastic–plastic substrate should be considered.

2.10 Scratch Test Analysis of Thin Films

The scratch test is used to measure the interfacial adhesion for a range of different coatings. During the test (Figure 2.37), a diamond indenter is drawn over the surface of a sample tested under a normal force, which is increased either stepwise or continuously until a critical normal force F is reached, at which a well defined coating failure occurs (Bull, 1997). Then, F is taken as a measurement of the adhesion between coating and substrate. The onset of coating failure can be monitored by optical microscopy, acoustic emission (AE) and friction force measurements (Hedenqvist & Hogmark, 1997). It has been suggested that coating adhesive failure is directly associated with a sudden increase in the friction force (Valli, 1987; Sekler, Steinmann & Hintermann, 1988). It is generally accepted that the scratch test is suitable for coatings of thickness ranging from 0.1 to 20 μm and this covers a large number of engineering applications (Holmberg, 2003).
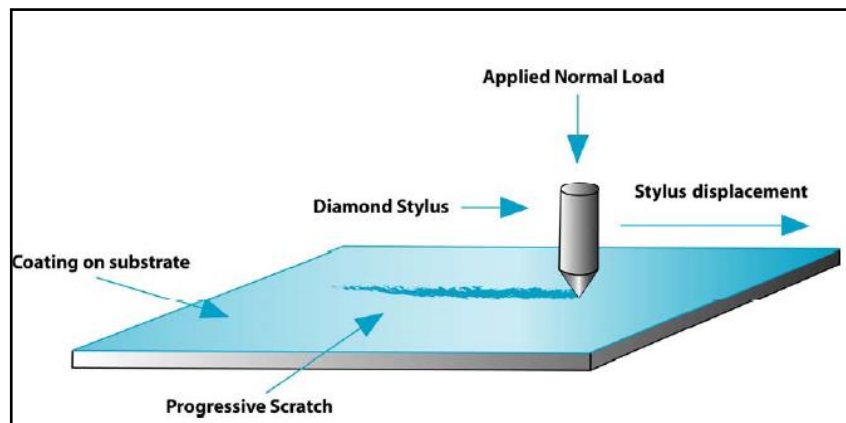
Figure 2.37 Schematic illustration of the indenter, coordinate system and the coating/ substrate under normal and tangential loading during the scratch test.

The scratch was examined with an optical microscope and critical force (W_c) value at which the coating is removed from substrate was determined. After microhardness value of substrate was converted to Brinell Hardness (H) from Vickers Microhardness by Standard Hardness Conversion Tables for materials, the adhesion strength (F) of the coatings was calculated as MPa unit by Eq. (2.54):

$$F = \frac{H}{[(\pi R^2 H - W_c)/W_c]^{1/2}} \tag{2.54}$$

where H is Brinell hardness value in kg/mm^2 of the STO substrate and R is radius of stylus in μm. In addition, it is possible to evaluate adhesion of coatings using Equation 2.54. As the test force applied to coating increases, peeling of coating occurs. At this time peeled pieces of coating cause a high frequency noise in a cartridge output signal. Detecting this noise makes it possible to determine a critical force. Normally, this critical force can be used the adhesion value of coating. However, in the case that a hardness of the substrate has been known, Eq. (2.54) can show adhesion strength. As a result of this, test force–cartridge output graph is obtained from this measurement. Cartridge output (%) represents percentage of indentation of the stylus as a function of loading during the test. The percentage increases with a increasing load, that applied by stylus, due to the adhesion resistance of the coating to substrate.

2.11 Atomic Force Microscopy analysis of surfaces

The atomic force microscope (AFM) also referred to as the scanning force microscope (SFM), is part of a larger family of instruments termed the scanning probe microscopes (SPMs). These also include the scanning tunneling microscope (STM) and scanning near field optical microscope (SNOM), amongst others. The common factor in all SPM techniques is the use of a very sharp probe, which is scanned across a surface of interest, with the interactions between the probe and the surface being used to produce a very high resolution image of the sample, potentially to the sub-nanometer scale, depending upon the technique and sharpness of the probe tip. In the case of the AFM the probe is a stylus which inter-acts directly with the surface, probing the repulsive and attractive forces which exist between the probe and the sample surface to produce a high resolution three-dimensional topographic image of the surface (Johnson, Hilal & Bowen, 2000).

The AFM was first described by Binnig (1986) as a new technique for imaging the topography of surfaces to a high resolution. It was created as a solution to the

limitations of the STM, which was able to image only conductive samples in vacuum. Since then the AFM has enjoyed an increasingly ubiquitous role in the study of surface science, as both an imaging and surface characterization technique, and also as a means of probing interaction forces between surfaces or molecules of interest by the application of force to these systems. The AFM has a number of advantages over electron microscope techniques, primarily its versatility in being able to take measurements in air or fluid environments rather than in high vacuum, which allows the imaging of polymeric and bio-logical samples in their native state. In addition, it is highly adaptable with probes being able to be chemically functionalized to allow quantitative measurement of interactions between many different types of materials. At the core of an AFM instrument is a sharp probe mounted near to the end of a flexible micro cantilever arm. By raster-scanning this probe across a surface of interest and simultaneously monitoring the deflection of this arm as it meets the topographic features present on the surface, a three-dimensional picture can be built up of the surface of the sample to a high resolution. Many different variations of this basic technique are currently used to image surfaces using the AFM, depending upon the properties of the sample and the information to be extracted from it. These variations include 'static' techniques such as contact mode, where the probe remains in constant contact with the sample, and 'dynamic' modes, where the cantilever may be oscillated, such as with the intermit-tent or non-contact modes. The forces of interaction between the probe and the sample may also be measured as a function of distance by the monitoring of the deflection of the cantilever, providing that the spring constant of the lever arm is sufficiently calibrated. In this chapter the basic principles of operation of an AFM will be presented, outlining the most common imaging modes and describing the acquisition of force distance measurements and techniques to calibrate cantilever spring constants (Johnson, Hilal & Bowen, 2000).

In Figure 2.38 the basic set-up of a typical AFM is shown. Cantilevers are commonly either V-shaped, as shown, or a rectangular, 'diving board' shaped. The cantilever has at its free end a sharp tip, which acts as the probe of interactions. This probe is most commonly in the form of a square-based pyramid or a cylindrical cone.

A few examples of different configurations for levers and probes are shown in Figure 2.39. Commercially manufactured probes and cantilevers are predominantly of silicon nitride (the formula normally given for silicon nitride is Si_3N_4, although the precise stoichiometry may vary depending on the manufacturing process) or silicon (Si). Typically the upper surface of the cantilever, opposite to the tip, is coated with a thin reflective surface, usually of either gold (Au) or aluminium (Al). The probe is brought into and out of contact with the sample surface by the use of a piezocrystal upon which either the cantilever chip or the surface itself is mounted, depending upon the particular system being used (these two configurations are referred to as tip-scanning or surface scanning, respectively).
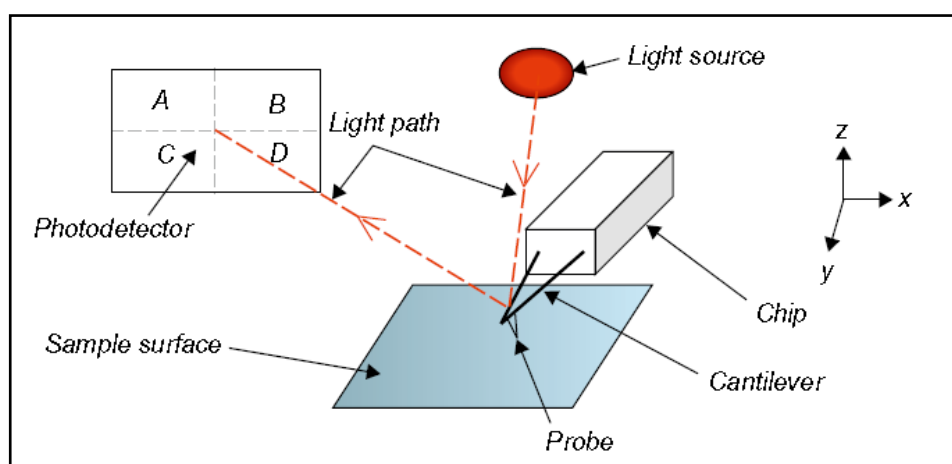
Figure 2.38 Basic AFM set-up. A probe is mounted at the apex of a flexible Si or Si_3N_4 cantilever. The cantilever itself or the sample surface is mounted on a piezocrystal which allows the position of the probe to be moved in relation to the surface. Deflection of the cantilever is monitored by the change in the path of a beam of laser light deflected from the upper side of the end of the cantilever by a photodetector. As the tip is brought into contact with the sample surface, by the movement of the piezocrystal, its deflection is monitored. This deflection can then be used to calculate interaction forces between probe and sample (Johnson, Hilal & Bowen, 2000).

Movement in this direction is conventionally referred to as the *z*-axis. A beam of laser light is reflected from the reverse (uppermost) side of the cantilever onto a position-sensitive photodetector. Any deflection of the cantilever will produce a change in the position of the laser spot on the photodetector, allowing changes to the deflection to be monitored. The most common configuration for the photodetector is

that of a quadrant photodiode divided into four parts with a horizontal and a vertical dividing line. If each section of the detector is labeled A to D as shown in Figure 2.38, then the deflection signal is calculated by the difference in signal detected by the A + B versus C + D quadrants. Comparison of the signal strength detected by A + C versus B + D will allow detection of lateral or torsional bending of the lever. Once the probe is in contact with the surface, it can then be raster-scanned across the surface to build up relative height information of topographic features of the sample (Johnson, Hilal & Bowen, 2000).
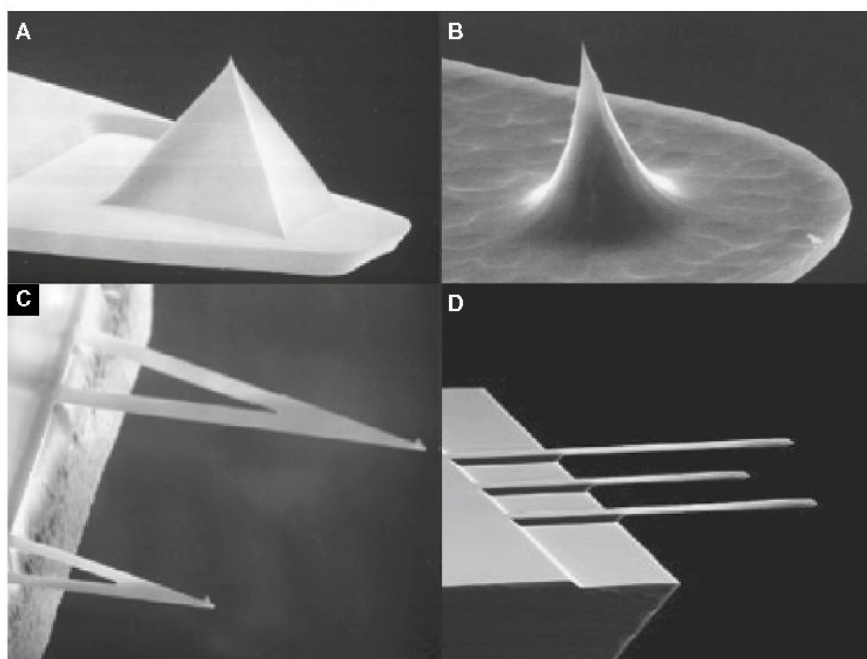
Figure 2.39 Example of SEM images of different probes and cantilever types. A: pyramidal probe; B: conical high aspect ratio probe for high resolution imaging; C: two V-shaped cantilevers for contact mode imaging; D: chip with a series of beam-shaped levers of different lengths. In this case the levers are tipless to allow mounting of particles of interest for force measurements (Johnson, Hilal & Bowen, 2000).

2.12 Introduction to ABAQUS Software Package

Commercial finite element analysis (FEA) software package ABAQUS version 6.6.1 is used in the indentation simulation. ABAQUS is developed by Hibbitt, Karlsson & Sorensen, Inc. It is a suite of powerful engineering simulation programs, based on the finite element method, which can solve problems ranging from relatively simple linear analysis to the most challenging nonlinear simulations.

ABAQUS consists of two main analysis modules ABAQUS/Standard and ABAQUS/Explicit. ABAQUS/Standard is a general-purpose analysis module that can solve a wide range of linear and nonlinear problems efficiently, accurately and reliably. ABAQUS/Explicit is a special-purpose analysis module that uses an explicit dynamic finite element formulation. It is suitable for short, transient dynamic events. The indentation procedure is assumed to be quasi-static problem, in which no rate effect is considered. So ABAQUS/Standard is employed in this work. A complete ABAQUS analysis usually consists of three distinct stages: preprocessing, simulation and post processing.

ABAQUS/CAE is the complete ABAQUS environment that includes capabilities for creating ABAQUS models, interactively submitting and monitoring ABAQUS jobs and evaluating results. In our job, the ABAQUS/CAE is used as the preprocessor (Part, Property, Assembly, Step, Interaction, Load, Mesh, Job modules) and postprocessor (Visualization module) (Abaqus documentation, 2000).

2.13 Indentation Analysis by Finite Element Method (FEM)

In the indentation simulation, there are two sources of nonlinearity: material nonlinearity and geometric nonlinearity. Most metals have a fairly linear stress/strain relationship at low strain values but at higher strains the material yields, at which point the response becomes nonlinear and irreversible (material nonlinearity). Also, the indentation procedure produces large deformation in the solids underneath and

near the indenter. The magnitude of displacement affects the response of the structure (geometry nonlinearity).

ABAQUS uses the Newton-Raphson method to obtain solutions for nonlinear problems. The solution is found by applying the specified loads gradually and incrementally working towards the final solution. Therefore, ABAQUS breaks the simulation into a number of load increments and finds the approximate equilibrium configuration at the end of each load increment. It often takes ABAQUS several iterations to determine an acceptable solution to a given load increment. The sum of all of the incremental responses is the approximate solution for the nonlinear analysis.

The load history for a simulation consists of one or more steps. Users define the steps, which generally consists of an analysis procedure option, loading options and output requests options. An increment is a part of a step. In nonlinear analysis the total load applied in a step is broken into smaller increments so that the nonlinear solution path can be followed. Users suggest the size of the first increment and ABAQUS automatically chooses the size of the subsequent increments. At the end of each increment the structure is in approximate equilibrium and results are available for writing to the restart, data or results files. In each increment, ABAQUS uses several iterations to attempt to find equilibrium solution. In a nonlinear analysis a step takes place over a finite period of "time", although this "time" has no physical meaning unless inertial effects or rate dependent behavior are important.

2.13.1 Module description of Abaqus Package Program

2.13.1.1 Part Module

There are several ways to create a part in ABAQUS/CAE:

1. Create the part using the tools available in the Part module.

2. Import the part from a file containing geometry stored in a third-party format, the part mesh from an output database and a meshed part from an ABAQUS/Standard or ABAQUS/Explicit input file.

3. Merge or cut part instances in the Assembly module.

4. Create a meshed part in the Mesh module.

A part created using the Part module tools is called a native part and has a feature-based representation. A feature captures design intent and contains geometry information as well as a set of rules that govern the behavior of the geometry. For example, a circular through cut is a feature, and ABAQUS/CAE stores the diameter of the cut along with the information that it should pass all the way through the part. If users increase the size of the part, ABAQUS/CAE recognizes that the depth of the cut should increase so that it continues to pass through the part.

Consumers use the Part module to create, edit, and manage the parts in the current model. ABAQUS/CAE stores each part in the form of an ordered list of features. The parameters that define each feature—extruded depth, hole diameter, sweep path, etc.—combine to define the geometry of the part as represented in Figure 2.40 (Abaqus documentation, 2000).

The Part module allows users to do the following:

1. Create deformable, discrete rigid, or analytical rigid parts. The part tools also allow you to edit and manipulate the existing parts defined in the current model and the features—solids, shells, wires, cuts, and rounds—that define the geometry of the part.

2. Use the Feature Manipulation toolset to edit, delete, suppress, resume, and regenerate a part's features and assign the reference point to a rigid part.

3. Use the sketcher to create, edit, and manage the two-dimensional sketches that form the profile of a part's features. These profiles can be extruded, revolved, or swept to create part geometry; or they can be used directly to form a planar or axisymmetric part.

4. Use the Set toolset, the Partition toolset, and the Datum toolset. These toolsets operate on the part in the current viewport and allow us to create sets, partitions, and datum geometry, respectively.
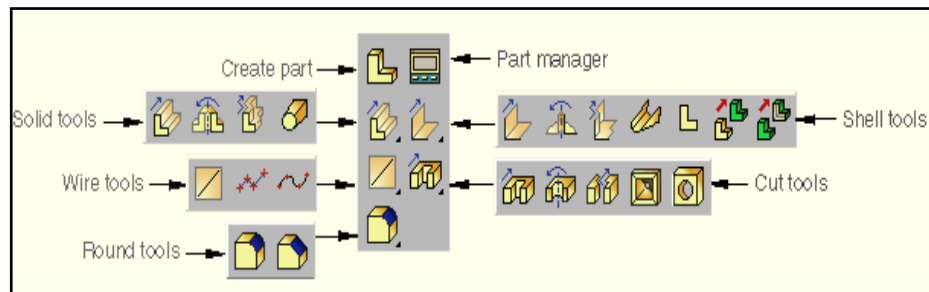
Figure 2.40 Part module of Abaqus finite element modeling program.

When users create a new part, you must specify the modeling space in which the part will reside. User can assign the following three types of modeling space:

1. Three-dimensional: ABAQUS/CAE embeds the part in the *X*, *Y*, *Z* coordinate system. A three-dimensional part can contain any combination of solid, shell, wire, cut, round, and chamfer features. User model a three-dimensional part using three-dimensional solid, shell, beam, truss, or membrane elements.

2. Two-dimensional planar: ABAQUS/CAE embeds the part in the *X–Y* plane. A two-dimensional planar part can contain a combination of only planar shell and wire features, and all cut features are defined as planar through cuts. User model a two-dimensional planar part using two-dimensional solid continuum elements, as well as truss or beam elements.

3. Axisymmetric: ABAQUS/CAE embeds the part in the *X–Y* plane with the *Y*-axis indicating the axis of revolution. An axisymmetric part can contain a combination of only planar shell and wire features, and all cut features are defined as planar through cuts. Users model an axisymmetric part using axisymmetric solid continuum elements or axisymmetric shell elements (Abaqus documentation, 2000).

2.13.1.2 Property Module

Users can use the property module to perform the following tasks:

1. Define materials, beam section profiles and sections.
2. Assign sections, orientations, normals, and tangents to parts.
3. Define skin reinforcement, inertia (point mass, rotary inertia, and heat capacitance) on a part and, springs and dashpots between two points or between a point and ground.

A material definition specifies all the property data relevant to a material. Users specify a material definition by including a set of material behaviors, and supply the property data with each material behavior. Consumers use the material editor to specify all the information that defines each material as represented in Figure 2.41. Each material that users create is assigned its own name and is independent of any particular section; they can refer to a single material in as many sections as necessary. ABAQUS/CAE assigns the properties of a material to a region of a part when users assign a section referring to that material to the region. Profile specifies the properties of a beam section that are related to its cross-sectional shape and size (for example, cross-section area and moments of inertia) (Abaqus documentation, 2000).
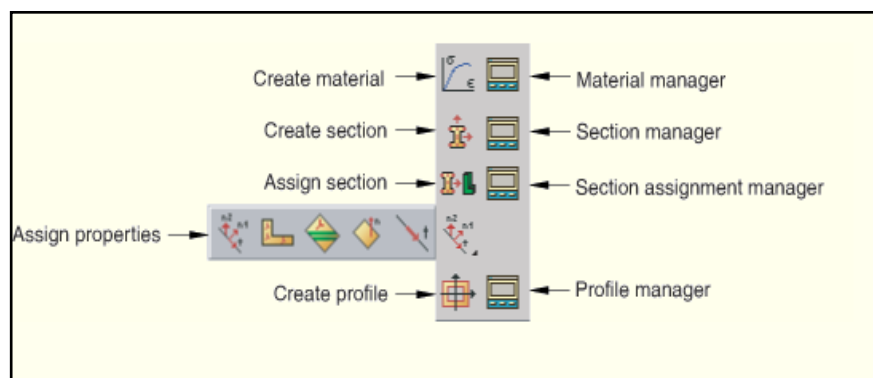
Figure 2.41 Property module of axisymmetric model for entire indentation problem.

2.13.1.3 Assembly and Step Module

When users create a part, it exists in its own coordinate system, independent of other parts in the model. In contrast, consumers use the assembly module to create instances of their parts and to position the instances relative to each other in a global coordinate system, thus creating the assembly. Users place part instances by sequentially applying position constraints that align selected faces, edges, or vertices or by applying simple translations and rotations with tools as shown in Figure 2.42. An instance maintains its association with the original part. If the geometry of a part changes, ABAQUS/CAE automatically updates all instances of the part. A model can contain many parts, and a part can be instanced many times in the assembly; however, a model contains only one assembly. Loads, boundary conditions, predefined fields, and meshes are all applied to the assembly.
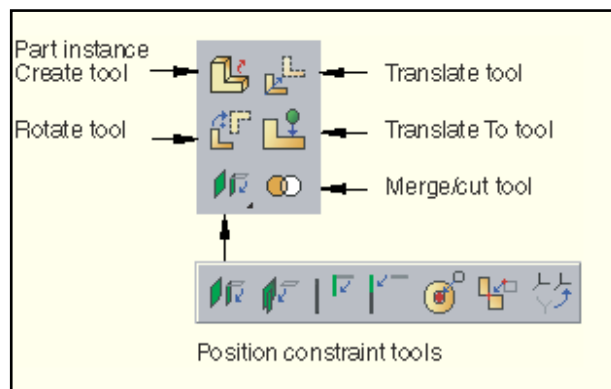
Figure 2.42 Assembly module of axisymmetric model for entire indentation problem.

Within model users define a sequence of one or more analysis steps. The step sequence provides a convenient way to capture changes in the loading and boundary conditions of the model, changes in the way parts of the model interact with each other, the removal or addition of parts, and any other changes that may occur in the model during the course of the analysis as illustrated in Figure 2.43. In addition, steps allow users to change the analysis procedure, the data output, and various controls. Users can also use steps to define linear perturbation analyses about

nonlinear base states. They can use the replace function to change the analysis procedure of an existing step. ABAQUS writes output from the analysis to the output database; users specify the output by creating output requests that are propagated to subsequent analysis steps. An output request defines which variables will be output during an analysis step, from which region of the model they will be output, and at what rate they will be output. For example, user might request output of the entire model's displacement field at the end of a step and also request the history of a reaction force at a restrained point. ABAQUS/CAE creates a special initial step at the beginning of the model's step sequence and names it Initial. ABAQUS/CAE creates only one initial step for users model, and it cannot be renamed, edited, replaced, copied, or deleted. The initial step allows user to define boundary conditions, predefined fields, and interactions that are applicable at the very beginning of the analysis. For example, if a boundary condition or interaction is applied throughout the analysis, it is usually convenient to apply such conditions in the initial step. Likewise, when the first analysis step is a linear perturbation step, conditions applied in the initial step form part of the base state for the perturbation. The initial step is followed by one or more analysis steps. Each analysis step is associated with a specific procedure that defines the type of analysis to be performed during the step, such as a static stress analysis or a transient heat transfer analysis. Users can change the analysis procedure from step to step in any meaningful way, so users have great flexibility in performing analyses. Since the state of the model (stresses, strains, temperatures, etc.) is updated throughout all general analysis steps, the effects of previous history are always included in the response for each new analysis step (Abaqus documentation, 2000).
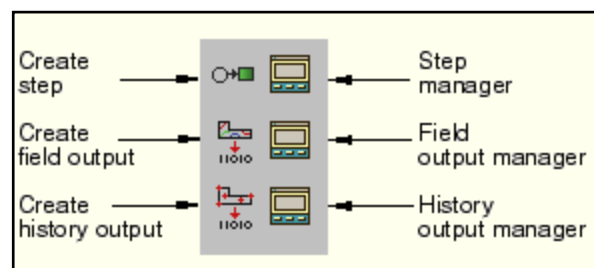
Figure 2.43 Step module of axisymmetric model
for entire indentation problem.

2.13.1.4 Interaction Properties Module

Surface-to-surface contact interactions describe contact between two deformable surfaces or between a deformable surface and a rigid surface. Self-contact interactions describe contact between different areas on a single surface. If users' model includes complex geometries and numerous contact interactions, they may want to customize the variables that control the contact algorithms to obtain cost-effective solutions. These controls are intended for advanced users and should be used with great care. General contact interactions allow users to define contact between many or all regions of the model with a single interaction. Typically, general contact interactions are defined for an all-inclusive surface that contains all exterior faces, shell perimeter edges, edges based on beams and trusses, and analytical rigid surfaces in the model. To refine the contact domain, users can include or exclude specific surface pairs. Surfaces used in general contact interactions can span many disconnected regions of the model. Attributes, such as contact properties, surface properties, and contact formulation, are assigned as part of the contact interaction definition but independently of the contact domain definition, which allows users to use one set of surfaces for the domain definition and another set of surfaces for the attribute assignments. Tools of interaction module were shown in Figure 2.44 (Abaqus documentation, 2000). General contact interactions and surface-to-surface or self-contact interactions can be used together in the same analysis. Only one general contact interaction can be active in a step during an analysis.
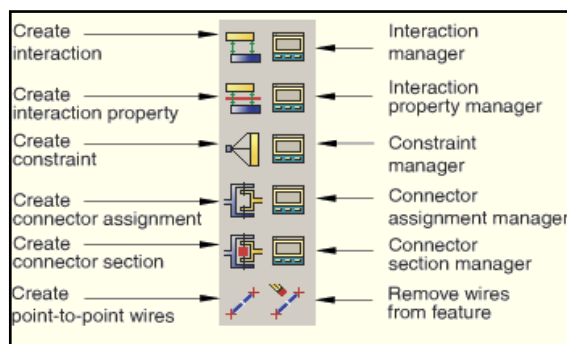
Figure 2.44 Interaction module of axisymmetric model for entire indentation problem.

2.13.1.5 Load Module and Boundary Conditions

Prescribed conditions in ABAQUS/CAE are a step-dependent object, which means that users must specify the analysis steps in which they are active. They can use the load, boundary condition, and predefined field managers to view and manipulate the stepwise history of prescribed conditions. Users can also use the Step list located under the toolbar to specify the steps in which new loads, boundary conditions, and predefined fields become active by default.

Users can use the amplitude toolset in the load module to specify complicated time or frequency dependencies that can be applied to prescribed conditions. The set and surface toolsets in the load module allow users to define and name regions of their model to which they would like to apply prescribed conditions. The analytical field toolset allows you to create analytical fields that user can use to define spatially varying parameters for selected prescribed conditions. Tools of load and boundary condition modulus were illustrated in Figure 2.45 (Abaqus documentation, 2000).
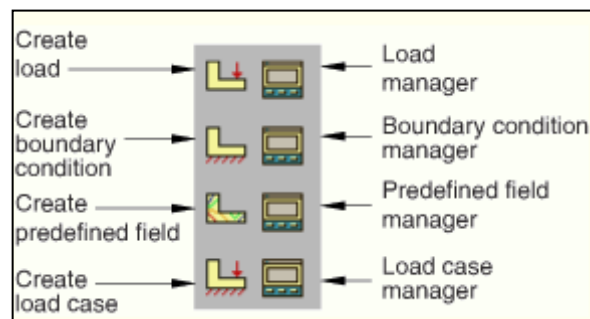
Figure 2.45 Load and Boundary Condition Module of
axisymmetric model for entire indentation problem.

2.13.1.6 Mesh Design

The mesh module allows user to generate meshes on parts and assemblies created within ABAQUS/CAE. Various levels of automation and control are available so that user can create a mesh that meets the needs of their analysis. As with creating parts and assemblies, the process of assigning mesh attributes to the model—such as

seeds, mesh techniques, and element types—is feature based as represented in Figure 2.46. As a result users can modify the parameters that define a part or an assembly, and the mesh attributes that users specified within the mesh module are regenerated automatically.

The mesh module provides the following features:

1. Tools for prescribing mesh density at local and global levels.
2. Model coloring that indicates the meshing technique assigned to each region in the model.
3. A variety of mesh controls, such as: Element shape, meshing technique, meshing algorithm, adaptive remeshing rule.
4. A tool for assigning ABAQUS/Standard and ABAQUS/Explicit element types to mesh elements. The elements can belong either to a model that you created or to an orphan mesh.
5. A tool for verifying mesh quality.
6. Tools for refining the mesh and for improving the mesh quality.
7. A tool for saving the meshed assembly or selected part instances as an orphan meshes part (Abaqus documentation, 2000).
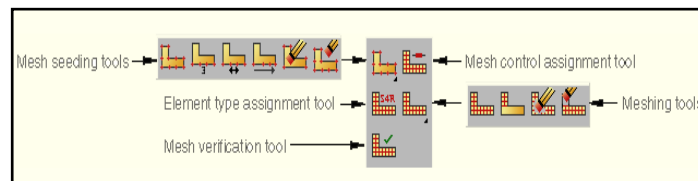
Figure 2.46 Mesh Module of axisymmetric model for entire indentation problem.

2.13.1.7 Job Module and Analysis Results

Once user have finished all of the tasks involved in defining a model (such as defining the geometry of the model, assigning section properties, and defining contact), users can use the job module to analyze their model. The Job module

allows users to create a job, to submit it to ABAQUS/Standard or ABAQUS/Explicit for analysis, and to monitor its progress. If desired, users can create multiple models and jobs and run and monitor the jobs simultaneously (Abaqus documentation, 2000).

2.14 Modeling Theories of Vickers, Berkovich and Equivalent cone

In order to improve the calculation accuracy in the continuous FEM simulation of the nanoindentation, an axisymmetric FEM model of the semi-infinite layered half space was built. To fulfill this target it was necessary to replace the Vickers pyramid through an equivalent cone. This replacement increases the calculation accuracy, since it enables the description of a three-dimensional problem through the application of a plane axisymmetric model. The lack of edge regions of the pyramid indenter negligibly affects the penetration procedure, because these regions are limited in comparison to the whole contact indenter-specimen area. The applied Vickers pyramid and the corresponding defined equivalent cone are demonstrated in the upper part of Figure 2.47.

The criterion that governs this replacement is that the cross-section areas A and B of the pyramid and conical indenter, respectively, at the same penetration depth h, are equal. The equivalent cone data are defined equalizing the rectangle area of section A, to a circular area of section B. Thus, the equivalent cone cross-section radius r_{egv} at the penetration depth h, is calculated by means of the equation:

$$r_{eqv} = \frac{a}{\sqrt{\pi}} \tag{2.55}$$

where a is the Vickers pyramid rectangle side length. At the bottom part of the figure, the equivalent cone, penetrating the coated specimen is illustrated. In the case of a Berkovich indenter, a triangular cross-section shape is considered. Taking into account the aforementioned assumptions, a deformable diamond equivalent cone was used to establish the FEM model, simulating the nanoindentation procedure (Bouzakis, 2001).
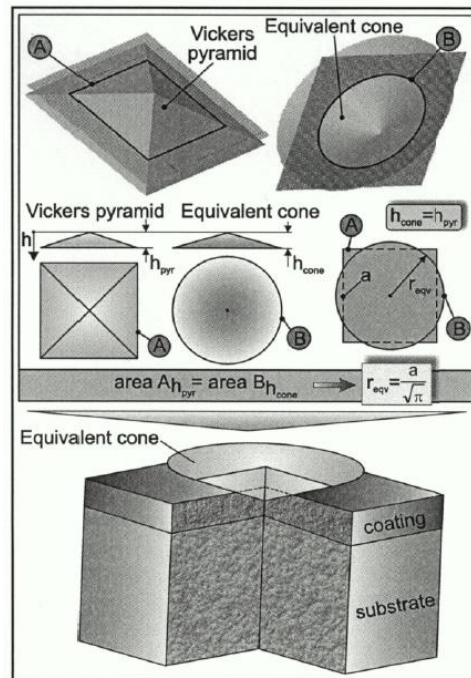
Figure 2.47 Determination of an equivalent cone to the Vickers pyramid nanoindenter, used in the developed FEM simulation of the nanoindentation (Bouzakis, 2001).

In order to achieve a flexible and reproducible model, the indenter, the coating and the substrate material properties as well as the penetration depth are variable and changeable parameters. The simulation of the nanoindentation test has been performed considering two load steps. The first load step, the so-called loading stage, represents the indentation phase into the coating. During the second load step, the so-called relaxation stage, the indenter cone is removed, leading to a material elastic-plastic recovery.

The indenter had a conical tip with semi-vertical angle of 70.3, which gives the same area-to-depth function as Berkovich and Vickers indenters. At the very tip of the indenter, a spherical rounding with a radius of 0.5 mm was constructed because of the fact that no real indenter can be ideally sharp. The indenter had a cylindrical body which was large enough to uniformly transfer the load from the top surface to

the contact area. The material of the indenter was taken as diamond and assumed to be elastic with Young's modulus of $E_s = 1140$ GPa and Poisson's ratio=0.04. The geometry of the Berkovich indentation test is shown schematically in Figure 2.48. Basically researchers attack the mechanical problem resulting when a rigid indenter is pressed into a homogeneous, isotropic and semi-infinite body.

Indentation is considered to take place under quasi-static and isothermal conditions. Furthermore, bulk constitutive behaviour is assumed for the indented material which essentially means that the derived results are meaningful only when the indentation depth is much greater than the characteristic microstructural size of the indented material. Nix and Gao (1998) established an axisymmetric model of indentation for sharp, conical indenters. They obtained a simple relation between the micro-indentation hardness H and depth h:

$$\left(\frac{H}{H_o}\right)^2 = 1 + \frac{h^*}{h^1}$$
(2.56)

where H_o is the macro-indentation hardness for a large indentation depth:

$$h^* = \frac{27M^2}{2} \frac{b\alpha^2}{tan^2\theta} \left(\frac{\mu}{H_o}\right)^2$$
(2.57)

is a characteristic length that depends on both the angle θ of the conical indenter (Figure 2.54), Burgers vector b, shear modulus μ, empirical coefficient α around 0.3, and $M = 3.06$ for fcc metals. The linear relation between the square of micro-indentation hardness H^2 and the reciprocal of indentation depth $1/h$ agrees with the experimental data for single crystal and polycrystalline copper (McElhaney et al., 1998) and single crystal silver (Ma & Clarke, 1995). The above relation for micro-indentation of conical indenters has been extended to spherical indenters (Swadener et al., 2002; Qu et al., 2006) or conical indenters with spherical tips (Xue et al., 2002; Qu et al., 2004) or different indenter angles (Qin et al., 2007), to nanoindentation (Huang et al., 2006, 2007), and to bcc metals (Qiu et al., 2001) and thin films on substrates (Saha et al., 2001; Zhang et al., 2007).
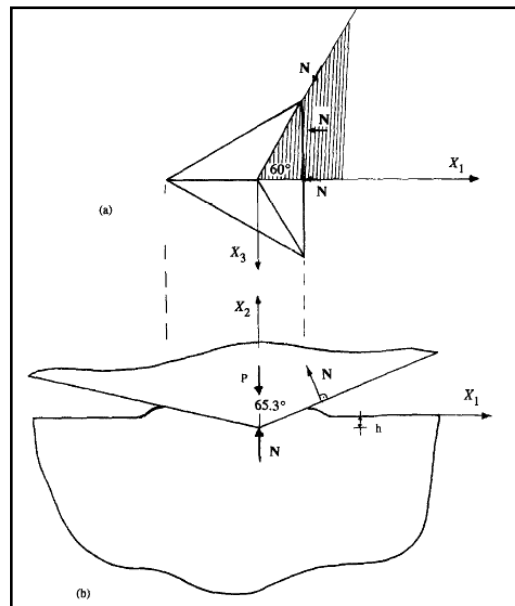
Figure 2.48 Schematic of the geometry of the Berkovich test. (a) Top view. (b) Side view.

There are other studies of indentation size effect (e.g., Begley & Hutchinson, 1998; Niordson & Hutchinson, 2003; Abu Al-Rub and Voyiadjis, 2004) based on strain gradient plasticity theories (e.g., Fleck & Hutchinson, 1993, 1997; Chen et al., 1999; Huang et al., 1999). The above micro-indentation models assume axisymmetric indenters, but the Berkovich indenter in experiments, shown in Figure 2.49, or Vickers indenter and cubic indenter (tip of a cube), are all non-axisymmetric.

For the Berkovich indenter, the equivalent angle h of the axisymmetric indenter is determined by assuming the same base area of contact at any indentation depth h. As illustrated in Figure 2.49 (a), the projected area of a regular triangular pyramid indenter with the indenter angle Ψ (i.e., triangle ABC) is the same as the projected area of the equivalent conical indenter (i.e., of circle P).
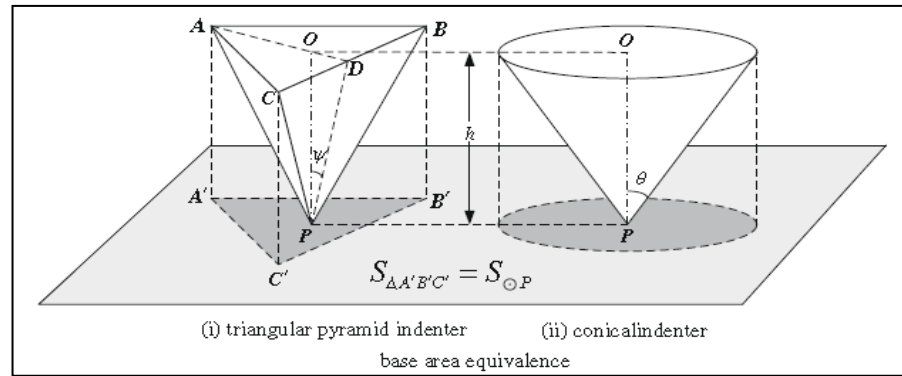
Figure 2.49 Schematic diagram of a triangular pyramid indenter with the indenter angle ψ, and its equivalent axisymmetric indenter with the indenter angle θ based on the equivalence of equal base area (Gao, 2008).

This gives the indenter angle h for the conical indenter as:

$$\theta = tan^{-1}\left(\sqrt{\frac{3\sqrt{3}}{\pi}tan\psi}\right) \tag{2.58}$$

For Berkovich indenter ($\psi = 65.3^{\circ}$), it gives the angle $\theta = 70.3^{\circ}$ of equivalent conical indenter. Three-dimensional finite element analysis shows that this equivalence holds approximately for the indentation load–displacement curve in macroindentation hardness (Li et al., 2004), but not for contact area due to the indenter pile-up or sink-in effect (Qin et al., 2009). The difference in macro-indentation hardness (ratio of indentation load to contact area) given by the Berkovich indenter and axisymmetric indenter based on Equation 2.57 is about 13% for copper.

However, as shown in Figure 2.50, this difference increases as the indentation depth decreases in micro-indentation (indentation depth on order of micrometer or submicrometer), and reaches 30% for the indentation depth of 1.5 µm in iridium (Qin et al., 2009). The difference in micro-indentation hardness of iridium given by the Berkovich indenter and axisymmetric indenter based on $\theta = \psi$ is only a few percent, as shown in Figure 2.50.
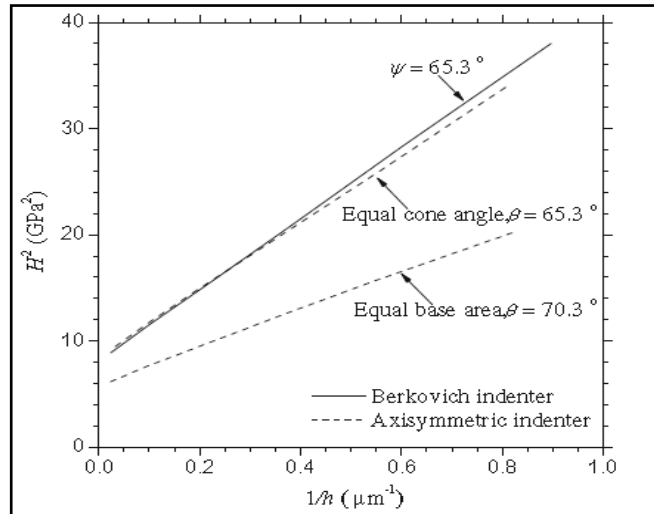
Figure 2.50 The square of micro-indentation hardness (H^2) of iridium (Qin et al., 2009) versus the reciprocal of indentation depth (1/h) for the Berkovich indenter (ψ = 65.3°) and axisymmetric indenters with the equal cone angle (θ= 65.3°) and with equal base area (θ= 70.3°).

For micro-indentation of iridium, Qin et al. (2009) established the equivalence of Berkovich and axisymmetric indenters by inscribing the axisymmetric cone to the triangular pyramid (Figure 2.51), i.e., $\boldsymbol{\theta = \psi}$.
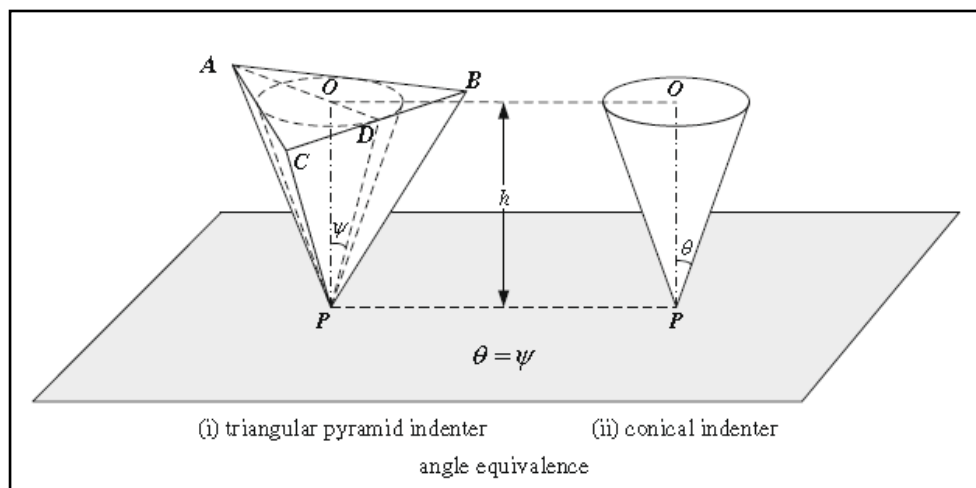
Figure 2.51 Schematic diagram of a triangular pyramid indenter with the indenter angle ψ, and its equivalent axisymmetric indenter with the indenter angle $\theta = \psi$ (Gao, 2008).

CHAPTER THREE

EXPERIMENTAL AND THEORETICAL STUDIES

3.1 The Aim of Thesis

Superconducting films with poor mechanical properties are useless, even if they possess a good transport and flux pinning properties. Since additive particles as a pinning center are important changes in microstructure, their effect on micromechanical properties such as Young's modulus, hardness and adhesion strength have to be investigated depending on additional particles type and quantity. As the main aim of this study was to determine the additional particle effects on mechanical (hardness and Young's modulus) and superconducting properties (T_c) of YBCO, flux pinning properties of YBCO with $BaMnO_3$ did not need to determine. In addition, mechanical property variations of pure YBCO and YBCO thin films with Mn (react as $BaMnO_3$) were obtained by indentation and scratch techniques. Thus, $BaMnO_3$ nanoparticle effects on superconducting, structural and mechanical properties of films were studied.

In order to determine solution characteristics which influence thin film structure; turbidity, pH values and rheological properties of the prepared solutions were measured by Turbidimeter, pH meter and Rheometer machines before drying and heating processes. Prior to coating process, (100) STO single crystalline substrates with dimension of 10 mm x 10 mm x 0.75 mm were rinsed in acetone using a standard ultrasonic cleaner. In order to use suitable process regime and to define chemical structure and reaction type of intermediate temperature products, DTA-TG and FT-IR analysis were performed in the powder production using xerogels produced at different temperatures. Structural analysis of the powders was performed through multipurpose XRD. Surface morphologies of the films were investigated using SEM/EDS and AFM. Mechanical properties of thin films will be determined as

a function of deposition parameters. Elastic properties and limit (E and σ_y) of film and substrate materials will be designated by using finite element method (FEM) and nanohardness experiments. Failure properties of films (σ_f) will be obtained using a different algorithm with FEM.

3.2 Materials

3.2.1 Substrate

It is necessary to use YBCO thin films in the high temperature superconducting (HTS) applications because of high technical features such as high J_c of YBCO, usage of the suitable lithographic techniques to pattern to the component in a film and micromechanics of YBCO on buffered Si, sapphire, MgO, Y-stabilized ZrO_2 (YSZ) and STO substrates. The successful design and fabrication of composite HTS applications requires the selection of not only a high quality HTS film, but also of an optimal substrate. The selected substrate must be compatible with high quality HTS film growth and micromachining processes for architecturing thinned membranes. The substrate not only serves as the template for high quality HTS growth, but also as a heat sink for the devices and as such can place large constraints on the response time.

Several factors related to HTS film growth influence substrate selection. These factors include: optimization of J_c that requires lattice matching, minimization of T_c suppression by substrate–film interactions and structural stability originating from coefficient of thermal expansion (CTE) matching. In addition, the substrate material should be chemically stable and should not exhibit any phase transitions in the temperature range between the deposition temperature and the bolometer operating temperature. A particular advantage of STO as a substrate material for good HTS application performance is that the crystal structure, high strength, better CTE match and high thermal conductivity (12 W/m K), i.e. high Debye temperature.

3.2.2 Precursor Materials

All chemicals which were used for production of YBCO and YBCO with BaMnO$_3$ based films are listed in Table 3.1. This YBCO based powder precursor was diluted by different solvents which are generally alcohol-based liquids. Chelating agent was used to dissolve powder precursors.

Table 3.1 All chemicals used for production of both buffer layer and YBCO film

	Chemical Type	Chemical	Formula	Purity
YBCO SOLUTION WITH TFA-MOD METHOD	Powder	YBCO powder	YBa$_2$Cu$_3$O$_{6.56}$	99.99 %
	Chelating agent	Trifluoroacetic acid	C$_2$HF$_3$O$_2$	≥99 %
		Propionic acid	CH$_3$CH$_2$COOH	99 %
	Solvent	Methyl alcohol	CH$_3$OH	99.90 %
	Mn alkoxide	Mn alkoxide	Mn 2, 4-pentanedionate	99.9 %

3.3 Production Techniques

3.3.1 Substrate Preparation

STO single crystalline substrates were cleaned with the ultrasonic cleaner in acetone in order to eliminate impurities, oil or dirty materials on the surface prior to heat treatment.

3.3.2 Solution Preparation

The preparation of YBCO precursor solutions was carried out from a commercial YBa$_2$Cu$_3$O$_{6.56}$ powder (yttrium-barium-copper oxide) with propionic acid, trifloroacetic acid (TFA), acetone and 2, 4-pentanedionate under atmospheric conditions at room temperature. The 8.3045 g of YBCO powder was weighted out in a standard balance in order to prepare 0.25 M and 50 ml solution. After 10 ml of

propionic acid was added to YBCO powder, the mixture was dissolved in 25 ml of TFA at 45 ^{o}C for 60 minutes using ultrasonic mixer (Sonorex digital 10P). The solvents were removed at 100°C for 60 minutes by hot plate to yield a blue-sticky-glassy residue with high viscosity. The coating solution was made of dissolving the residue with up to 50 ml of TFA. The solvents were evaporated from the solution again at 60°C for 60 min until highly viscous solution with transparent blue colour was obtained. After adding up to 50 ml of acetone into the solution, 15 ml of propionic acid and 5 ml of TFA were incorporated into the obtained viscous solution, and then a standard transparent solution was prepared. Finally, Mn alkoxide were separately added into 5 ml of transparent solutions with a low content 2, 4-pentanedionate as represented Figure 3.1.
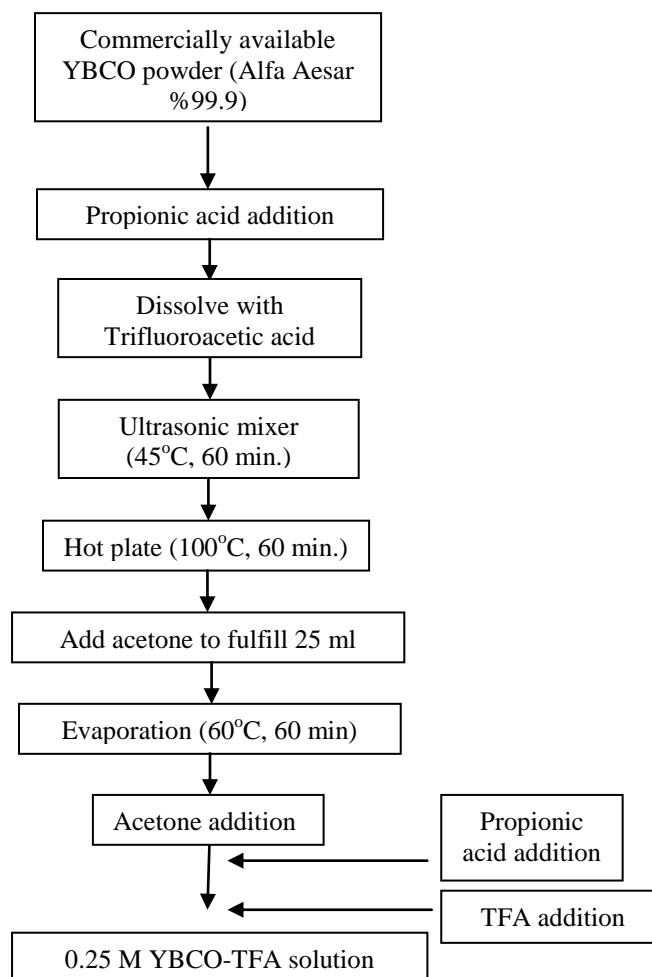
Figure 3.1 Schematic illustration of YBCO-TFA solution preparation

3.3.3 Coating Technique

3.3.3.1 Spin Coating

The YBCO based films were spin coated on the glass and Si(100) metallic substrates from the prepared suspension solutions through Cookson Electronics Equipment SCS G3P-8 model spin coater, as is evident from Figure 3.2.

Different spinning parameters such as spinning rate, acceleration time were used to control the film thickness in this system. A spinning rate of 1000-3000 rpm for 10 to 30 seconds and an acceleration time of 10 seconds were used for YBCO based films as optimum parameters.

Figure 3.2 G3P–8 Cookson model spin coater
(Ceramics Lab., DEU)

The spinning regime which was used in this technique is diagrammatically presented in Figure 3.3. As shown in the figure spin coating process which is executed at air atmosphere possess three steps. At first 30 seconds the spinner accelerates up to 2000 rpm to spread the solution and remove the excess of solution. In the range of 30th sec. to 50th sec., spinner turns in a constant speed at 2000 rpm. At this step of operation, the deposited solution easily spreads on the substrate. There exists a unique relationship between deposition quality and solution parameters such as film thickness, wettability, viscosity, pressure etc. Each parameter is expected to improve surface quality depending on solution characteristics. Third step is the

deceleration step here vaporizing of the volatiles and residual solutions were removed to improve surface quality and homogeneity in 30 seconds at 25 $^{\circ}$C in air.
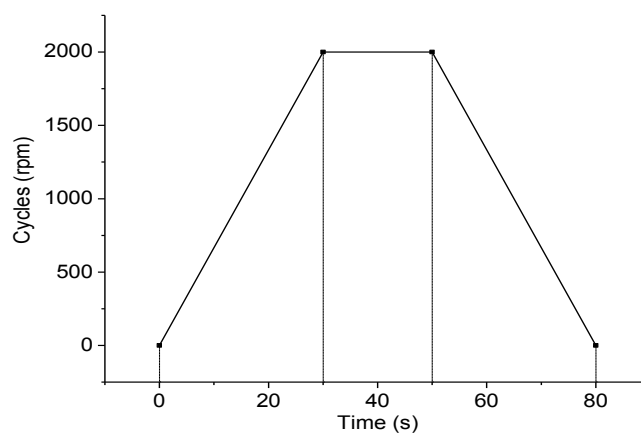
Figure 3.3 Spin coating regime for YBCO based solution

3.3.3.2 Dip Coating

The dip coating involves the formation of a film through a liquid entraiment process that may be either batch or continuous in nature. The general steps include immersion of the substrate into the dip-coating solution, start-up, where withdrawal of the substrate from the solution begins, film deposition, solvent evaporation, and continued drainage as the substrate is completely removed from the liquid bath. The film thickness formed in dip coating is mainly governed by viscous drag, gravitational forces, and the surface tension. After that, the solutions were deposited on the substrates by dip coating process with a withdrawal speed of 0.3 cm/sec in a vacuum atmosphere. The temperature of solutions was kept at room temperature in our laboratory.

3.3.4 Heat Treatment

The deposited gel films were converted to an epitaxial pure and YBCO film with BaMnO$_3$ nanoparticles through a combined calcining and heat treatment procedures. Heat treatment regime and furnace conditions were illustrated in Figure 3.4.

The gel film was dried from 80°C to 406°C in 12 % humidified oxygen. After the calcining was performed at 406°C for 0.4 hour in 12 % humidified nitrogen, the film was heated up 811°C for 1 hour in 12 % humidified nitrogen and the fired film was consequently heat treated at 465°C for 2.2 hours in a dry oxygen atmosphere.

In order to obtain highly textured thin films on STO substrate, oxygen content was 500 ml O_2 during heat treatment process at 465°C for 2.2 hours.
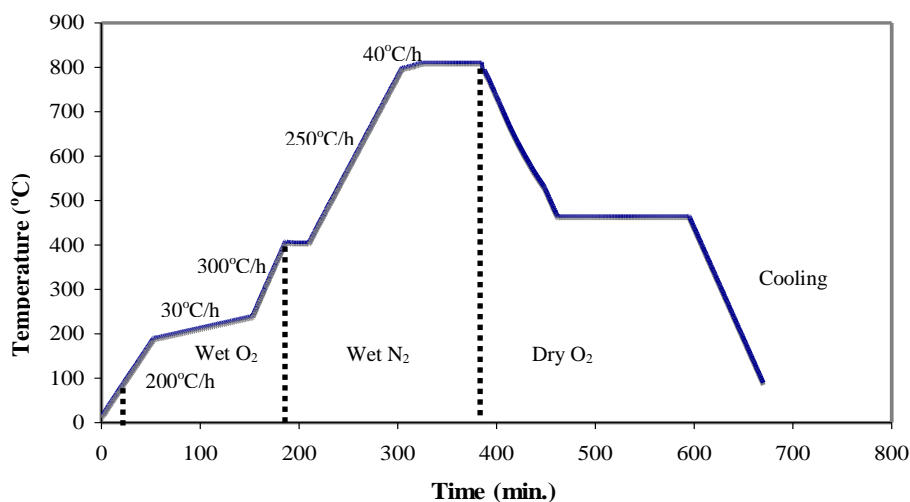
(a)
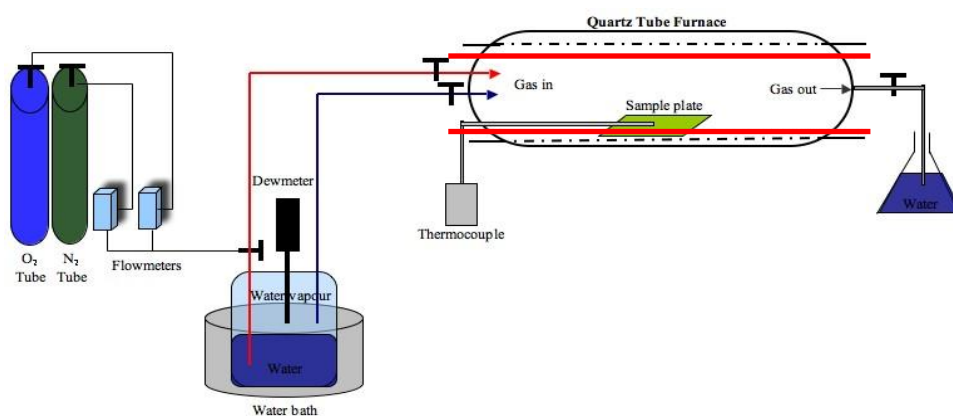
(b)

Figure 3.4 (a) Heat treatment regime and (b) furnace condition

3.4 Solution Characterization

In order to determine solution characteristics which affect the last products thin film properties, pH values, turbidity, rheological properties and spectroscopic properties of the prepared solutions were respectively measured by pH meter, turbidimeter, rheometer machines and FT-IR before powder and thin film fabrication.

3.4.1 pH Measurement

The pH measurement refers to determination of the activity of hydrogen ions in an aqueous solution. Many important properties of a solution can be determined from an accurate measurement of pH, including the acidity of a solution and the extent of a reaction in the solution. Many chemical processes and properties, such as the speed of a reaction and the solubility of a compound, can also depend greatly on the pH of a solution. In the study, pH values of the sol solutions were determined through Mettler Toledo Inlab 412 pH meter.

3.4.2 Turbidity Measurement

Turbidity (or the relative cloudiness of a liquid) measurement gives the optical characteristics of suspended particles in a liquid. Light is passed through the sample and is scattered in all directions. The light that is scattered at a 90° angle to the incident light is then detected by a photo diode and is converted into a signal linearized by the analyzer and displayed as an NTU (Nephelometric Turbidity Units) value. The more suspended particles there are in a liquid, the more light will be scattered, resulting in a higher NTU value. In the experiment, turbidity measurements of the prepared precursor solutions were performed by using TB1 Turbidimeter just like in Figure 3.5. The sample was placed in the vessel with a dimension of Ø25 mm and height of 50 mm. Formazine is recognized throughout the world as a primary standard. Formazin solution was used to calibrate the turbidity. It

was determined whether powder based precursors are well-dissolved in the used solvent.

Figure 3.5 TB1 Turbidimeter, VELP, Scientifica Srl, Italy (Chemistry Lab., DEU)

3.4.3 Rheometer

The rheological properties that lead to further characteristic knowledge concerning coating quality without depositing YBCO based coatings include viscosity, gelation time, shear, elastic and viscous modulus. The rheological measurements of YBCO based solutions were conducted with the help of a Bohlin Instruments CVO 100 Rheometer (see Figure 3.6 for details) with 2° conic plate geometry 60 mm in diameter and 0.7 µm gap sizes between plates. The viscosity values of YBCO based solutions were performed at constant 300 Hertz frequency and single shear mode at 20 ^{o}C. As far as the elastic and viscous moduli were concerned, these parameters were determined using oscillatory shear at 1 Hertz frequency for all YBCO based solutions/suspension. The rheological properties of the YBCO based solutions were comparatively studied to characterize their gelation behaviours.

Figure 3.6 Bohlin Instruments CVO 100 Rheometer
(Ceramics Lab., DEU)

3.5 Material characterization

In order to determine thin films characteristics of YBCO based materials which affect the last application products, thermal behavior of xerogel powders, and phase analyses of YBCO powders and thin films. In addition, thin film morphologies were observed by the way of microscopic techniques. Mechanical properties of YBCO based thin films were measured for optimum samples. All of mentioned measurement and tests were respectively made by DTA/TG, XRD, SEM, AFM, nanoindenter, scratch tester after powder and thin film fabrication process.

3.5.1 Differential Thermal Analysis-Thermo Gravimetric Analysis (DTA-TG)

The thermal analysis of the gel was studied under N_2 flowing by means of Shimadzu 60H Model Differential Thermal Analysis-Thermal Gravimetry (DTA-TG) as shown in Figure 3.7 in order to obtain information about the decomposition behaviour of the gels and adjust the thermal treatment accordingly. More precise data regarding as process optimization in YBCO based film production depending on temperature were obtained after DTA-TG analysis. Thermal data were analyzed using TA60 software program supplied with the instruments.

Thermal analysis is defined as a group of techniques in which a physical thermal analysis is defined as a group of techniques in which a physical property of the substance and its reaction products are measured as a function of temperature whilst the substance is subjected to a controlled temperature program (Hill, 1991). In addition to these, thermal methods are based upon the measurement of the dynamic relationship between temperature and some property of the system such as mass and heat absorbed by or evolved from it. Differential Thermal Analysis (DTA) and Thermogravimetry (TG) are the most important thermal methods used in characterization of materials (Kayatekin, 2006).

DTA is a technique in which the difference in energy between the sample and the reference material is measured against time or temperature. The DTA curve is generally a plot of the difference in energy as the ordinate against temperature T, as the abscissa. By convention, in DTA endothermic peaks are drawn downwards and exothermic upwards (Ak, 2008). As for TG, it is a technique in which the mass of the sample is monitored against time or temperature while the temperature of the sample is programmed. A plot of mass loss or percent loss versus temperature or time can be obtained. The reaction is shown as one or more steps, each of which represents a mass change.

Temperature change in the samples brings about the chemical (phase transition, reduction, oxidation and decomposition) and physical (boiling, melting and sublimation) changes of a sample and these can be endothermic or exothermic. DTA is able to be used to study any process in which heat is absorbed or evolved. The number, shape and position of the various endothermic and exothermic peaks in DTA curve can be used for qualitative identification of the substance. Simultaneous techniques refer to the application of two or more techniques to a sample at the same time. In the present study, DTA-TG simultaneous techniques are used. It is an advantage to use simultaneous techniques because it saves time and sample and it gives an opportunity to set an experiment at the same conditions (Ak, 2008).

Figure 3.7 Shimadzu DTG-60H/TA-60WS simultaneous thermal analyzer (Ceramics Lab., DEU)

3.5.2 Fourier Transform Infrared Spectroscopy (FT-IR)

An analytical technique, Fourier Transform Infrared (FTIR or IR) spectroscopy is generally a non-destructive technique, which is used to measure the absorption of various infrared light wavelengths of organic or inorganic materials of interest. The infrared absorption bands identify the specific molecular components or structures, and provide chemical bonding information of the YBCO based materials because of the vibrational motions of the chemical bond showing frequencies in the infrared regime. Infrared spectra record the infrared intensity (transmission percentage or absorption) versus wavelength (wavenumber) of light. The IR spectrum can be generally divided into three frequency (or wavenumber/wavelength) regions: the far IR ($10{\sim}400$ cm^{-1}), the middle IR ($400{\sim}4,000$ cm^{-1}) and the near IR ($4,000{\sim}14,000$ cm^{-1}), with the middle IR region being employed in most IR spectroscopic investigations. The basic infrared experiment is to measure the changes of infrared light intensity after interacting with the sample. Intensity can be expressed as percent transmittance (%T) or absorbance (A). If I_o is the energy, or radiant power, reaching the infrared detector with no sample in the beam, and I is the energy detected with a sample present, transmittance is,

$$T = \frac{I}{I_0} \tag{3.1}$$

and percent transmittance:

$$\%T = \frac{I}{I_0} \times 100 \qquad\qquad (3.2)$$

Absorbance is:

$$A = \log\left(\frac{1}{T}\right) = \log\left(\frac{I_0}{I}\right) \qquad\qquad (3.3)$$

Figure 3.8 Schematic illustration of FTIR system having ATR
apparatus (Electronic Materials Lab., DEU)

The technique of Attenuated Total Reflectance (ATR) (as represented in Figure 3.8) has in recent years revolutionized solid and liquid sample analyses because it combats the most challenging aspects of infrared analyses namely sample preparation and spectral reproducibility. An ATR accessory operates by measuring the changes that occur in a totally internally reflected infrared beam when the beam comes into contact with a sample as indicated in Figure 3.9 (Ak, 2008). An infrared beam is directed onto an optically dense diamond crystal with a high refractive index at a certain angle. This internal reflectance creates an evanescent wave that extends beyond the surface of the crystal into the sample held in contact with the crystal. It

can be easier to think of this evanescent wave as a bubble of infrared that sits on the surface of the crystal. This evanescent wave protrudes only a few microns (0.5-5 μm) beyond the crystal surface and into the sample. Consequently, there must be good contact between the sample and the crystal surface. In regions of the infrared spectrum where the sample absorbs energy, the evanescent wave will be attenuated or altered. The attenuated energy from each evanescent wave is passed back to the IR beam, which then exits the opposite end of the crystal and is passed to the detector in the IR spectrometer. The system then generates an infrared spectrum.
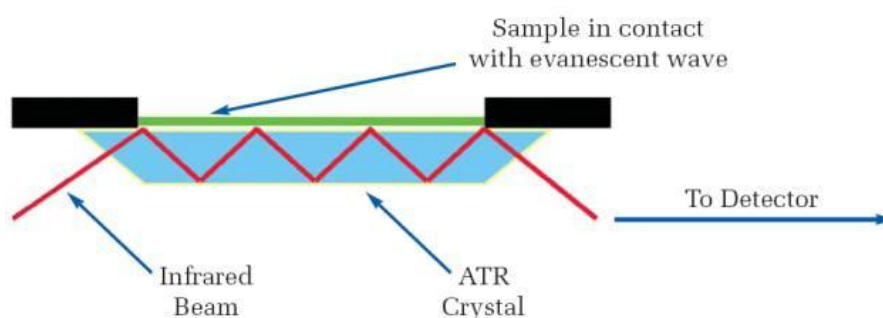
Figure 3.9 Schematic illustration of FTIR detection

The infrared spectra of all liquid and coated samples were recorded with a Perkin Elmer Spectrum BX instrument equipped with ATR (Figure 3.8) apparatus in the spectra range between 4000 and 650 cm^{-1} with a resolution of 4 cm^{-1}. With this concept, we were particularly interested in what happened to YBCO based xerogels and films when they regularly heated up from 25 ^{o}C from perovskite formation temperatures. Based on this, it was determined the chemical ingredient of dried and annealed samples.

3.6 Thin Film Characterization

3.6.1 X-Ray Diffractometer (XRD)

X-ray diffraction (XRD) is one of the primary techniques to analyze all kinds of materials such as powders and crystals. XRD can provide information about

crystalline structure and structural phases. It is extensively used to investigate the structural properties of YBCO based thin films on substrates. Synthesized coatings were analyzed by means of XRD in Figure 3.10 with a grazing angle attachment and an incident angle of 1° (Rigaku, D/Max-2200/PC). X-Ray radiation of CuK_α was set at 40 kV and 36 mA with a scanning speed of 2°/min, from 3° to 90°.

Figure 3.10 X-Ray Diffractometer, Rigaku, D/Max-2200/PC (X-Ray Lab., DEU)

3.6.2 Scanning Electron Microscopy with Energy Dispersive Spectroscopy (SEM-EDS)

Scanning electron microscopy (SEM), as depicted in Figure 3.11, is one of the most common analytical methods to examine surface morphology of the solid-state specimen. In SEM, a tiny high-energy electron beam is scanned across the sample surface. Series of radiations can be produced in terms of the interaction between the electron beam and the sample. Normally, two types of radiation are utilized for image formation: primary backscattered electrons and secondary electrons. Backscattered electrons reveal the compositional and topographical information of the specimen.
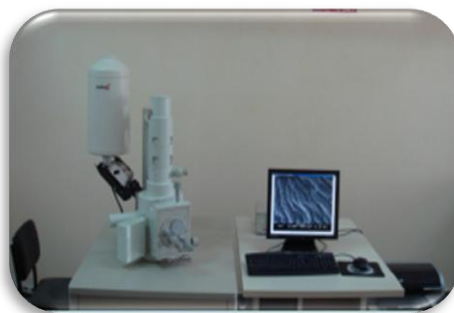
Figure 3.11 Scanning electron microscopy-
energy dispersive spectroscopy-JEOL JSM-
6060 (SEM Lab., DEU)

The secondary electron images produce a depth of field which shows the surface topography. The signal modulation of the two types of radiation is viewed as images in the CRT and provides the morphology, surface topology and composition of the specimen surface. The energy dispersive spectroscopy (EDS) is often attached to the SEM. The X-rays generated from the interaction between the electron beam and the specimen is used to identify and measure quantitatively the elemental composition of the specimen. Therefore, SEM/EDS can detect the elemental composition and obtain the morphology of the specimen simultaneously. In this study, the surface and elemental composition of the YBCO based films were examined by using JEOL JSM-6060 instrument operating at an accelerating voltage of 15 kV.

3.6.3 Atomic Force Microscopy (AFM)

Atomic Force Microscopy (AFM) is a powerful tool for assessing the three dimensional surface topography and morphological quality of YBCO based films. A Digital Nanosurf AFM easyscan as denoted in Figure 3.12 was used in tapping mode to obtain AFM images of at least one film in each batch measured. In 'Tapping Mode' technique the probe is oscillated at a constant frequency as the AFM head scans across the surface. The amplitude of oscillation of the tip varies as it moves nearer to the surface of the film, this change is used as feedback to control the sample-tip distance and deduce the surface height of the film. In general AFM measurements revealed that it was difficult to obtain vicinal films with as high a

quality as the best c-axis films. Even the best films exhibited pin-hole defects or outgrowths. The AFM employed was well-calibrated in the z-axis, a maximum error of +/- 2 nm was observed imaging 180 nm deep pits on a calibration sample. The AFM was therefore be used to obtain film thickness by measuring the height of chemically etched steps.

Figure 3.12 Nanosurf easyscan AFM machine (Metallography Lab., DEU)

3.7 T_c Measurement

Transition temperature (T_c) was determined using an induction method and a criterion of 90 % increase in induced voltage during sample heating. The films were photolithographically patterned and structured using Ar^+ ion etching. Electrical transport properties were studied using four-probe geometry on bridges of 50 µm width and 0.8 mm length in magnetic fields up to 9 T using a Quantum Design PPMS.

3.8. Mechanic Tests

3.8.1 Nanoindenter

Instrumented indentation testing (IIT) has emerged as an important method for the evaluation of a material's mechanical response to applied loading. The technique is

based on the continuous recording of applied force and resulting depth of penetration of an indenter throughout the whole loading and unloading cycle of YBCO based thin films, when applied force is controlled. Displacement control is also possible. The technique allows for the determination of the traditional values of hardness without the need to measure the residual size of an indentation produced by an applied force.

CSM Instruments and its mother company CSEM (Swiss Center for Electronics and Micro technology) have been an active part of the development of nano mechanical testing instruments for surface and coatings characterization, as represented in Figure 3.13.

(a)   (b)
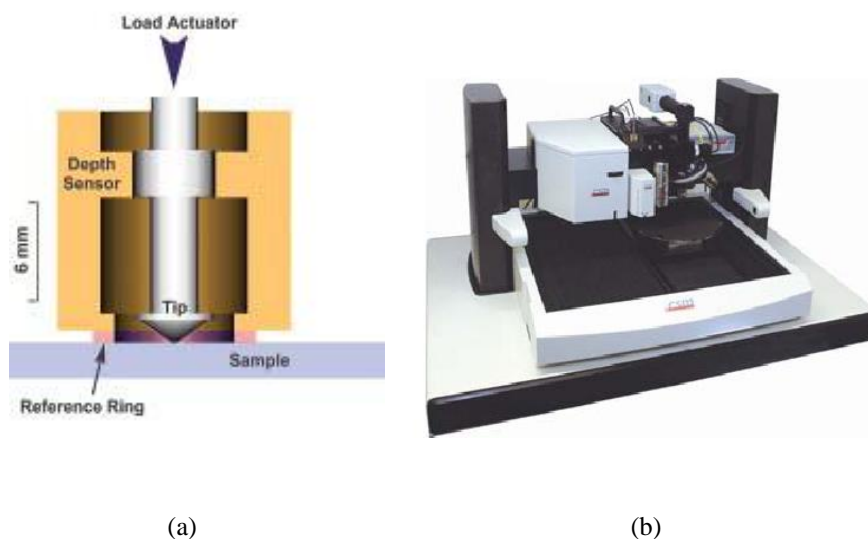
Figure 3.13 (a) Schematic representation of indentation and (b) nanoindentation tester

3.8.2 Scratch Testing

Adhesion strength of YBCO based coatings were evaluated using a scanning scratch tester in Figure 3.14 (Instruction Manual, Shimadzu Scanning Scratch Tester SST-W101, 2002, Shimadzu Corporation.) with a 15 μm tip radius diamond stylus. During the test, a stylus was drawn on coating surface with a sliding speed of 5

µm.s^{-1} keeping scanning amplitude of 10 µm which perpendicular to the scratching direction at the same time. Load was carried out progressively to the stylus with a loading speed of 2µm.s^{-1}. Friction on the stylus increases with increasing load, which causes a delay in movement between cartridge body and stylus. This delay is defined as a cartridge output. As a result of tests, test force versus cartridge output (%) curves are obtained.

Figure 3.14 Schimadzu, SST-W101 scratch testing machine (Metallography Lab., DEU)

3.9 Modeling of YBCO based Thin Films by Axisymmetric Equivalent Cone

Finite Element Modeling (FEM) was performed with the commercial software package ABAQUS 6.6-1. The model was constructed with axisymmetric geometry as illustrated Figure 3.15. The indenter had conical tips with semi-vertical angle of 70.3^{o}, which gives the same area-to-depth function as Berkovich and Vickers indenters as represented Figure 3.15. The material of the indenter was taken as diamond and assumed to be elastic with Young's modulus of $E_s = 1140$ GPa and Poisson's ratio=0.04 (Brookes, 1979). Figure 3.15 shows the schematic of the finite element model used in this work for 300 nm film thickness.
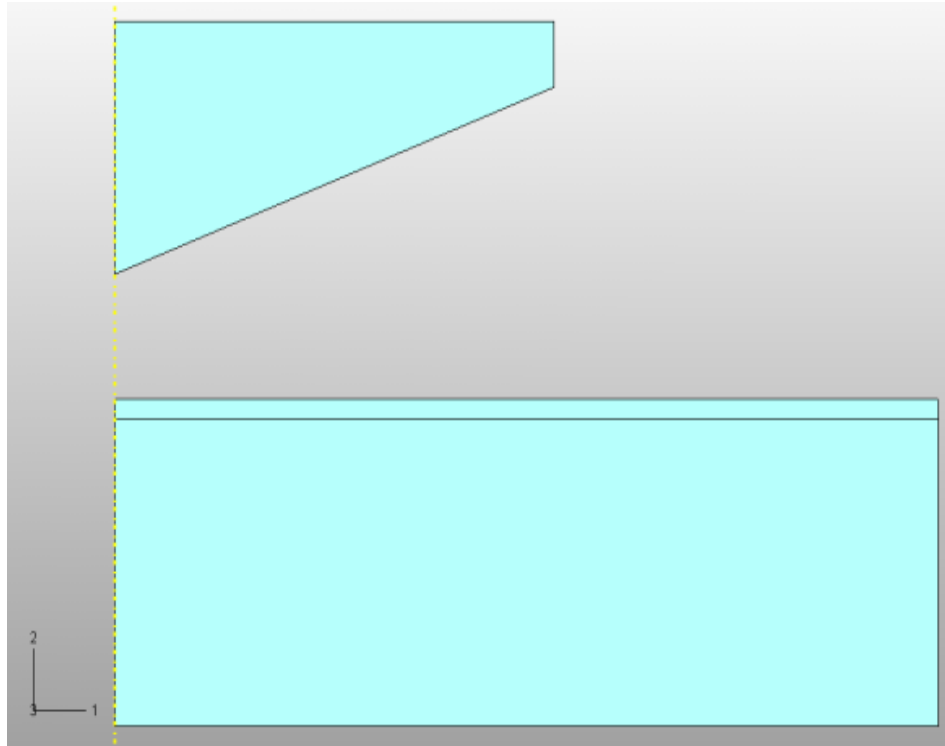
Figure 3.15 Axisymmetric 70.3^o equivalent cone models representation of YBCO based thin film with 300 nm thickness.

CHAPTER FOUR

RESULTS AND DISCUSSION

The general aim of this study is to determine superconducting and mechanical properties of $YBa_2Cu_3O_{6.56}$ (YBCO) and YBCO thin films with different content Manganese (Mn) addition. With this regard, YBCO superconducting films with/without Mn were spin-coated onto (001) $SrTiO_3$ (STO) single-crystal substrates by metalorganic deposition using trifluoroacetate (TFA-MOD) technique. Microstructure and superconducting properties of YBCO based thin film can be changed depend on solution-coating characteristics and influenced the mechanical properties. In addition, mechanical strength of YBCO thin films also determines the stability of thin film based devices against internal stresses and mechanical wear. In spite of their importance, mechanical properties such as adhesion strength; *F*, hardness; *H*, and Young's modulus; *E*, failure stress; σ_f, modeling of thin film-substrate system and stress-strain relationships of pure YBCO and YBCO thin films with $BaMnO_3$ nanoparticles are poorly investigated in nanoscale with details.

4.1 Solution Characterization

4.1.1 Turbidity

Hydrolysis, chealation and condensation reactions which have a great importance in solution preparation will be investigated and optimum precursors, solvents and chelating agents will be determined to inhibit aging of solution. Aging can cause nucleation and growth of the structure prior to the coating process. Therefore, it must be controlled by measuring turbidity of the obtained solution. Turbidity which means the relative cloudiness of a liquid gives the optical characteristic of suspense particles in a liquid. While measuring the turbidity, light is passed through the sample and is scattered in all directions. The light that is scattered at 90° angle to the incident light

is then detected by a photo diode and is converted into a signal linearized by analyzer and displayed as ntu (nephelometric turbidity unit). The measurement range is between 0 ntu and 1000 ntu. It is interpreted that powder based precursors is completely dissolved as turbidity value approaches to 0 ntu and they are not dissolved and some powder particles are suspended in a solution as it approaches to 1000 ntu. The fabrication of homogeneous, continuous thin film is directly related to turbidity value which approaches 0 ntu.
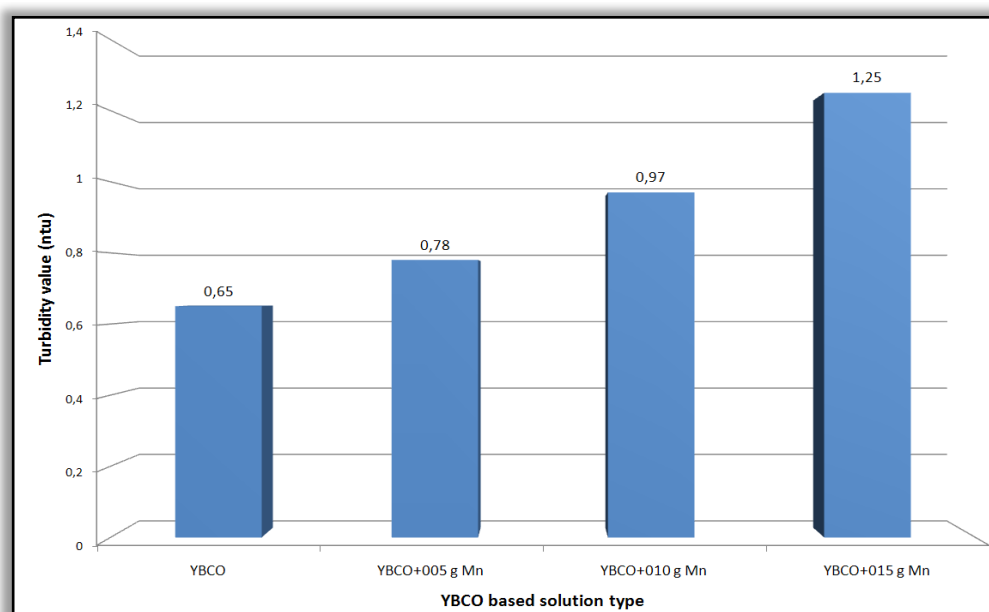
Figure 4.1 Turbidity values variations of prepared YBCO based solutions

A relationship between turbidity values and Mn content of the prepared YBCO based solutions is indicated in Figure 4.1. Turbidity values of the solutions including pure YBCO, YBCO thin films with 0.05 g, 0.1 g and 0.15 g Mn were measured as 0.65, 0.78, 0.97 and 1.25 ntu, respectively. According to the turbidity values, it can be pointed that powder based precursors are completely dissolved in the solutions. Moreover, these values present an important clue for further processing. Notably, films which are prepared from completely undissolved solutions are not homogeneous, continuous and thin.

4.*1.2 pH*

The pH value of the solution must be measured to determine acidic or basic character of solution. Now that pH value of the solution is an important factor influencing the formation of the polymeric three-dimensional structure of the gel during the gelation process, it should be taken into consideration while preparing solutions. While ramified structure is randomly formed in acidic conditions, separated clusters are formed from the solutions showing basic characters. The other factor is dilution of the solution by using solvent. Because the liquid phase during the aging procedures mainly consists of the excess solvent, it physically affects the structure of the gel. The changes in the gel structure at this stage partly influence the structure of the final film (Brinker, 1990). Figure 4.2 demonstrated pH values of the solutions depending on Mn content for YBCO based solutions. According to this result, acidity of the solutions decreases with increasing Mn content. The pH values of the solutions with 0 g, 0.05 g, 0.10 g and 0.15 g Mn content were found to be 0.74, 0.78, 0.82 and 0.98, respectively.
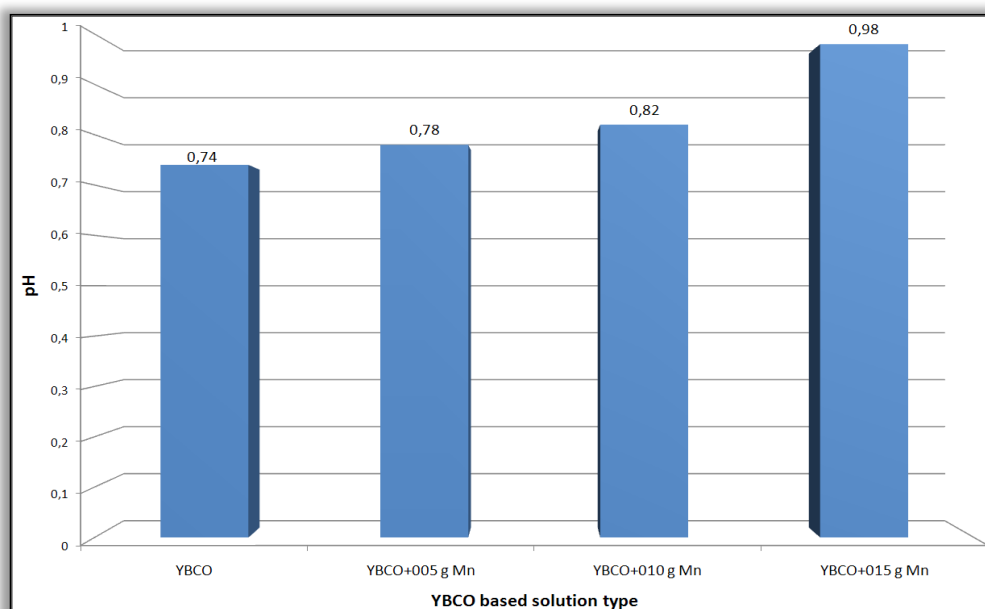
Figure 4.2 pH values of YBCO based solutions

4.1.3 Rheological Properties

Rheological properties of the solution such as viscosity, shear stress, elastic/viscous modulus and gel point will be determined to prepare optimum solutions. Gelation occurs when aggregation of particles or molecules takes place in a liquid, under the action of Van der Waals forces or via the formation of covalent or noncovalent bonds. The process can be investigated using rheological measurement techniques (Phonthammachai et al., 2004). Since the microstructure of the film is obtained in this part of the process, this evaluation is extremely important. Table 4.1 shows rheological properties such as viscosity and shear stress for the prepared solutions as a function of Mn content, in details.

Table 4.1 Rheological properties of YBCO based solutions under 300 s^{-1} frequency.

Solution Type	Viscosity (Pa.s)	Shear Stress (Pa)
Pure YBCO	0.0060	1.80
YBCO with 0.05 g Mn	0.0045	1.35
YBCO with 0.10 g Mn	0.0065	1.95
YBCO with 0.15 g Mn	0.0070	2.10

Viscosity measurement of pure YBCO based solutions with and without Mn at room temperature was demonstrated in Figure 4.3. The relative viscosity values of the obtained solution having 0 g, 0.05 g, 0.10 g and 0.15 g Mn found to be 0.0060 Pa.s, 0.0045 Pa.s, 0.0065 Pa.s and 0.0070 Pa.s, respectively, at room temperature. As it can be understood from these results, the viscosity of the solution is controlled by content of the Mn. Solutions containing different Mn content usually show a more complex behaviour of their viscosity, gel point, shear stress, viscous and elastic modulus. Notably, the rheological properties of precursor solutions directly influences the thickness of sol-gel coated films-higher viscosities results in higher film thickness as explained elsewhere (Celik et al., 2004). As shown from Table 4.1, when Mn content in solution was increased from 0 g to 0.15 g, the viscosity was fluctuated and thus also other rheological properties such as shear stress, viscous and elastic modulus are varied until gelation process started by temperature and time.
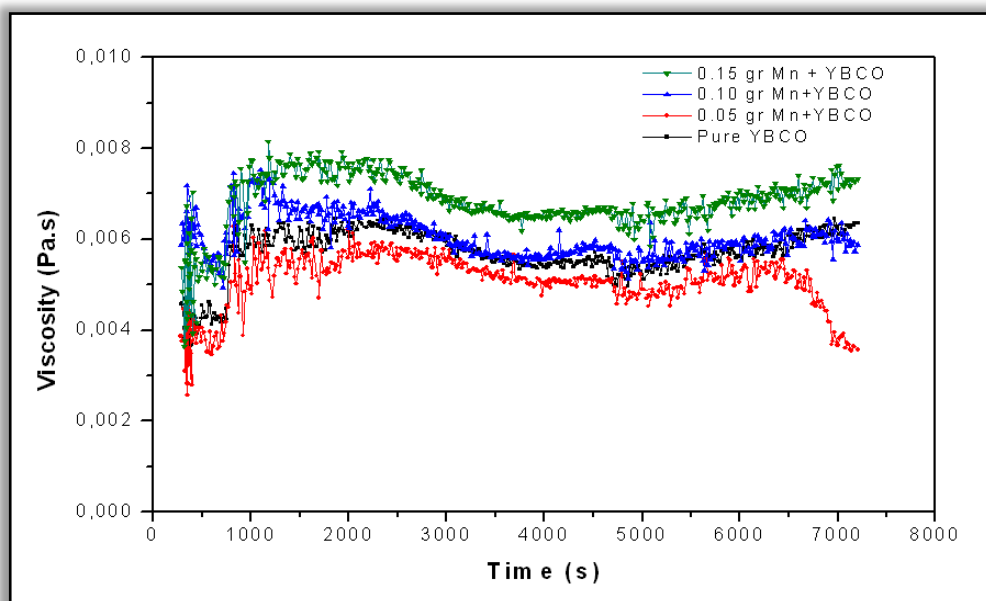
Figure 4.3 Viscosity measurement of YBCO based solutions with and without Mn at room temperature at 25 ^{o}C.
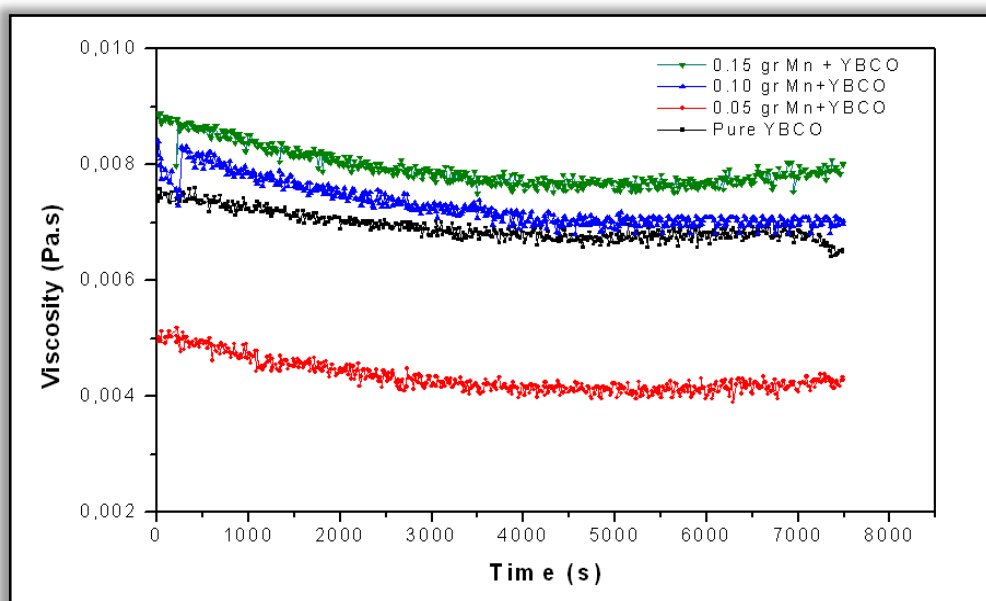
Figure 4.4 Viscosity measurement of YBCO based solutions with and without Mn while increasing temperature from 25 ^{o}C to 60 ^{o}C

Figure 4.4 showed viscosity measurement of YBCO based solutions with and without Mn while increasing temperature from 25 ^{o}C to 60 ^{o}C. Time and temperature dependency of YBCO based solution could be seen by increasing temperature from 25 ^{o}C to 60 ^{o}C. It was obviously seen that viscosity of solutions showed no tendency to the temperature. As known, viscosity is an internal property of a fluid that offers

resistance to flow. In other words, it is a measure of the resistance of a fluid to deform under shear stress. Furthermore, viscosity describes a fluid's internal resistance to flow and may be thought of as a measure of fluid friction. Newton defined viscosity as the ratio of the shear stress (the force per unit area pulling one layer of fluid across another) to the shear rate (the speed at which layers move relative to each other) (Darby, 2001).

Table 4.2 Viscous and elastic modulus variations of YBCO based solutions under 1 sn^{-1} frequency with oscillation mode at 60°C.

Solution Type	Viscous modulus (Pa)	Elastic modulus (Pa)	Gel point (s)
Pure YBCO	1.50	1.75	15.000
YBCO with 0.05 g Mn	0.10	0.16	16.500
YBCO with 0.10 g Mn	0.10	0.45	6.000
YBCO with 0.15 g Mn	0.45	0.65	> 20.000

As listed in Table 4.2, viscous and elastic modulus of YBCO based samples decreased. However, elastic modulus and viscous modulus of solution were decreased from 1.75 Pa to 0.16 Pa and 1.50 Pa to 0.10 Pa by increasing Mn content from 0 g to 0.05 g, respectively. After that elastic modulus and viscous modulus of solution were increased from 0.45 Pa to 0.65 Pa and 0.10 Pa to 0.45 Pa, correspondingly. According to the Figure 4.5 and 4.6, viscous and elastic modulus variations of pure YBCO and YBCO with 0.05 g Mn based solution were represented depend on time at 60 ^{o}C.

According to the theory of gelation process, viscous and elastic modules of solutions were conflicted together by increasing time for 1 hertz frequency under fixed temperature. Gelation point of pure YBCO under standard condition determined as 15.000 s at 60 ^{o}C as illustrated in Figure 4.5. At that point, elastic and viscous modulus values were 1.65 Pa. Figure 4.6 showed that gel point of YBCO with 0.05 g Mn based solution 16.500 s and elastic-viscous modulus of solutions superimposed at 0.16 Pa. According to rheological results, gel point of solutions was increased by increasing Mn content from 0 g to 0.05 g.
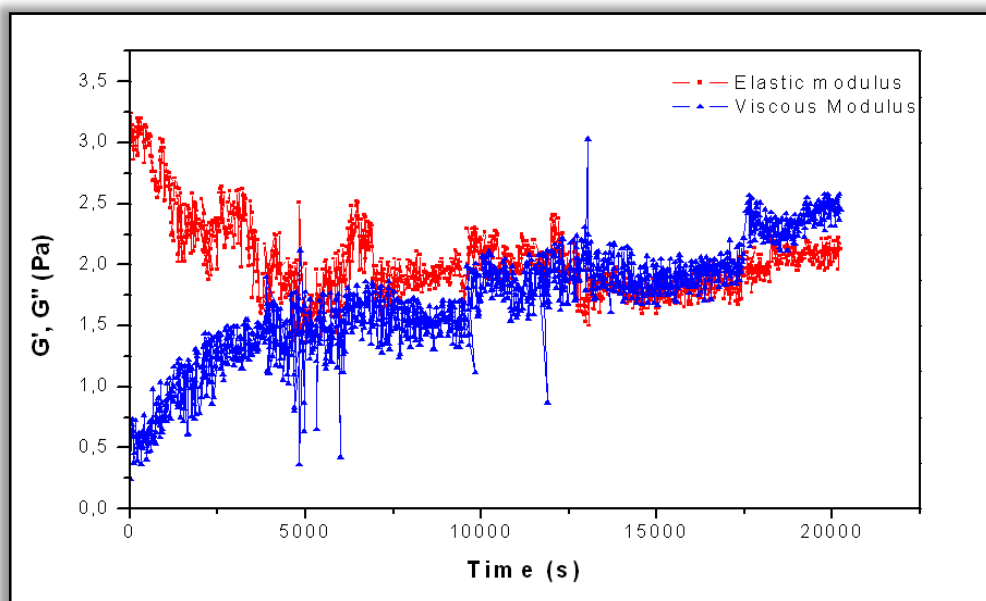
Figure 4.5 Viscous and Elastic Modulus variations of pure YBCO based solutions at 60 ^{o}C
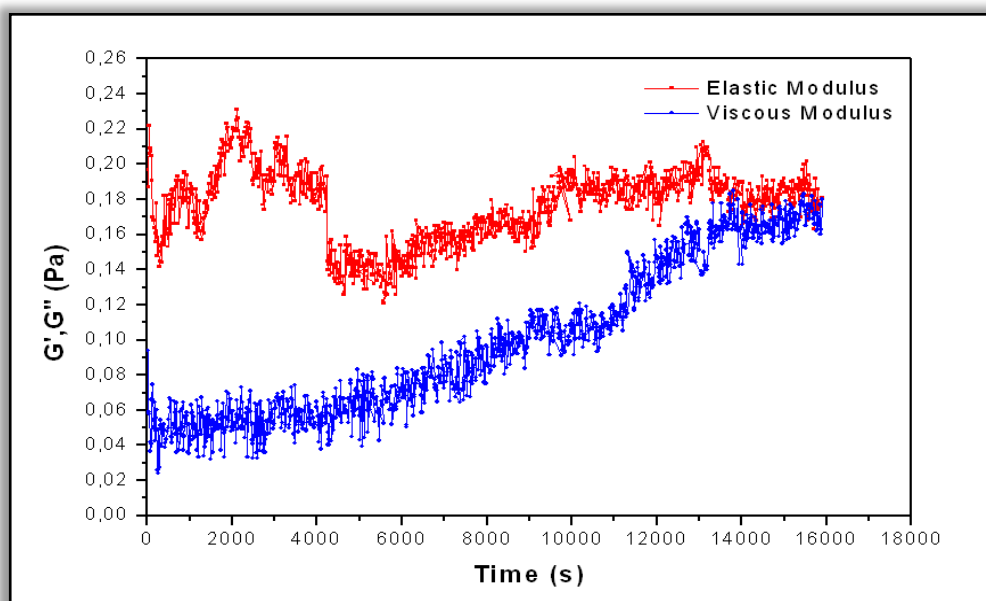
Figure 4.6 Viscous and Elastic Modulus variations of YBCO based solution with 0.05 g Mn at 60 ^{o}C

Figure 4.7 and 4.8 indicated that viscous and elastic modulus variations of YBCO with 0.10 g Mn and 0.15 g Mn based solution at 60 ^{o}C depend on time. Viscous and elastic modulus of YBCO based solution with 0.10 g Mn conflicted and separated near 6.000 s test time at 60°C. Viscous modulus of solution

increased, conflicted and separated from elastic modulus values. This characteristic behaviour showed that gel point of YBCO based solution with 0.10 g Mn was near 6.000 s. At this point elastic and viscous modulus values were same as 0.055 Pa.
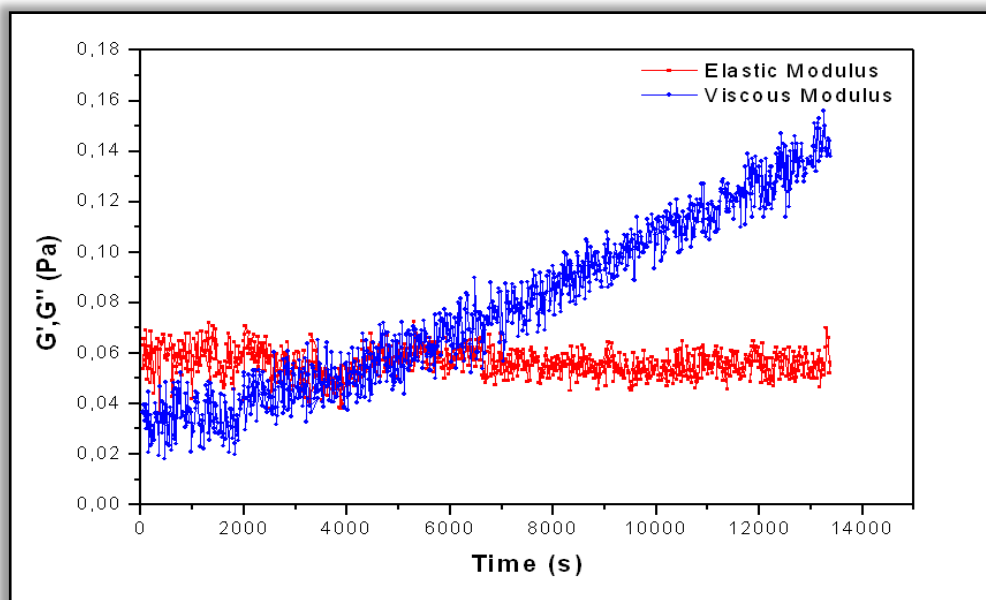
Figure 4.7 Viscous and Elastic Modulus variations of YBCO based solution with 0.10 g Mn at 60 $^{\circ}$C
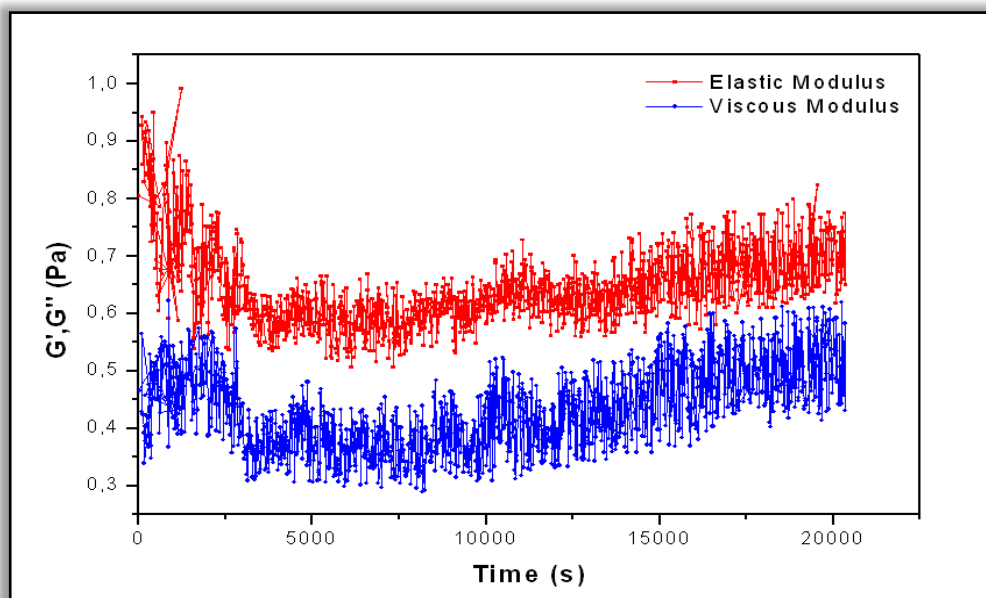
Figure 4.8 Viscous and Elastic Modulus variations of YBCO based solution with 0.15 g Mn at 60 $^{\circ}$C

4.2 Process Optimization

4.2.1 DTA/TG Analysis

Differential thermal analysis was conducted to understand thermal decomposition of YBCO based solutions on STO substrate during heat treatment process. Figures 4.9 a), b), c) and d) show the DTA-TG curves of pure YBCO, YBCO with 0.05 g Mn, YBCO with 0.10 g Mn and YBCO with 0.15 g Mn based xerogels, which were dried at 200 ^{o}C for 3 hours in air, respectively. According to the graphs, there are three main reactions occurred from room temperature to the oxide ceramic formation. Smooth gel films started to decompose at about 100-120 ^{o}C and solvent was removed from the structure. The first endothermic peaks represent this solvent removal. At this temperature, the endothermic reaction is mostly owing to evaporation of volatile organic components. The combustion process of organic groups occurred at ~250°C as a second thermal phenomenon due to the fact that carbon based materials coming from alkoxide, solvents, chelating agent and modifying liquid chemicals burnt out. Thermograviometric analysis of the samples showed that the total weight loss of samples were near 50 % near 250 ^{o}C for all four different YBCO based powder.
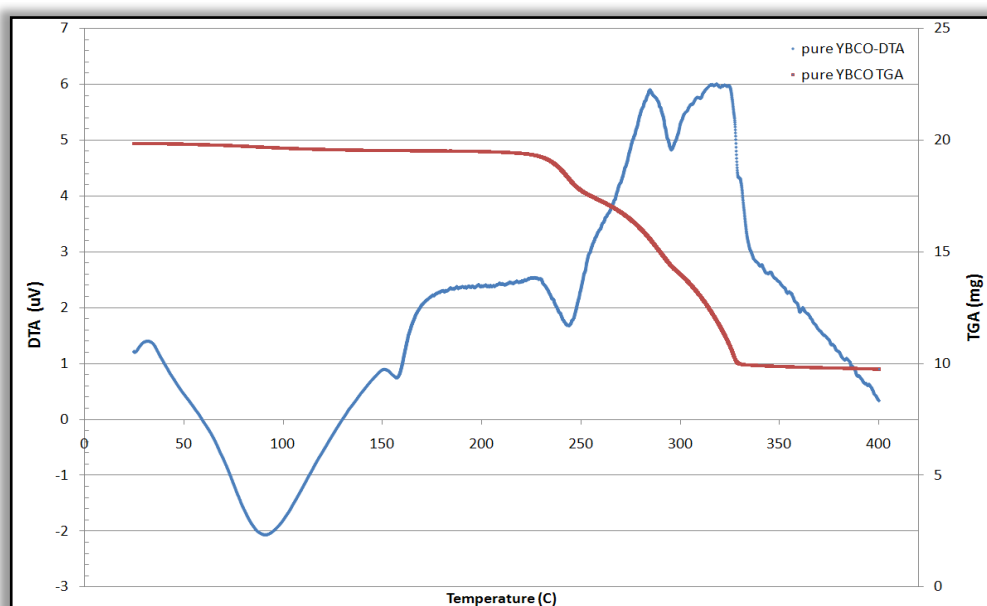
(a)
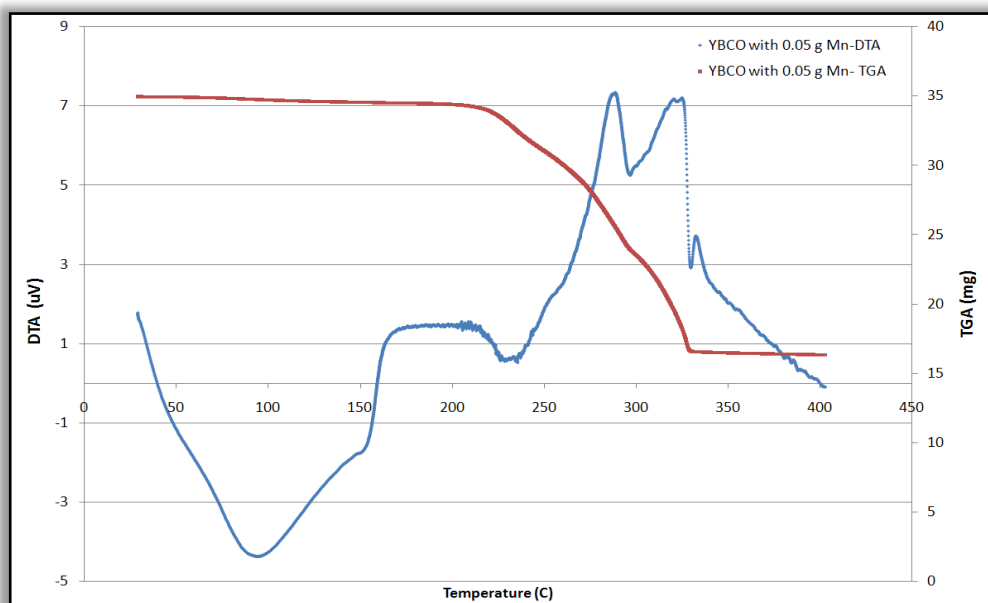
(b)
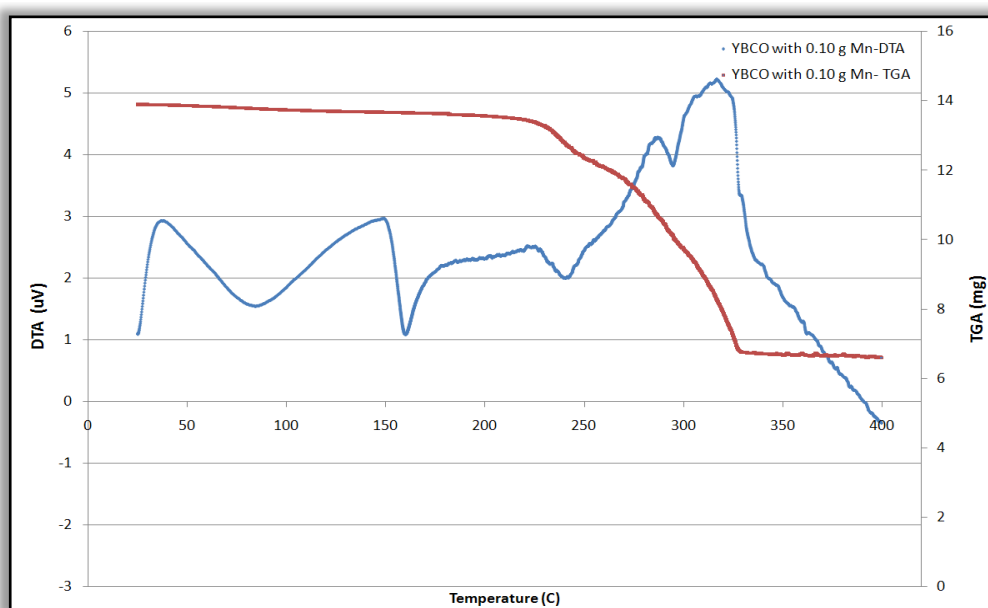
(c)
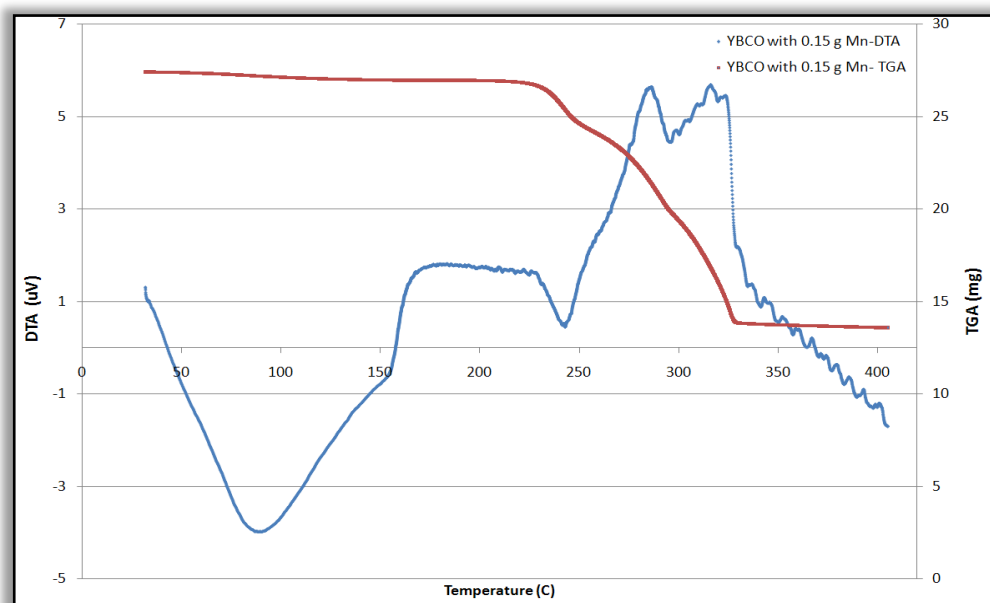
(d)

Figure 4.9 DTA and TGA analysis of a) pure YBCO, b) YBCO with 0.05 g Mn, c) YBCO with 0.10 g Mn and d) YBCO with 0.15 g Mn based powders produced at 200 °C for 3 hours.

4.2.2 FT-IR analysis

FTIR spectra are commonly used to identify specific substances like organic groups. The spectrum reflects the characteristic vibrations of certain bonds between particular groups of atoms. The FTIR spectra may also be employed to analyze the decomposition process of the organic gels if we collect the spectra at different stages of the process. The resulting spectra produce a profile of the sample, a distinctive molecular fingerprint that can be used to easily screen and scan samples from many different components. It is an effective analytical instrument for detecting functional groups and characterizing covalent bonding information. YBCO based solutions were dried at 200 °C and 3 hour have some information about the decomposition of YBCO layers during thermal treatments. The pelleting technique was used to prepare the samples. The powders were ground into a KBr matrix in the ratio of 1 mg sample to 150 mg KBr. The FTIR absorbance spectra of pure YBCO and YBCO with Mn addition based powder recorded as 4000-650 cm^{-1} with 4 cm^{-1} resolution as represented in Figure 4.10. According to the produced peak from YBCO based

powders, CO_2 based peaks emerged at 2356 cm^{-1} wave number which came from atmosphere and heat treated material. Furthermore, C=O based peaks appeared at near 1660 cm$^{-1.}$ Nonsymmetrical CO_2^{-1} ion and δ-CH_3 based absorbance peak came forward 1550 cm^{-1}and 1450 cm^{-1} wave number, respectively. The low intensity peaks produced from M-O bonding appeared near 1100cm^{-1}. Y_2O_3 phases, Ba-O and Y-O stresses could be determined under 854 cm^{-1}, 800 cm^{-1} and 730 cm^{-1} wave numbers, respectively.
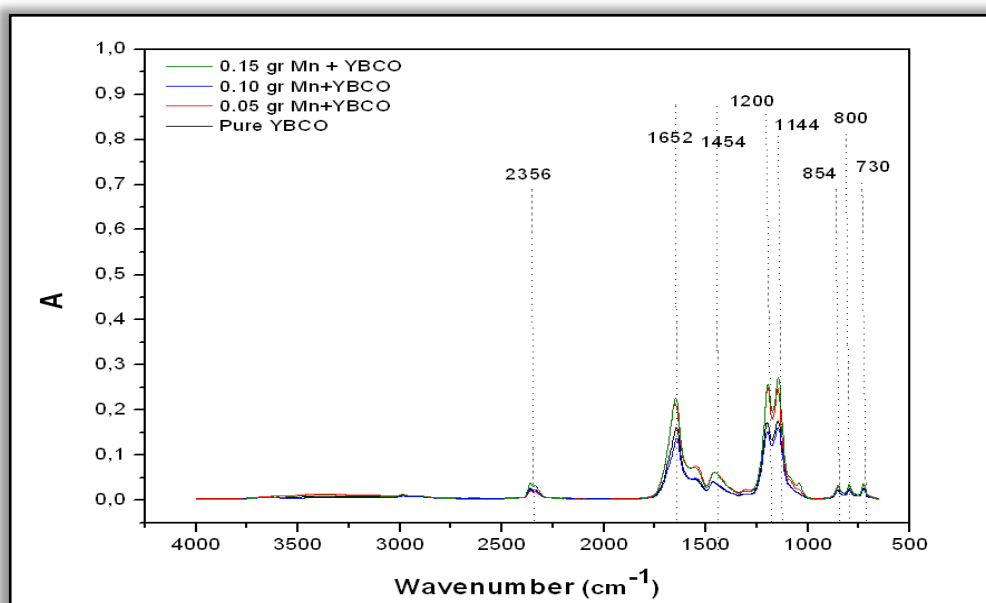
Figure 4.10 FT-IR analysis of YBCO based powders produced at 200 ^{o}C for 3 hours.

4.3 Thin Film Properties

4.3.1 Phase Analysis

Figure 4.11 showed the XRD patterns of pure YBCO, YBCO with 0.05 g, 0.10 g and 0.15 g $BaMnO_3$ nanoparticles on STO single crystal substrate by TFA-MOD method, respectively. XRD patterns showed that YBCO films have (001) and parallel plane reflections for pure YBCO thin film. The major diffraction peaks corresponding to the (00l) parallel plane was developed. It is worth mentioning that YBCO films with high intensity were grown on STO substrate by TFA-MOD

method. In addition, no second phases such as $Y_2Cu_2O_5$, BaF_2, and CuO were found, where upon only pure YBCO phase formed. Apart from that, $BaMnO_3$ preovskite peaks with low intensity were determined on account of Mn doping effect. However, XRD peaks from $BaMnO_3$ preovskite second phase were hardly detected even for the film that prepared using a precursor solution containing 0.15 g Mn dopant. In general, the overall reaction for the decomposition of the precursors and the formation of YBCO phase can be given as the following reaction;
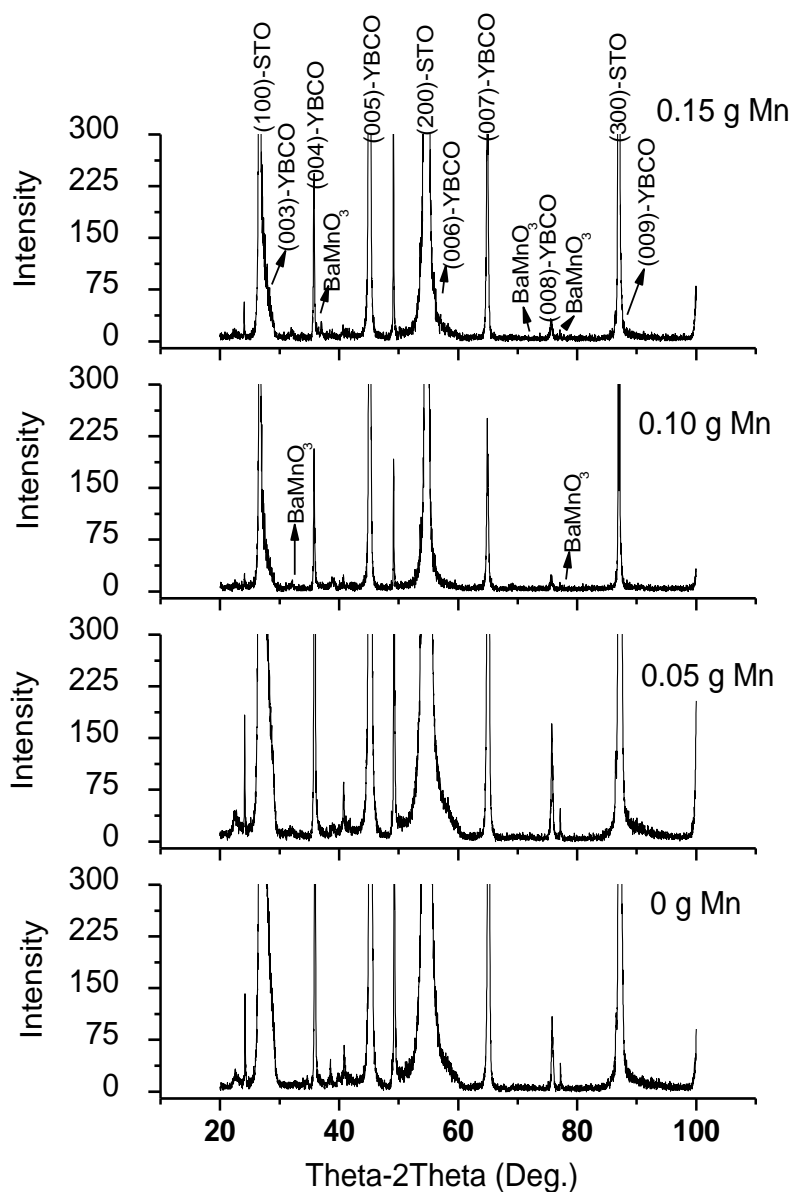
Figure 4.11 XRD phase analysis of YBCO based films

$$\frac{1}{2}Y_2Cu_2O_5(s) + 2BaF_2(s) + 2CuO(s) + 2H_2O \rightarrow YBa_2Cu_3O_{6.5}(s) + 4HF(g) \qquad (4.1)$$
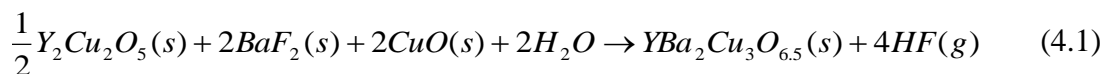
This reaction implies that $Y_2Cu_2O_5$, BaF_2, and CuO are converted into YBCO and HF when H_2O is supplied at the growth interface. Therefore, the formation of YBCO is limited during the firing process in a low humidity atmosphere (Lim et al., 2006). The diffraction patterns of the samples examined in this study did not change dramatically with Mn addition and $BaMnO_3$ formation. For all of the films produced under different Mn content, only the (00l) based paralel plane YBCO reflections were observed.

4.3.2 Microstructure

4.3.2.1 Scanning Electron Microscopy (SEM) Analysis

Figure 4.12, 4.13, 4.14 and 4.15 showed SEM micrographs of pure YBCO and YBCO films with $BaMnO_3$ nanoparticles prepared by TFA-MOD technique. Figure 4.12 illustrated surface topographies of pure YBCO film with a-axis which decrease superconducting properties. These films were produced using the standard YBCO transparent solution. However, decreasing superconducting properties with a-axis were eliminated using Mn doping in the standard YBCO precursor solution as clearly depicted in Figure 4.13, 4.14 and 4.15. SEM micrographs indicate that structural defects can be reacted as nanodots or nanoparticles (due to Mn addition) along the *c*-axis of YBCO film. These properties result in the enhanced pinning over the pure YBCO film. Since Mn reacts with Ba and $BaMnO_3$ preovskite structure forms in YBCO film during heat treatment process, microstructure of superconducting thin films were changed, as expected.
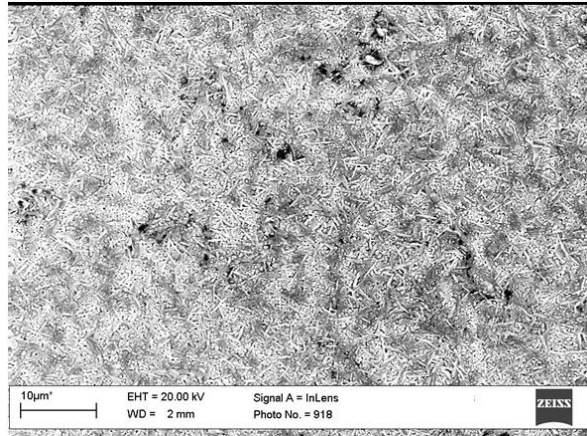
(a)
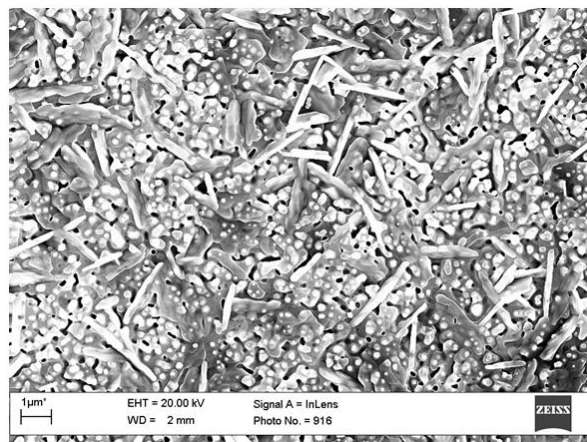
(b)

Figure 4.12 Surface topographies of pure YBCO film with a-axis produced using the standard YBCO transparent solution.
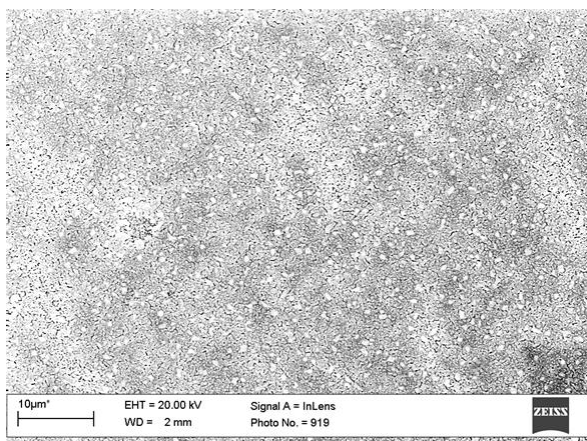
(a)
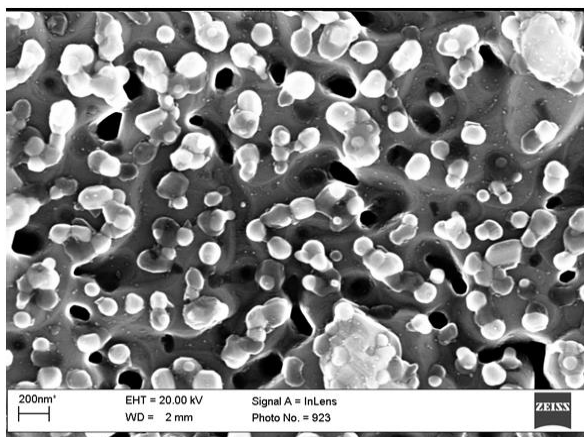
(b)

Figure 4.13 Surface topographies of YBCO film with BaMnO$_3$ nanoparticle produced using the YBCO transparent solution with 0.05 g Mn doping.
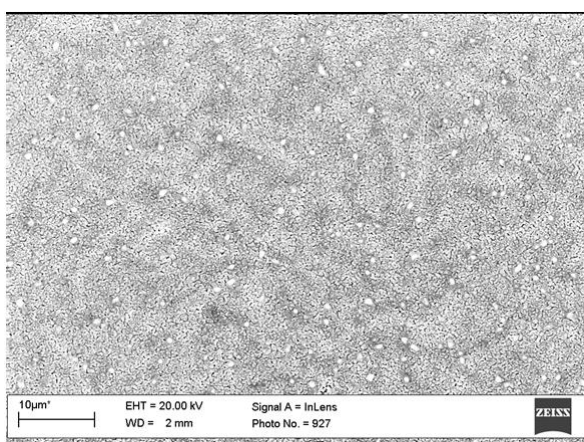
(a)
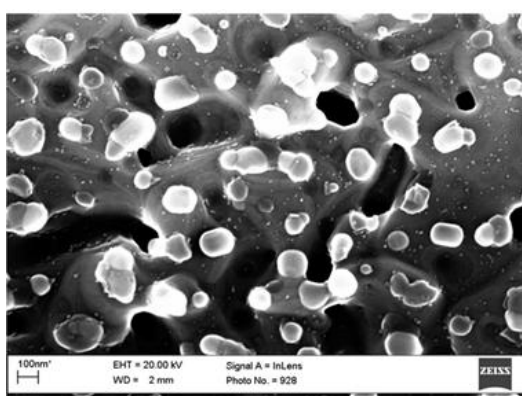
(b)

Figure 4.14 Surface topographies of YBCO film with BaMnO$_3$ nanoparticle produced using the YBCO transparent solution with 0.10 g Mn.
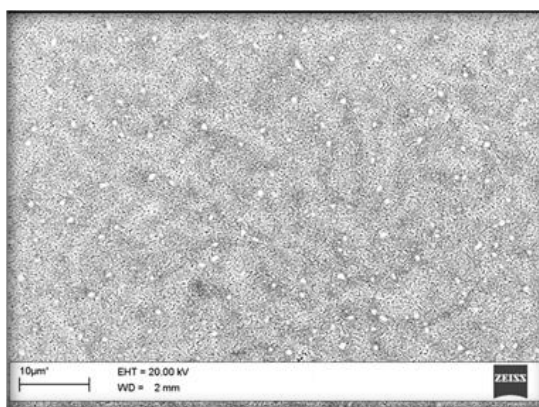
(a)
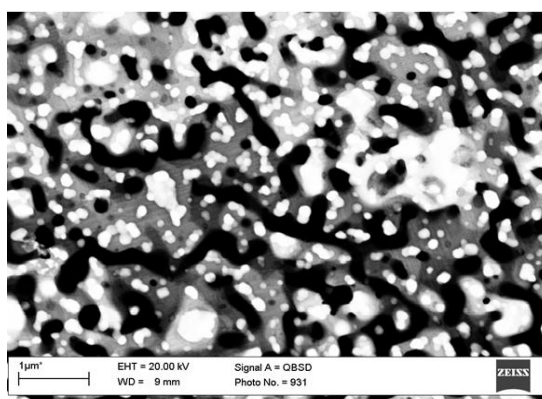
(b)

Figure 4.15   Surface topographies of YBCO film with BaMnO$_3$ nanoparticle produced using the YBCO transparent solution with 0.15 g Mn.

4.4.2.2 Atomic Force Microscopy (AFM) Analysis

The effects of BaMnO$_3$ nanoparticles in microstructure of YBCO thin films were identified in AFM images as shown in Figure 4.16. All films show typical CuO$_x$ precipitatates of 100-200 nm diameters, which regularly found on surface of TFA-MOD samples. When the Mn content increased from 0 g to 0.15 g, surface roughness values of pure YBCO thin films and YBCO thin films with BaMnO$_3$ nanoparticles changed from 14 nm to 22 nm depending on Mn doping content. Nevertheless, a clear change of YBCO surface was observed.
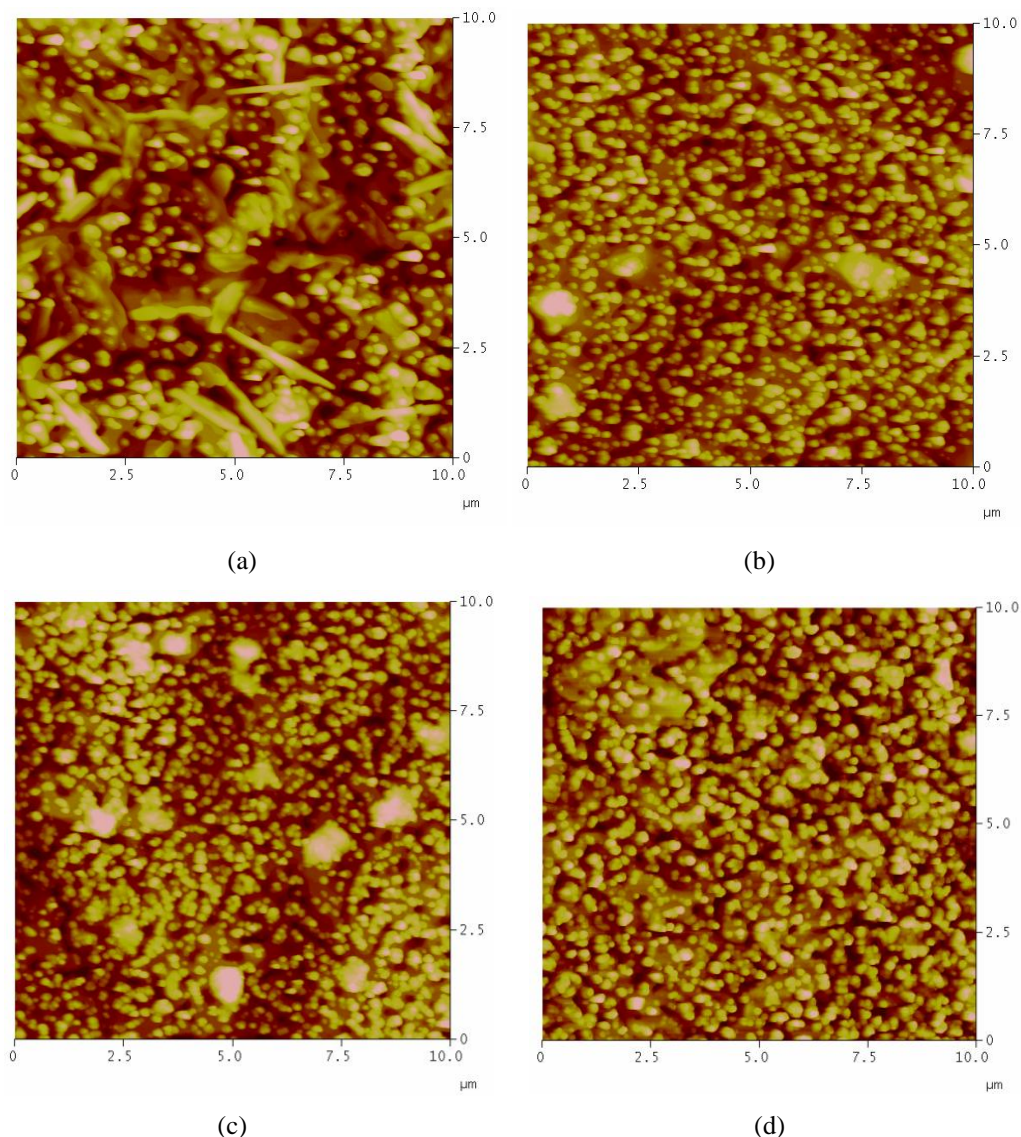
Figure 4.16 AFM micrographs of YBCO films depending on (a) 0 g, (b) 0.05 g, (c) 0.1 g and (d) 0.15 g Mn content in YBCO films.

4.4 Superconducting Properties

Transition temperature (T_c) was determined using an induction method and a criterion of 90 % increase in induced voltage during sample heating. The films were photolithographically patterned and structured using Ar^+ ion etching. Electrical transport properties were studied using four-probe geometry on bridges of 50 μm width and 0.8 mm length in magnetic fields up to 9 T using a Quantum Design PPMS. The critical current density J_c was defined with an electric-field criterion of 1

μVcm^{-1}. Figure 4.17 depicted inductively T_c and ΔT_c curves of 0 g, 0.05 g, 0.10 g and 0.15 g Mn doping YBCO films prepared on STO substrates by TFA-MOD technique. It can be seen that there is sharp decrease in resistivity near 90 K where critical temperature value of pure YBCO is 90.4 K. When the quantity of additional particles increased from 0.05 g to 0.15 g, critical temperature did not change clearly.
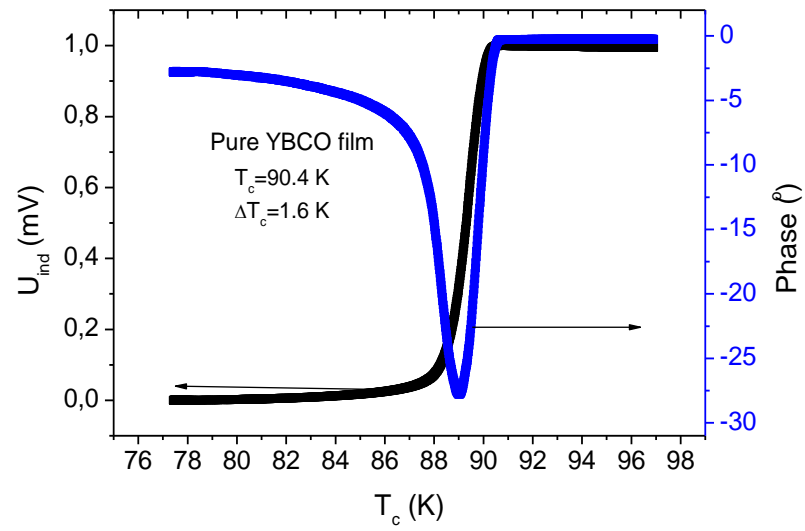
(a)
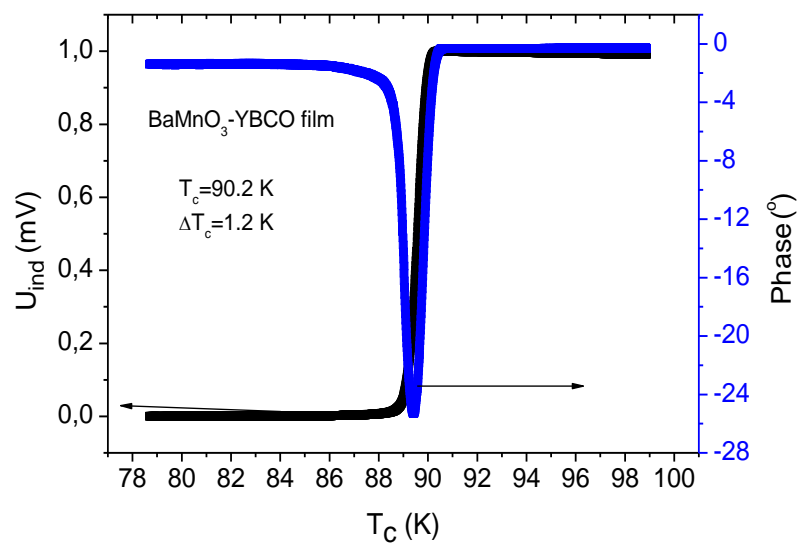
(b)
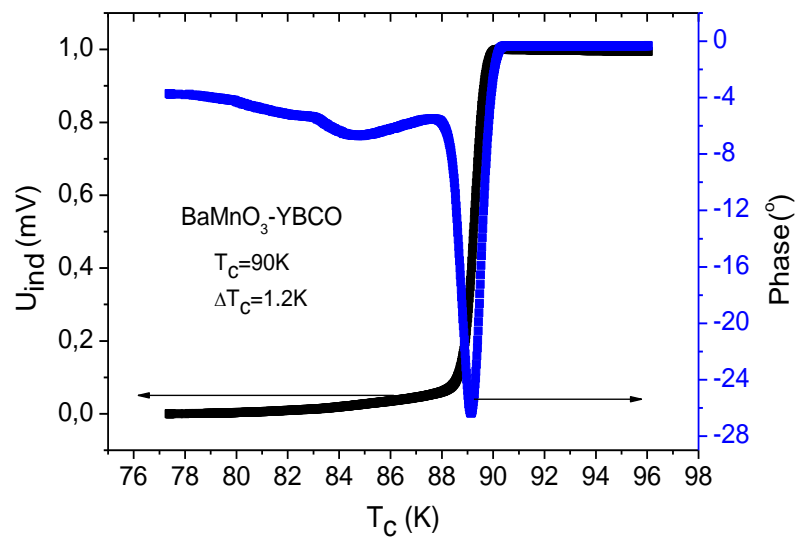
(c)
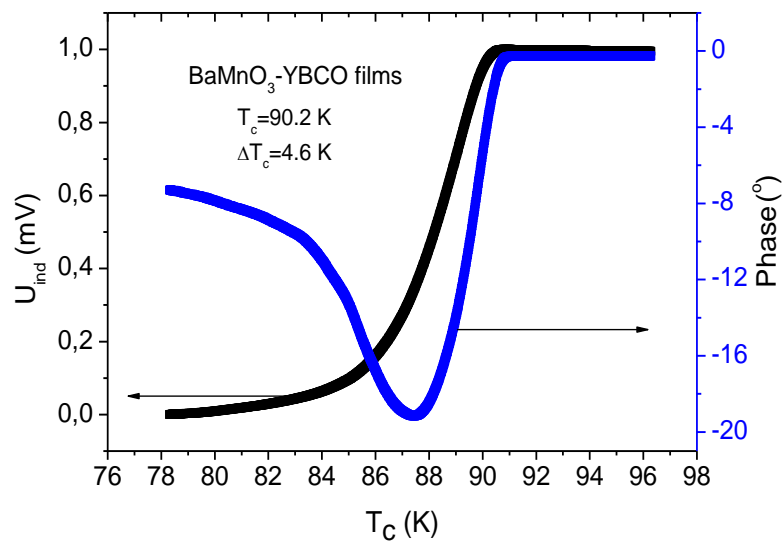
(d)

Figure 4.17 Critical temperature (T_c) and ΔT_c values of (a) 0 g, (b) 0.05 g, (c) 0.10 g and (d) 0.015 g Mn doping YBCO films prepared on STO substrates by TFA-MOD technique.

4.5 Mechanical Properties

4.5.1 Characteristic Loading-Unloading Curves of YBCO Based Thin Films

Thin films are increasingly used in a wide variety of technologies ranging from microsystems packaging to cutting tool coatings. For example, in microsystems packaging, thin films are used to fabricate multi-layered thin-film build-up substrates as well as chip-to-substrate interconnects. The semi and superconductor thin-film based technologies provide higher performance, higher density and smaller overall size to the microsystems package. Although thin films are increasingly used for performance, functionality, and size reasons, the mechanical behavior of the thin films is important to understand to address reliability concerns. In order to understand, predict and improve the reliability of microelectronic devices containing thin films, it is necessary to characterize the mechanical properties of thin films. As explained in chapter 2, one of the challenges in studying mechanical properties of thin films is that the traditional methods used to evaluate mechanical properties of bulk materials are not applicable for thin films and so far there is no standard test method for the evaluation of mechanical properties of thin films. However, depth-sensing nanoindentation technique provides a continuous record of variation of indentation load with penetration depth into the specimen and this technique has been an area of considerable attention in recent years due to its high resolution at low load scale.

High-T_c superconductor's thin films are important for high critical current density and trapping of high magnetic fields. In addition to its electrical and magnetic properties, they must also have good mechanical performance for actual technological applications. HTS needs to possess very high critical current density (J_c) values at low temperature even in high magnetic fields. The J_c values rapidly decrease with increasing temperature in magnetic field due to the lack of effective pinning centers in structure. With this regard, in this study, increasing J_c and improvement of flux pinning properties of YBCO films with different quantity BaMeO$_3$ perovskite nanoparticles (Me:Mn), as pinning centers, on SrTiO$_3$ (STO) are

aimed by trifluoroacetic acid-metal organic deposition (TFA-MOD). Since the general purpose is to determine the mechanical properties such as Young's modulus and hardness of pure YBCO thin film and YBCO thin films with Mn (Mn reacts as $BaMnO_3$) addition, instrumented nanoindentation test was used. At this time, importance of applied load is appeared. The indentation response of YBCO based thin films on STO substrate is a complex function of the elastic and plastic properties of both film and substrate and it is critical to understand how the intrinsic mechanical properties of the film can be determined from the overall mechanical response of the film/substrate system. So that the values of elastic modulus and hardness, determined from indentations, do not depend on the value of *h (indentation depth)* and, therefore, on the value of the maximum load, the indentation depth should not exceed 10-20 % of the film thickness, otherwise the results will be affected by the properties of the substrate. Another parameter, which can be influence the indentation test, is surface roughness. It has very active role in indentation experiment in nano scale. If the surface roughness is bigger than maximum indentation depth for applied load, curve has very scattered loading and unloading part. According to the AFM analysis, surface roughness of pure YBCO thin film is 21 nm ± 5.

As represented in Table 4.3, ratio of indentation depths and film thicknesses are applicable for instrumented indentation for 300 μN applied load. Smoothing procedure was applied all of the instrumented indentation results of samples. The loading-unloading (load–displacement) curves of pure YBCO films under 300 μN applied peak load were shown in Figure 4.18 in nanometric scale for 3 times and total test time is 60 s. Additionally, force-time and depth-time graphs of pure YBCO thin film were determined. Maximum indentation depth, residual depth and elastic recovery rate of pure YBCO thin film were 40.24 nm, 30.12 nm, and 25.14 %, respectively. Ratio of indentation depth to film thickness of pure YBCO thin film was 13.78 %. Furthermore, elastic modulus and instrumented hardness of pure YBCO thin films were calculated as 88.54 ± 3.1 GPa and 12.51 ± 5.1 GPa under 300 μN applied load. Loading and unloading part of curves have some fluctuations due to surface roughness of pure YBCO thin film. For that reason standard deviations were

added all indentation test characteristics, such as maximum indentation depth, residual depth, elastic modulus and instrumented hardness of pure YBCO thin film.
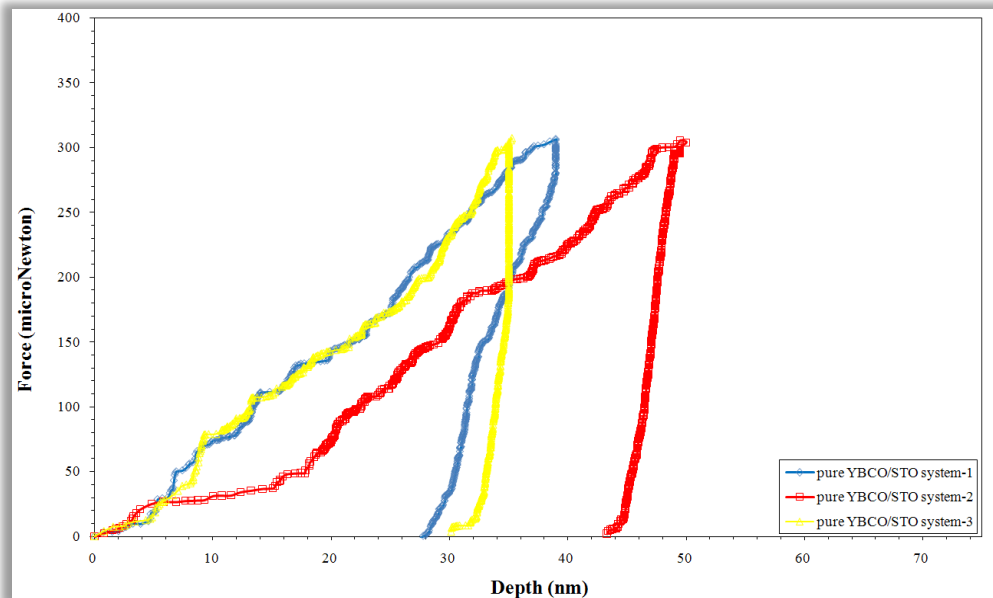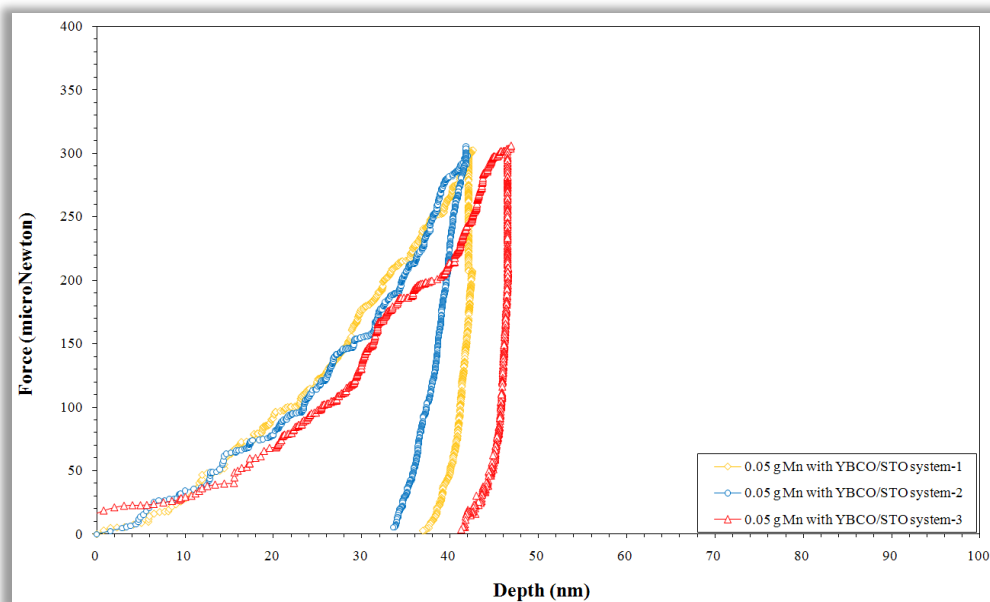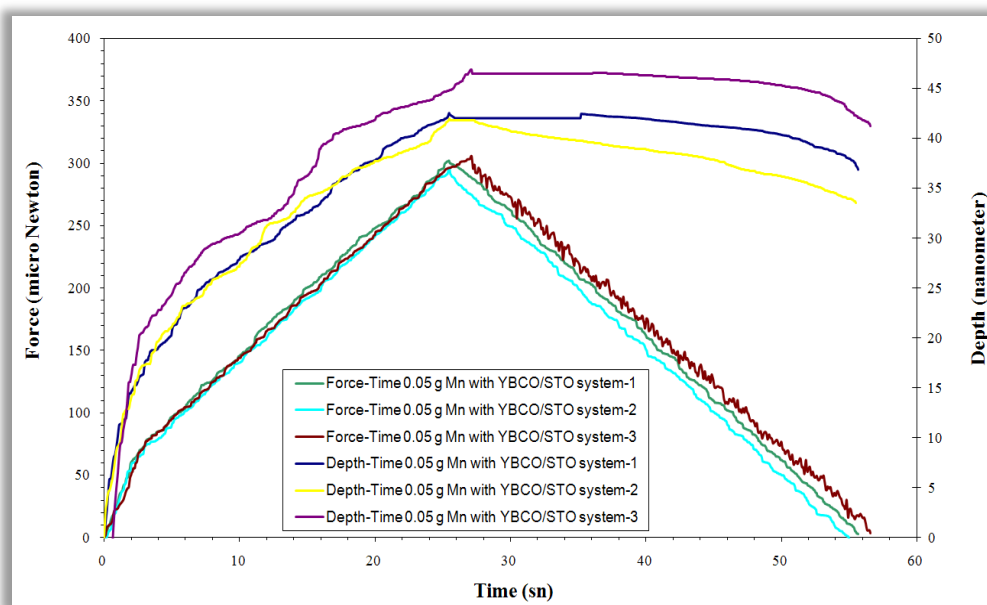

(a)
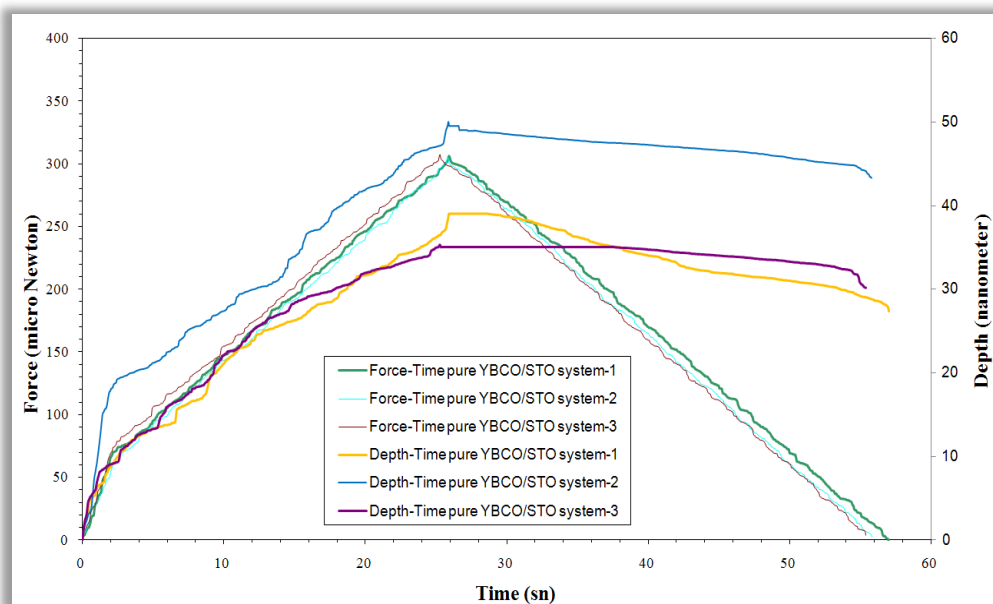
(b)

Figure 4.18 (a) Loading and unloading curves of pure YBCO thin film under 300 μN applied load and (b) Force-Time-Depth graphs of pure YBCO based thin films.

As known, flux pinning in YBCO thin films can be engineered by materials processing. Columnar defects, second phase, and antiphase boundaries provide extended linear defects as strong pinning centers. Currently, a few other methods to increase flux pinning have been realized for YBCO films. These are; including multilayering of YBCO with second-phase materials, mixed rare-earth doping, target compositional modifications either by second phase $BaMeO_3$ (Me:Mn in this study). The main reasons for the choice of $BaMeO_3$ are; (a) while it can grow heteroepitaxially with YBCO, it has a large lattice mismatch (~9%) so strain between the phase could introduce defects for enhanced pinning, (b) it is a high melting temperature phase and so growth kinetics should be slow, leading to small particles, and (c) Me does not substitute in the YBCO structure. It is important to control the doped defect density. A defect density which is too high will inevitably degrade superconductivity, and a balance between the increased pinning strength and loss of superconductivity must be found by optimizing the dopant concentration. The pinning centers, in order to be effective, need to be nanoparticles, less than 10 vol. % of the superconductor, and be randomly distributed to provide isotropic 3-dimensional pinning. A defect density which is too high will inevitably degrade superconductivity, and a balance between the increasing pinning strength and loss of superconductivity must be found by optimizing the dopant concentration. Thus, four different compositions was prepared and produced by sol-gel method as pure YBCO, YBCO with $BaMnO_3$ particles. Since the formation of second phase, porosity in microstructure of pure YBCO and YBCO with $BaMnO_3$ particles and roughness was occurred, instrumented indentation of film fluctuated with increasing penetration depth at applied peak loads. The loading-unloading (load–displacement) curves, force-time and depth-time of graphs of YBCO films with 0.05 g Mn (react as a $BaMnO_3$) under 300 μN applied peak load were shown in Figure 4.19 Maximum indentation depth, residual depth and elastic recovery rate of YBCO thin film with 0.05 $BaMnO_3$ were listed in Table 4.3 as 42.31 nm, 32.11 nm, and 24.10 %, respectively. Characteristic depth and thickness ration of YBCO thin film with 0.05 g Mn addition was 14.14 %. Furthermore, elastic modulus and instrumented hardness of YBCO thin films with 0.05 g Mn addition were calculated as 83.41 ± 1.8 GPa and 8.21 ± 1.2 GPa under 300 μN applied load. As mentioned for pure YBCO thin film,

loading and unloading part of curves have some fluctuations. For that reason standard deviations were added. Additional pop-in effects on loading part of curves can be seen easily. This can be due to additional particles and defects in YBCO microstructure.
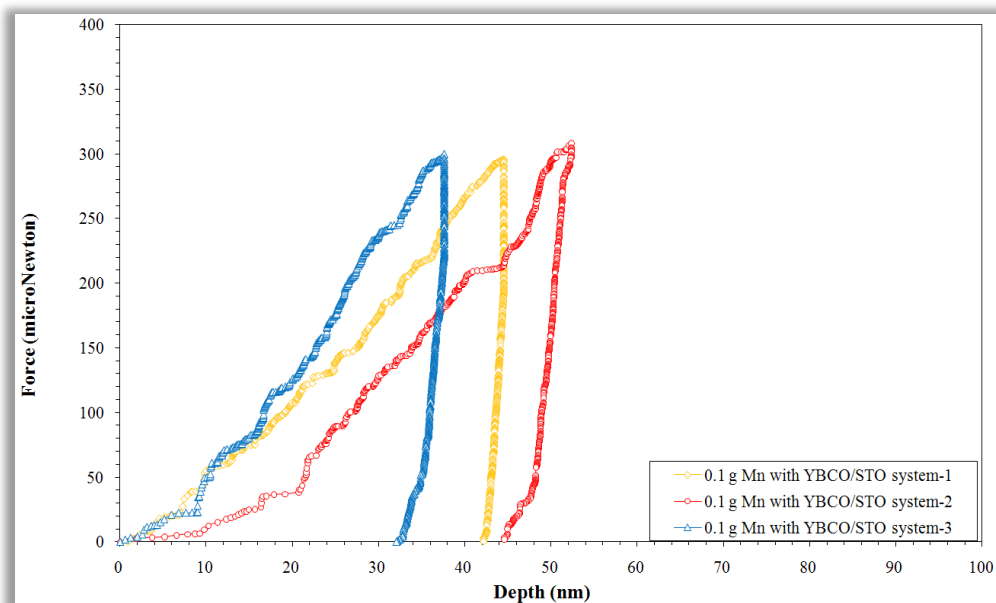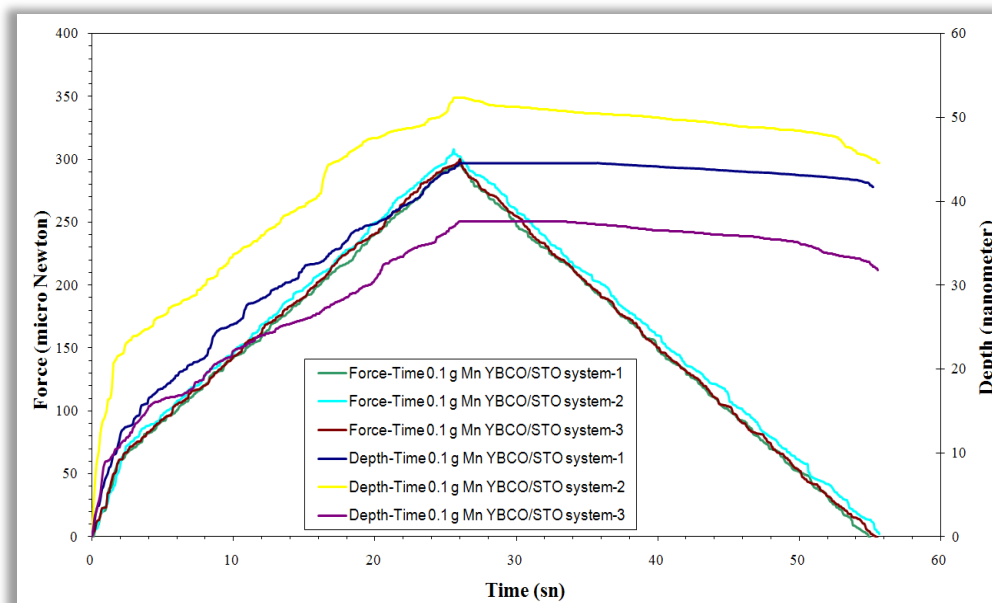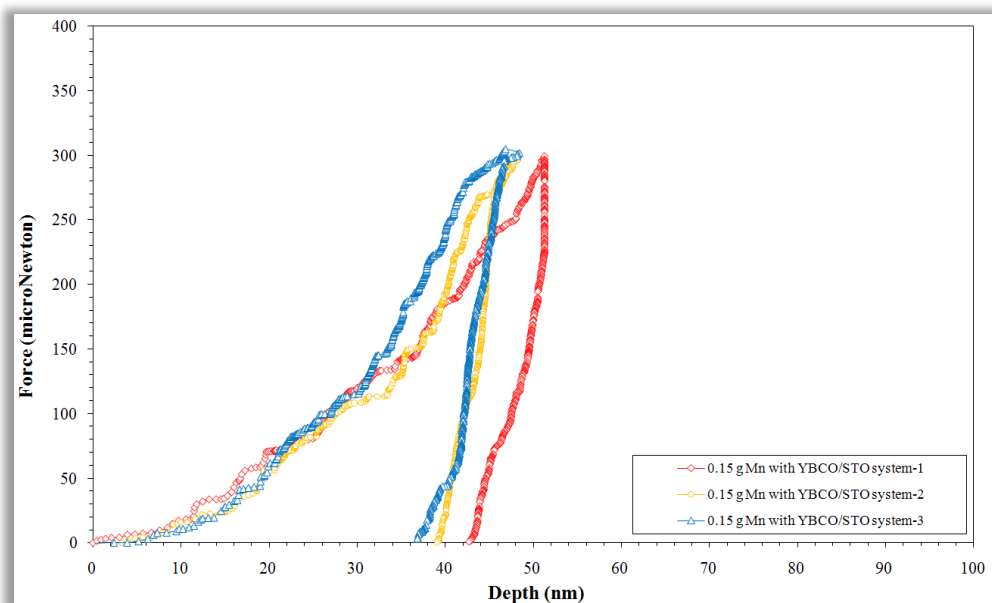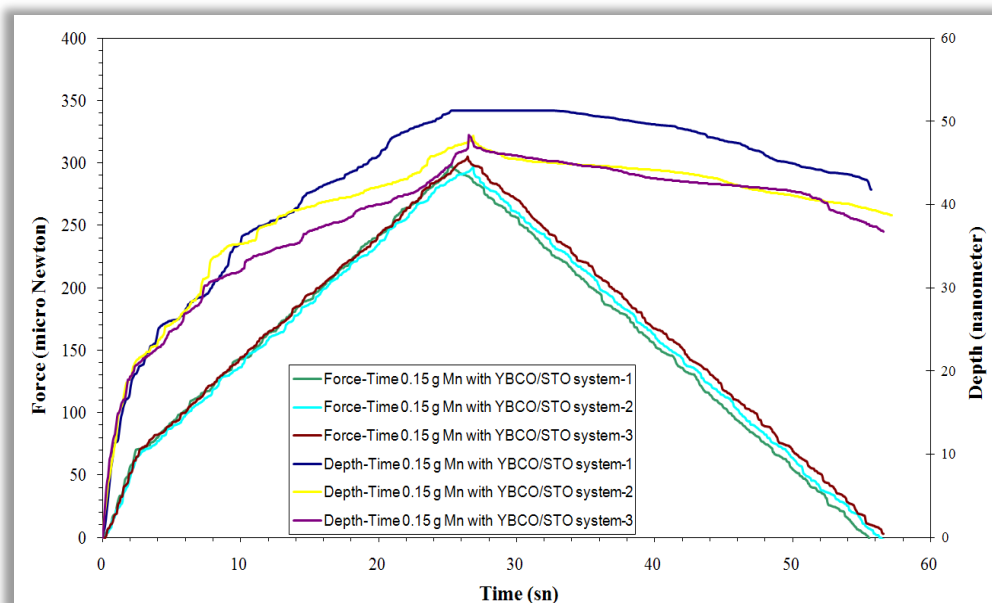

(a)

(b)

Figure 4.19 (a) Loading and unloading curves of YBCO thin film with 0.05 g Mn (reacted as BaMnO$_3$ particles) under 300 μN applied load and (b) Force-Time-Depth graphs of pure YBCO based thin films.

The indentation curves, force-time and depth-time graphs of YBCO films with 0.1 g Mn under 300 µN applied peak load were shown in Figure 4.20. Maximum indentation depth, residual depth and elastic recovery rate of YBCO thin film with 0.1 g Mn illustrated in Table 4.3 as 42.45 nm, 33.53 nm, and 21.01 %, respectively. Limiting ratio of indentation depth and film thickness was 14.43 %. Furthermore, elastic modulus and instrumented hardness of YBCO thin films with 0.10 g Mn addition were calculated as 79.11 ± 1.9 GPa and 5.75 ± 1.1 Gpa under 300 µN applied load.

Generally speaking, when the additional particles in microstructure of YBCO thin film were increased from 0.05 g to 0.1 g, elastic modulus and hardness were changed as listed in Table 4.4. However, as the indentation results of YBCO thin films with additional particles compared by pure YBCO thin films, maximum indentation and residual depth were increased from 40.24 nm to 42.45 nm and 30.12 nm to 33.53 nm, respectively. In addition, elastic modulus and hardness were decreased systematically from 88.54 GPa to 79.11 GPa and 12.51 GPa to 5.75 GPa. These values were reasonable according to the instrumented indentation theories and flux pinning properties of superconducting thin films.

(a)

(b)

Figure 4.20 (a) Loading and unloading curves of YBCO thin film with 0.10 g Mn (reacted as BaMnO$_3$ particles) under 300 µN applied load and (b) Force-Time-Depth graphs of pure YBCO based thin films.

The characteristics indentation curves of YBCO films with 0.15 g Mn under 300 µN applied peak load were shown in Figure 4.21. Maximum indentation depth, residual depth and elastic recovery rate of YBCO thin film with 0.15 g Mn illustrated in Table 2.2 as 47.04 nm, 37.48 nm, and 20.32 %, respectively.

Furthermore, elastic modulus and instrumented hardness of YBCO thin films with 0.15 g Mn addition were calculated as 76.47 ± 1.3 GPa and 3.88 ± 0.8 GPa under 300 µN applied load as listed Table 4.4. Indentation curves were stabile due to the increases of indentation depth. According to the limiting theory of indentation depth in thin film applications, ratio of indentation depth and film thickness must not be over the 10-20 %. For YBCO thin film with 0.15 g Mn, this ratio was approximately 15.04 %.

(a)

(b)

Figure 4.21 a) Loading and unloading curves of YBCO thin film with 0.15 g Mn (reacted as BaMnO$_3$ particles) under 300 μN applied load and b) Force-Time-Depth graphs of pure YBCO based thin films

Table 4.3 Maximum, residual depth and film thickness of pure YBCO and YBCO with additional particles

Material	Force (micro N)	Maximum depth (nm)	Residual depth (nm)	Film thickness (nm)	% ERR
YBCO	300	40.24 ± 6.4	30.12 ± 7.8	292 ± 9	25.14
YBCO with 0.05 g Mn	300	42.32 ± 9.4	32.11 ± 8.7	297 ± 5	24.12
YBCO with 0.10 g Mn	300	42.45 ± 5.9	33.53 ± 4.4	294 ± 6	21.02
YBCO with 0.15 g Mn	300	47.04 ± 6.1	37.48 ± 5.7	305 ± 8	20.32

Table 4.4 Indentation experiments results of pure YBCO and YBCO with additional particles

Material	Force (micro N)	Hardness (HV)	Indentation Hardness (GPa)	Young's Modulus (GPa)
YBCO	300	695 ± 28	12.51 ± 4.8	88.54 ± 3.1
YBCO with 0.05 g Mn	300	525 ±16	8.21 ± 1.2	83.41 ± 1.8
YBCO with 0.10 g Mn	300	495 ± 21	5.75 ± 1.1	79.11 ± 1.9
YBCO with 0.15 g Mn	300	454 ± 18	3.88 ± 0.8	76.47 ± 1.3

According to the Figure 2.28, which represented the classical loading-unloading curve of materials in chapter 2, gives the details about loading part. During loading, the curve generally follows the relation, $P = Ch^2$, where C is the indentation curvature which is a measure of the "resistance" of the material to indentation. C is important parameter for materials. If the C constant is higher, penetration of indenter to the surface of material is more difficult. So it means that resistance of material is very high and material is very hard. C constant values of Pure YBCO and YBCO with additional particles showed in Figure 4.22 According to the graph, when the additional particles quantity was increased from 0 g to 0.15 g, C constant was decreased from 0.20 μN / nm² to 0.14 μN / nm². On the other hand, as mentioned above, when the additional particles quantity increased, maximum indentation depths of thin films were increased. Decreasing C constant by additional particles caused increasing indentation depth, systematically.
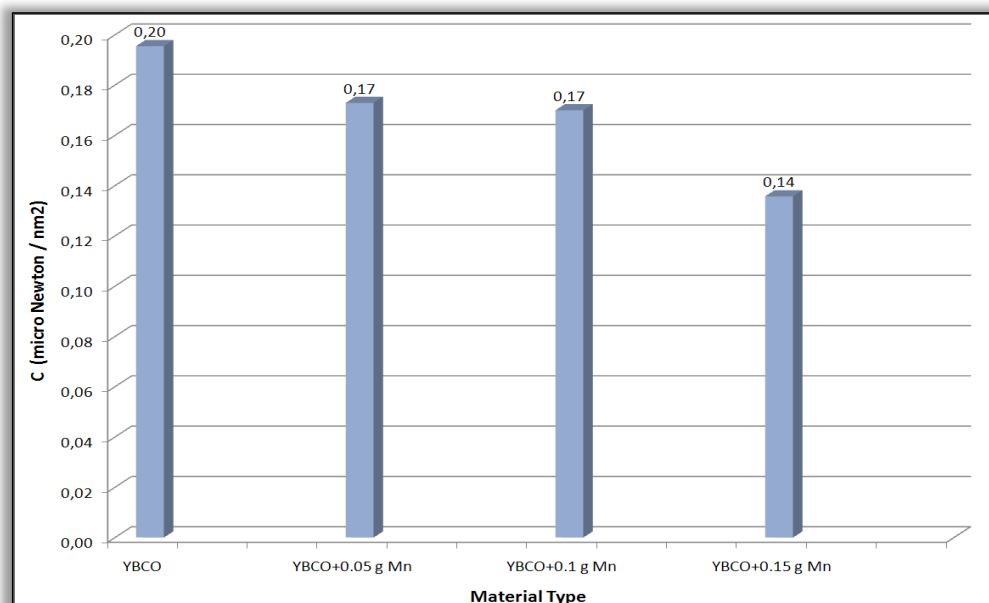
Figure 4.22 *C* constant values of YBCO based thin films

As mentioned chapter 2, Giannakopoulos and Suresh had theories about indentation depth and apparent area. Most of these applications of instrumented indentation are limited, however, by complications in clearly interpreting the indentation results. Such a complication arises from the "pile-up" or "sink-in" of the material around the indenter, which is primarily affected by the plastic properties of the material. According to the indentation experiment and numerical solution, pile-up occurs when $0.875 < (h_r/h_{max}) \leq 1$ and sink-in occurs when $0 \leq (h_r/h_{max}) < 0.875$. Pure YBCO and YBCO with additional particles showed great variation of maximum and residual depth under 300 μN applied load. Maximum indentation depth changed from 40.24 nm to 47.04 nm and residual depth altered from 30.12 to 37.48 nm. So, ratio of residual depth and maximum indentation depth changed from 0.74 to 0.79 depend on Mn addition under same applied load, as represented in Figure 4.23 with maximum, residual and contact depth variations. All YBCO based thin film with additional particles demonstrated sink-in effect when the indenter penetrated to their surfaces.
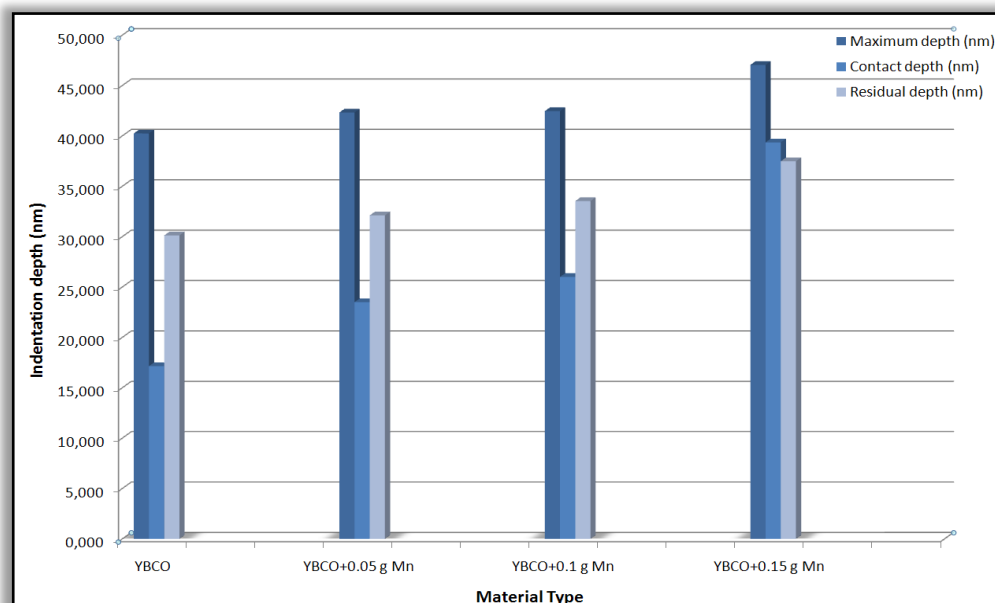
(a)
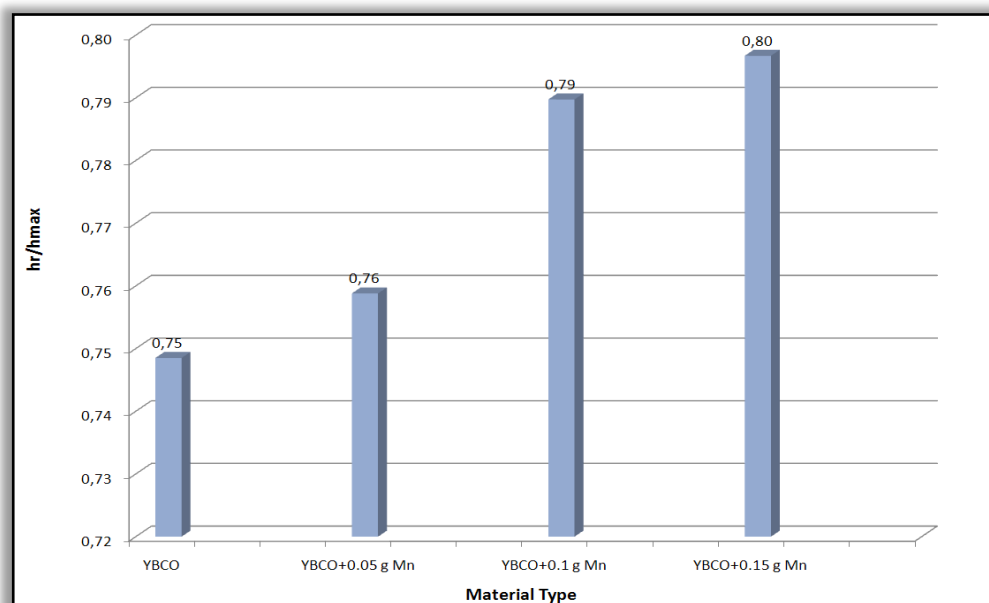
(b)

Figure 4.23 (a) Indentation depth analysis and (b) h_r/h_{max} ratio of YBCO based thin films

In addition, indentation hardness variation of YBCO based thin films was showed in Figure 4.24. It was seen that indentation hardness of films decrease with increasing Mn content. Depending on Mn content, maximum indentation depth, residual depth and indentation hardness were changed scientifically. Since the Mn content increased in microstructure of YBCO based films, intensity of $BaMnO_3$

phases in X-ray analysis increased. Furthermore both AFM and SEM analysis showed that $BaMnO_3$ phase structure dispersed and agglomerated each other in YBCO film structure. So, characteristic indentation curves of YBCO based thin films changed depend on Mn content-$BaMnO_3$phase structure.

As explained in chapter two and beginning of the indentation results, $BaMnO_3$ reacted as a defect and so pinning center in structure. When the defect concentration increased by increasing Mn content, stability of structure and interatomic bonding mechanism changed for particle doped YBCO based thin film. As expected, second phase formation due to Mn addition was changed the microstructure. Although lattice parameter was much closed to YBCO, $BaMnO_3$ based structure in YBCO thin films cause some distortion (residual stress) and irregularity as shown in AFM results. Second phase, shown in SEM and AFM results, influenced the basically indentation hardness of films.
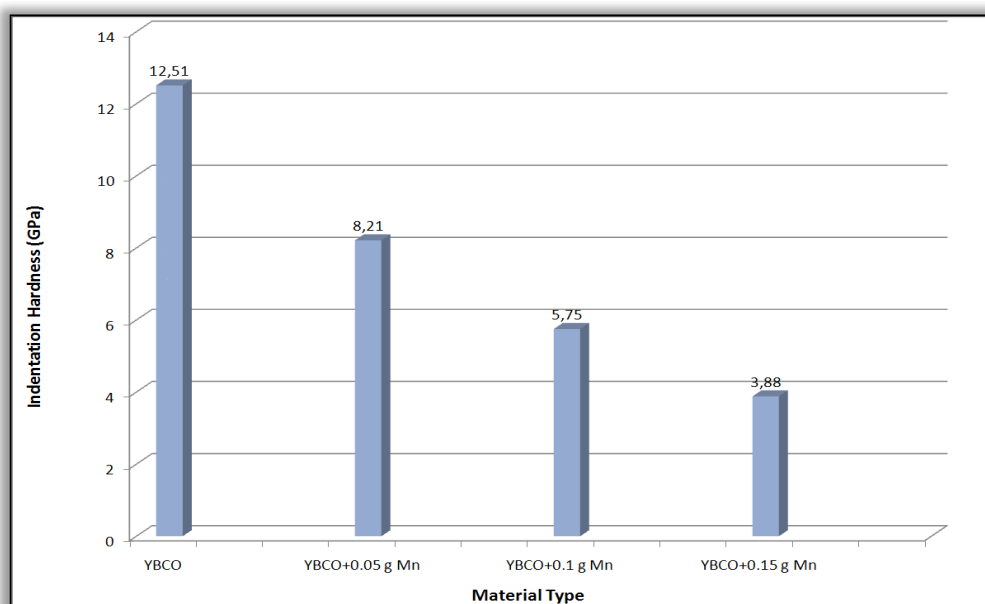
Figure 4.24 Indentation hardness variations of YBCO based thin films

Although indentation load was fixed at 300 μN, indentation hardness was decreased as if indentation size effect formation on mechanical properties. Since hardness is accepted as an inherent material property, it should not vary with indentation load and size but can change with different phase formation. Decrease in

hardness with increasing $BaMnO_3$ content in YBCO thin film structure caused from differences in indentation depth. According to this explanation, it can be exposed that pure YBCO thin film is harder and brittle than $BaMnO_3$ additional ones. As represented in Figure 4.24, indentation hardness of YBCO based thin films decreased from 12.51 GPa to 3.88 GPa depend on Mn content in structure.
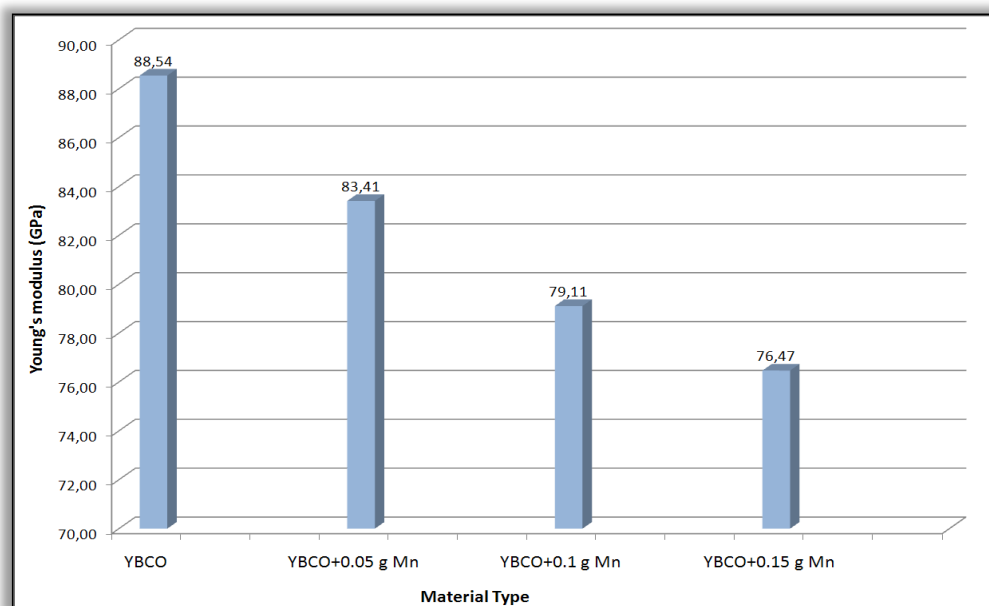

Figure 4.25 Young's modulus variations of YBCO based thin films

The elastic modulus variation of YBCO based thin films was demonstrated in Figure 4.25 Although hardness was very sensitive to the maximum indentation depth and thickness ratio of samples as represented in Figure 4.23 and changed from 12.51 GPa to 3.88 GPa, elastic modulus of YBCO based thin films did not show the sharp decrease scientifically. However, as listed in Table 4.4 elastic modulus of pure YBCO, YBCO with 0.05 g Mn, YBCO with 0.10 g Mn and YBCO with 0.15 g Mn measured 88.54 GPa, 83.41 GPa, 79.11 GPa and 76.47 GPa, respectively.

As explained, hardness and elastic modulus of YBCO based thin films considered together with AFM, SEM and critical temperature value, T_c, second phase of $BaMnO_3$ did not continuously improve the both mechanical and superconducting properties. When the Mn content increased from 0 g to 0.15 g, $BaMnO_3$ phases

occurred and made structure more ductile than pure one. According to the T_c measurement, sharp decrease on T_c could be considered and ΔT_c values of YBCO based films were very small until 0.15 g Mn addition. In this content, ΔT_c were 4.2 K for YBCO thin film with 0.15 g Mn addition ($BaMnO_3$) and sharp decrease on resistivity could not seen easily as represented Figure 3.17.

YBCO based thin film has suitable properties for ceramic materials, such as hardness and stiffness, together with tendency to fracture. However, references about the mechanical properties of this material particularly yield strength and stress–strain curve, are scarce. The mechanical properties (hardness, Young's modulus and fracture toughness) of YBCO samples have been examined with techniques such as ultrasound (Sandiumenge et al., 2000), X-ray diffraction (Block et al., 1987) and nanoindentation (Johansen, 2000). Reported values of Young's modulus for Y- 123 are within the range $E = 40$–200 GPa. This large scatter may be due to the residual porosity and poor contact between the grains (Ledbeddter et al.,1987).

Other authors, (Rao et al, 2007) also using nanoindentation, reported a value of $E = 171$–181 GPa for YBCO samples textured by the Bridgman technique, which is in agreement with Johansen, who applied between 30 and 100 mN. Nanohardness values in the range of 7.8–8.0 GPa at maximum loads of 30mN were recently reported by Lim and Chaudhri (2002) for bulk, single-crystal YBCO. Roa et al. (2007) found a hardness value of 8.9±0.1 GPa by nanoindentation on YBCO samples textured by the Bridgman technique.

4.5.2 Adhesion Properties

The analysis of scratch test gives critical force values of the produced films. These critical force values correspond to be the first peak in the cartridge output percentage – test force graphical curve obtained from scratch test machine. Bond strengths, critical force and Brinell hardness value of pure YBCO and YBCO with $BaMnO_3$ nanoparticles are presented in Table 4.5 and Figure 4.26. Hardness value of substrate was converted to Brinell Hardness (H) from Moh's to Brinell by using Standard

Hardness Conversion Tables; the adhesion strength (F) of the coatings was calculated as MPa unit. It is clearly seen from Table 4.5 that pure YBCO, YBCO with 0.05 g, 0.1 g and 0.15 g BaMnO$_3$ nanoparticle based thin film had 56 mN, 58 mN, 60 mN and 61 mN critical forces, respectively. In addition, calculated adhesion strength of films increased from 160 MPa to 175 MPa depend on BaMnO$_3$ addition due to increase in critical forces.

Table 4.5 Brinell hardness, critical force and bond strengths of YBCO and YBCO with Mn

Substrate	Brinell Hardness substrate (HB)	Indenter radius (μm)	Materials	Average Critical Force (mN)	Adhesion Strength (MPa)
STO	143	15	Pure YBCO	56 ± 1.2	160 ± 1.1
			YBCO with 0.05 g Mn	59 ± 1.8	168 ± 1.7
			YBCO with 0.1 g Mn	60 ± 1.6	173 ± 1.5
			YBCO with 0.15 g Mn	61 ± 1.4	175 ± 1.1
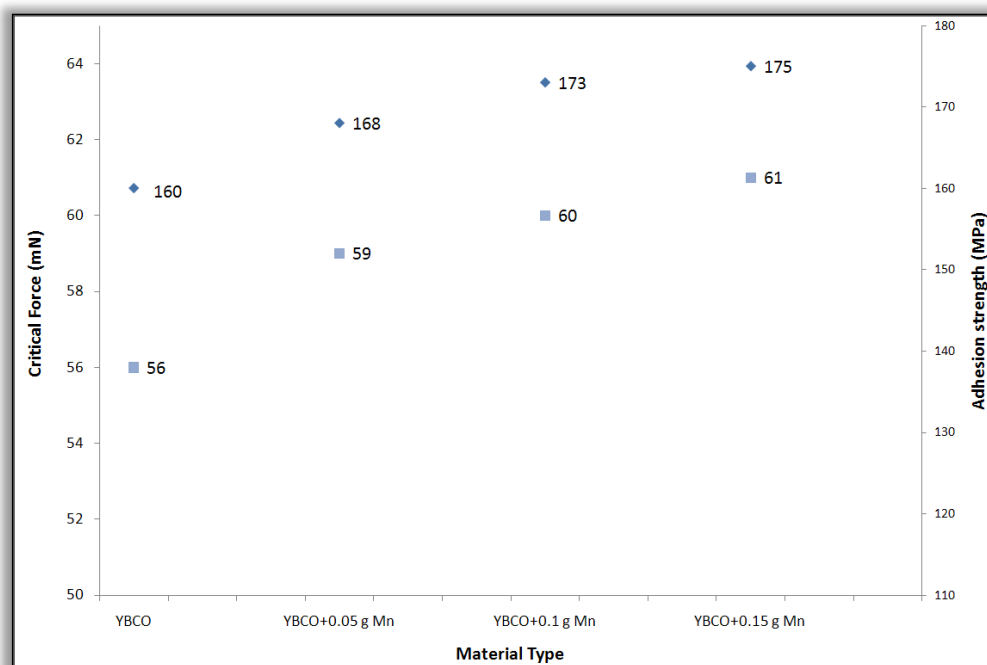
Figure 4.26 Critical force and adhesion strength of YBCO based thin films

4.6 Finite Element Modeling of Indentation Analysis

Numerical methods provide a suitable technique for analyzing nanoindentation experiments when multiple layers are present. Finite element analysis was performed with the commercial finite element software package ABAQUS, which is capable of modeling the contact between either two deformable bodies or one rigid body and another deformable body. ABAQUS defines contact between two bodies in terms of a contact pair with two surfaces: the master surface, and the slave surface. In order to achieve a flexible and reproducible model, the indentor, the coating and the substrate material properties as well as the penetration depth are variable and changeable parameters. The simulation of the nanoindentation test has been performed considering two load steps. The first load step, the so-called loading stage, represents the indentation phase into the coating. During the second load step, the so-called relaxation stage, the indentor cone is removed, leading to a material elastic-plastic recovery (Bouzakis, 2001).

FEM was performed with the commercial software package ABAQUS 6.6-1. The model was constructed with axial symmetry geometry as illustrated Figure 4.27. The indenter had a conical tip with semi-vertical angle of 70.3, which gives the same area-to-depth function as Berkovich and Vickers indenters. At the very tip of the indenter, a spherical rounding with a radius of 0.5 mm was constructed because of the fact that no real indenter can be ideally sharp. The indenter had a cylindrical body which was large enough to uniformly transfer the load from the top surface to the contact area. The material of the indenter was taken as diamond and assumed to be elastic with Young's modulus of $E_s = 1140$ GPa and Poisson's ratio=0.04 (Brookes, 1979).

4.6.1 Part Design of YBCO Based Thin Films

The Finite element modeling (FEM) technique was applied for studying the very complex stress-strain field of YBCO based thin film subjected to a nanoindentation process. In this study, Berkovich indentation experiments were simulated with the

ABAQUS finite element software package. As mentioned, the FEM systems were four different YBCO based thin films on STO single crystal substrate. The system was simulated by axisymmetric model in which the conical indenter has the same contact area as the Berkovich indenter.
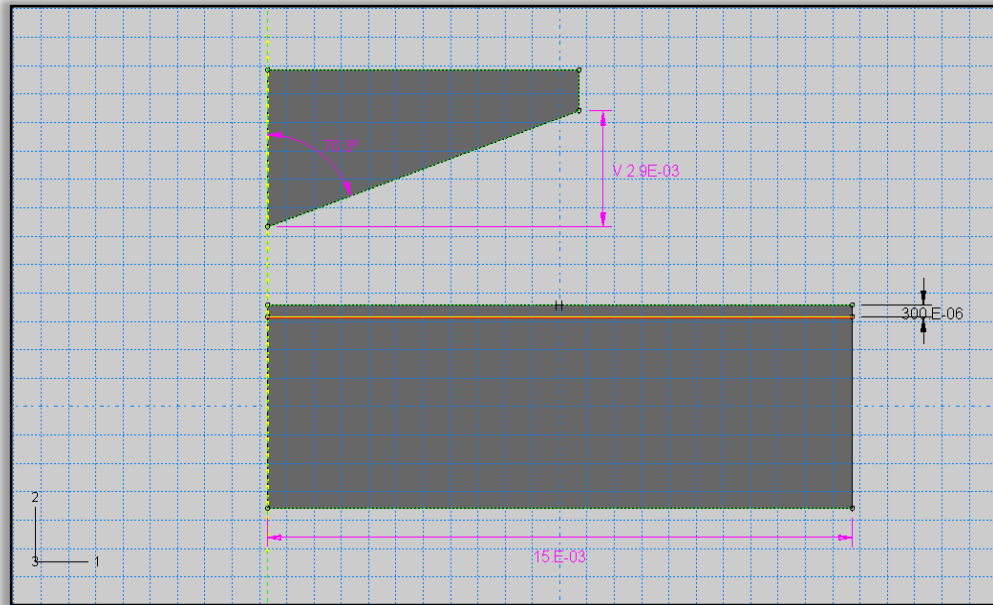
The indentation analysis of YBCO based thin films was started with design of axisymmetric model. A diamond conical surface with half apex angle of 70.3° was used to model the widely used Berkovich indenter. In addition, thickness of YBCO based thin films and substrates were 300 nm and 5000 nm, respectively and the ratio of film thickness and substrate was 6 % in this model. The substrate dimensions (both width and height) are taken to be at least 16 times larger than the film thickness, so as to simulate the semi-infinite substrate.

Assuming no material size effect occurs, the normalized indentation load $C = P/h^2$ (which is also referred to as the loading curvature) is constant during conical indentation of a bulk YBCO based material; consequently, only one material parameter can be measured from the loading curve of such an indentation. By contrast, for YBCO based thin films, the stress field and plastic flow beneath the indenter were disturbed by the presence of the substrate, and the loading curvature depends on the penetration depth. So, the ratio of indentation depth-film thickness and film-substrate thickness affected together to the indentation curves. According to the experimental results, applicable ratios were used for this indentation part as represented Figure 4.27.

Figure 4.27 a) represented that dimensions of entire axisymmetric thin film model. Construction of axisymmetric thin film model was demonstrated in Figure 4.27 b) according to this dimension and part design.

Part design of Abaqus package program showed great advantages about modeling of axisymmetric indentation analysis. According to the program, the users could model together with indenter and thin film-substrate system at the same model tree

and applied different material property to the different part-section of constructed analysis.

(a)
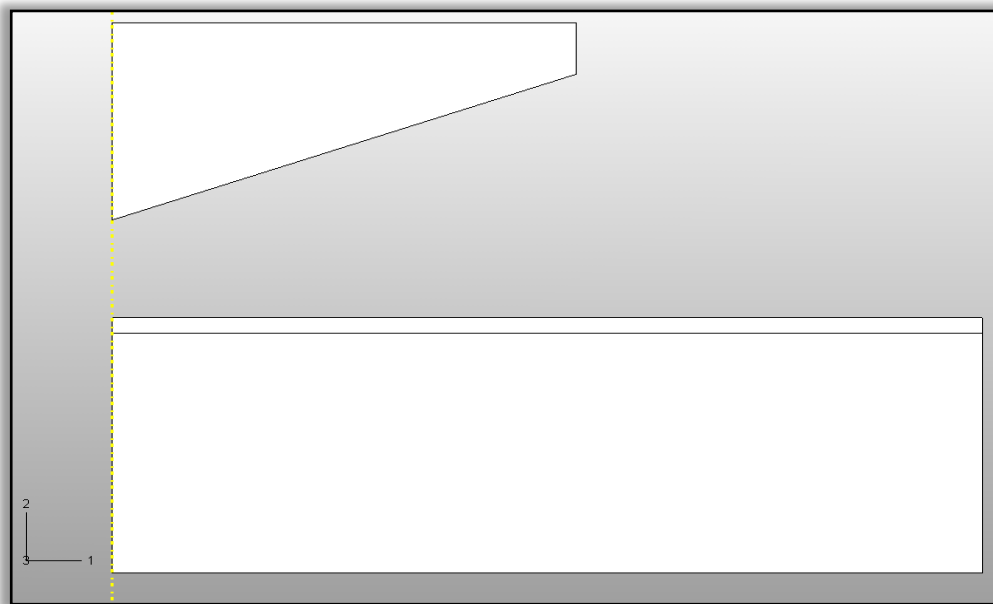
(b)

Figure 4.27.(a) Dimensions of entire YBCO thin film model and b) Construction of YBCO based thin films in Abaqus package program.

4.6.2 Property Variations of YBCO Based Films for Numerical Indentation

Four different material input was loaded to the model as pure YBCO thin film, YBCO thin film with 0.05 g Mn, YBCO thin film with 0.10 g Mn and YBCO thin film with 0.15 g Mn. In addition, Mn reacted as $BaMnO_3$ particles in pure YBCO thin film structure. So, structure of YBCO based thin films were changed as represented characterization part of study. Especially, mechanical properties of YBCO based thin films clearly changed with increasing Mn content ($BaMnO_3$) in structure. Instrumented indentation analysis showed that Elastic modulus of films decreased with increasing $BaMnO_3$ quantity as listed in Table 4.4. According to the nanoindentation experiments, elastic modulus and hardness of four different YBCO based thin films determined under 300 µN applied load. So, elastic moduli were loaded to entire model as listed in Table 4.6. Input data of axisymmetric thin film model's material properties with substrate and equivalent cone were listed in Table 4.6.

Table 4.6 Material properties of entire model

Material type	Elastic Modulus (GPa)	Poisson ratio (v)	Yield strength (GPa)	Ratio of Yield Strength and Elastic modulus
Pure YBCO thin film	88.54		7.50-9.50	0.0847-0.1073
YBCO thin film with 0.05 g Mn	83.41		6.50-9.00	0.0779-0.1079
YBCO thin film with 0.10 g Mn	79.11	0.261	5.00-6.75	0.0632-0.0853
YBCO thin film with 0.15 g Mn	76.47		2.75-4.25	0.0360-0.0556
STO substrate	278	0.238	-	-
Equivalent Cone	1040	0.07	-	-

Elastic modules were determined from indentation unloading curves for four different YBCO based thin film models. So, determined elastic modules were loaded with Poisson ratio as material elastic properties in finite element simulation. While fixing elastic properties as represented in Table 4.6 for each sample, yield strength of YBCO based thin films were changed to determine same penetration depth-force curve with experimental indentation analysis. After loaded this experimentally

determined elastic and plastic properties, entire model was represented in Figure 4.28.
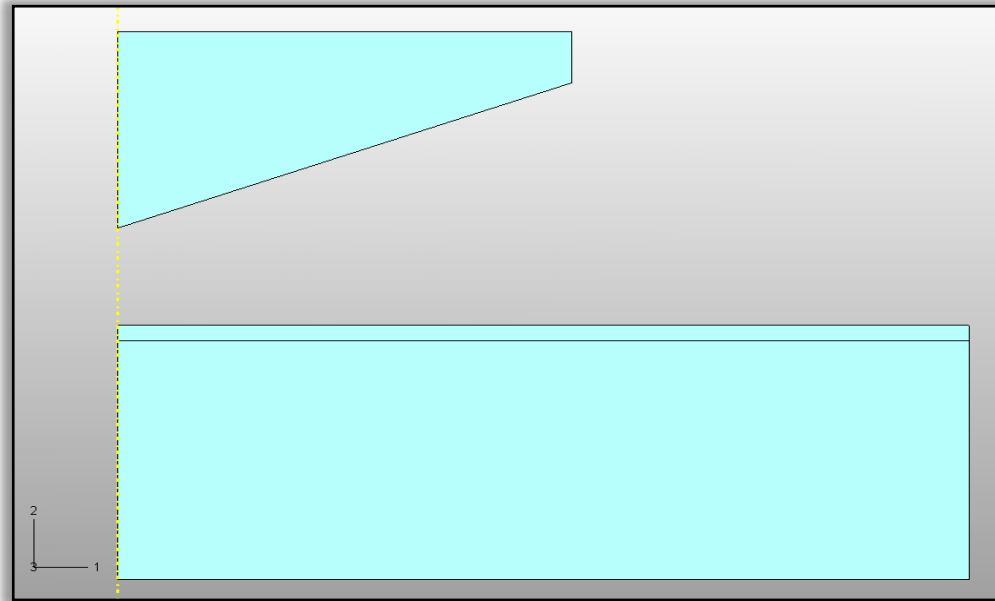

Figure 4.28 Axisymmetric model of YBCO based thin film after loading material property to the each section.

4.6.3 Assembly, Interaction and Step Properties of Entire Model

Contact region properties between indenter and surface of thin film-substrate system could be design in assembly and interaction modulus of Abaqus package program. The contact area of YBCO based thin film was divided to the partitions as represented Figure 4.29. As known from indentation analysis theory, fine mesh design could be applied in mesh part due to creating partitions near contact region. Contact region of YBCO based thin films were estimated as the dimensions of 300 nm x 400 nm (thickness x length) as represented in Figure 4.29 a). After this area determination depend on indentation depth, whole model began to partition from contact region to the substrate with the dimensions of 500 nm and 400 nm, respectively. This partitioned model also used for different element type and region determination for fine mesh design of contact area.

Interaction properties between indenter and film surface established as finite sliding formulation and surface to surface constraint enforcement method. Contact property of entire model was assumed tangential behaviour and frictionless between indenter and surface of film.
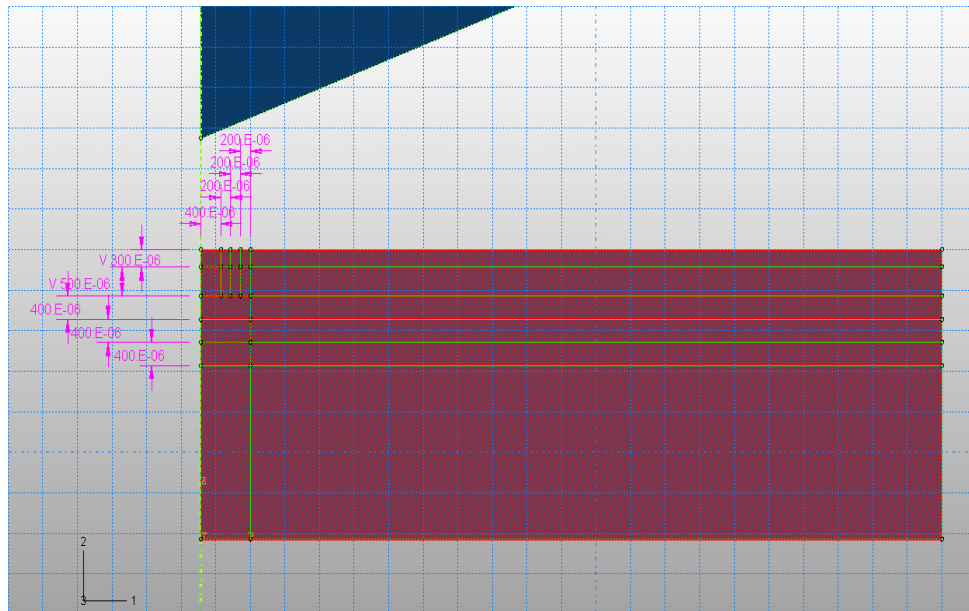
(a)
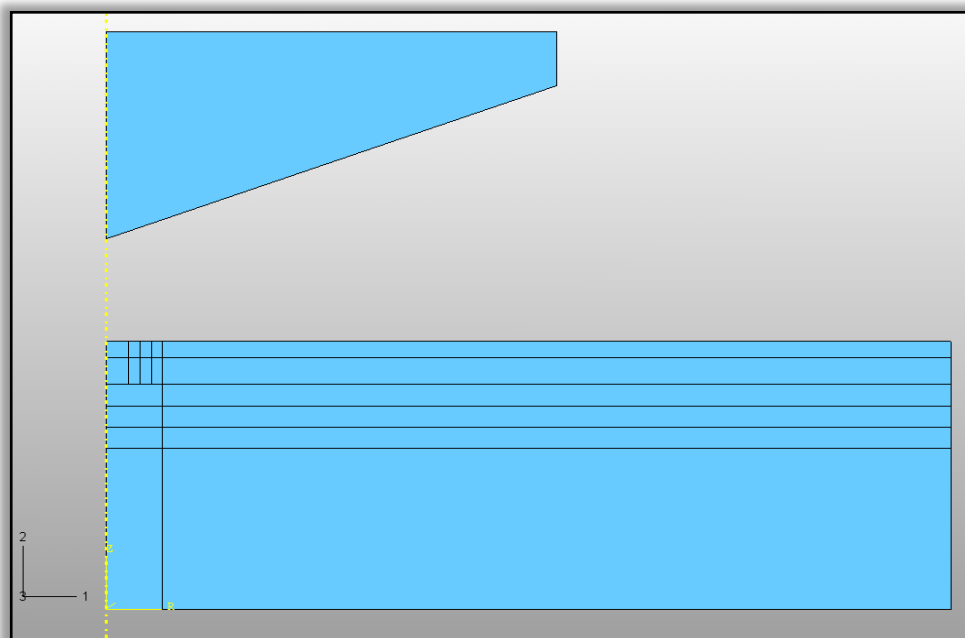
(b)

Figure 4.29. (a) Dimensions of partitioned region in whole model and (b) Assembly presentation of axisymmetric model under partitioned condition for fine mesh design near the contact region.

After loaded interaction properties to the entire model, yellow icons were added to surfaces of film and indenter by Abaqus package program as represented Figure 4.30.
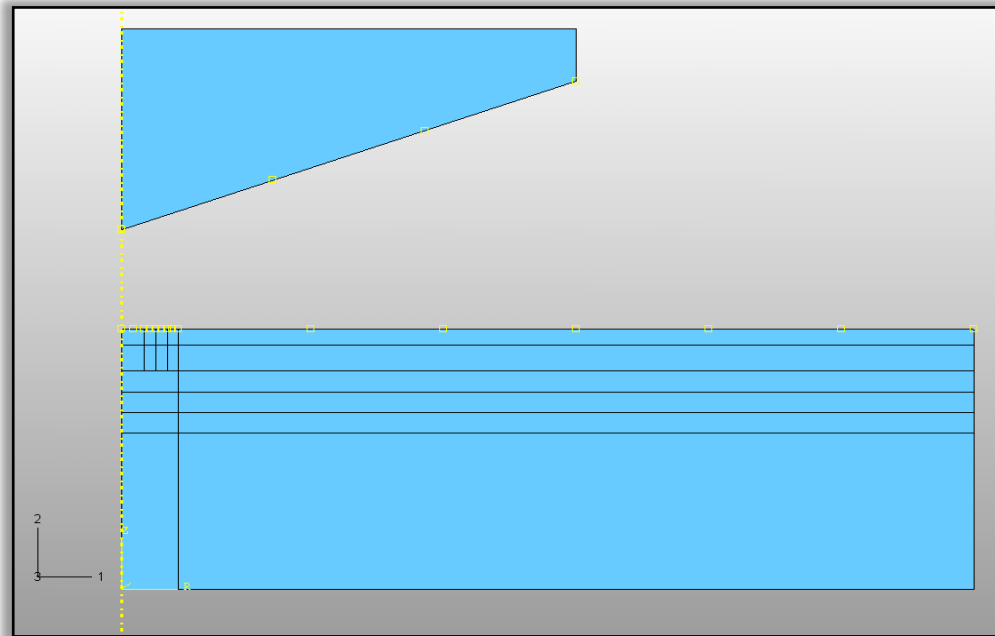
Figure 4.30 Interaction presentation of axisymmetric model under partitioned condition for initial step.

Steps of indentation analysis were determined as approaching, loading, holding, unloading and go back with static-general steps procedure of finite element program as illustrated in Figure 4.31. Each part of steps was modeled as full Newton solution technique and used 500 numbers of increments.

Name	Procedure	Nlgeom	Time
Initial	(Initial)	N/A	N/A
Approaching	Static, General	ON	1
Loading	Static, General	ON	1
Holding	Static, General	ON	1
Unloading	Static, General	ON	1
Go back	Static, General	ON	1

Figure 4.31 Steps of indentation analysis in finite element solutions.

4.6.4 Load and Boundary Condition of Entire Model

Applied load for indentation analysis of YBCO based thin film was 300 µN as the same value with experimental indentation. 300 µN applied load was determined from step load-unload test mode of nanoindenter. According to the results, when the applied load increased from 100 µN to 1000 µN, indentation depth increased proportionally from 22 nm to 110 nm, respectively. So, this depth-force analysis results showed that 300 µN applied load had possible indentation depth with the ratio of maximum indentation depth and film thickness as listed in Table 4.3. According to the Figure 4.32 a), 300 µN applied load was established to the only loading and unloading steps of indentation simulation. As seen in Figure 4.32 b) fixing, contact, holding, go back and y-axis displacement control of axisymmetric model was added to the initial, approaching, holding, go back and initial steps of entire model, respectively.
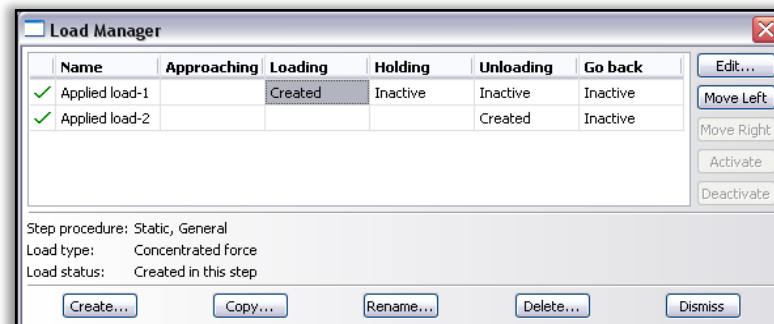
(a)
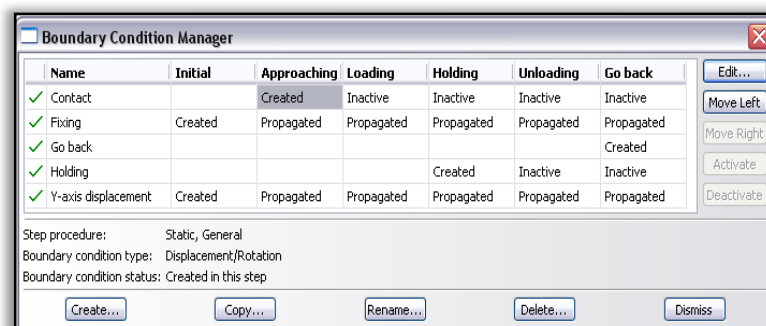
(b)

Figure 4.32. (a) Load modulus of entire model for loading and unloading step and (b) Boundary conditions of axisymmetric model for each step.
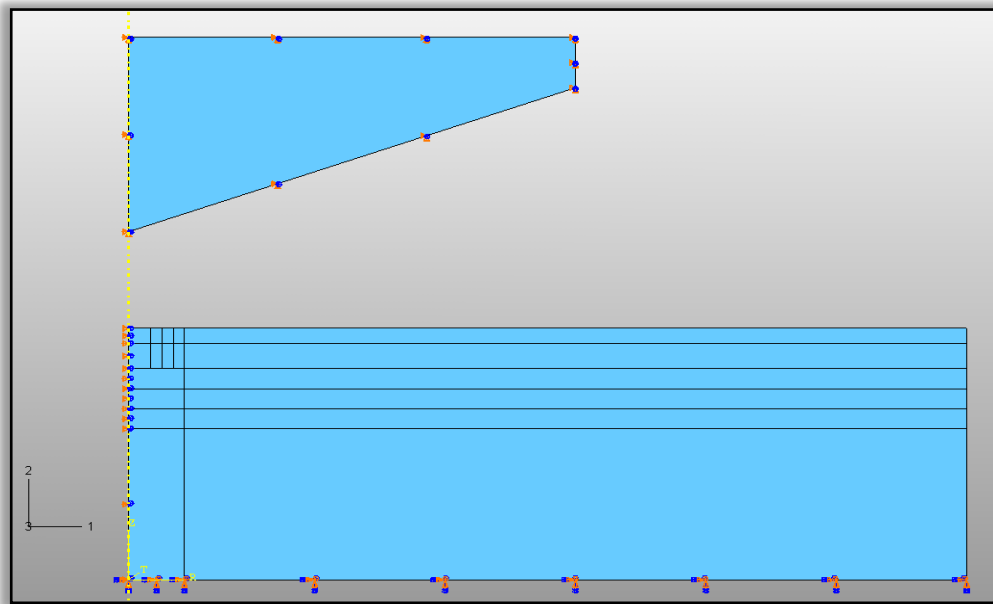
Figure 4.33 Boundary condition and load of axisymmetric model under partitioned condition for initial step.

After loading the boundary condition and load procedures of indentation model of YBCO based thin films, Abaqus program represented whole model as illustrated in Figure 4.33.

4.6.5 Mesh design and Job Modulus of Entire Model

Creating mesh design of entire model was very important, especially when the problem had contact region between two separated surfaces. As known, instrumented indentation analysis had a diamond indenter which penetrated to surface of thin film in nanoscale and deformed contact region, not whole surface, plastically under applied load. Importance of divided surface near contact region was to take very correct and sensitive results for simulated loading-unloading curves of YBCO based thin films. For that reason, elements were finest in the central contact area and became coarser outwards for entire model and magnified view of contact region could be seen as represented in Figure 4.34 and Figure 4.34, respectively. According to the Figure 4.34, contact region was meshed as structured CAX4R element type, A-4 node bilinear axisymmetric quadrilateral, reduced integration and hourglass control

with 2, 4, 8, 16, 32 and 40 number for determination of indentation depth and load dependency to the mesh element number.

In this model, as represented Figure 4.29 a), contact region size of YBCO based thin films was 300 nm x 400 nm. When the element number increased from 2 to 40, element size was decreased from approximately 200 nm to 10 nm. The smallest element size and total element number were 10 nm and 3764, respectively, which enables an accurate determination of the real impression size.
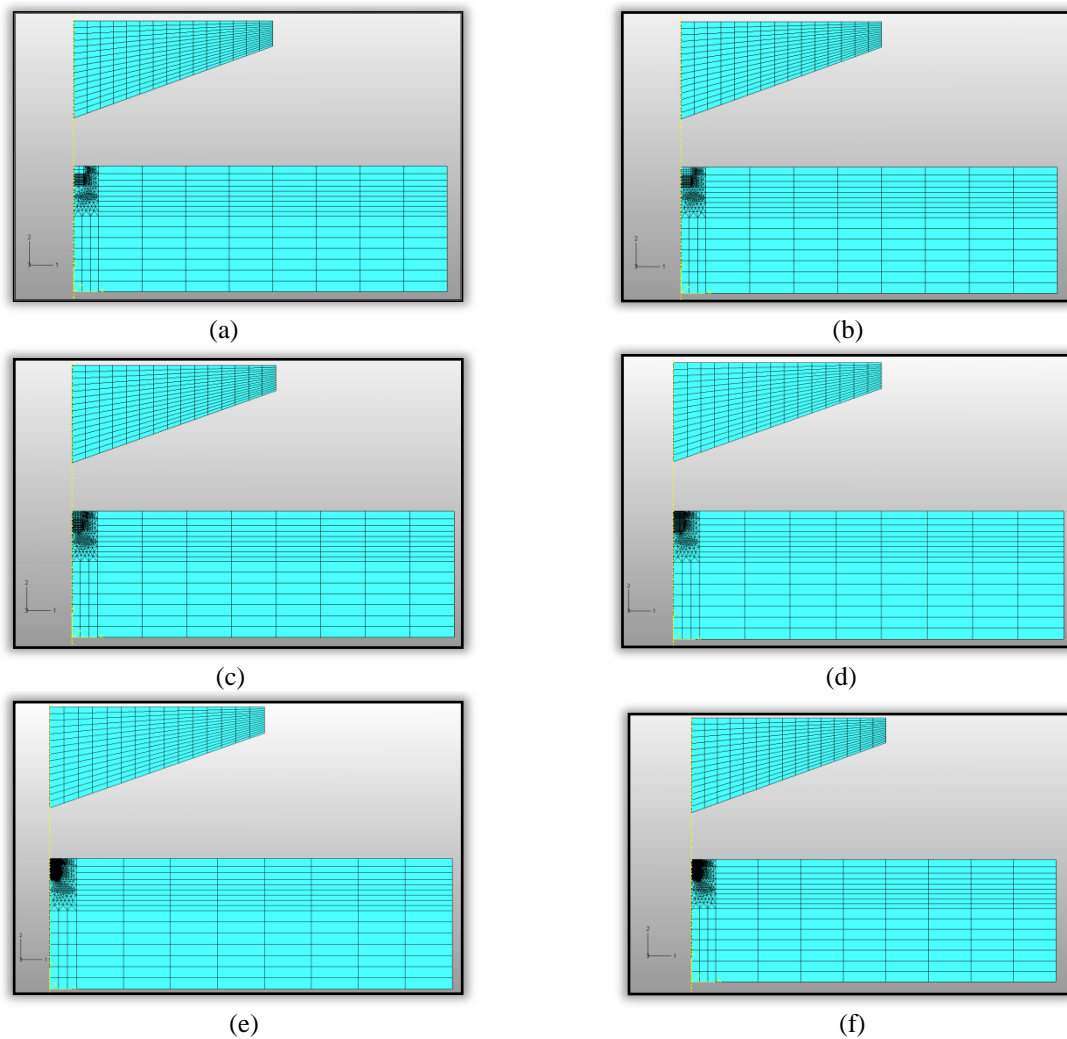

(a)	(b)
(c)	(d)
(e)	(f)

Figure 4.34 Mesh design of YBCO based thin film with a) 2, b) 4, c) 8, d) 16, e) 32 and f) 40 element.
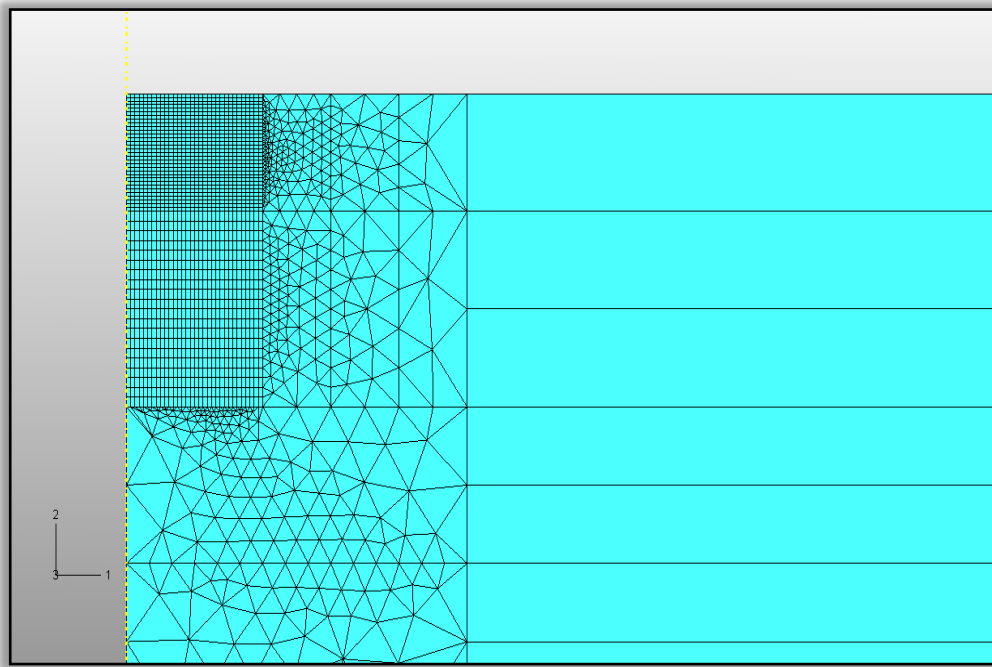
Figure 4.35 Magnified mesh image near contact region of YBCO based thin films.

4.6.6 Finite Element Analysis of YBCO Based Thin Films

Simulation of YBCO based thin films' indentation analysis was exposed very important mechanical properties such as yield strength which influenced the mechanical stability of coated superconductor under service conditions. Elastic modulus and hardness of YBCO based thin films could be determined from instrumented indentation loading-unloading curves. However, yield strength, stress-strain relationship, substrate and thickness effect on characteristic loading-unloading curves could not be obtained from experimental results. At this time, researchers used simulation and finite element modeling with developed algorithms as explained chapter two.

Usually, finite element analysis of indentation problem was applied to the bulk ceramic and metallic based material until 2000s. However, after development of thin film technologies and materials increased and used, determination of mechanical properties of films and coatings were more concerned. For instance, the thin-film based technologies provide higher performance, higher density and smaller overall

size to the microsystems package. Although thin films are increasingly used for performance, functionality, and size reasons, the mechanical behavior of the thin films is important to understand to address reliability concerns. As mentioned chapter two, depth-sensing instrumented nanoindentation technique provided a continuous record of variation of indentation load with penetration depth into the specimen and this technique had been an area of considerable attention in recent years due to its high resolution at low load scale for determination of elastic modulus and hardness of thin films. Importance of mechanical stability of superconductor thin films with/without additional particles under service condition had to expose by experimental and finite element modeling. Additional particles behave as defect center and increases superconducting properties under given temperature as explained chapter one. While increasing superconducting properties by additional particles, in this study Mn ($BaMnO_3$), elastic modulus and hardness of thin films were decreased from 88.54 GPa to 76.47 GPa and 12.51 GPa and 3.88 GPa. However, variations of plastic properties of YBCO based thin films with additional particles could not be reached by instrumented indentation test. For that reason, finite element modeling of YBCO based thin films with and without $BaMnO_3$ particles was considered by Abaqus 6.6-1 package program with experimentally determined elastic properties of films.

4.6.6.1 Property Variations and Analysis of YBCO Based Thin Films

Instrumented indentation analysis of YBCO based thin films with additional particles showed variations for elastic modulus and hardness under 300 μN applied load. The differences of elastic modulus and hardness between pure YBCO thin film and YBCO thin film with 0.05 g, 0.10 g and 0.15 g Mn were exposed from indentation depth and area variations under same applied load. If the indentation depth and area increased under same applied load for YBCO based thin films, additional particles made the film structure more ductile than pure one. So, in order to determine plastic properties of YBCO based film, finite element modeling was used. Mechanical properties of YBCO based thin films were listed in Table 4.6. The

plastic properties were changed to obtain same penetration depth-force curves with experimental data.

4.6.6.2 Mesh Effects on Indentation Analysis of YBCO Based Thin Films

The axisymmetric model was constructed depend on given dimensions, properties, steps, load-boundary conditions and mesh number-type. First of all, mesh effect could be determined because of sensitivity of indentation depth results. Figure 4.36 a) and b) showed that maximum and residual indentation depth variations by increasing yield stress from 7.50 GPa to 9.50 GPa with five step for pure YBCO based thin films under 300 µN applied load. According to the results, maximum and residual indentation depth varied from 40.74 nm to 39.58 nm and from 22.17 nm to 19.18 nm for 10 nm smallest element size by fixing elastic modulus at 88.54 GPa and increasing yield stress from 7.50 GPa to 9.50 GPa, respectively. In addition, maximum and residual indentation depth increased until increasing element number from 2 to 8 at contact region. When the 16, 32 and 40 element was used for finest mesh design, maximum and residual depth variation was very small at nanometric scale.
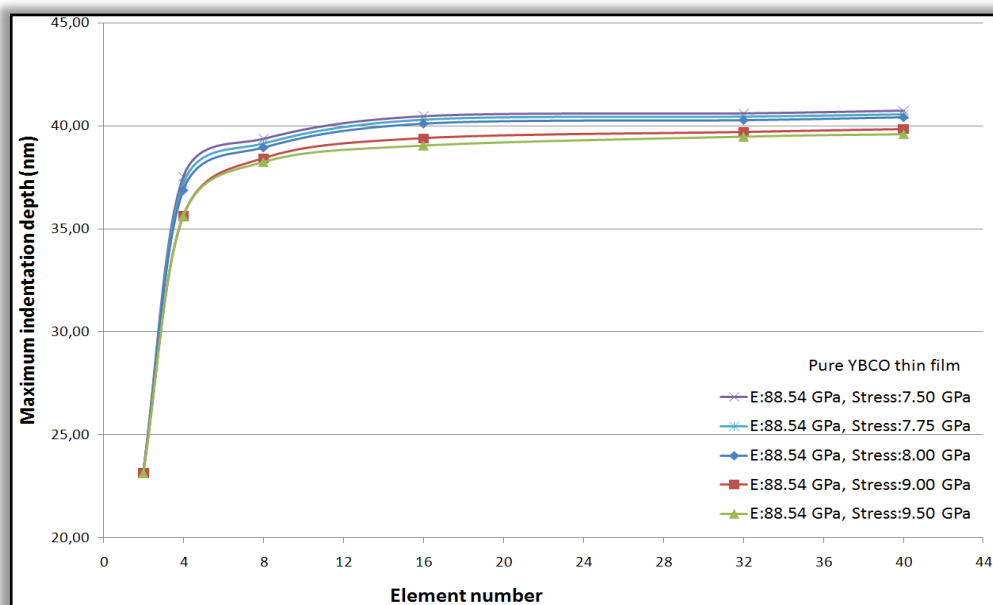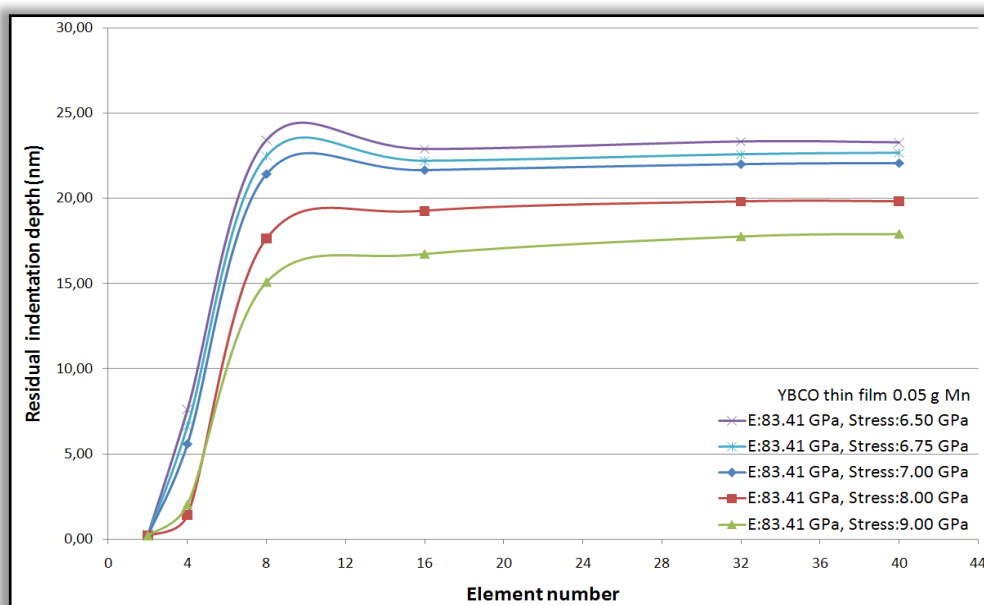

(a)
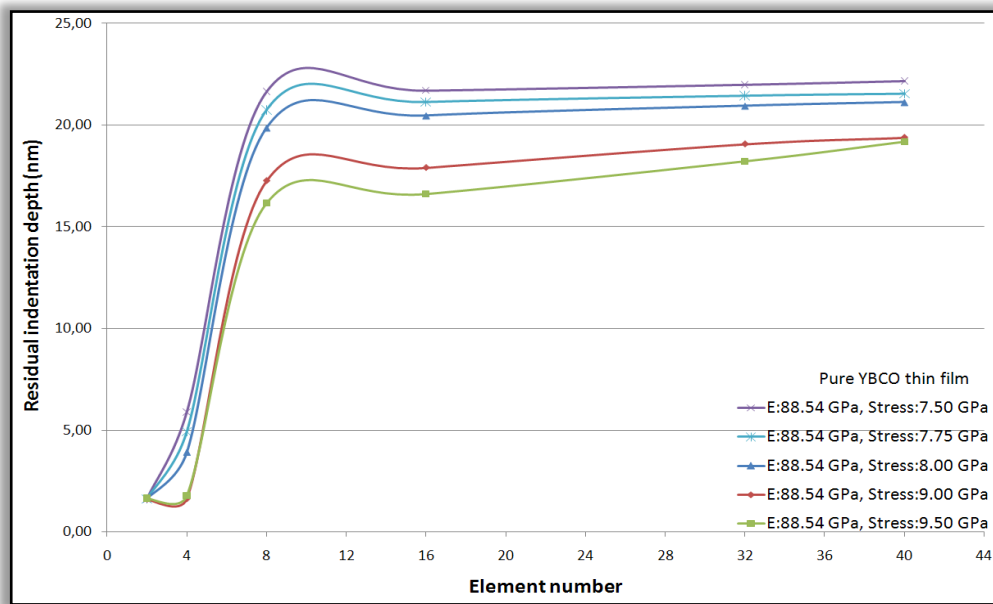
(b)

Figure 4.36 Mesh element number effect on (a) maximum indentation depth and (b) residual indentation depth of pure YBCO based thin film under 300 µN applied load.

Mesh element number effect on indentation depth analysis for YBCO thin film with 0.05 g Mn addition showed in Figure 4.37. Maximum indentation depth increased from 25.35 nm to 43.13 nm, from 25.35 nm to 42.91, from 25.35 nm to 42.69 nm, 25.35 nm to 41.91 and from 25.35 to 41.36 nm by increasing element number from 2, 4, 8, 16, 32 and 40, respectively for fixing elastic modulus at 83.41 GPa and changed yield stress from 6.50 GPa to 9.00 GPa with five step. Similarly, residual indentation depth was increased by increasing element number for given material properties under 300 µN applied load. As expected, when the yield stress was increased from 6.50 GPa to 9.00 GPa, maximum and residual indentation depths were decreased as represented in Figure 4.37 a) an b). As pure YBCO based thin films, when 16, 32 and 40 element number loaded to the contact region of YBCO based thin film with 0.05 g Mn, both maximum and residual indentation depth did not changed systematically.
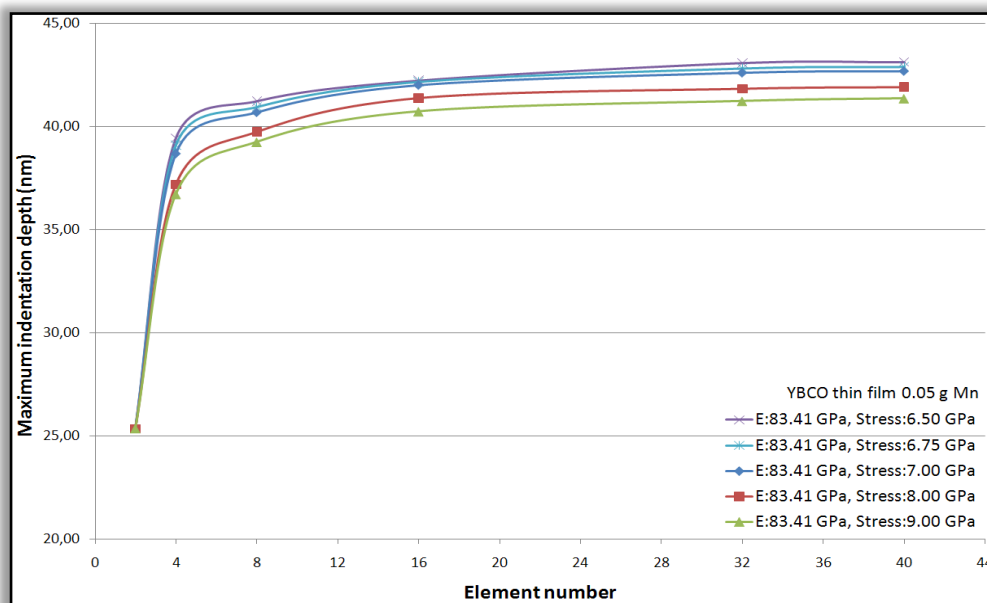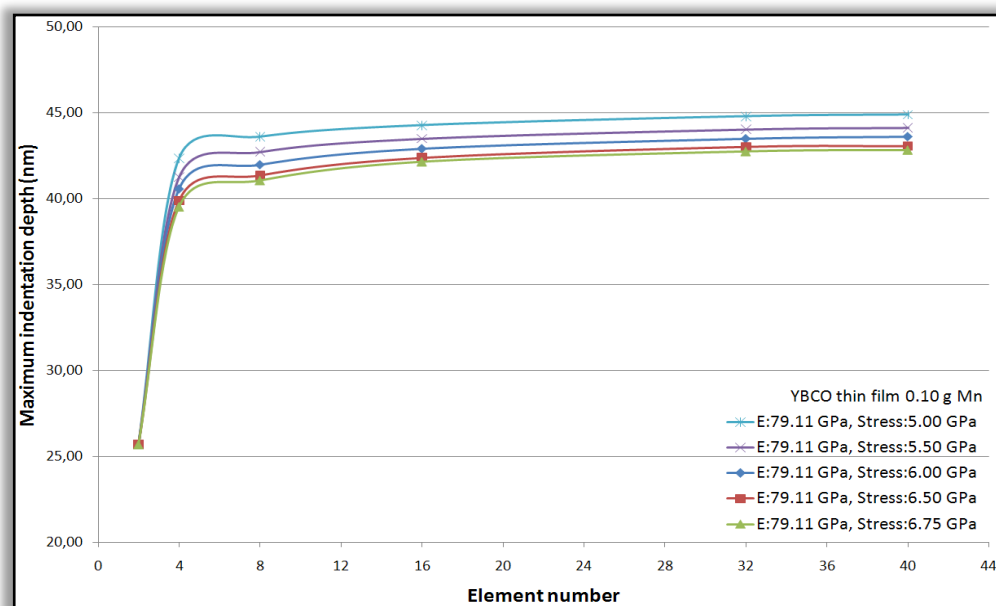
(a)

(b)

Figure 4. 37 Mesh element number effect on (a) maximum indentation depth and (b) residual indentation depth of YBCO based thin film with 0.05 g Mn under 300 µN applied load.
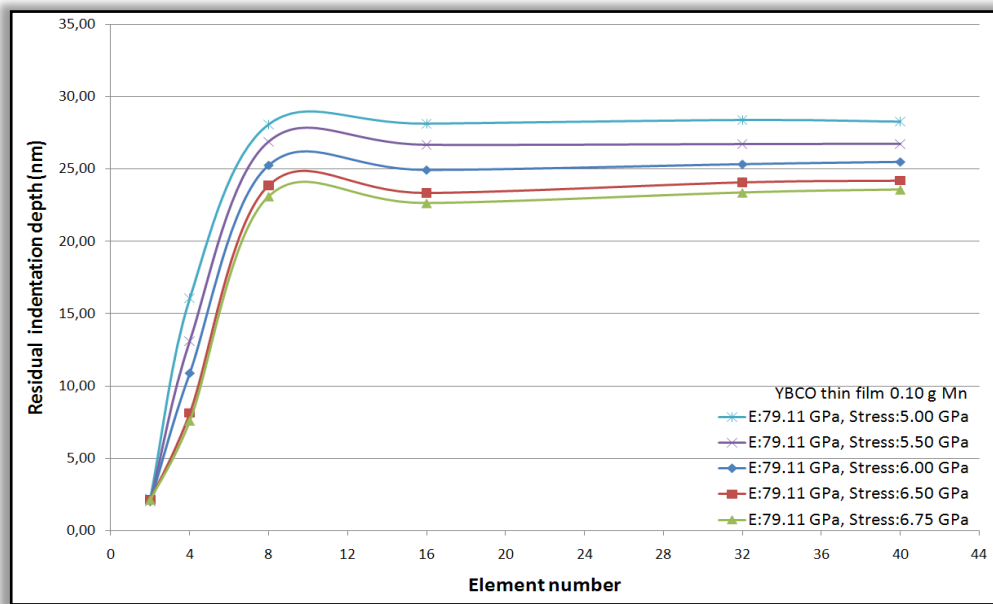
Indentation analysis of YBCO thin film with 0.10 g Mn for given material properties, listed in Table 4.6, demonstrated in Figure 4.38. Generally speaking, maximum and residual indentation depth was increased by increasing mesh element number. Especially, when the element number increased from 2 to 8, maximum and

residual indentation depth was increased from 25.71 nm to 43.60 nm, from 25.71 nm to 42.73, from 25.71 nm to 41.98, from 25.71 nm to 41.36 and from 25.71 nm to 41.07 nm, respectively for elastic modulus fixed at 79.11 GPa and yield stress increased from 5.00 GPa to 6.75 GPa.

As illustrated from Figure 4.38 a) and b) sharp increase could be seen both maximum and residual indentation depth until increasing element number from 2 to 8. When the element number increased from 16 to 40, maximum indentation depth was increased from 44.27 nm to 44.89 nm, from 43.50 nm to 44.14 nm, from 42.91 nm to 43.61 nm, from 42.38 nm to 43.06 nm and from 42.16 nm to 42.84 nm, respectively for increasing yield stress from 5.00 GPa to 6.75 GPa with five step. Similar effects could be seen for residual indentation depth. According to the values of maximum indentation depth, changes were in nanometric scale and very small. So, usage of 40 elements with 10 nm smallest element size could have more sensitive and correct results both maximum and residual indentation depth values.
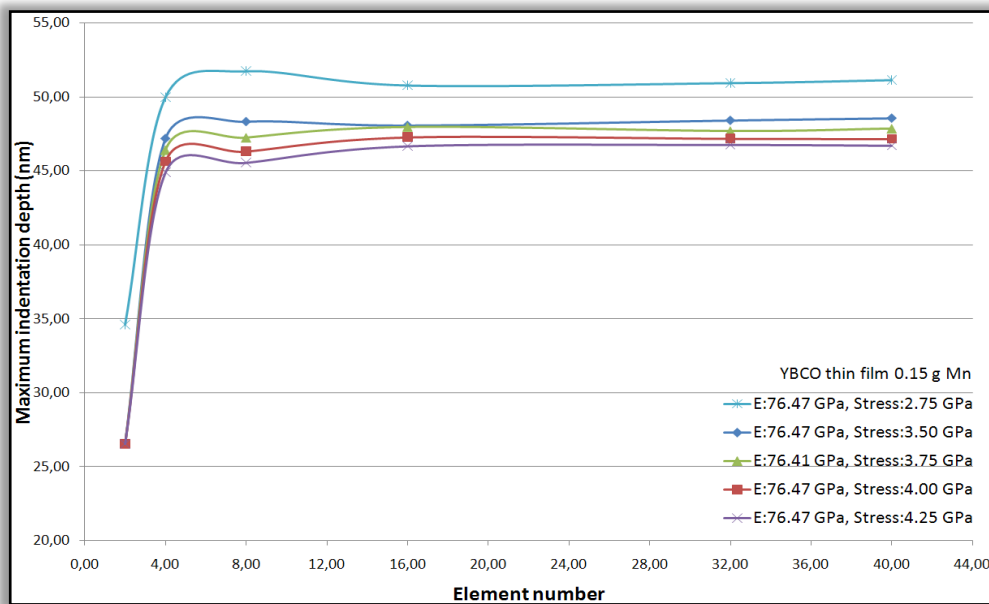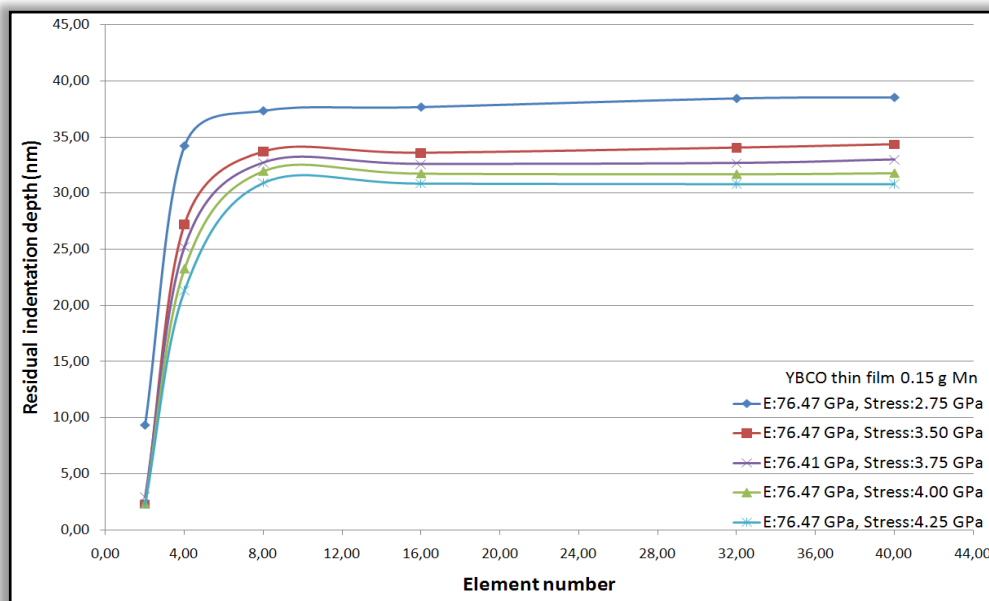

(a)

(b)

Figure 4.38 Mesh element number effect on (a) maximum indentation depth and (b) residual indentation depth of YBCO based thin film with 0.10 g Mn under 300 µN applied load.

Simulation indentation analysis of YBCO thin film with 0.15 g Mn demonstrated in Figure 4.39. Mesh nuber effects on maximum and residual indentation depth could be seen in Figure 4.39 a) and b), respectively. When the element number increased from 2 to 8, sharp increase for maximum indentation depth obtained and depth values were increased from 34.61 nm to 51.75 nm, from 26.56 nm to 48.33 nm, from 26.56 nm to 47.26 nm, 26.56 nm to 46.32 nm, from 26.56 nm to 45.55 nm for fixing elastic modulus as 76.47 GPa and increasing yield stress from 2.75 GPa to 4.25 GPa with five step.

Correspondingly, residual indentation depth of YBCO based thin film with 0.15 g Mn addition increased by increasing element number from 2 to 8 as represented in Figure 4.39.b) for given material propertiey. However, when the element number increased from 16 to 40, sharp increase could not seen and residual indentation depth did not change scientifically.

(a)

(b)

Figure 4. 39 Mesh element number effect on (a) maximum indentation depth and (b) residual indentation depth of YBCO based thin film with 0.15 g Mn under 300 µN applied load.

Mesh element number analysis showed that when the element number increased from 2 to 40, depth values of YBCO based thin films increased systematically. On the other hand, sharp increases in depths could not be seen after 8 element number.

Consequently, 40 elements with 10 nm element size was chosen due to its sensitivity in nanometric scale for simulated loading and unloading curves of pure YBCO thin film, YBCO thin film with 0.05 g Mn, YBCO thin film with 0.10 g Mn and YBCO thin film with 0.15 g Mn. Figure 4.40 showed that simulated maximum and residual indentation depth variations of four different YBCO based thin films depend on yield stress raises under 300 µN indentation load.

Maximum and residual indentation depth decreased from 40.74 nm to 39.58 nm and from 22.17 nm to 19.18 nm, respectively by increasing yield stresses from 7.50 GPa to 9.50 GPa for pure YBCO thin film as represented in Figure 4.40 a). It is very normal to reduce of depth results by increasing yield stress. Figure 4.40 b) showed that indentation depth analysis of YBCO thin film with 0.05 g Mn addition.

When the yield stress was increased from 6.50 GPa to 9.00 GPa, maximum and residual indentation depth was decreased from 43.13 nm to 41.36 and from 23.28 nm to 17.91 nm, respectively. For YBCO based thin films and YBCO thin films with 0.05 g Mn addition, ratio of maximum indentation depth to film thickness was 13.58 % and 14.38 %, respectively. So, depth analysis and input file of material properties was applicable for finite element analysis of experimental indentation.
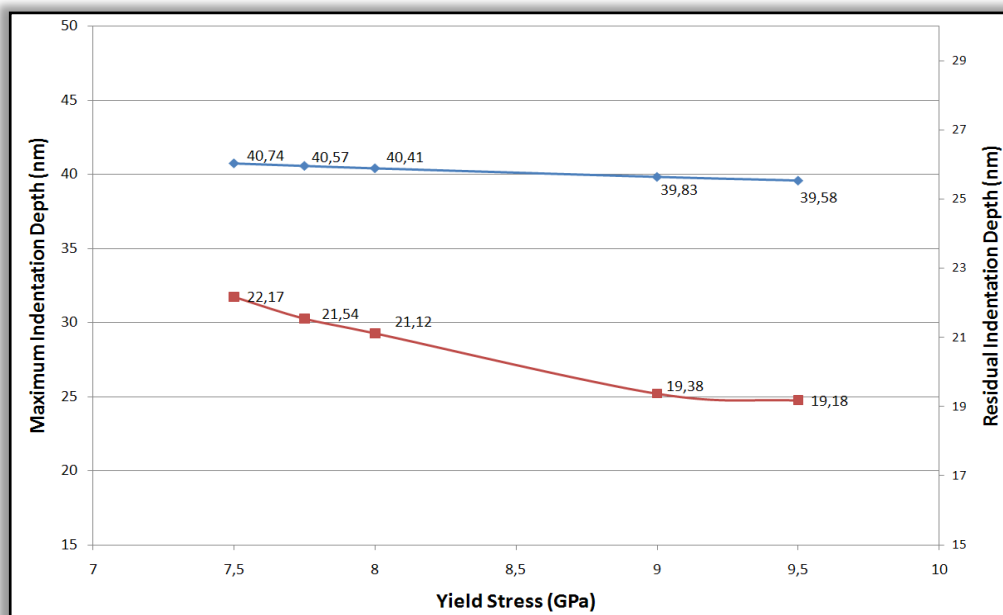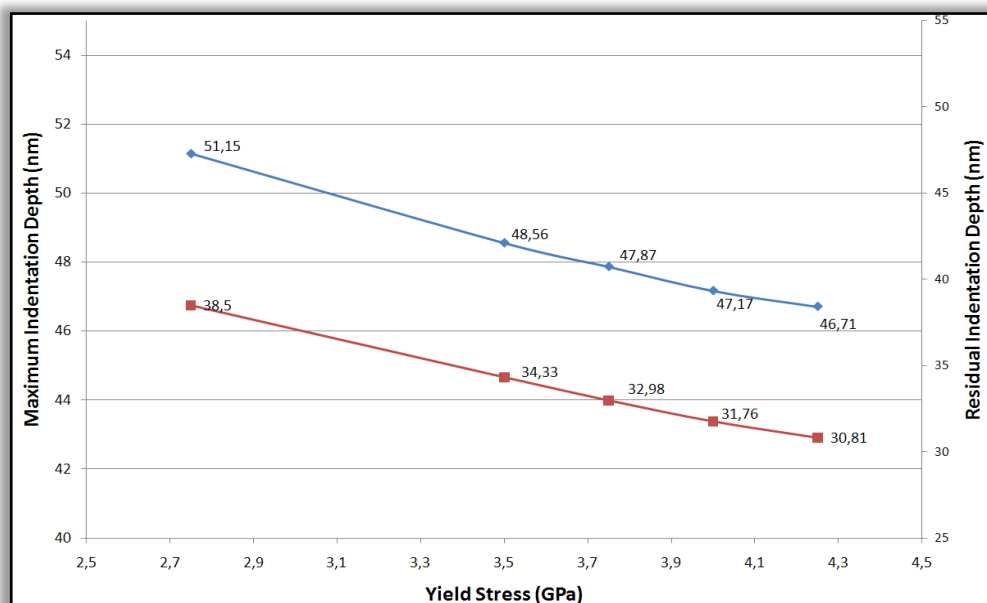

(a)
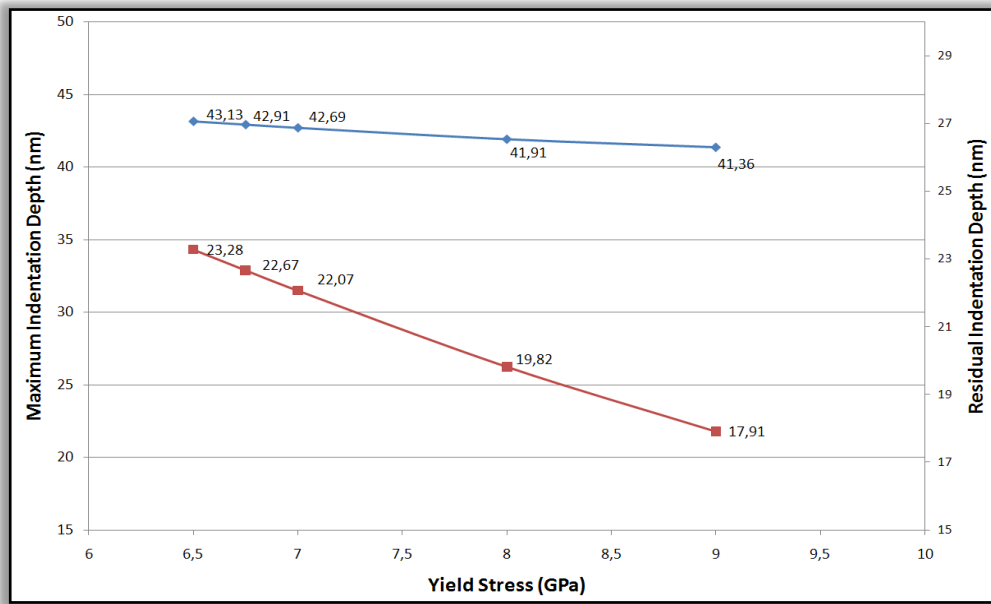
(b)
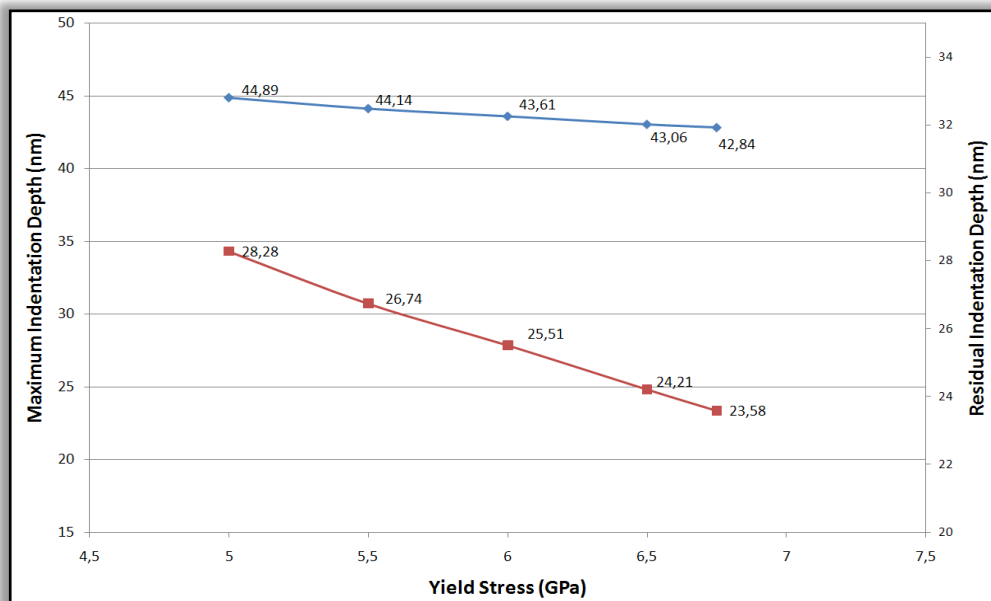
(c)

(d)

Figure 4.40 Depth analysis of (a) pure YBCO thin film, (b) YBCO thin film with 0.05 g
Mn, (c) YBCO thin film with 0.10 g Mn and (d) YBCO thin film with 0.15 g Mn depend
on yield strength variations with 10 nm element size.

Characteristic depth analysis of YBCO based thin films with 0.10 g Mn
demonstrated in Figure 4.40 c). Maximum and residual indentation depth values of
film under 300 μN applied load decreased from 44.89 nm to 42.84 nm and from
28.28 nm to 23.58 nm, respectively by increasing yield stress from 5.00 GPa to 6.75
GPa. Figure 4.40 d) illustrated depth analysis of YBCO based thin film with 0.15 g
Mn addition. When the yield stress of film increased from 2.75 GPa to 4.25 GPa,
maximum and residual indentation depth decreased from 51.15 nm to 46.71 nm and
from 38.50 nm to 30.81 nm, respectively. Figure 4.40 a), b), c) and d) showed same
yield stress tendency of indentation depth under same applied load and element size
for pure YBCO thin film, YBCO thin film with 0.05 g Mn, YBCO thin film with
0.10 g Mn and YBCO thin film 0.15 g Mn addition.

However, raises of Mn content in structure of YBCO based thin film made
significant variation for mechanical properties. When indentation results of pure
YBCO based thin films and 0.15 g Mn added compared under same simulation
condition, especially, maximum and residual depth was increased from 40.74 nm to

51.15 nm and from 19.18 nm to 30.81 nm (Figure 4.40 d)). It means that ductility of YBCO based thin films was increasing by increasing Mn content in structure (BaMnO$_3$ formation).

4.6.7 Comparisons of Experimental and Modeling Indentation Curves

Instrumented indentation, with its potential versatility, could enable easy determination of the elastoplastic properties of a broad class of materials over a wide range of size scales (nano, micro and macro), and thus has been the subject of considerable research. A theoretical framework for instrumented sharp indentation and a general methodology that enables determination of the elasto-plastic properties of materials through an analysis of the force-depth (*P-h*) relationship has been presented in chapter two. Depending on the experimental set-up used to perform the indentation, the loading and unloading characteristics of the *P-h* curve, and thus the material properties estimated from the analysis of the *P-h* curves, could be obtained to varying levels of accuracy. Thus, the sensitivity of the estimated elasto-plastic properties to variations in the input parameters obtained from the *P-h* curves is an important issue.

In this section we want to investigate the structural model of the instrumented indentation test. We can make use of axisymmetry and therefore have to model in two dimensions only. The indentation process is complex, so simplifications and assumptions have to be made to achieve low numerical cost but of course sufficient accuracy. For the time being, the problem is idealized: We assume the surface of the specimen as ideally smooth, whereas in reality a certain roughness may be present as well as e.g. a thin film of four different YBCO. The indenter is a equivalent cone and furthermore isothermal conditions are adopted.

In the following, the model set-up is described. First, appropriate boundary conditions and define the modeling of contact was chosen. Next we model the indenter, before the discretization of the specimen as half-space is discussed. All simulations are carried out under load-controlled conditions. Two reasons can be

given for this: First, a real indentation experiment is hard to execute under displacement-controlled conditions, i.e. up to a maximal displacement. Second, regarding numerical cost and accuracy, neither displacement-controlled nor load-controlled experiments show an important advantage. Load-depth (P-h) curve is the straightforward characterization of indentation results, which could be precisely obtained by instrumented indentation equipment. For each material model, finite element simulation results gave a set of P and hs data for each loading step and then these data points are plotted in Excel. As described above, surface of YBCO based thin films were ideally smooth. However, instrumented indentation results affected by surface roughness of materials. Both loading and loading part of indentation curves could have more scattered data depending on ratio of indentation depth and roughness to the film thickness.

According to the experimental indentation results of YBCO based thin films as represented Figure 4.41; scattered raw data of four different YBCO based films can be seen. Three different load-penetration depth curves were obtained for three different indented regions of film's surfaces. Figure 4.41 represented both indentation and simulation results of pure YBCO based thin films. Same maximum penetration depth was obtained by setting E: 88.54 GPa and yield stress: 8.00 GPa for experimental and simulation analysis. Surface roughness effect on indentation simulation could not be seen due to the chosen ideally smooth surface. According to the experimental indentation results, h_{max} and h_r were 40.24 ± 6.4 nm and 30.12 ± 7.8 nm, respectively, under 300 μN applied load. Similarly, finite element modeling of pure YBCO based thin film's indentation had maximum and residual indentation depth as 40.41 nm and 36.55 nm. Good agreement could be said for maximum indentation depth and loading curves of pure YBCO based thin films with 0.4 % error. However, residual indentation depth value had 20 % error for numerical results. In addition when the average experimental indentation loading-unloading was considered, this error value was graphically obtained as 7 %, as represented Figure 4.41. This may be due to differences in the yield strength or due to use of constitutive model of both YBCO based thin films like elastic-perfect plastic one without strain hardening exponent.
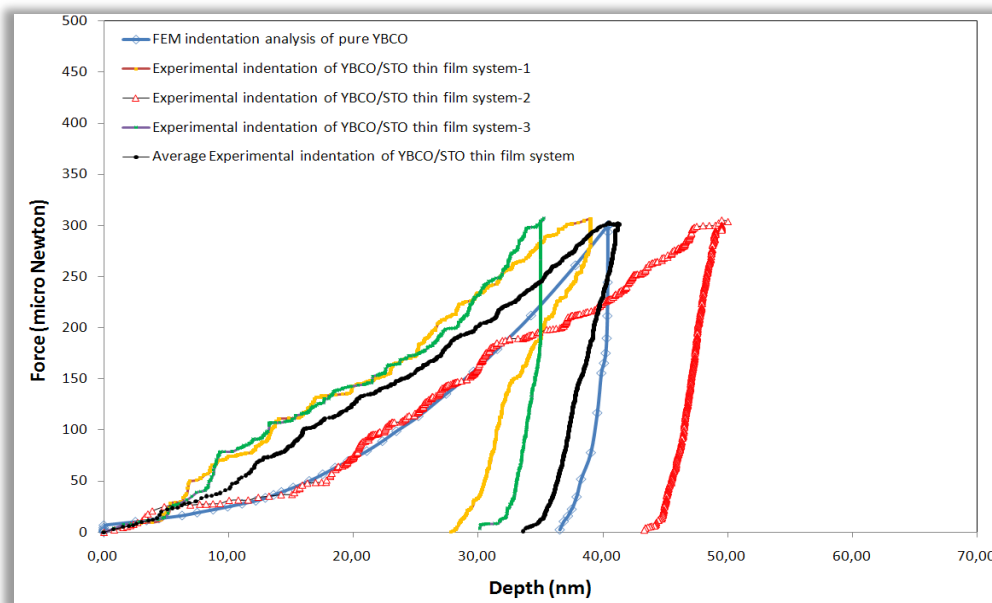
Figure 4. 41 Comparisons of experimental and simulation indentation analysis of pure YBCO thin film.

Figure 4.42 represented instrumented (for three different regions) and simulation indentation results of YBCO based thin film with 0.05 g Mn addition under 300 μN applied load. Experimentally determined maximum and residual indentation depth were 42.31 ± 9.4 nm and 32.11 ± 8.7 nm where as 42.69 nm and 38.61 nm for numeric solutions of indentation under condition of E: 83.41 GPa and yield stress: 7.00 GPa for YBCO based thin film with 0.05 g Mn addition. For a second time, good agreement was obtained for maximum indentation depth with 0.3 % error. However, residual indentation depth had 20 % error after comparison with experimental one. When the average curve was considered, this error decreased to 4 %. Loading part of curves was very closed to numerically determine one. As pure YBCO thin film indentation results, unloading part of curves had separated due to the modeled without strain hardening exponent. Strain hardening exponent of ceramics and especially oxide thin films was near zero. Ceramics and oxide based materials did not plastically deform and harden as metals with deformation. Additionally they showed brittle failure at the maximum stress. In this study, the computed load–displacement curve was compared with the experimental load–displacement curve and iteratively modified until a good agreement was reached between the computed and experimental load–displacement curves.
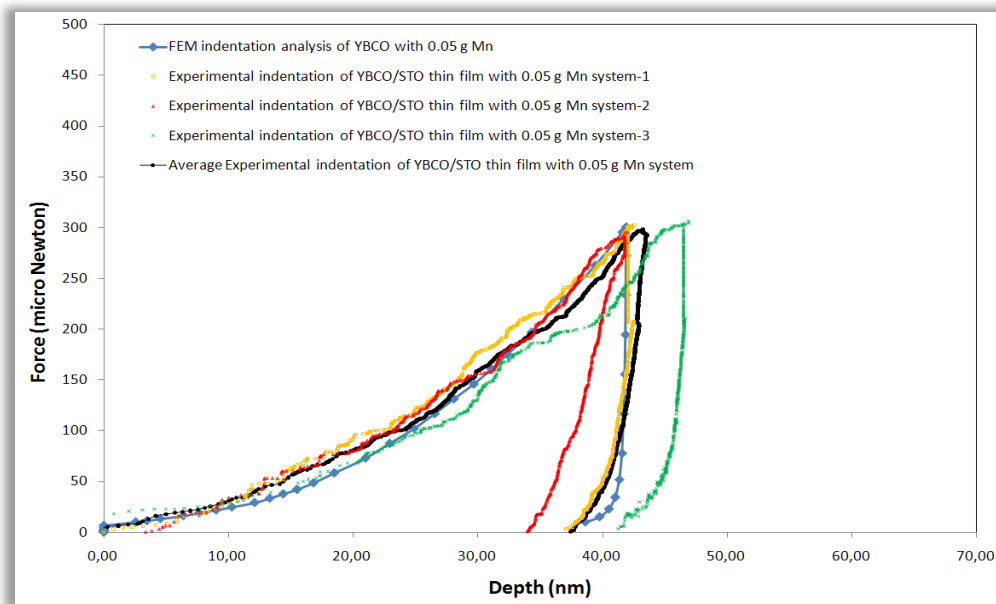
Figure 4. 42 Comparisons of experimental and simulation indentation analysis of YBCO thin film with 0.05 g Mn.

Figure 4.43 showed that finite element and instrumented indentation analysis of YBCO based thin film with 0.10 g Mn addition under 300 μN applied load. Maximum and residual indentation depths were determined by instrumented indentation as 42.45 ± 5.9 nm and 33.53 ± 4.4 nm, respectively. According to the finite element indentation analysis, maximum and residual indentation depths were 42.84 nm and 39.42 nm. When the average indentation curves of experimentally indented YBCO based thin films with 0.10 g Mn and finite element analysis curves compared, % error variations were very small both loading and unloading part of curves. Maximum indentation and residual depths were determined as 42.84 nm and 39.42 nm for FEM analysis. % error of depth analysis was near 1 %. So, experimentally determined loading and unloading curves of films had good agreement with numeric results of indentation under E: 79.11 GPa and yield stress: 6.75 GPa input data of material property.
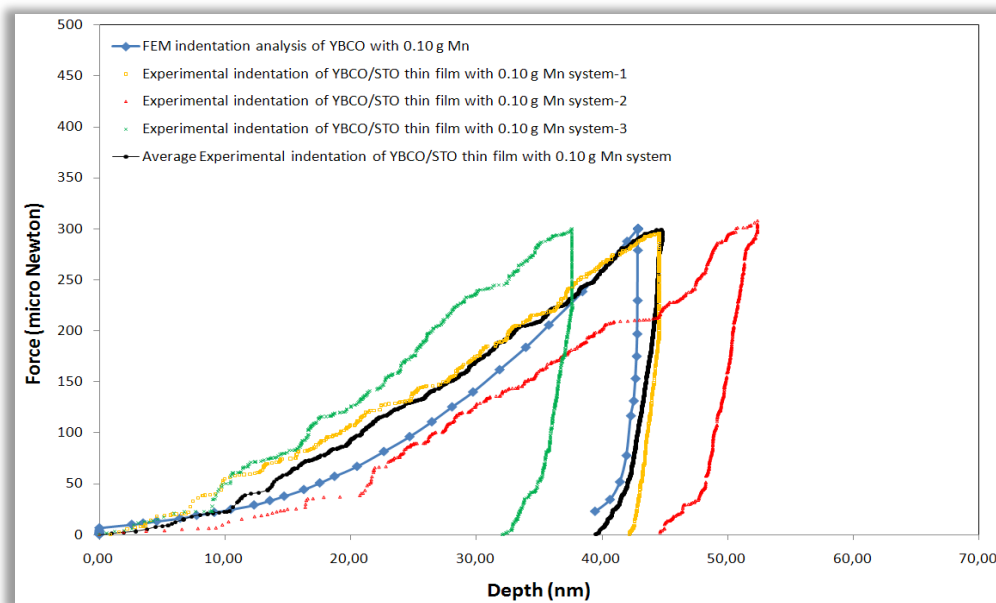
Figure 4.43 Comparisons of experimental and simulation indentation analysis of YBCO thin film with 0.10 g Mn.

Instrumented indentation and finite element analysis of YBCO thin film with 0.15 g Mn was demonstrated in Figure 4.44. Maximum and residual depths were obtained experimentally as 47.04 ± 6.1 nm and 37.48 ± 5.7 nm where as 47.17 nm and 40.43 nm for simulation. When the elastic modulus and yield stress were loaded to finite element simulation program as 76.47 GPa and 4.00 GPa, average load-displacement curve of sample and FEM numerical results showed good agreement both loading and unloading part of indentation curve.

Finite element analysis of instrumented indentation for given material property was represented in Figure 4.45. Elastic and plastic properties of model were iterated until same experimental and numeric load-unload curves obtained. According to the material property variation listed in Table 4.6, yield or failure stress of YBCO based films were determined as represented in Figure 4.46. When the Mn content increased from 0 g to 0.15 g and supplied $BaMnO_3$ formation in structure, yield stress of films decreased from 8.00 GPa to 4.00 GPa.
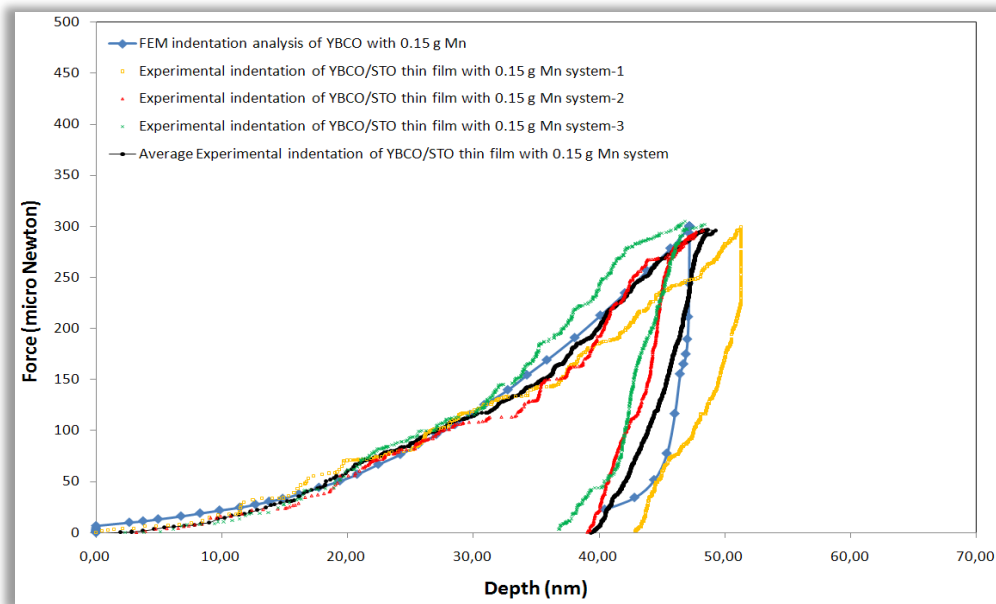
Figure 4.44 Comparisons of experimental and simulation indentation analysis of YBCO thin film with 0.15 g Mn.
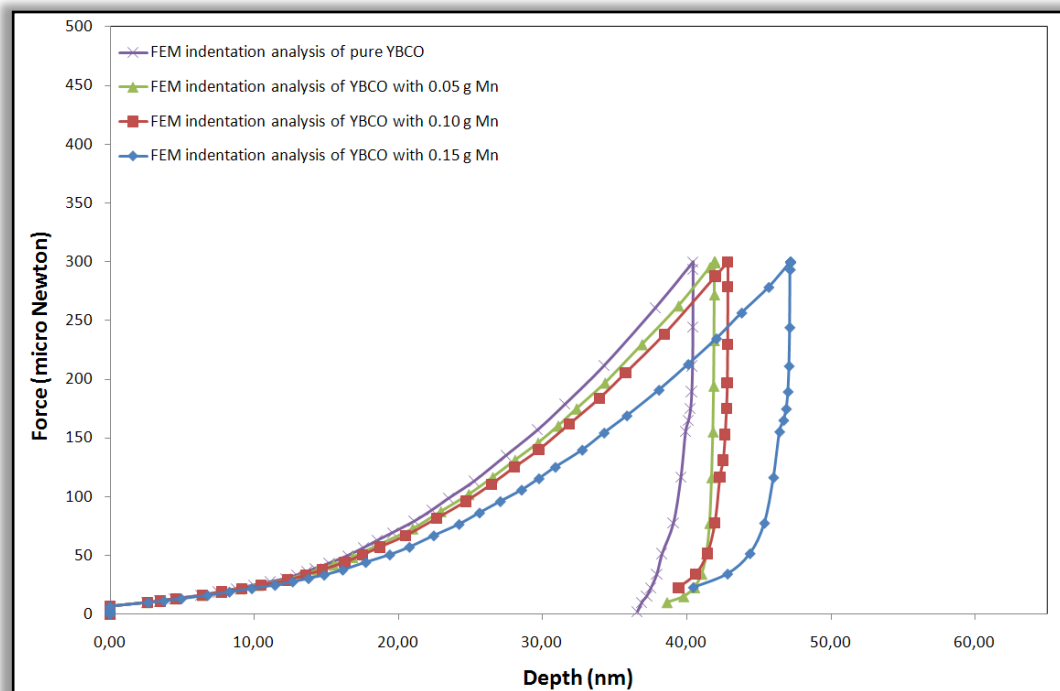

Figure 4.45 General FEM load-unload analysis of YBCO based thin films for given Material property.
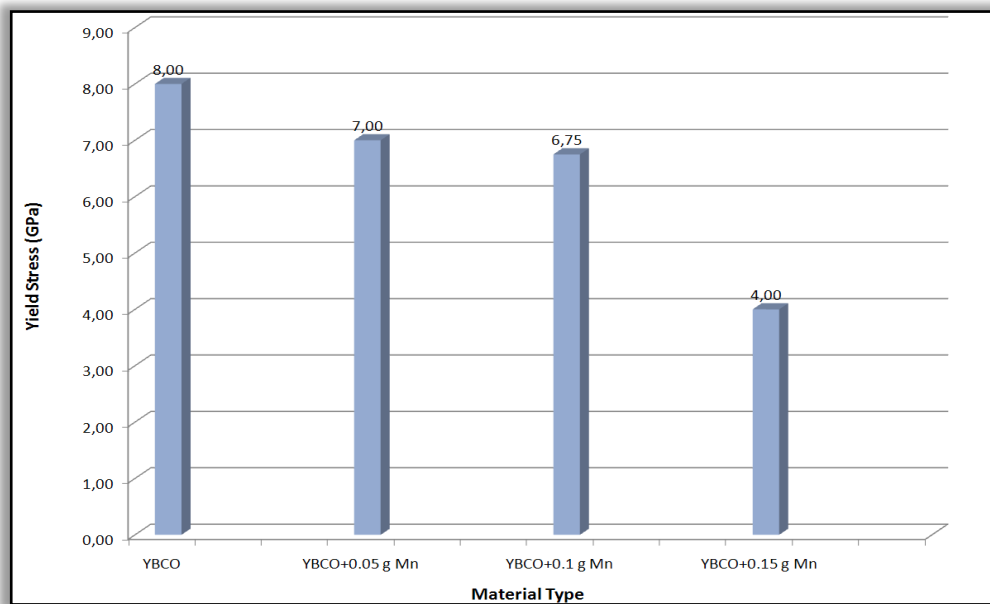
Figure 4.46 Yield Strength variations of YBCO based thin films determined by finite element analysis.

4.6.8 Stress Distribution of YBCO Based Films Under Applied Load

Stress distribution near contact region of indented material and indenter give very important information about simulation of experimental indentation. Maximum depth, residual depth and film thickness effects on substrate-film system under applied load can be observed when the field output request of indentation analysis was undertaken depend on steps of simulations. Figure 4.41 showed that Von misses equivalent stress distribution of pure YBCO based thin films under 300 μN applied at contact region.

Figure 4.47 a) and b) represented that approaching and beginning of contact steps of model. So, there was no stress both surface of indenter and film. However, when the loading step was started and load was increased linearly by time, diamond based indenter began to penetrate from surface to inside of pure YBCO based thin film, as represented Figure 4.47 c). According to the image at the end of the loading step, stress distributions penetrated to the substrate in very very small scale such as 25 MPa. This value could not effected clearly to the indentation results of pure YBCO

based thin films had 8.00 GPa yield stress. It was clearly considered that penetration of stresses to the substrate affected the indentation depth results in most cases. However, according to the Figure 4.47 e), stress distributions of indentation analysis was gone out from substrate and plastically indented surface of YBCO based thin films occurred when the unloading step finished.
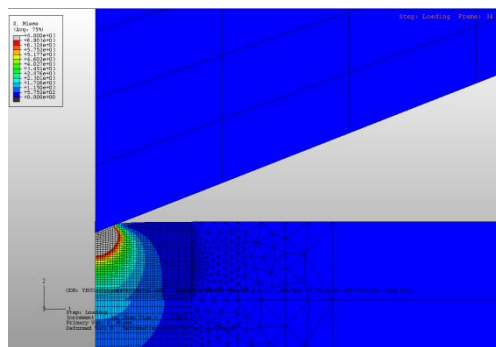
Elastic recovery of YBCO based thin film showed that there was a no residual stress on substrate while pure YBCO based thin film had due to plastically deformed contact region as illustrated in Figure 4.48 a) and b) for loading and unloading step of simulation.
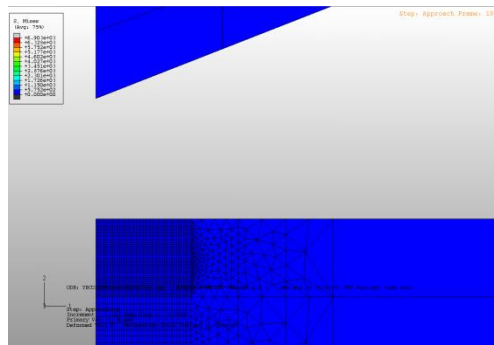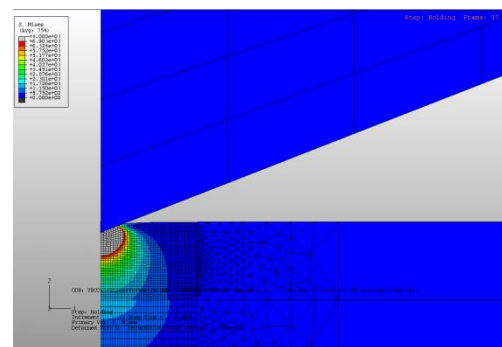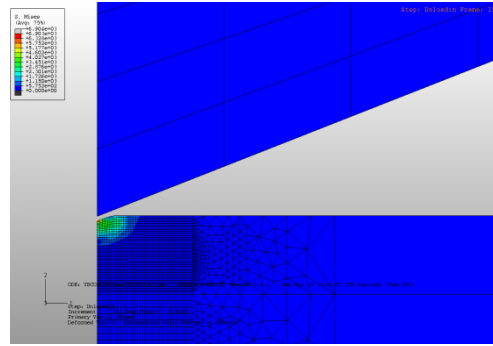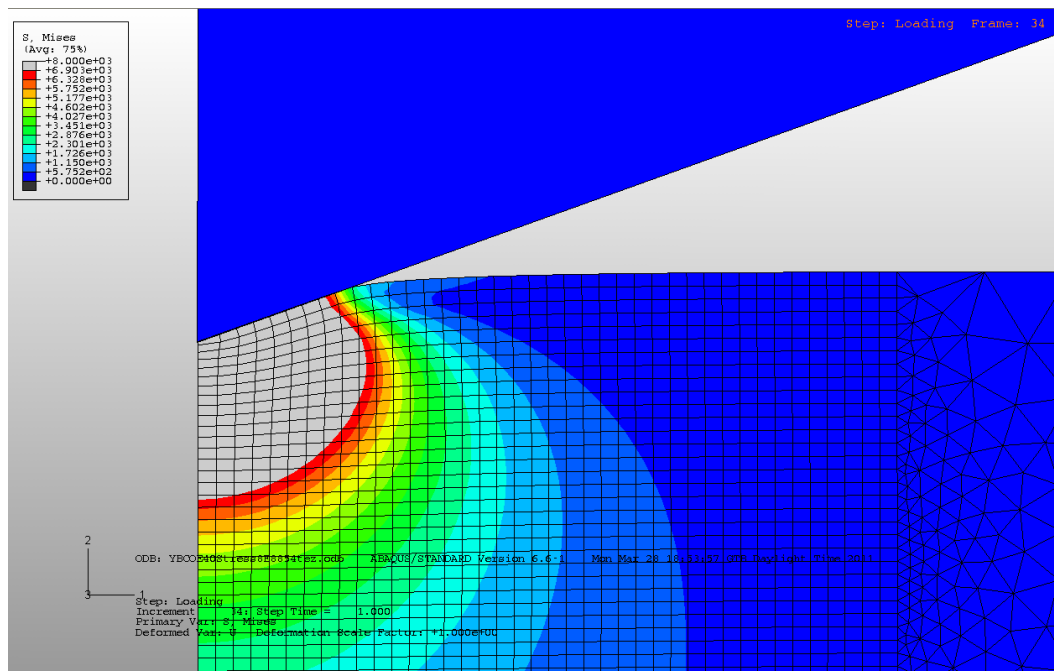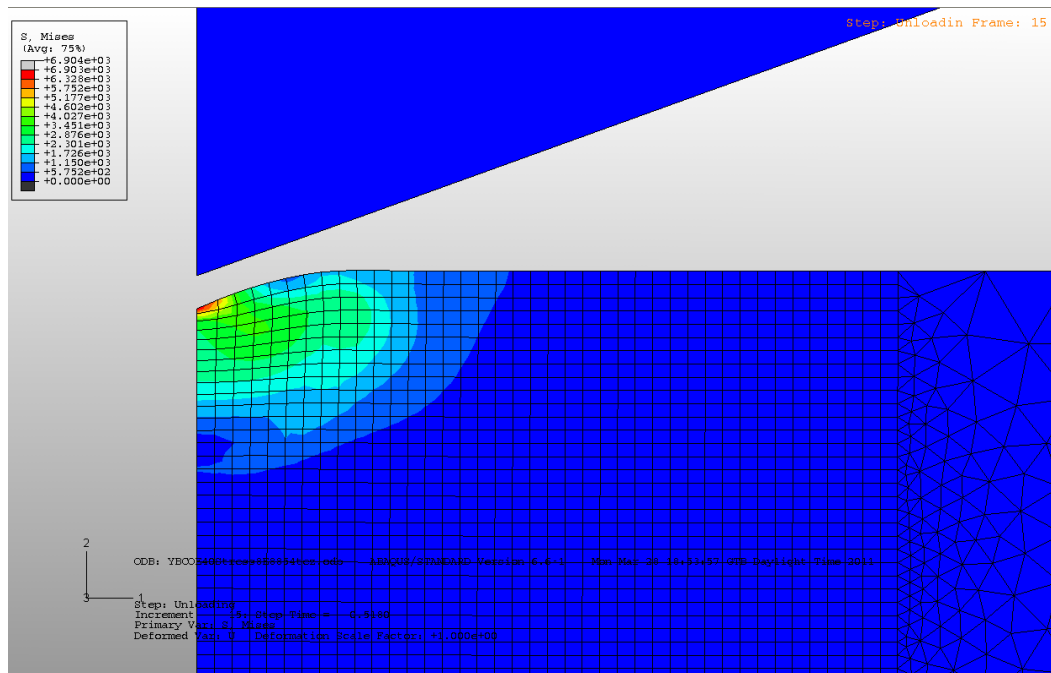

(a)
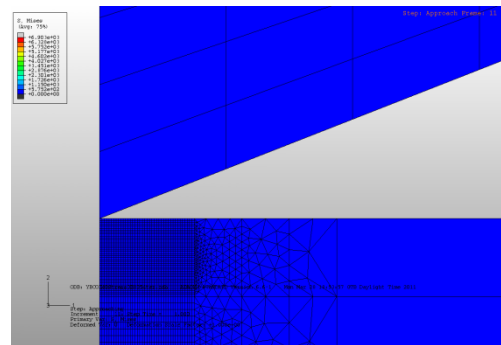
(b)

(c)

(d)

(e)

Figure 4.47 Von Misses Stress distributions of pure YBCO based thin film for (a) Approaching, (b) Contact, (c) Loading, (d) Holding and (e) Unloading part of indentation simulation with Abaqus 6.6-1 package program under 300 μN applied load.

(a)

(b)

Figure 4.48 Magnified view of (a) Loading and (b) Unloading part of pure YBCO based thin film under 300 µN applied load.

According to the analysis of indentation, firstly indenter approached and contact with surface. Secondly, indenter penetrated to surface until 300 µN applied was reached. As seen in Figure 4.48 a), stress distribution showed the yielded elements near contact region of indenter with surface. It is applicable that if the arise of stress formation is upon the set yield stress during loading step, plastically deformed part of contact region can be analyzed easily when the unloading step of simulation finished as represented in Figure 4.48 b).

Furthermore, depth analysis of pure YBCO based thin films together with stress distribution showed similar values with "sink in" formation theories. According to the depth analysis, h_r/h_{max} ratio of pure YBCO based films was 0.52 at the condition of E: 88.54 GPa and yield stress: 8.00 GPa under 300 µN applied load. Additionally, sink in effect observed in the magnified view of loading step in Figure 4.48 a) and b).

Von misses stress distribution of YBCO based thin film with 0.05 g Mn
(BaMnO$_3$) was shown in Figure 4.49. Figure 4.49 represented that approaching,
contact, loading, holding and unloading steps of entire model with condition of E:
83.41 GPa and yield stress: 7.00 GPa under 300 µN applied load. Stress formations
started from loading step while increasing applied load and penetration of indenter
into the surface. When the produced stresses was reached to the set yield stress value
at the end of the loading step, plastically deformed elements could be observed until
unloading step of analysis finished in simulation as represented Figure 4.49 e).

When the depth analysis of YBCO based thin films with 0.05 g Mn was
investigated, h_r/h_{max} ratio was obtained as 0.51. For a second time, sink in effect
occurred for YBCO based thin film with 0.05 g Mn under given input data to the
simulation.

(a)

(b)

(c)

(d)
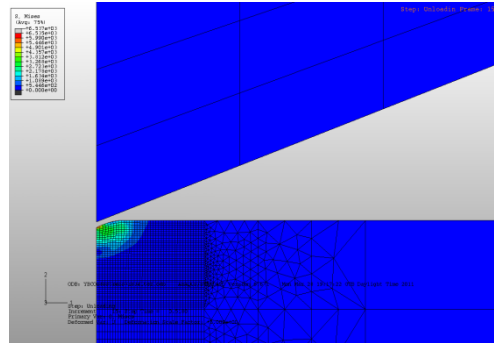
(e)

Figure 4. 49 Von Misses Stress distributions of YBCO based thin film with 0.05 g Mn for (a) Approaching, b) Contact, c) Loading, d) Holding and e) Unloading part of indentation simulation with Abaqus 6.6-1 package program under 300 μN applied load.
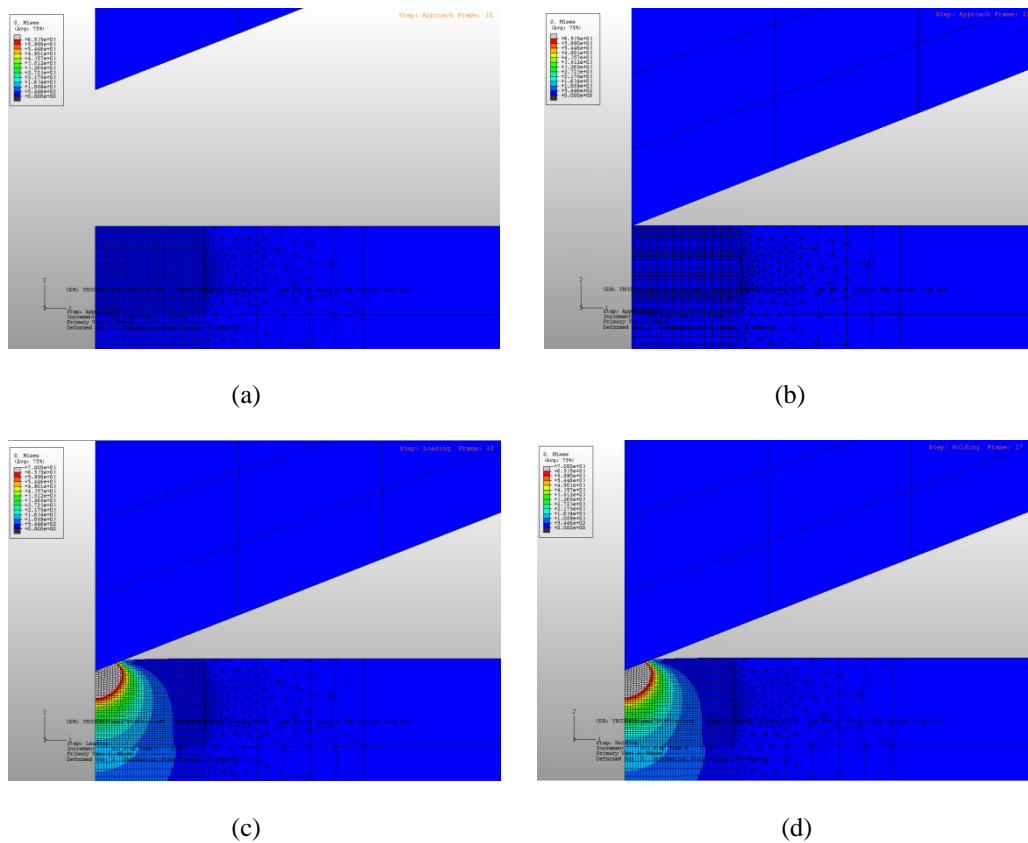
Magnified view of indentation and indented surface was illustrated in Figure 4.50 a) and b), respectively. Sink in effect and yielded elements of modeled YBCO based thin film with 0.05 g Mn addition was observed.
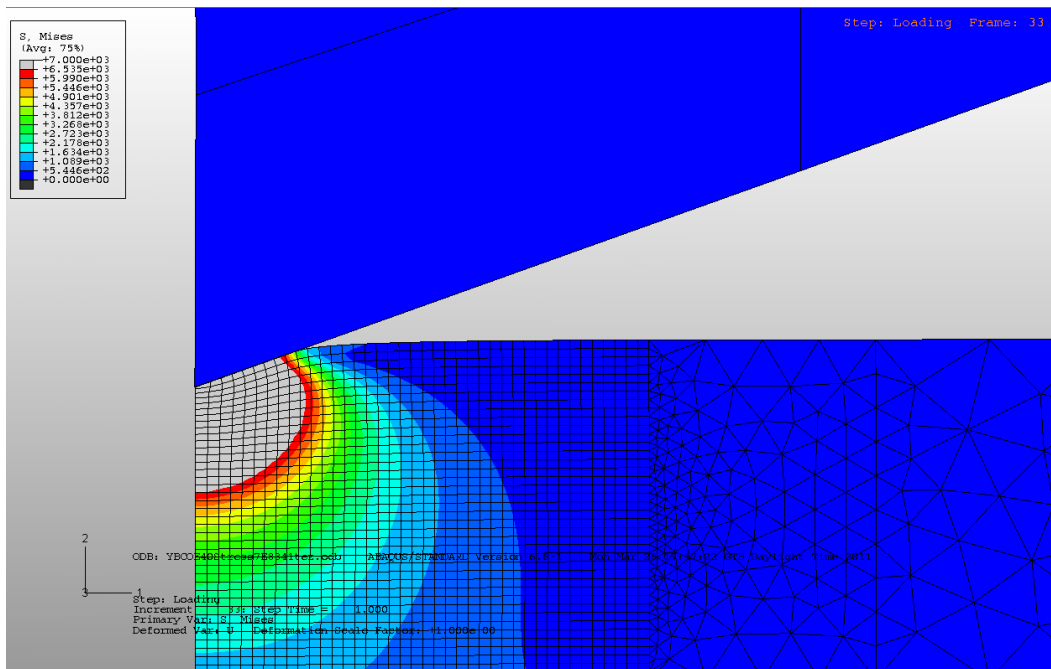
(a)
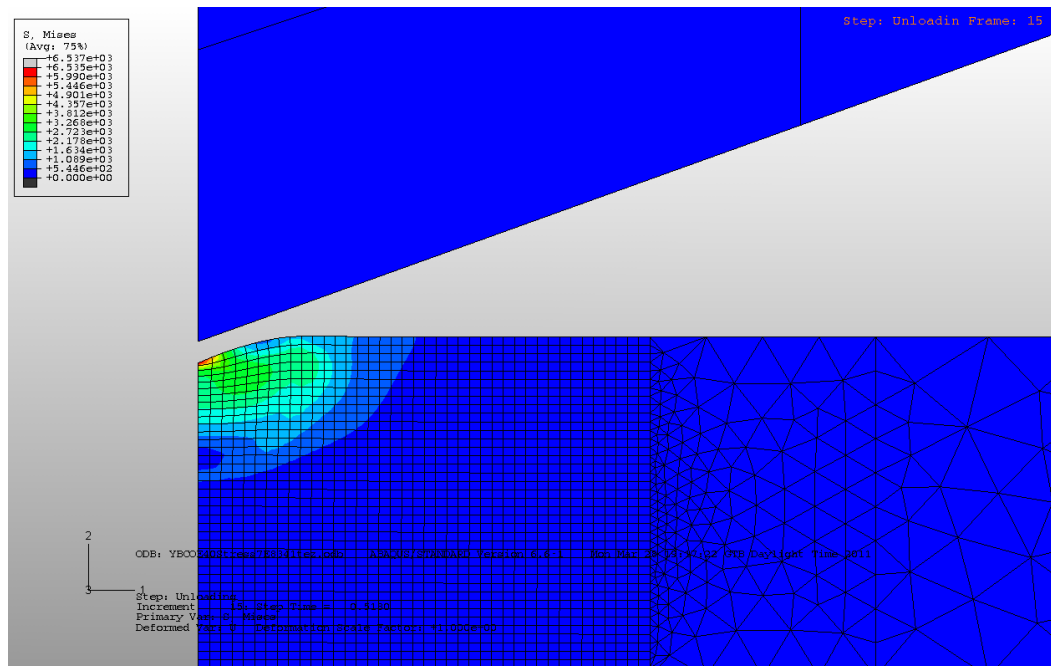
(b)

Figure 4.50 Magnified view of (a) Loading part and (b) Unloading part of YBCO based thin film with 0.05 g Mn under 300 µN applied load.

Von misses stress distribution of YBCO based thin film with 0.10 g Mn (BaMnO$_3$) was shown in Figure 4.51. Figure 4.51 represented that loaded steps of entire model with condition of E: 79.11 GPa and yield stress: 6.75 GPa under 300 µN applied load. Stress formations started from loading step by increasing applied load and penetration of indenter into the surface. As the produced stresses was upon to the set yield stress value at the end of the loading step, plastically deformed elements could be observed until unloading step of analysis finished in simulation as represented Figure 4.51 e).

When the depth analysis of YBCO based thin films with 0.10 g Mn was investigated, h_r/h_{max} ratio was obtained as 0.55. Thus, sink in effect occurred for YBCO based thin film with 0.10 g Mn under given input property to the simulation.

(a)

(b)

(c)

(d)

(e)

Figure 4.51 Von Misses Stress distributions of YBCO based thin film with 0.10 g Mn for (a) Approaching, (b) Contact, (c) Loading, (d) Holding and (e) Unloading part of indentation simulation with Abaqus 6.6-1 package program under 300 μN applied load.

Magnified view of penetration of indenter into the surface and indented surface was illustrated in Figure 4.52 a) and b), respectively. Sink in effect and yielded elements of YBCO based thin film with 0.10 g Mn addition was exposed by field output modulus of simulation program.
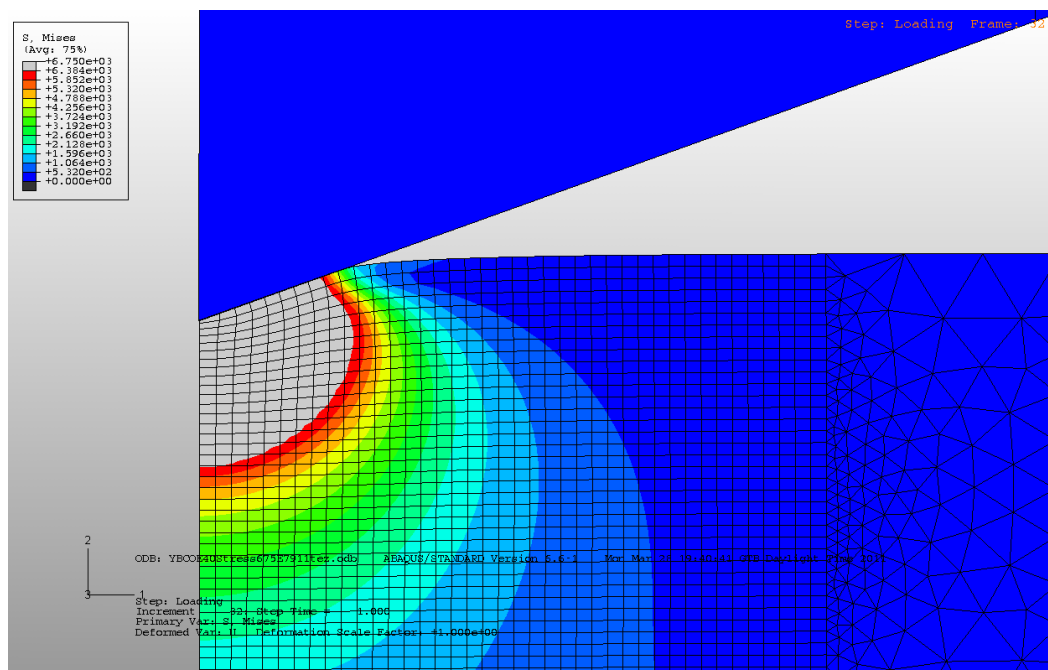
(a)
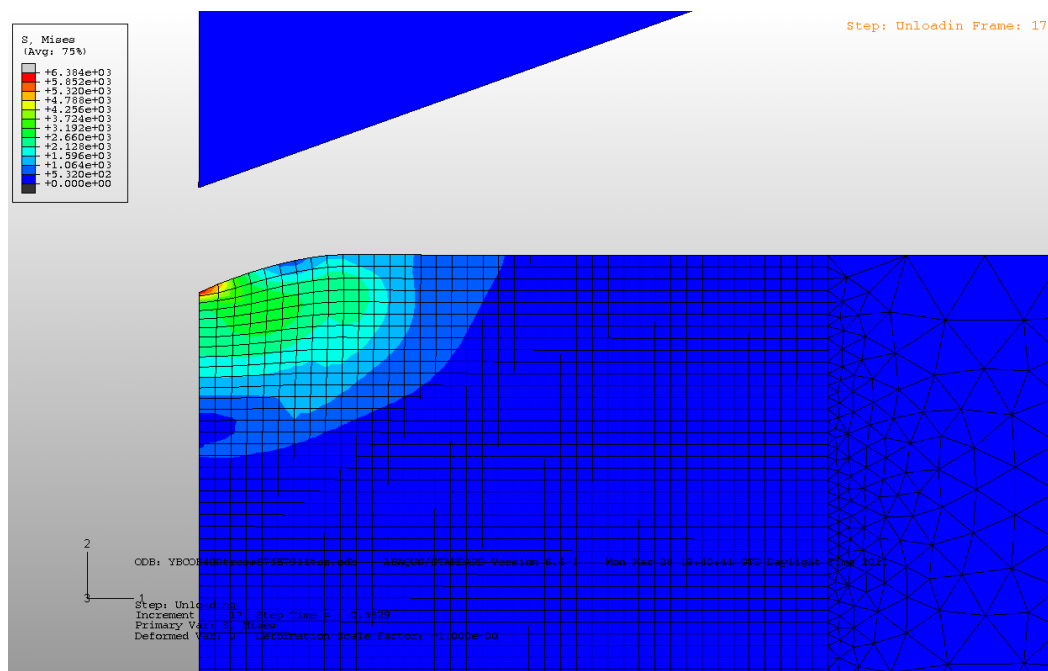
(b)

Figure 4.52 Magnified view of (a) Loading part and (b) Unloading part of YBCO based thin film with 0.10 g Mn under 300 μN applied load.

Von misses stress distribution of YBCO based thin film with 0.15 g Mn (BaMnO$_3$) was shown in Figure 4.53. Figure 4.53 represented the loaded steps of

entire model with condition of E: 76.47 GPa and yield stress: 4.00 GPa under 300 μN applied load. Stress formations started from loading step by increasing applied load and penetration of indenter into the surface. As the produced stresses was upon to the set yield stress value at the end of the loading step, plastically deformed elements could be observed until unloading step of analysis finished in simulation as represented Figure 4.53 e).

When the depth analysis of YBCO based thin films with 0.10 g Mn was investigated, h_r/h_{max} ratio was obtained as 0.67. Thus, sink in effect occurred for YBCO based thin film with 0.10 g Mn under given input property to the simulation.
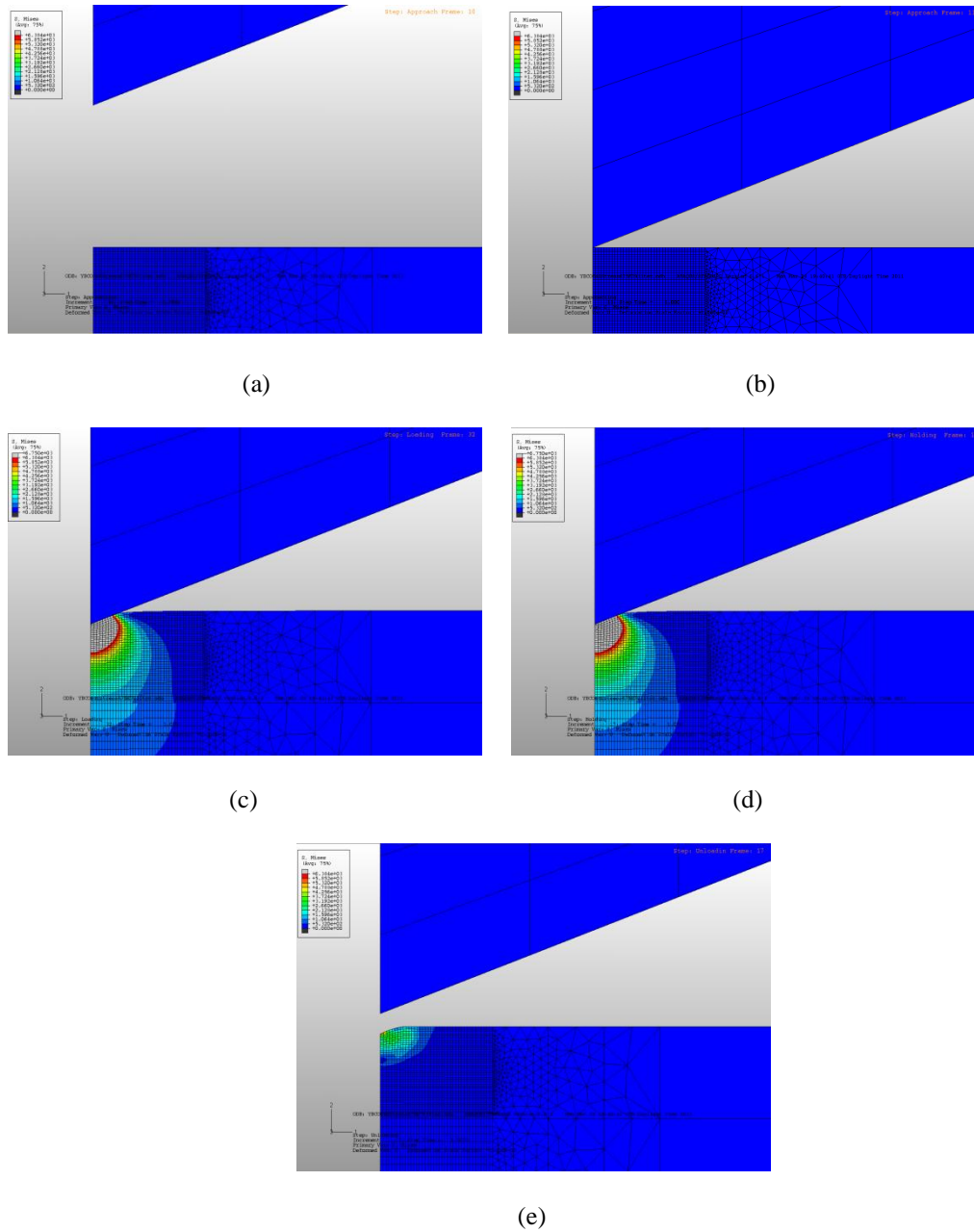

(a)

(b)

(c)

(d)

(e)

Figure 4.53 Von Misses Stress distributions of YBCO based thin film with 0.15 g Mn for (a) Approaching, (b) Contact, (c) Loading, (d) Holding and (e) Unloading part of indentation simulation with Abaqus 6.6-1 package program under 300 μN applied load.

Magnified view of penetration of indenter into the surface and indented surface was illustrated in Figure 4.54 a) and b), respectively. Sink in effect and yielded elements of YBCO based thin film with 0.15 g Mn addition was exposed by field output modulus of simulation program.
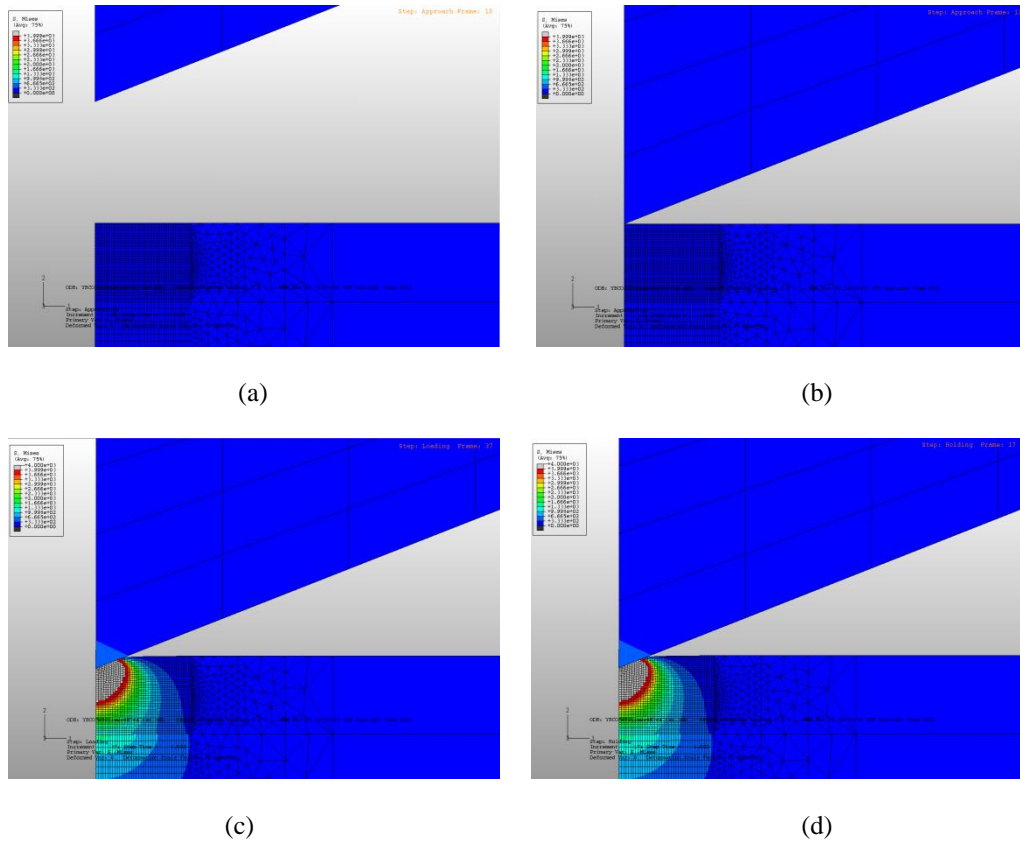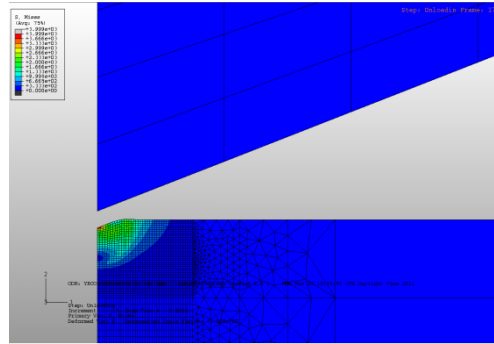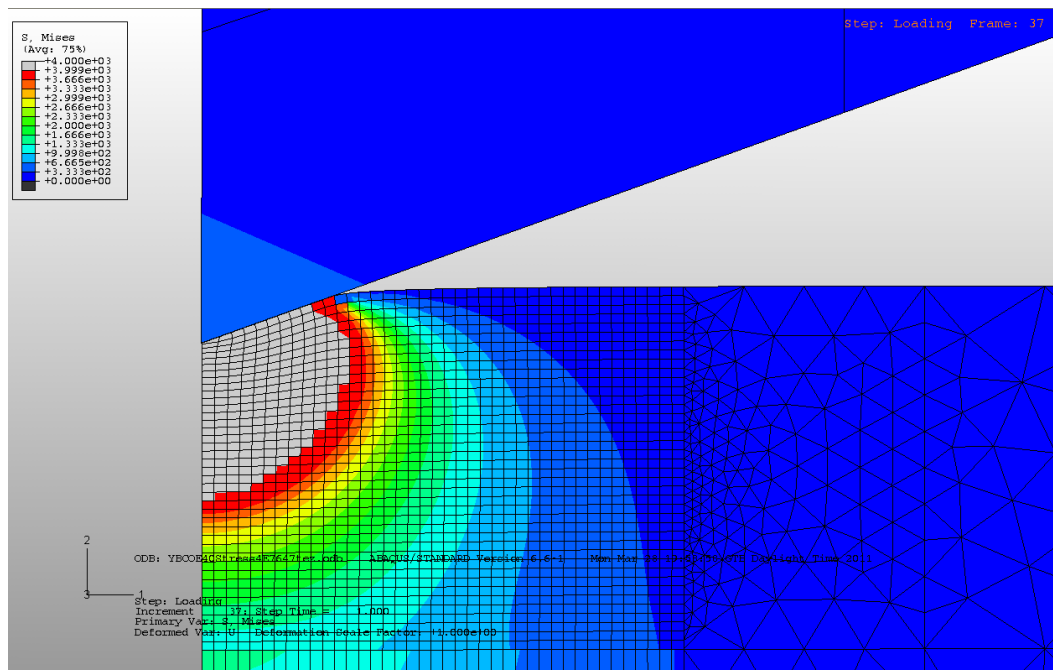

(a)
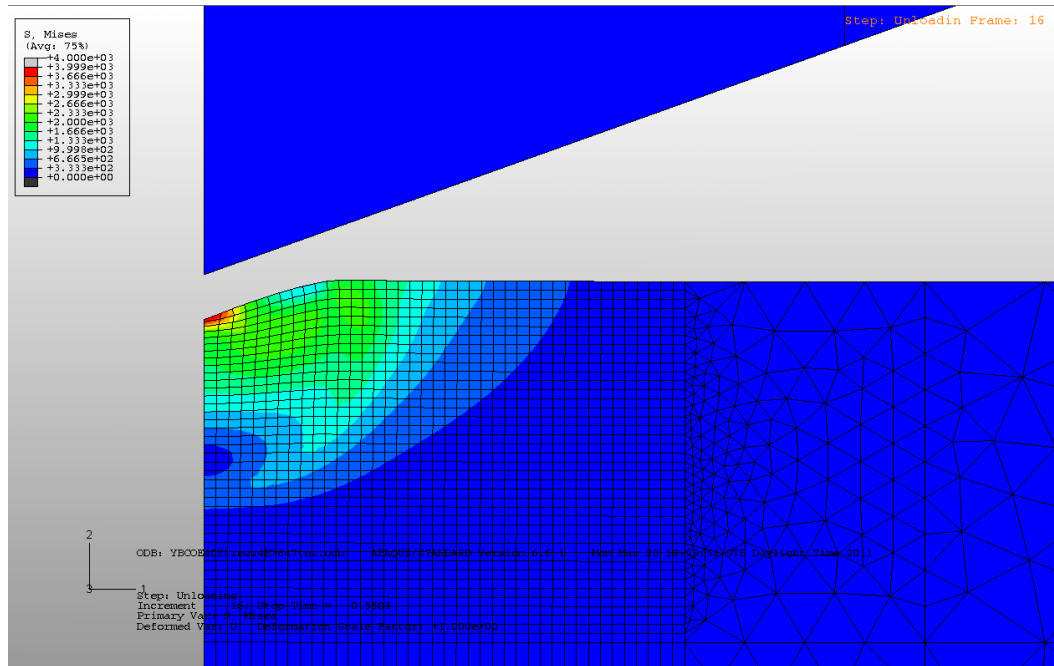
(b)

Figure 4.54 Magnified view of a) Loading part and b) Unloading part of YBCO based thin film with 0.15 g Mn under 300 µN applied load.

CHAPTER FIVE

CONCLUSION

5.1 General Results

In this study, YBCO with/without BaMnO$_3$ solutions were prepared by dissolving commercially available powders in propionic acid and trifluoroacetic acid (TFA). The prepared solutions were spin coated on STO single crystal substrate to determine the additional particles effects on both structural and mechanical properties. So, following results were obtained:

1- Turbidity values of pure YBCO, YBCO with 0.05 g Mn, YBCO with 0.10 g Mn and YBCO with 0.15 g Mn based solutions were measured as 0.65, 0.78, 0.97 and 1.25 ntu, respectively. These values pointed that powder based precursors are almost completely dissolved in all solutions.

2- The pH values of pure YBCO, YBCO with 0.05 g Mn, YBCO with 0.10 g Mn and YBCO with 0.15 g Mn based solutions were found to be as 0.74, 0.78, 0.82 and 0.98, respectively. This greater acidity could be caused by trifluoroacetic acid.

3- Viscosity values of pure YBCO, YBCO with 0.05 g Mn, YBCO with 0.10 g Mn and YBCO with 0.15 g Mn based solutions were 0.0060 Pa.s, 0.045 Pa.s, 0.065 Pa.s and 0.070 Pa.s, respectively. In addition, shear stress values of prepared solutions were changed as 1.80 Pa, 1.35 Pa, 1.95 Pa and 2.10 Pa depend on Mn content. Viscous modulus and elastic modulus of solutions were varied from 1.50 Pa to 0.45 Pa and from 1.75 Pa to 0.65 Pa, correspondingly.

4- Generally, three thermal phenomena in the xerogel were determined for the YBCO films. The first endothermic peaks represent this solvent removal. The

combustion process of organic groups occurred at ~250°C as a second thermal event. The significant amount of these weight losses as 50 % was observed.

6- FTIR analyses were performed to determine the removal of organic components in the structure.

7- XRD patterns show that YBCO films have (001) and parallel plane reflections for pure YBCO and YBCO with BaMnO$_3$ thin film.

8- According to the AFM study, when the amount of nanoparticle (roles as a pinning center) increases in film structure, topographies of sample became different from pure YBCO film.

9- SEM micrographs indicate that structural defects comprised of nanodots or nanoparticles of BaMnO$_3$ along the c-axis of YBCO film. These properties result in the enhanced pinning over the pure YBCO film.

10- It can be seen from the T_c analysis that there is sharp decrease in resistivity near 90 K.

11- Critical force values of YBCO based thin films were increased from 56 mN to 61 mN by increasing Mn content for scratch test. Likewise, the calculated adhesion strength of the films increased.

12- The calculated Young's modulus of YBCO based thin films with/without BaMnO$_3$ were decreased to in the range of 88.54 GPa and 76.41 GPa with increasing Mn content in microstructure. In addition indentation hardness values of films were decreased from 12.51 GPa to 3.88 GPa depend on Mn content.

13- Finite element analysis resulted that yield or failure stress of YBCO based thin films decreased by increasing Mn content in microstructure. Yield stress of pure YBCO thin films, YBCO thin films with 0.05 g Mn, YBCO thin films with 0.10 g

Mn and YBCO thin films with 0.15 g Mn were found to be 8.00 GPa, 7.00 GPa, 6.75 GPa and 4.00 GPa, respectively, by comparison of experimental and numerical load-penetration depth analysis under 300 μN applied load.

5.2 Future Plans

As known, mechanical properties variations of thin film superconductor is very important. Especially, residual stress caused by differences of thermal expansion coefficient of thin films and single crystal substrate affects superconducting properties and life time of film/substrate systems. For that reason, It is foreseen that residual stress calculation and mechanical coherency between superconductor film and single crystal substrate under cryogenic condition will be surveyed, in details.

REFERENCES

Abaqus theory manual version 6.1, Pawtucket: Hibbitt, Karlsson and Sorensen, Inc., 2000.

Abrikosov, A., (1957). Type II superconductors and the vortex lattice. *Journal of Experimental and theoretical physics, 32,* 1442.

Ak Azem, F, (2008). *Production of hydroxyapatite coatings by sol-gel technique on 316L stainless steel and its corrosion properties*. Dokuz Eylül University, Graduate School of Natural and Applied Sciences.

Alcala, J., Giannakopoulos, A. E. & Suresh, S., (1998). Sharp indentation of solids with gradients in elastic properties. *J. Mater. Res. 13,* 1390.

Araki, T., & Hirabayashi, I. (2003). Review of a chemical approach to YBa2Cu3O7-x coated superconductors-metalorganic deposition using trifluoroacetates. *Superconducting Science and Technology*, *16,* 71-94.

Araki, T., Kato, T., Muroga, T., Niwa, T., Yuasa T., Kurosaki, H., et al. (2003). Carbon Expelling scheme and required conditions for obtaining high-Jc $YBa_2Cu_3O_{7-x}$ film by metalorganic deposition using trifluoroacetates. *IEEE Transactions on Applied Superconductivity*, *13 (2).* 2803-2808.

Araki, T., Kurosaki, H., Yamada, Y., Hirabayashi I., Shibata, J., & Hirayama, T. (2001). Coating processes for $YBa_2Cu_3O_{7-x}$ superconductor by metalorganic deposition method using trifluoroacetates. *Superconducting Science and Technology, 14*, 783-786.

Araki, T., Kurosaki, H., Yuasa, T., Iijima, Y., Saitoh, T., Yamada, Y., et al. (2002). Dip coated $YBa_2Cu_3O_{7-x}$ film by metalorganic deposition using trifluoroacetates. *Physica C, 372-376*, 821-824.

Araki, T., Takahashi, Y., Yamagiwa, K., Iijima, Y., Takeda, K., Yamada, Y., et al. (2001). Firing condition for entire reactions of fluorides with water vapor in metalorganic deposition method using trifluoroacetates. *Physica C, 357-360*, 991-994.

Araki, T., Yamagiwa, K. & Hirabayashi, I., (2001).Fabrication of $YBa_2Cu_3O_{7-x}$ film by metalorganic deposition method using trifluoroacetates and its process conditions. *Cryogenics*, *41(9),* 675-681.

Araki, T., Yamagiwa, K., Hirabayashi, I., Suzuki, K. & Tanaka, S., (2001). Large-area uniform ultrahigh- $J_{(c)}$ $YBa_2Cu_3O_{7-x}$ film fabricated by the metalorganic deposition method using trifluoroacetates. *Superconductor Science & Technology, 14 (7),* 21-24.

Balian, R., Flocard, H. & Veneroni, M., (1999). Variational extensions of bcs theory. *Physics Reports, 317, (5-6),* 251-358.

Bardeen, J. & Stephen, M.J. (1965). Theory of Motion of Vortices in *Superconductors Physical Review, 140(4A)* 1197.

Barnes, N.P., Haugan, J.T., Sumption, D.M. & Harrison, C.B., (2005). Pinning enhancement of $YBa_2Cu_3O_{7-x}$ thin films with Y_2BaCuO_5 nanoparticles. *IEEE Transactions on Applied Superconductivity, 15, (2),* 3766-3769.

Bednorz and Muller, (1986). Possible High T_c Superconductivity in the Ba-La-Cu-O system. *Zeitschrift fur Physik B, 64*, 189.

Bhattacharya, A.K., Nix, W.D., (1988). Finite Element Simulation of Indentation Experiments'. *Int. J. Solids Structures., 24,* 881-891.

Bhuiyan, M. S., Paranthaman M, & Salama, K. (2006). Solution-derived textured

oxide thin films-a review. *Superconducting Science Technology, 19*, 1-21.

Binnig, G., Quate, C.F. & Gerber, C. (1986). Atomic force microscope, *Phys. Rev. Lett., 56 (9)*, 930-933.

Birlik, I., (2006). *Synthesis and characterization of buffer layers and YBa$_2$Cu$_3$O$_x$ superconducting coatings by chemical solution deposition method*. Dokuz Eylül University, Graduate School of Natural and Applied Sciences.

Block, S., Piermarini, G.J., Munro, R.G., Wong-Ng, W., (1987). The bulk modulus and Young's modulus of the superconductor Ba$_2$Cu$_3$YO$_7$. *Adv. Ceram. Mater*. 2, 601.

Bolshakov, A., Pharr, G. M., (1998). Influence of Pileup on the Measurement of Mechanical Properties by Load and Depth Sensing Indentation Techniques. *J. Mater. Res, Vol. 13(4)* 1049-1058.

Borodich, F.M., Keer, L.M., Korach, C.S., (2003). Analytical study of fundamental nanoindentation test relations for indenters of nonideal shapes. *Nanotechnology 14 (7)*, 803-808.

Bower, A.F., Fleck, N.A., Needleman, A. & Ogbonna, N. (1993). Indentation of a power law creeping solid. *Proc. R. Soc. Lond., 97*, 441-5471.

Breval, E. & MacMillan, N. H., (1985). Elastic recovery at Vickers hardness impressions. *J. Mater. Sci. Lett. 4,* 741.

Brinker, J. C. & Scherer, W. G. (1990). Sol- Gel Science the Physics and Chemistry of Sol-Gel Processing. USA: Academic Press.

Bull, S.J., (1997). Failure mode maps in the thin film scratch adhesion test. *Tribol. Int. 30,* 491-498.

Bull, S.J., (2005). Nanoindentation of coatings. J*ournal of Physics D: Applied Physics 38*, 393-413.

Callister D. W. (2000). *Materials science and engineering an introduction (5)*. USA: Wiley.

Casals, O., Alcala, J., (2005). The duality in mechanical property extractions from Vickers and Berkovich instrumented indentation experiments. *Acta Materialia 53 (13),* 3545-3561.

Celik, E., Avci, E. & Hascicek, Y.S. (2004). Growth Characteristic of ZrO_2 Insulation Coatings on Ag/AgMg Sheathed Bi-2212 Superconducting Tapes. *Mat. Sci. Eng. B 110,* 213-220.

Chae, H.K., Payne, D.A., Xu Z.K., & Ma, L.Q., (1994). Molecular-Structure of a New Lead Titanium Bimetallic Alkoxide Complex, $[Pbti_2(Mu(_4)-O)(Oocch_3)(Och_2ch_3)(_7)]_{(2)}$ - Evolution of Structure on Heat-Treatment and the Formation of Thin-Layer Dielectrics. *Chemistry of Materials, 6(10),* 1589-1592.

Chen, J. & Bull, S.J., (2009). On the factors affecting the critical indenter penetration for measurement of coating hardness. *Vacuum, 83,* 911-920.

Chen, J. Bull, & S.J., (2006). A critical examination of the relationship between plastic deformation zone size and Young's modulus to hardness ratio in indentation testing. *Journal of Materials Research 21*, 2617- 2627.

Chen, X., Vlassak, JJ., (2001). Numerical study on the measurement of thin film mechanical properties by means of nanoindentation. *J. Mater. Res.16*, 2974.

Cheng, Y.T. & Cheng, C.M. (2004). Scaling, dimensional analysis, and indentation measurements. *Mater. Sci. Eng., 44,* 91.

Chollacoop, N., Dao, M., Suresh, S., (2003). Depth-sensing instrumented indentation with dual sharp indenters. *Acta Materialia 51 (13),* 3713- 3729.

Cooper, B.R., (1965). Theory of Superconductivity. *Ieee Spectrum, 1965. 2(8),* 158.

Cui, M. B., Tao, W., Tian, Z. J., iong, X., Zhang X. F. & Li, Y. R., (2006) Enhancement of flux pinning of TFA-MOD YBCO thin films by embedded nanoscale Y_2O_3. *Supercond. Sci. Technol. 19*, 844-847.

Cui, X.M., Tao, B.W., Xiong, J., Liu, X.Z., Zhu, J., Li, Y.R., (2005). Effect of annealing time on the structure and properties of YBCO films by the TFA-MOD method. *Physica C 432,* 147-152.

Dao, M., Chollacoop, N., Van Vliet, K.J., Venkatesh, T.A. & Suresh, S., (2001). Computational modeling of the forward and reverse problems in instrumented sharp indentation. *Acta Materialia 49 (19)*, 3899-3918.

Dao, N., Chollacoop, K., Van Vlient, J., Venkatesh, T. A. & Suresh, S., (2001). Computational modeling of the forward and reverse problems in instrumented sharp indentation. *Acta mater. 49*, 3899-3918.

Dawley, J.T., Clem, P.G., Siegal, M.P., Overmyer, D.L. & Rodriguez, M.A. (2001) Thick sol-gel derived $YBa_2Cu_3O_{7-x}$ films. *Ieee Transactions on Applied Superconductivity*, *11(1),* 2873-2876.

Dey, S.K., Budd, K.D. & Payne, D.A. (1988). Thin-Film Ferroelectrics of PZT by Sol-Gel Processing. *Ieee Transactions on Ultrasonics Ferroelectrics and Frequency Control, 35(1)*, 80-81.

Doerner, M. F. & Nix, W. D., (1986). A Method For Interpreting the Data From Depth-Sensing Indentation Instruments. *J. Mater. Research, 4,* 601.

Doi, T.J., Yuasa, T., Ozawa, T. & Higashiyama, K., (1994). Advance in Superconductivity VII. Springer-Verlag, Tokyo.

Dwir, B., Pavesi, L., James, J.H., Keilelt, B., Pavuna, D. & Reinhart, F.K., (1989). A simple high temperature superconducting thin film optical bolometer, *Supercond. Sci. Technol. 2,*314-316.

Eickemeyer, J., Selbmann, D., Opitz, de Boer R., Holzapfel, B., Schultz, B. L. & Miller, U. (2001) Nickel-refractory metal substrate tapes with high cube texture stability. *Superconductor Science & Technology, 2001. 14(3),* 152-159.

Feenstra, R., (2002). YBCO by Ex-situ BaF_2 Process. *International Workshop on Processing & Application of Superconductors*, Gatlinburg Tennessee, USA, 2002.

Feenstra, R., Lindemer, T.B., Budai, J.D. & Galloway, M.D., (1991). Effect of Oxygen-Pressure on the Synthesis of $YBa_2Cu_3O_{7-x}$ Thin Films by Postdeposition Annealing. *Journal of Applied Physics, 1991. 69(9).* 6569-6585.

Ficher-Cripps, A.C., Ling, F.F., (2002). Nanoindentation. Springer, London.

Fischer-Cripps, A.C., (2001). Use of Combined Elastic Modulus in the Analysis of Depth-Sensing Indentation Data. *Journal of Materials Research, 16,* 3050-3052.

Fleck, N.A., Hutchinson, J.W., 1993. A phenomenological theory for strain gradient effects in plasticity. *Journal of the Mechanics and Physics of Solids 41 (12),* 1825-1857.

Freund, L.B. & Suresh, S., (2004). Thin Film Materials: Stress, Defect Formation and Surface Evolution, Cambridge University Press, New York.

Freyhardt, H.C., (2002). YBCO by Laser Deposition. *International Workshop on*

Processing & Application of Superconductors, Gatlinburg Tennessee, USA.

Gamonpilas, C., Busso, E.P., (2004). On the effect of substrate properties on the indentation behaviour of coated systems. *Materials Science and Engineering A 380 (1-2),* 52-61.

Gavaler, J.R., (1973). Superconductivity in Nb-Ge Films above 22 K. *Applied Physics Letters, 23(8),* 480-482.

Gerberich, W.W., Nelson, J.C., Lilleodden, E.T., Anderson, P., Wyrobek, J.T., (1996). Indentation induced dislocation nucleation: the initial yield point. *Acta Materialia 44 (9),* 3585-3598.

Giannakopoulos, A. E. & Larson, P.L., (1997). Analysis of pyramid indentation of pressure-sensitive hard metals and ceramics. *Mech. Mater. 25,* 1-35.

Giannakopoulos, A. E. & Suresh, S., (1999). Determination of elastoplastic properties by instrumented sharp indentation. *Scripta Materialia., 40-10,* 1191-1198.

Giannakopoulos, A. E., Larson P.L. & Vestergaard R., (1994). Analysis of Vickers indentation. *Inter. J. Solids Struc., 31,* 2679-2688.

Ginzburg, V.L. and Landau, L.D., (1950). Zh. Eksperim. i Teor. Fiz., 20: p. 1064.

Goyal, A., Lee, D.F., List, F.A., Specht, E.D., Feenstra, R., Paranthaman, M., Cui, X., et al., (2001). Recent progress in the fabrication of high-$J_{(c)}$ tapes by epitaxial deposition of YBCO on RABiTS. *Physica C, 357*, 903-913.

Goyal, A., Norton, D.P., Christen, D.K., Specht, E.D., Paranthaman, M., Kroeger, D.M., Budai, J.D., et al., (1996). Epitaxial superconductors on rolling-assisted biaxially- textured substrates (RABiTS): A route towards high critical current

density wire. *Applied Superconductivity, 4(10-11),* 403-427.

Grady, D.E. (1983), Impact strength and indentation hardness of high-strength ceramics, *Proc. of the Topical Conf. on Shock Waves in Condensed Matter*, Colorado Springs, CO.

Gross, M.E., Hong, M. Liou, S.H., Gallagher, P.K. & Kwo, J., (1988). Versatile New Metalorganic Process for Preparing Superconducting Thin-Films. *Applied Physics Letters, 52(2),* 160-162.

Groves, J.R., Arendt, P.N., Foltyn, S.R., DePaula, R.F., Wang, C.P. & Hammond, R.H. (1999). Ion-beam assisted deposition of bi-axially aligned MgO template films for YBCO coated conductors. *Ieee Transactions on Applied Superconductivity,* 9(2), 1964-1966.

Gupta, A., Cooper, E.I., Jagannathan, R., Hussey, B.W. & Giess, E.A., (1988). Processing and Patterning of Superconducting Oxide-Films Using Solution Precursors. *American Chemical Society, 196,* 45.

Gupta, A., Jagannathan, R., Cooper, E.I., Giess, E.A., Landman, J.I. & Hussey, B.W. (1988) Superconducting Oxide-Films with High Transition-Temperature Prepared from Metal Trifluoroacetate Precursors. *Applied Physics Letters, 52(24)* 2077-2079.

Hari Babu, N., Iida, K. & Cardwell, D.A., (2006). Enhanced magnetic flux pinning in nanocomposite Y-Ba-Cu-O superconductors. *Physica C 445-448*, 353-356.

Haruta, M., Fujiyoshi, T., Sueyoshi, T., Dezaki, K., Ichigosaki, D., Miyahara, K., Miyagawa, R., Mukaida, M., Matsumoto, K., Yoshida, Y., Ichinose, A. & Horii, S., (2006). Flux pinning properties of $ErBa_2Cu_3O_y$ thin films with $BaZrO_3$ nanorods. *Superconductor Science and Technology, 19,* 803-807.

Heard, H.C. & Cline, C.F., (1980). Mechanical behavior of polycrystalline BeO, AI$_2$0$_3$ and AIN at high pressure. *J. Mater. Sci. 15*, 1889-1897.

Hedenqvist, P. & Hogmark S., (1997). Experiences from scratch testing of tribological PVD coatings. *Tribol. Int. 30,* 507-516.

Hilgenkamp, H. & Mannhart, J., (2002). Grain boundaries in high-T_c superconductors. *Reviews of Modern Physics, 74(2),* 485-549.

Hill, R.,(1992). Similarity analysis of creep indentation test. *Proc. R. Soc. Lond., A 436*, 617.

Hirano, S.I. & Kato, K., (1987). Synthesis of LiNBO$_3$ by Hydrolysis of Metal Alkoxides. *Advanced Ceramic Materials*, 2(2), 142-145.

Holmberg, K., Laukkanen, Ronkainen, A., Wallin, H. K. & Varjus, S., (2003). A model for stresses, crack generation and fracture toughness calculation in scratched TiN-coated steel surfaces. *Wear 254,* 278.

Huber, N., Nix, W.D., Gao, H., (2002). Identification of elastic-plastic material parameters from pyramidal indentation of thin films. *Proc. Roy. Soc. Lond. A, 458*:1593.

Jee, Y.A., Li, M., Ma, B., Maroni, V.A., Fisher, B.L., Balachandran, U., (2001). Comparison of texture development and superconducting properties of YBCO thin films prepared by TFA and PLD processes. *Physica C 356*, 297-303.

Jin, M., Han, S., Sung, T. & No, K., (2000). Biaxial texturing of Cu sheets and fabrication of ZrO$_2$ buffer layer for YBCO HTS films. *Physica C, 334(3-4).* 243-248.

Johansen, H.T., (2000). Flux-pinning-induced stress and magnetostriction in bulk

superconductors. *Superconducting Science and Technology, 13*, 121-137.

Johansen, T.H., (2000). Flux-pinning-induced stress and magnetostriction in bulk superconductors. *Supercond. Sci. Technol.* 13,121.

Johnson, D., Hilal, N., & Bowen, W. R. (2000). Basic Principles of Atomic Force Microscopy Atomic Force Microscopy in Process Engineering.

K. L. Johnson, J. Mech. Phys. Solids. 18, 115 (1970).

Kakihana, M., (1996). Sol-Gel preparation of high temperature superconducting oxides. *Journal of Sol-Gel Science and Technology, 1996. 6(1),* 7-55.

Kessler, V.G., Hubertpfalzgraf, L.G., Daniele, S. & Gleizes, A., (1994). Single-Source Precursors for $BaTiO_3$- Synthesis and Characterization of Beta-Diketonato Alkoxides and Molecular- Structure. *Chemistry of Materials, 6(12), 2336-2342*.

Kindrachuk, V.M., Galanov, B.A., Kartuzovl, V.V. & Dub, S.N., (2006). On elastic nanoindentation of coated half-spaces by point indenters of non-ideal shapes. *Nanotechnology 17 (4),* 1104-1111.

Klee, M., Eusemann, R., Waser, R., Brand, W. & Vanhal, H., (1992). Processing and Electrical-Properties of $Pb(Zr_xTi_{1-X})O_3$ (X = 0.2-0.75) Films - Comparison of Metalloorganic Decomposition and Sol-Gel Processes. *Journal of Applied Physics, 1992. 72(4)*, 1566-1576.

Korsunsky, A.M. et al., (1998). On the hardness of coated systems. *Surface & Coatings Technology 99*, 171-183.

Lakew, B., Brasunas, J.C., Aslam, S., & Pugel, D.E., (2004). High-T_c, transition-edge superconducting (TES) bolometer on a monolithic sapphire membrane-construction and performance. *Sensor. Actuat. A-Phys. 114*, 36-40.

Lange, F.F.,(1996). Chemical solution routes to single-crystal thin films Science, 273 (5277), 903-909.

Lankford, J. (1977), Compressive strength and microplasticity in polycrystalline alumina, *J. Mater. Sci. 12,* 791-796.

Larbalestier, D., Gurevich, A., Feldmann, D.M. & Polyanskii, A., (2001). High-Tc superconducting materials for electric power applications. *Nature 414 (6861)*, 368-377.

Larson, P.L., Giannakopoulos, A. E., Soderlund, E. D., Rowcliffe, J. & Vestergaard, R., (isim). *Int. J. Solids Struct. 33*, 221.

Lawn, B. R., (1993). Fracture of Brittle Solids. Cambridge University Press, UK.

Ledbetter, H.M., Austin, M.W., Kim, S.A., Lei, M., (1987). Elastic constants and Debye temperature of polycrystalline yttrium barium copper oxide ($YBa_2Cu_3O_{7-x}$). *J. Mater. Res.* 2, 786.

Lee D.F, e.a., (2002). Continuous Reel-to-Real Ex-situ Processing of YBCO on Textured Substrates. *International Workshop on Processing & Application of Superconductors,* Gatlinburg Tennessee, USA.

Lee Hee-Gyoun, C.G., et al., (2002). Reel-to-Real Fabrication of High Tc YBCO Coated Conductors by Metalorganic Chemical Vapor Deposition. *International Workshop on Processing & Application of Superconductors*, Gatlinburg Tennessee, USA.

Lee, S.Y., Song, S.A., Kim, B.J., Park, J.A., Kim, H.J. & Hong, G.W., (2006). Effect of precursor composition on J_c enhancement of YBCO film prepared by TFA-MOD method. *Physica C 445-448*, 578-581.

Li, M., Chen, W.M., Liang, N.G., Wang, L.D., (2004). A numerical study of indentation using indenters of different geometry. *Journal of Materials Research 19*, 73-78.

Lim, J.H., Jang, S.H., Ha, H.S., Lee, J. S., Yoon, K.M., Joo, J., Jung, S., et al., (2006). Fabrication of YBCO coated conductor by TFA-MOD using the "211 process. *Physica C: Superconductivity 445-448,* 594-597.

Lim, Y.Y, Chaudhri, M.M., (2002). Nanohardness mapping of the curved surface of spherical macroindentations in fully annealed polycrystalline oxygen-free copper. *Phys. Status. Solid. A: Appl. Res.*, 194, 19–29.

Lockett, F. J.,(1963). Plastic indentation in metals with cones. *J. Mech. Phys. Solids. 11*, 345.

London, F. & London, H., (1935). The Electromagnetic Equation of the Superconductor. *Proceedings of the Royal Society (London) A149*, 71-88.

Loubet, J. L., Georges, J. M., Marchesini, J. M. & Meille, G. (1984). Vicker's indentation curves of magnesium oxide (MgO). *J. Tribology, 106*, 43.

Ma, D.J., Xu, K.W., He, J.W., Lu, J., (1999). Evaluation of the mechanical properties of thin metal films. *Surface and Coatings Technology 116- 119*, 128-132.

MacManus-Driscoll, J.L., (1998). Recent developments in conductor processing of high irreversibility field superconductors. *Annual Review of Materials Science*, *28,* 421-462.

Malozemoff, A., (2002).Application of Coated Conductors International Workshop on Processing & Application of Superconductors, Gatlinburg Tennessee, USA.

Manabe, T., Yamaguchi, I., Kondo, W., Mizuta, S. & Kumagai, T., (1997). Preparation of epitaxial La$_{1-x}$Sr$_x$MnO$_3$ films on SrTiO$_3$(001) by dipping-pyrolysis process. *Journal of Materials Research*, *12(2)* 541-545.

Mankiewich, P.M., Scofield, J.H., Skocpol, W.J., Howard, R.E., Dayem, A.H. & Good, E., (1987). Reproducible Technique for Fabrication of Thin-Films of High Transition-Temperature Superconductors. *Applied Physics Letters, 1987. 51(21)*, 1753-1755.

Mannhart, J. and Chaudhari, P., (2001). High-T$_c$ bicrystal grain boundaries. *Physics Today, 54(11),* 48-53.

McIntyre, P.C., Cima, M.J. & Roshko, A., (1995). Epitaxial Nucleation and Growth of Chemically Derived Ba$_2$YCu$_3$O$_{7-X}$ Thin-Films on (001) SrTiO$_3$. *Journal of Applied Physics, 1995. 77(10)*, 5263-5272.

McIntyre, P.C., Cima, M.J., Ng, M.F., Chiu, R.C. & Rhine, W.E., (1990). Texture Development in Ba$_2$YCu$_3$O$_{7-X}$ Films from Trifluoroacetate Precursors. *Journal of Materials Research, 5(12),* 2771-2779.

McIntyre, P.C., Cima, M.J., Smith, J.A., Hallock, R.B., Siegal, M.P. & Phillips, J.M., (1992). Effect of Growth-Conditions on the Properties and Morphology of Chemically Derived Epitaxial Thin- Films of Ba$_2$YCu$_3$O$_{7-X}$ on (001) LaAlO$_3$ *Journal of Applied Physics, 71(4),* 1868-1877.

Mele, P., Matsumoto, K., Horide, T., Miura, O., Ichinose, A., Mukaida, M., Yoshida, Y.& Horii, S., (2005). Control of Y$_2$O$_3$ nanoislands deposition parameters in order to induce defects formation and its influence on the critical current density of YBCO films. *Physica C: Superconductivity, 426-431*, 1108-1112.

Meng, R.L., Wang, Y.Q., Lewis, K., Garcia, C., Cao, Y. & Chu, C.W., (1998). Hg-1223 thick film on flexible Ni substrates. *Journal of Superconductivity, 11(1),*

181-184.

Nix W.D. & Gao H., (1998). Indentation size effects in crystalline materials: a law for strain gradient plasticity. *J. Mech. Phys. Solids., 46,* 411.

Nix W.D., (1989). Mechanical properties of thin films. *Metal. Mater. Trans. A 20*, 2217.

Norton, D.P., Goyal, A., Budai, J.D., Christen, D.K., Kroeger, D.M., Specht, E.D., et al., (1996). Epitaxial YBa2Cu3O7 on biaxially textured nickel (001): An approach to superconducting tapes with high critical current density Science, 274 (5288), 755-757.

Oliver, W. C., Pharr, G. M., (1992). 'An Improved Technique for Determining Hardness and Elastic Modulus Using Load and Displacement Sensing Indentation Experiments. *J. Mater. Res, 7(6)* 1564-1583.

Oliver, W.C. & Pharr, G.M., (1992). An improved technique for determining hardness and elastic modulus using load and displacement sensing indentation experiments. *J. Mater. Res. 7,* 1564.

Oliver, W.C. & Pharr, G.M., (2004). Measurement of hardness and elastic modulus by indentation. *J. Mater. Res., 19,* 3.

Owens, F. J., & Poole, C. P. Jr. (1996). *The new superconductors*. New York: Plenum Press.

Panich, N., Sun, Y., (2004). Effect of penetration depth on indentation response of soft coatings on hard substrates: a finite element analysis. *Surface and Coatings Technology 182 (2-3),* 342-350.

Paranthaman, M., (2002). Non-fluorine based solution techniques to grow

superconducting $YBa_2Cu_3O_{7-x}$ films-A Review, in Next Generation HTS Conductors. A. Goyal, Editor. Plenum Publishing Corporation.

Parmigiani, F., Chiarello, Ripamonti, G., Goretzki, N. H. & Roll, U., (1987). Observation of Carboxylic Groups in the Lattice of Sintered $Ba_2YCu_3O_{7-Y}$ High-T_c Superconductors. *Physical Review B, 36(13),* 7148-7150.

Paterson, M.S. (1969), The ductility of rocks, Physics of Strength and Plasticity, ed. A.S. Argon, MIT press, pp. 377-392.

Peterson, D.E.,(2002). YBCO by Plused Laser Deposition International Workshop on Processing & Application of Superconductors, Gatlinburg Tennessee, USA.

Pharr, G.M. Oliver, W.C. & Brotzen, F.R., (1992). On the Generality of the Relationship Among Contact Stiffness, Contact Area, and Elastic Modulus During Indentation. *Journal of Materials Research, 7,* 613-617.

Pharr, G.M., (1998). Measurement of mechanical properties by ultra-low load indentation. *Materials Science and Engineering A 253,* 151-159.

Pharr, G.M., Oliver, W.C. & Brotzen, F.R., (1992). On the generality of the relationship among contact stiffness, contact area, and elastic modulus during indentation J. *Mater. Res. 7*, 613.

Phonthammachai, N., Rumruangwong, M., Gulari, E., Jamieson, A.M., Jitkarnka, S., Wongkasemjit, S. (2004). Synthesis and rheological properties of mesoporous nanocrystalline CeO_2 via sol-gel process. *Colloids and Surfaces A: Physicochem. Eng. Aspects, 247*, 61-68.

Pierre, A. C. (1998). *Introduction to sol-gel processing*. USA: Kluwer Academic Publishers.

Poisl, W.H., Oliver, W.C., Fabes, B.D., (1995). High temperature nanoindentation. *J. Mater. Res. 10,* 2024.

Poole, C.P., (1988). *Copper Oxide Superconductors*. New York: John Wiley & Sons Inc.

Qin, J., Huang, Y., Xiao, J., Hwang, K.C., (2009). The equivalence of axisymmetric indentation model for three-dimensional indentation hardness. *Journal of Materials Research 24*, 776-783.

Rillings, K.W. and J.F. Roberts, (1974.) A thermal study of hydrated lanthanide heptafluorobutyrates. *Thermochim. Acta, 10*, 285.

Roa, J.J., Capdevila, X.G., Martinez, M., Espiell, F., Segarra, M., (2007). Nanohardness and Young's modulus of YBCO samples textured by the Bridgman technique. *Nanotechnology*, 18, 385.

Rubich, M.W., Schoop, U., Verebelyi, D.T., Thieme, C. & Zhang, W., (2002). YBCO coated conductors. In Applied Superconductivity Conference. Houston-Texas, USA.

Saha, R. & Nix, W.D., (2002). Effects of the substrate on the determination of thin film mechanical properties by nanoindentation. *Acta Materialia 50 (1)*, 23-38.

Sandiumenge, F., Puig, T., Rabier, J., Plain, J., Obradors, X., (2000). Optimization of flux pinning in bulk melt textured 1–2–3 superconductors; Bringing dislocations under control. *Adv. Mater.* 12, 375.

Scheel, H.J., Berkowski, M., & Chabot, B., (1991). Substrates for High-Temperature Superconductors. *Physica C, 185,* 2095-2096.

Schrieff, Jr, & Mattis D. C., (1965). Localized Magnetic Moments in Dilute Metallic

Alloys - Correlation Effects. *Physical Review, 140(4A),* 1412-&.

Schwartz, R.W., Reichert, T.L., Clem, P.G., Dimos, D., & D. Liu, (1997). A comparison of diol and methanol-based chemical solution deposition routes for PZT thin film fabrication. *Integrated Ferroelectrics, 18(1-4),* 275-286.

Schwartz, R.W., Voigt, J.A., Tuttle, B.A., Payne, D.A., Reichert, T.L., & DaSalla R.S., (1997). Comments on the effects of solution precursor characteristics and thermal processing conditions on the crystallization behavior of sol-gel derived lead zirconate titanate thin films. *Journal of Materials Research, 12(2),* 444-456.

Sekler, J., Steinmann, P.A. & Hintermann, H.E., (1998). The scratch test: different critical load determination techniques. *Surf. Coat. Technol. 36,* 519-529.

Sheahen, T. P., (2002). Magnetism and currents in superconductors. In the Introduction to high-temperature superconductivity (17-18), New York: Kluwer Academic Pubishers.

Sheahen, T.P., (1994*). Introduction to High-Temperature Superconductivity*, New York: Plenum.

Shekhter, R. I., Galperin, Y., Garelik, L. Y., Isacsson, A., & Jonson, M., (2003). Shuttling of electrons and cooper pairs. *Journal of Physics: Condensed Matter, 15,* R441-R 469.

Shi, D., (1995). High Temperature Superconducting Materials Science and Engineering, New York: Pergamon Inc.

Smith, J.A., Cima, M.J., & Sonnenberg, N., (1999). High critical current density thick MOD-derived YBCO films. *IEEE Transactions on Applied Superconductivity, 9(2),* 1531-1534.

Sneddon, N., (1965). 'The Relation between load and penetration in the axisymmetric boussinesq problem for a punch of arbitrary profile. *Int. J. Eng. Sci,3,* 47-57.

Solovyov, V.F., Wiesmann, H.J., Wu, L.J., Zhu, Y.M., & Suenaga, M., (2000). Kinetics of YBa2Cu3O7 film growth by postdeposition processing. *Applied Physics Letters, 76(14),* 1911-1913.

Storåkers, B., Larsson, P.L., (1994). Analysis of cold and hot isostatic compaction of spherical particles. *J. Mech. Phys. Solids, 42*, 307.

Suresh S. & Giannakopoulos, A. E., (1998). On the use of nanoindentation for cementitious materials. Massachusetts Institute of Technology, *Report Inst-2/98.*

Suresh S. & Giannakopoulos,(1998). Determination of elastoplastic properties by instrumented sharp indentation. *Acta Mater. 46,* 5755.

Suresh, S., Alcala, J. & Giannakopoulos, A. E. MIT Case No. 7280, Massachusetts Institute of Technology (1996). Patent application pending.

Suresh, S., Giannakopoulos, A. E. & Alcala,(1997). Depth-Sensing Indentation Mechanism and Methodology for Mechanical Property Measurements. J. *Acta Mater. 45*, 1307.

Suryanarayanan, R., Nagarajan, R., Selih, H., & Ben-Dor, L., (2001). Preparation by sol-gel, structure and superconductivity of pure and fluorinated LaBa2Cu3O7-d. *Physica C, 361,* 40-44.

Tabor, D., (1951). *Hardness of Metals*, Clarendon Press, Oxford, UK.

Utke, I., Klemenz, C., Scheel, H.J., Sasaura, M., & Miyazawa, S., (1997). Misfit problems in epitaxy of high-Tc superconductors. *Journal of Crystal Growth 174(1-4),* 806-812.

Valli, J., (1987). Applications of the scratch test method for coating adhesion assessment. *Wear 115,* 215-221.

Varanasi, C.V., Barnes, P.N., Burke, J., Brunke, L., Maartense1, I., Haugan, T.J., Stinzianni, E.A., Dunn, K.A. & Haldar, P., (2006). Flux pinning enhancement inYBCO films with BaSnO3 Nanoparticles. *Supercond. Sci. Technol., 19*, L37-L41.

Vest, R.W. & Xu, J.J., (1988). PbTiO3 Films from Metalloorganic Precursors. *IEEE Transactions on Ultrasonics Ferroelectrics and Frequency Control, 35(6),* 711-717.

Wang, C.P., Do, K.B., Beasley, M.R., Geballe, T.H., & Hammond, R.H., (1997). Deposition of in-plane textured MgO on amorphous Si3N4 substrates by ion-beam-assisted deposition and comparisons with ion-beam-assisted deposited yttria-stabilized-zirconia. *Applied Physics Letters, 71(20),* 2955-2957.

Warnes, W. H., (2003). Principles of superconductivity. *ASM Handbook, Vol 2,* 1030-1042. ASM International.

Whelan, C. (2003). *BCS theory of superconductivity*. Physical Review.

Wu, M.K., (1987). Superconductivity at 93K in a new mixed phase Y-Ba-Cu-O compound system at ambient pressure. *Physics Review Letters, 58*, 908.

Wu, M.K., Ashburn, J.R., Torng, C.J., Hor, P.H., Meng, R.L., Gao, L., Huang, Z.J., Wang, Y.Q., & Chu, C.W., (1987). Superconductivity at 93-K in a New Mixed-Phase Y-Ba-Cu-O Compound System at Ambient Pressure. *Physical Review Letters, 58(9),* 908-910.

Xu, Y., & Shi, D. (n.d.). A review of coated conductor development. Dept. of

Chemical and Materials Engineering, University of Cincinnati 2 Metals & Ceramics Division, Oak Ridge National Laboratory (ORNL).

Xu, Y., Goyal, A., Rutter, N.A., Shi, D., Paranthaman, M., Sathyamurthy, S., Martin, P.M., & Kroeger, D.M., (2003). Fabrication of High Jc YBa2Cu3O7-d Films Using A Fluorine-Free Sol Gel Approach. *J. Mater. Res. 18(3)*, 677-681.

Xu, Y.L., Shi, D.L., McClellen, S., Buchanan, R., Wang, S.X., & Wang, L.M., (2001). Deposition of epitaxial YBCO thin film on single domain YBCO substrate for the development of RF components. *IEEE Transactions on Applied Superconductivity 11(1)*, 2865-2868.

Yamada, Y., Kim, S., Araki, T., Takahashi, Y., Yuasa, T., Kurosaki, H., (2001). Critical current density and related microstructures of TFA-MOD YBCO coated conductors. *Physica C 357,* 1007-1010.

Yoshida, Y., Matsumoto, K., Miura, M., Ichino, Y., Takai, Y., Ichinose, A., Mukaida M., Horii, S., (2006). Controlled nanoparticulate flux pinning structures in RE1+xBa2-xCu3Oy films. *Physica C 445-448,* 637-642.

Zhao, M.H., Ogasawara, N., Chiba, N., Chen, X., (2006). A new approach to measure the elastic-plastic properties of bulk materials using spherical indentation. *Acta Materialia 54 (1)*, 23-32.

Zielinski, W., Huang, H., & Gerberich, W., (1993). Microscopy and microindentation mechanics of single crystal Fe−3 % Si. *J. Mater. Res. 8,* 1300.